

Ottawa F-65 Sand Characterization

By

ANA MARIA PARRA BASTIDAS
B.S. (Pontificia Universidad Javeriana Cali) 2008
M.S. (University of Florida) 2010

DISSERTATION

Submitted in partial satisfaction of the requirements for the degree of

DOCTOR OF PHILOSOPHY

in

Civil and Environmental Engineering

in the

OFFICE OF GRADUATE STUDIES

of the

UNIVERSITY OF CALIFORNIA

DAVIS

Approved:

Ross W. Boulanger, Chair

Jason T. DeJong

Bruce L. Kutter

Committee in Charge

2016

To God for providing this amazing opportunity

To my parents for their infinite love, support, encouragement and comprehension

To my family and my friends for cheering for me up during this whole process

Ottawa F-65 Sand Characterization

Abstract

A comprehensive characterization of Ottawa F-65 sand is presented. Specific gravity, maximum and minimum dry density tests are included; different values of maximum and minimum dry densities result from using different testing methods. Constant head hydraulic conductivity tests are included over a range of relative densities; hydraulic conductivity decreases with relative density. IDC tests are included for loose and dense specimens loaded to different high stress levels to study the influence of these two variables in the particle crushing of this sand; particle crushing increases with stress and decreases with density. Simple shear (DSS) undrained monotonic tests are included for loose and dense normally consolidated specimens consolidated to various stress levels; dilation tendencies decrease with increasing void ratio and confining stress. DSS undrained cyclic tests are included for loose and dense normally consolidated specimens consolidated to various stress levels, as well as for loose over-consolidated specimens with an over-consolidation ratio (OCR) of 4 sheared with an initial vertical effective stress of a 100 kPa; cyclic resistance increases with density and OCR and decreases with consolidation stress. Pre-straining DSS undrained cyclic tests are included for loose and dense normally consolidated specimens consolidated to a vertical effective stress of a 100 kPa; cyclic resistance increases with recurrent liquefaction and cyclic pre-straining on loose and dense specimens, this is due to a combination of densification and the evolution of a more stable fabric within the specimens. Element loading simulations using the PM4Sand model with two calibrations are included: calibration No. 1 which only included adjusting one model parameter and calibration No. 2 which included adjusting two model parameters. Calibration No. 2 provided model responses which are closer to the experimental responses.

Acknowledgements

This dissertation would have not been possible without the support, comprehension and generous friendship from many individuals.

Thanks to God for this awesome opportunity of allowing me to accomplish some of my dreams that seemed very difficult in the past, and for all the blessings he sends to me specially in the form of the presence of wonderful people in my life.

Thanks to my parents for their infinite love, support and comprehension. I would not have been able to conclude my PhD without their support. I would like to thank the rest of my family for their love, encouragement and comprehension. I really loved all the support that I received from all of you in the form of messages, calls and Facebook interactions while being in California.

Thanks to my advisors Professors Ross Boulanger and Jason DeJong for their wisdom, encouragement, support and patience. They fostered my technical and professional skills. Ross has been an excellent mentor and major professor, who really encouraged me to be a more critical engineer. I really admire his extraordinary ability to switch from a very practical engineer to a very fundamental scientist when the circumstances required so; he is able to understand many complicated phenomenon in depth and he is able to explain those phenomenon with simplicity. Jason has been an excellent laboratory mentor with a very deep experimental knowledge and I am really grateful for his help to understand some complicated phenomenon that I observed in my experiments. I have been really honored to have the opportunity to work with them to accomplish this project.

Thanks to Professor Bruce Kutter for his feedback and encouragement, but also for his immense curiosity which pushed me hard and leaded me to use my imagination to understand some mechanical behaviors that I observed in the materials I tested. He also encouraged me to challenge ideas about soil mechanics.

Thanks to Professor John Harvey for being part of my PhD exam committee. His comments on my research proposal were very helpful during the preparation for my qualifying exam and his Asphalt Mixes Design class was great.

Thanks to Colciencias and Colfuturo for fully funding my PhD and for giving me the opportunity of participating of their international doctoral scholars program. It has been an honor for me to be part of the Colombian scientific community working outside Colombia and to represent our country with love and pride. This have never been possible without their support.

Thanks to all my GGSS and SILLAB colleagues for their company and friendship during my PhD. Thanks to Mohammad Khosravi for being a great friend and colleague, for providing advice on so many professional and personal matters, for providing support and comprehension constantly but also for challenging my ideas and attitudes when required: for being an awesome and unconditional friend. Thanks to Sean Munter for being a wonderful friend and colleague. Thanks to Adam Price and Professor Katerina Ziotopoulou for providing feedback and discussion of my work. Thanks to Trevor Carey for helping to put my online database together and for interesting conversations about my data. Thanks to Professor Mason Ghafghazi for great friendship, interesting conversations about my One-dimensional compression results and professional advice. Thanks to R.P Erickson for teaching me to run the One-dimensional compression tests. Thanks Kate Darby for including my data in her Geo-structures 2016 conference paper. Thanks to the centrifuge visitor scholars for their friendship and for sharing their awesome adventures in Davis with me: Riccardo Cappa, Eva Agapaki, Kenneth Miles, Deepak Rayamajhi and Professors Samuel Yniesta, Ali Khosravi and Suji Tamura. Thanks to Sean Salazar for working with me in the lab during his PEER internship program. Thanks to Sean Ahdi for his friendship and time during the conferences. Thanks to Bill Sluis and Daret Kehlet for their patience, support and help with the One-dimensional compression equipment design, troubleshooting and testing.

Thanks to my Davis friends, they have been my second family in California. Thanks to Grazy Tresoldi and Mr. Bentley AuAu for unconditional friendship, support and company. Thanks to my Latinx

friends for their friendships, parties and trips: Angie Cortez, Maciel Hernandez, Rachel Restani, Ana Maria Eljah, Maira Pulido, Arturo Castillo, Lira Palmer, Rosa Manzo, Diana and Tono Guzman, Lynda Lee and Paul Barajas, Carlos Alva and Maria Cariaga Font. Thanks to the Spanish-Portuguese club/ Sophia's latin night friends: Theresa Bauch, Anna Cusco Marti, Aurea Soriano and Oscar Cuadros, Branko Popovich, Parsa Taheri, Tiago Mendez, Anna Crestani, Marzieh Gh, Jennifer Tyrehageman,, Joao Ventrici, Leana Goetz and Leandro D'Abronzio; with them I experienced the finest bbqs and latin parties in Davis. Thanks to my Colombian UCD fellow scholars and friends: Natalia Owens, Cristina Bustamante, Maria Isabel Hernandez, Wilson Ramirez, Federico Castillo, Andres Barragan, Ernesto Vela, Shirley Estupinan and Alejandro Triana, for making me to feel in Colombia while in California. Thanks to Mohammad's friends: Masoud Rahman, Sina Beбето Gilani, Kamran Asadpour and Hesam Nabi for becoming my good friends as well.

Thanks to the Professors at the University of Florida for giving me excellent geotechnical engineering knowledge but also for giving me a very different perspective on geotechnical engineering than the one I got at the University of California, Davis. Specially, thanks to Professor Frank Townsend for believing in my capacity of entering and finishing my PhD on a top US University and for his encouragement, mentoring, friendship, networking with the Colombian Gators and for the song of the day. Thanks to my colleagues and friends from UF for encouraging me to apply for my PhD and for their friendship: Juan Antonio Balderrama, Professor PCarlos Raul Rodriguez, Patrick Dunn, Javier Jimenez, Professor Alvaro Guarin, Professor Yu-Min Su, Scott Wasman, Porfessor Khiem Tran, Weitao Li, Reebie Sims, Cristian Cocconcelli, Marco Isola, Michael Bekoe, Patrick Bekoe and Jian Zou. Go Gatos!!.

Thanks to my Colombian friends and colleagues for their friendship and for keeping in touch while we are all living in different places of the world: Juan Jose Escobar, Juan Carlos Chacon, Pablo Taborda, Carolina Mosquera, Veronica Ramirez, Maria Alejandra Caicedo, Diego Muriel y Lina Yohana Henao.

Contents

Abstract	iii
Acknowledgements	iv
List of Figures	x
List of Tables	xiv
1. Introduction	1
1.1 Background	1
1.2 Scope.....	2
1.3 Organization of the Dissertation	3
2. Index characteristics	6
2.1 Introduction.....	6
2.2 Grain Size Distribution and Grain Characteristics.....	6
2.3 Specific Gravity of Solids.....	8
2.4 Minimum Dry Density.....	9
2.5 Maximum Dry Density	10
3. Hydraulic conductivity	20
3.1 Introduction.....	20
3.2 Hydraulic Conductivity Measurements	20

3.3 Hydraulic Conductivity Comparisons to Empirical Equations	23
4. One-dimensional Compression Characteristics	30
4.1 Introduction.....	30
4.2 IDC testing procedures.....	30
4.3 Stress strain response in compression.....	35
5. Monotonic Direct Simple Shear Characteristics	67
5.1 Introduction.....	67
5.2 Monotonic DSS testing procedures.....	67
5.3 Stress strain and stress path responses	69
5.4 Critical state friction angle.....	73
5.5 Critical state line	74
6. Cyclic Direct Simple Shear Characteristics	87
6.1 Introduction.....	87
6.2 Cyclic DSS Testing Procedures	87
6.3 Cyclic Stress-Strain Responses.....	88
6.4 Cyclic Resistance Ratio vs. Number of Cycles.....	91
6.5 Reconsolidation after Liquefaction.....	95
6.6 Post-Cyclic Monotonic Strengths	98

7. Pre-Straining Cyclic Direct Simple Shear Characteristics	111
7.1 Abstract.....	111
7.2 Introduction.....	112
7.3 Experimental Approach	115
7.4 Monotonic and Cyclic DSS Results for Virgin Specimens	117
7.5 Cyclic DSS with pre-straining	117
7.6 Discussion.....	120
7.7 Conclusions.....	121
8. Calibration of PM4Sand for Ottawa F-65 Sand	131
8.1 Introduction.....	131
8.2 PM4sand constitutive model.....	132
8.3 Small strain modulus, Critical State Line and other fixed parameters.....	135
8.4 Calibration No. 1.....	135
8.5 Calibration No. 2.....	138
8.6 Summary remarks	140
9. Conclusions and Future Directions	164
9.1 Summary and Conclusions	164
9.2 Future Directions	169
10. Bibliography	174

List of Figures

Figure 2.1 Grain size distribution	18
Figure 2.2 Grain size distribution from this project compared to those obtained by several other researchers.....	19
Figure 2.3 SEM images of Ottawa F-65 sand (images obtained by Michael Gomez).....	19
Figure 3.1 Permeameter cell	25
Figure 3.2 Permeameter configuration.....	25
Figure 3.3 Velocity vs. hydraulic gradient test # 2	26
Figure 3.4 Relative density vs. hydraulic conductivity.....	26
Figure 3.5 Void ratio vs. hydraulic conductivity	27
Figure 3.6 Square of void ratio vs. hydraulic conductivity.....	27
Figure 3.7 Cube of void ratio vs. hydraulic conductivity	28
Figure 3.8 Void ratio vs. hydraulic conductivity comparison to data from other researchers	28
Figure 3.9 Void ratio vs. hydraulic conductivity comparison to empirical equations	29
Figure 3.10 Void ratio vs. hydraulic conductivity comparison to empirical equations semi-log	29
Figure 4.1 500 lbs capacity consolidation frame	42
Figure 4.2 Pneumatic consolidation frame front view.....	43
Figure 4.3 Pneumatic consolidation frame back view	44
Figure 4.4 Pneumatic consolidation system detail.....	45
Figure 4.5 100 Kips capacity MTS load frame.....	46
Figure 4.6 IDC mold components (left) and assembly (right)	47
Figure 4.7 IDC mold vessel plans	48
Figure 4.8 IDC mold cap plans	49
Figure 4.9 IDC mold cap's top screw hole detail plans	50
Figure 4.10 IDC mold O-Rings specifications.....	51

Figure 4.11 Dry funnel deposition method	52
Figure 4.12 Air pluviation method.....	52
Figure 4.13 Aluminum pedestal for placing samples for SEM imaging.....	53
Figure 4.14 SEM microscope	53
Figure 4.15 Compression curve	54
Figure 4.16 Limited Compression Curve (redrawn from Pestana and Whittle 1995)	54
Figure 4.17 Volumetric strain vs. vertical effective stress (semi-log scale)	55
Figure 4.18 Volumetric strain vs. vertical effective stress (arithmetic scale)	55
Figure 4.19 From top to bottom: original sand, grains from loose specimen and grains from dense specimen loaded to $\sigma'_{vmax}=30$ MPa	56
Figure 4.20 GSD after 1DC with $\sigma'_{vmax}=30$ MPa.....	57
Figure 4.21 GSD after 1DC with $\sigma'_{vmax}=30$ MPa (log-log scale).....	57
Figure 4.22 From top to bottom: original sand, grains from loose specimen and grains from dense specimen loaded to $\sigma'_{vmax}=70$ MPa	58
Figure 4.23 GSD after 1DC with $\sigma'_{vmax}=70$ MPa.....	59
Figure 4.24 From top to bottom: original sand, grains from loose specimen and grains from dense specimen loaded to $\sigma'_{vmax}=140$ MPa	60
Figure 4.25 GSD after 1DC with $\sigma'_{vmax}=140$ MPa.....	61
Figure 4.26 GSD from dry sieving and hydrometer vs. wet sieving tests results on loose specimens after 1DC with $\sigma'_{vmax}=30$ MPa.....	61
Figure 4.27 GSD from dry sieving and hydrometer vs. wet sieving tests results on dense specimens after 1DC with $\sigma'_{vmax}=30$ MPa.....	62
Figure 4.28 GSD from dry sieving and hydrometer vs. wet sieving tests results on loose specimens after 1DC with $\sigma'_{vmax}=70$ MPa.....	62
Figure 4.29 GSD from dry sieving and hydrometer vs. wet sieving tests results on dense specimens after 1DC with $\sigma'_{vmax}=70$ MPa.....	63

Figure 4.30 GSD from dry sieving and hydrometer vs. wet sieving tests results on loose specimens after 1DC with $\sigma'_{vmax} = 140$ MPa.....	63
Figure 4.31 GSD from dry sieving and hydrometer vs. wet sieving tests results on dense specimens after 1DC with $\sigma'_{vmax} = 140$ MPa.....	64
Figure 4.32 GSD after 1DC from loose specimens.....	64
Figure 4.33 GSD after 1DC from dense specimens.....	65
Figure 4.34 Particle breakage stages (described by Nakata et al. 2001).....	65
Figure 4.35 Particle breakage stages examples, from top left to bottom right: (1) surface grinds, (2) asperities break, (3) asperities split, (4) particles split.....	66
Figure 5.1 Direct simple shear apparatus (Brandon 2013)	77
Figure 5.2 DSS Frame including assembly.....	77
Figure 5.3 Direct simple shear assembly components (left) and assembly (right)	78
Figure 5.4 DSS mold details	79
Figure 5.5 Stress path for $\sigma'_{vc}=100$ kPa DSS monotonic tests	80
Figure 5.6 Stress strain response for $\sigma'_{vc}=100$ kPa DSS monotonic tests	80
Figure 5.7 Stress path for $\sigma'_{vc}=400$ kPa DSS monotonic tests	81
Figure 5.8 Stress strain response for $\sigma'_{vc}=400$ kPa DSS monotonic tests	81
Figure 5.9 Stress path for $\sigma'_{vc}=800$ kPa DSS monotonic tests	82
Figure 5.10 Stress strain response for $\sigma'_{vc}=800$ kPa DSS monotonic tests	82
Figure 5.11 Stress path for tests on specimens with $D_R < 35\%$	83
Figure 5.12 Stress path for tests on specimens with $35\% < D_R \leq 69\%$	83
Figure 5.13 Stress path for tests on specimens with $69\% < D_R$	84
Figure 5.14 Constant volume friction angle selection	85
Figure 5.15 Constant volume friction angle from the quasi-steady state	86
Figure 5.16 Critical state line and monotonic tests results.....	86
Figure 6.1 Cyclic loading responses of a loose specimen under a 100 kPa sheared up to $\gamma_{peak}=5\%$	100

Figure 6.2 Cyclic loading responses of a dense specimen under a 100 kPa sheared up to $\gamma_{\text{peak}}=5\%$	101
Figure 6.3 Cyclic loading responses of a loose specimen under a 100 kPa sheared up to $\gamma_{\text{peak}}=20\%$	101
Figure 6.4 Cyclic loading responses of a dense specimen under a 100 kPa sheared up to $\gamma_{\text{peak}}=9\%$	102
Figure 6.5 CRR vs. $N_{\gamma=3\%}$ curves from DSS tests on loose specimens.....	102
Figure 6.6 CRR vs. N_{γ} curves from DSS tests on loose specimens for failure criteria of $\gamma=1, 3$ and 5% .	103
Figure 6.7 CRR vs. $N_{\gamma=3\%}$ curves from DSS tests on dense specimens.....	103
Figure 6.8 CRR vs. N_{γ} curves from DSS tests on dense specimens for failure criteria of $\gamma=1, 3$ and 5%	104
Figure 6.9 Consolidation and reconsolidation after cyclic shearing results from tests on loose specimens	104
Figure 6.10 Consolidation and reconsolidation after cyclic shearing results from tests on dense specimens	105
Figure 6.11 Consolidation and reconsolidation after cyclic shearing results from tests on loose specimens in semi-log scale	105
Figure 6.12 Consolidation and reconsolidation after cyclic shearing results from tests on dense specimens in semi-log scale	106
Figure 6.13 Young's modulus relationship from unloading portion from tests on OCR=4 specimens....	106
Figure 6.14 Reconsolidations results compared to Ishihara and Yoshimine's (1992) reconsolidation curves	107
Figure 6.15 Ishihara and Yoshimine's (1992) reconsolidation curves redrawn by Idriss and Boulanger (2008) to include experimental results.....	107
Figure 6.16 Results from a DSS cyclic test and from a DSS monotonic test performed after the cyclic test on a loose specimen consolidated under 50 kPa	108
Figure 6.17 Results from a DSS cyclic test and from a DSS monotonic test performed after the cyclic test on a dense specimen consolidated under 50 kPa	108

Figure 6.18 Results from a DSS cyclic test, from a DSS monotonic test performed after the cyclic test and from a DSS monotonic test on a virgin specimen. Tests are from loose specimens consolidated under 100 kPa	109
Figure 6.19 Results from a DSS cyclic test, from a DSS monotonic test performed after the cyclic test and from a DSS monotonic test on a virgin specimen. Tests are from dense specimens consolidated under 100 kPa	109
Figure 6.20 Results from a DSS cyclic test, from a DSS monotonic test performed after the cyclic test and from a DSS monotonic test on a virgin specimen. Tests are from loose specimens consolidated under 400 kPa	110
Figure 6.21 Results from a DSS cyclic test, from a DSS monotonic test performed after the cyclic test and from a DSS monotonic test on a virgin specimen. Tests are from dense specimens consolidated under 400 kPa	110
Figure 7.1 Conceptual effect of recurrent liquefaction events: (a) soil element in liquefied layer, (b) void ratio–vertical effective stress paths for a series of earthquake loadings causing liquefaction and subsequent reconsolidation, and (c) evolution of cyclic strength versus indices of density (after Price et al. 2016a)	123
Figure 7.2 Effects of freeze-thaw cycle on the cyclic resistance of saturated clean sand undrained cyclic triaxial tests: Left: Data from Singh et al. (1982) for sand at $D_R=48\%$. Right: Data from Goto and Nishio (1988) for sand at $D_R=90\%$ (after Yoshimine et al. 1994 and Idriss and Boulanger 2008)	124
Figure 7.3 Cyclic stress ratio versus number of uniform load cycles to cause $r_u = 100\%$ from shake table tests on air pluviated sand specimens with and without pre-straining (after Seed et al. 1977)	124
Figure 7.4 Cyclic stress ratio versus number of uniform load cycles to cause double amplitude (DA) axial strain of 5% from cyclic undrained triaxial tests results on air pluviated Toyoura sand specimens with pre-straining to different peak axial strains (after Oda et al. 2001).....	125
Figure 7.5 Monotonic responses for loose and dense virgin specimens of Ottawa F-65 sand	125
Figure 7.6 Cyclic resistance curves for loose and dense specimens of Ottawa F-65 sand	126

Figure 7.7 Number of cycles to peak 3% shear strain vs. loading stage on test PS6	126
Figure 7.8 Undrained cyclic DSS test results from loading stages A3, A6, B1 and D1 for test PS6	127
Figure 7.9 Undrained cyclic DSS test results on dense initially NC specimens: (a) virgin specimen from test V23, and (b) pre-strained specimen from test PS6 during loading stage D1	128
Figure 7.10 Conversion of applied CSR to $CSR_{N=15}$ cycles for $\gamma_{max} = 3\%$ for each loading stage in test PS6	129
Figure 7.11 Evolution of the $CRR_{N=15}$ for γ_{max} of 1% and 3% versus average void ratio for test PS6.....	129
Figure 7.12 Evolution of the $CRR_{N=15}$ to $\gamma_{max} = 3\%$ versus average void ratio for virgin and pre-strain specimens.....	130
Figure 8.1 G_o vs. D_R for PM4Sand	142
Figure 8.2 G_{max} vs. e from air pluviated specimens	143
Figure 8.3 G_{max} vs. e	143
Figure 8.4 Critical state line position bounds and initial points from monotonic DSS tests.....	144
Figure 8.5 CRR curves from DSS tests and PM4Sand simulations for loose specimens consolidated to 50 kPa	144
Figure 8.6 CRR curves from DSS tests and PM4Sand simulations for loose specimens consolidated to 100 kPa	145
Figure 8.7 CRR curves from DSS tests and PM4Sand simulations for loose specimens consolidated to 400 kPa	145
Figure 8.8 Stress-strain responses from cyclic DSS tests and PM4Sand calibration No. 1 simulations on a loose specimen consolidated to 50 kPa.....	146
Figure 8.9 Stress-strain responses from cyclic DSS tests and PM4Sand calibration No. 1 simulations on a loose specimen consolidated to 100 kPa.....	146
Figure 8.10 Stress-strain responses from cyclic DSS tests and PM4Sand calibration No. 1 simulations on a loose specimen consolidated to 400 kPa	147

Figure 8.11 Stress-strain responses from monotonic DSS tests and PM4Sand calibration No. 1 simulations on a loose specimen consolidated to 100 kPa	147
Figure 8.12 Stress-strain responses from monotonic DSS tests and PM4Sand calibration No. 1 simulations on a loose specimen consolidated to 400 kPa	148
Figure 8.13 Stress-strain responses from monotonic DSS tests and PM4Sand calibration No. 1 simulations on a loose specimen consolidated to 800 kPa	148
Figure 8.14 CRR curves from DSS tests and PM4Sand calibration No. 1 simulations for dense specimens consolidated to 50 kPa	149
Figure 8.15 CRR curves from DSS tests and PM4Sand calibration No. 1 simulations for dense specimens consolidated to 100 kPa	149
Figure 8.16 CRR curves from DSS tests and PM4Sand calibration No. 1 simulations for dense specimens consolidated to 400 kPa	150
Figure 8.17 Stress-strain responses from cyclic DSS tests and PM4Sand calibration No. 1 simulations on a dense specimen consolidated to 50 kPa	150
Figure 8.18 Stress-strain responses from cyclic DSS tests and PM4Sand calibration No. 1 simulations on a loose specimen consolidated to 100 kPa.....	151
Figure 8.19 Stress-strain responses from cyclic DSS tests and PM4Sand calibration No. 1 simulations on a dense specimen consolidated to 400 kPa	151
Figure 8.20 Stress-strain responses from monotonic DSS tests and PM4Sand calibration No. 1 simulations on a dense specimen consolidated to 100 kPa	152
Figure 8.21 Stress-strain responses from monotonic DSS tests and PM4Sand calibration No. 1 simulations on a dense specimen consolidated to 400 kPa	152
Figure 8.22 Stress-strain responses from monotonic DSS tests and PM4Sand calibration No. 1 simulations on a dense specimen consolidated to 800 kPa	153
Figure 8.23 CRR curves from DSS tests and PM4Sand calibration No. 2 simulations for loose specimens consolidated to 50 kPa	154

Figure 8.24 CRR curves from DSS tests and PM4Sand calibration No. 2 simulations for loose specimens consolidated to 100 kPa	154
Figure 8.25 CRR curves from DSS tests and PM4Sand calibration No. 2 simulations for loose specimens consolidated to 400 kPa	155
Figure 8.26 Stress-strain responses from cyclic DSS tests and PM4Sand calibration No. 2 simulations on a loose specimen consolidated to 50 kPa.....	155
Figure 8.27 Stress-strain responses from cyclic DSS tests and PM4Sand calibration No. 2 simulations on a loose specimen consolidated to 100 kPa.....	156
Figure 8.28 Stress-strain responses from cyclic DSS tests and PM4Sand calibration No. 2 simulations on a loose specimen consolidated to 400 kPa.....	156
Figure 8.29 Stress-strain responses from monotonic DSS tests and PM4Sand calibration No. 2 simulations on a loose specimen consolidated to 100 kPa	157
Figure 8.30 Stress-strain responses from monotonic DSS tests and PM4Sand calibration No. 2 simulations on a loose specimen consolidated to 400 kPa	157
Figure 8.31 Stress-strain responses from monotonic DSS tests and PM4Sand calibration No. 2 simulations on a loose specimen consolidated to 800 kPa	158
Figure 8.32 CRR curves from DSS tests and PM4Sand calibration No. 2 simulations for dense specimens consolidated to 50 kPa	158
Figure 8.33 CRR curves from DSS tests and PM4Sand calibration No. 2 simulations for dense specimens consolidated to 100 kPa	159
Figure 8.34 CRR curves from DSS tests and PM4Sand calibration No. 2 simulations for dense specimens consolidated to 400 kPa	159
Figure 8.35 Stress-strain responses from cyclic DSS tests and PM4Sand calibration No. 2 simulations on a dense specimen consolidated to 50 kPa	160
Figure 8.36 Stress-strain responses from cyclic DSS tests and PM4Sand calibration No. 2 simulations on a dense specimen consolidated to 100 kPa	160

Figure 8.37 Stress-strain responses from cyclic DSS tests and PM4Sand calibration No. 2 simulations on a dense specimen consolidated to 400 kPa	161
Figure 8.38 Stress-strain responses from monotonic DSS tests and PM4Sand calibration No. 2 simulations on a dense specimen consolidated to 100 kPa	161
Figure 8.39 Stress-strain responses from monotonic DSS tests and PM4Sand calibration No. 2 simulations on a dense specimen consolidated to 400 kPa	162
Figure 8.40 Stress-strain responses from monotonic DSS tests and PM4Sand calibration No. 2 simulations on a dense specimen consolidated to 800 kPa	162

List of Tables

Table 2.1 Summary of grain size distribution data for Ottawa F-65 sand (Carey et al. 2015)	12
Table 2.2 Summary of specific gravity of solids data for Ottawa F-65 sand (Carey et al. 2015).....	13
Table 2.3 Summary minimum dry density and maximum void ratio data for Ottawa F-65 sand.....	14
Table 2.4 Summary minimum dry densities obtained by the ASTM D4254 method for Ottawa F-65 sand (Carey et al. 2015).....	15
Table 2.5 Summary minimum dry densities obtained by the Ruffatto's method for Ottawa F-65 sand (Carey et al. 2015)	16
Table 2.6 Summary maximum dry density and minimum void ratio data for Ottawa F-65 sand.....	17
Table 2.7 Summary maximum dry densities obtained by the Ruffatto's method for Ottawa F-65 sand (Carey et al. 2015)	18
Table 3.1 Summary of hydraulic conductivity measurements by different researchers	24
Table 5.1 Effective friction angles at critical state measured by others.....	75

Chapter 1

Introduction

1.1 Background

The ability to design for and mitigate against the effects of liquefaction on civil infrastructure requires an understanding of dominant mechanisms and the ability to predict performance with various levels of analysis tools. Tools to predict performance of facilities vary from simple correlations to complex physical and numerical models. Dynamic centrifuge models are complex physical models that provide a means to understand fundamental mechanisms playing an important role in liquefaction phenomena, as well as to investigate the fundamental mechanisms of soil-structure interaction or remediation of soil-structure systems when subjected to dynamic loads. These physical models constitute a valuable tool to validate numerical methods for predicting liquefaction triggering and its consequences for a range of soil and soil-structure systems.

Dynamic centrifuge model tests provide a means to investigate fundamental mechanisms and to validate analysis tools for soils and soil-structure systems under earthquake loading. Some of the fundamental mechanisms or responses of the soil that can be studied in the centrifuge include: pore pressure generation and diffusion, ground deformations, lateral spreading, volumetric strains due to reconsolidation, void redistribution, changes in the dynamic response of the model due to liquefaction of the material within the model, soil-structure-foundation interaction, and remediation techniques. The detailed recordings obtained during centrifuge tests can provide a thorough test of how well numerical models are able approximate these various mechanisms and behaviors.

Recent efforts to advance the profession's ability to numerically simulate liquefaction problems have benefited from coordinated efforts under the NEES and NHERI programs and collaborative research projects like the Liquefaction Experiment and Analysis (LEAP) ([Manzari et al. 2014](#)). Numerical simulations of liquefaction problems will benefit from LEAP because this project will provide experimental data for validation and assessment of various constitutive models and numerical analysis platforms used by different researchers. It will also provide insight in the variation of liquefaction predictions due to differences in the calibration and modelling procedures used by different modelers.

1.2 Scope

Ottawa F-65 sand was recently adopted as the standard testing soil at the centrifuge facility at UC Davis and in the collaborative LEAP study, and thus there was a need for a detailed characterization of the physical and mechanical properties of this sand. This sand was chosen as the new standard testing soil at the centrifuge because it has ideal characteristics of a standard testing sand such as: uniform gradation, small fines content (<1%), rounded particles, high quartz content (>99%), reliable commercial source, and stable characteristics across batches obtained over time. The properties of this sand are consistent among different sand batches because the supplier monitors the screening process closely and the final product has fewer impurities than other grounded silica products from other companies ([US Silica 2016](#)). Additionally, the cost of each sand batch is reasonable and the supplier has guaranteed the availability of this sand in the long term.

Existing experimental data for Ottawa F-65 sand includes contributions from several past research studies, although there were certain limitations in the database that are important for the calibration of the numerical models. Limitations to the existing experimental data required for calibration of constitutive models included: variations in the fines content, specific gravity of solids and minimum and maximum dry densities from different research teams, absence of one-dimensional compression (1DC) results in the high stresses range and absence of undrained monotonic and cyclic direct simple shear (DSS) results.

Agreement among maximum and minimum dry densities and specific gravity results is important for constitutive modelling calibration because several constitutive models such as PM4Sand (Boulanger and Ziotopoulou 2015) utilize these index properties. One-dimensional compression results in the high stresses range are important because they enable definition of the Limiting Compression Curve (LCC) regime (Pestana and Whittle 1995), which is an input parameter of the MIT-S1 constitutive model (Pestana and Whittle 1999) that is currently in use at UC Davis in the “*CPT-Based Characterization of Intermediate Soils*” research project (Boulanger and DeJong 2012). The CPT project aims to validate liquefaction triggering curves for intermediate soils with a mechanics based framework and Ottawa F-65 sand is one of the soils used in this study. Monotonic and cyclic DSS tests are required for the CPT project and are also valuable for validation and calibration of several constitutive models used as part of the LEAP project.

The purpose of this thesis is to provide a thorough characterization of Ottawa sand F-65. The data is archived at the NEES project warehouse at www.NEESHub.org for public distribution. “*The NEES project warehouse is a centralized data repository for sharing and publishing earthquake engineering research data from experimental and numerical studies*” (NEES 2016). Researchers working at the UC Davis Center for Geotechnical Modeling and around the world have access to detailed information about the experimental results, including each test’s general information, procedures, and results. This information provides experimental data for researchers to validate numerical model responses against experimental results, including responses from specimens subjected to a wide range of loading paths and with a variety of initial dry density and confining stress conditions.

1.3 Organization of the Dissertation

The dissertation contains eight additional chapters. Chapters two through seven contain the experimental characterization of the physical and the mechanical properties of this sand. Chapter eight contains the results

from single-element simulations using the constitutive model PM4Sand. Chapter nine contains a summary of the findings from this work and future directions of this research project.

The organization of this dissertation is as follows:

Chapter 2 summarizes the index tests results for Ottawa F-65 sand including: Scanning Electron Microscope (SEM) images of the original particles, grain size distribution, grains characteristics, specific gravity of solids (G_s), minimum dry densities ($\rho_{d \text{ min}}$) and maximum dry densities ($\rho_{d \text{ max}}$).

Chapter 3 summarizes the hydraulic conductivity results for Ottawa F-65 sand including: results on specimens prepared to different dry densities, comparison with results obtained by others, and comparison with results predicted from empirical correlations.

Chapter 4 summarizes the IDC results for Ottawa F-65 sand including: drained IDC results on normally consolidated loose and dense prepared specimens loaded to maximum vertical compressive stresses (σ'_v) of 30 MPa, 70 MPa and 140 MPa, post-compression grain size distributions and SEM images on samples recovered from the compressed specimens.

Chapter 5 summarizes the monotonic DSS results for Ottawa F-65 sand including: undrained DSS results from tests on normally consolidated loose and dense prepared specimens consolidated to a vertical effective stress (σ'_{vc}) of 100 kPa, 400 kPa and 800 kPa. This chapter also presents the critical state friction angle (ϕ'_{cv}) and the inferred Critical State Line (CSL) for this sand.

Chapter 6 summarizes the cyclic DSS results for Ottawa F-65 sand including: undrained DSS results from tests on normally consolidated loose and dense prepared specimens consolidated to σ'_{vc} of 50 kPa, 100 kPa and 400 kPa, and undrained DSS results from tests on over-consolidated loose specimens with and Over Consolidation Ratio (OCR) of 4 and sheared with a vertical confining stress of σ'_{vc} of 100 kPa.

Chapter 7 summarizes the results of pre-straining cyclic DSS tests for Ottawa F-65 sand including: undrained DSS results on normally consolidated and over-consolidated (OCR=4) loose specimens consolidated to σ'_{vc} of 100 kPa and subjected to several shearing and reconsolidation stages.

Chapter 8 summarizes the results from element loading tests simulations using the PM4Sand constitutive model (Boulanger and Ziotopoulou 2015) including: calibration to cyclic resistance curves from undrained DSS cyclic tests in loose and dense specimens consolidated to σ'_{vc} of 100 kPa, model responses to monotonic undrained DSS loading in loose and dense specimens consolidated to σ'_{vc} of 100 kPa, 400 kPa and 800 kPa, and model responses to cyclic undrained DSS loading in loose and dense specimens consolidated to σ'_{vc} of 50 kPa, 100 kPa and 400 kPa.

Chapter 9 summarizes the main findings from this project as well the future directions to extend this research.

Chapter 2

Index Characteristics

2.1 Introduction

This chapter summarizes the index tests results for Ottawa F-65 sand including: SEM images of the original particles, grain size distribution and grains characteristics, specific gravity of solids (G_s), minimum dry densities ($\rho_{d \text{ min}}$) and maximum dry densities ($\rho_{d \text{ max}}$).

2.2 Grain Size Distribution and Grain Characteristics

The Ottawa F-65 sand batch was purchased from US Silica in 2014. Ottawa F-65 sand is classified as a whole grained silica sand that is produced by US Silica. This sand is an inert, white silica sand with rounded grains, with a quartz content of 99.7% and with little to no fines ([US Silica 2016](#)). Ottawa F-65 sand is mined and processed close to the Illinois and Fox Rivers near to Ottawa Illinois; soft loose or poorly consolidated and poorly cemented St. Peter Sandstone deposits are excavated near Ottawa and are separated by mechanical sorting. However, the St. Peter Sandstone formation is extensive as it “spans north-south from Minnesota to Arkansas and east-west from Illinois to Nebraska and South Dakota” (St. Peter Sandstone, [Wikipedia 2016](#)). This geologic formation is a sedimentary rock formation composed by rounded and highly spherical sand grains with silicon dioxide (SiO_2) contents that are higher than 99% and which have a hardness of 7 in the Mohs scale ([Missouri Department of Natural Resources 2016](#)). The depositional process of the formation is of great discussion, some attribute the origin to wind deposition, others attribute the origin to marine deposition and others attribute the origin to a combination

of both depositional processes; this has been of dispute because characteristics of the formation indicate it was originated by both processes ([Missouri Department of Natural Resources 2016](#)). The formation originated in the Ordovician period during the Paleozoic era.

The grain size distribution of Ottawa F-65 sand is shown in Table 2.1 and the mean grain size distribution from two tests is shown in Figure 2.1 Grain size distribution; this table summarizes fines content, grain sizes corresponding to 10% (D_{10}), 30% (D_{30}), 50% (D_{50}) and 60% (D_{60}) finer by weight, coefficient of uniformity (C_u), coefficient of curvature (C_c), and USCS classification. The grain size distribution was obtained by dry sieving following the [ASTM D422-63 \(2007\)](#) procedure. Mean values of these properties obtained from tests 1 and 2 are as follows: $D_{10}=0.14$ mm, $D_{30}=0.17$ mm, $D_{50}=0.20$ mm, $D_{60}=0.22$ mm, $C_u=1.61$ and $C_c=0.96$.

The grain size distributions obtained herein are compared to those obtained by several other researchers in Figure 2.2 and listed in Table 2.1. The grain size distributions from this project and from different authors plot close together in Figure 2.2, with the exception of the results from Yan-Guo Zhou (2014) that plot at the right of the grain size distributions from all the other authors. The coefficient of variation (CV) for all the parameters presented in Table 2.1 obtained by different authors are below 11% with the exception of the CV for fines content. The CV of the fines content from results from different authors is 73% which is significantly higher than for the other parameters, but this high CV is due to the mean value being small. The highest value of fines content was reported by Ruffatto (2013) and by Cooper Lab (2013) which are 0.9% and are 0.8% higher than the fines content reported by US Silica (2016). Differences in the results might be due to variations in the sieves, testing procedure, scales and sample particle segregation.

The grain characteristics are illustrated in the SEM images in Figure 2.3. The SEM images were taken using the HITACHIS-4100T Field Emission Scanning Electron Microscope (FE-SEM) with and OXFORD INCA Energy Dispersive X-ray Spectrometer (EDS). Further detail of the imaging process is described in Chapter 3. The sand grains are sub-rounded to rounded by the visual classification procedure

from [ASTM 2488 – 06 \(2006\)](#). The sand grains show two surface textures in Figure 2.3; the first surface texture is an abraded texture and is present in most of the grain's surface; the second surface texture consists of planes of etch polygonal marks in some specific points in some of the grains. Similar surface textures have been shown in SEM images from sand grains from the St. Peter formation by [Fitzpatrick and Summerson \(1971\)](#); these grains came from a sand sample that was mined hydraulically, washed, agitated and cleaned by air jets. [Fitzpatrick and Summerson \(1971\)](#) attributed the mixed texture of the sand grains surface to wind and water abrasion due to the formation's complex geologic history.

2.3 Specific Gravity of Solids

The specific gravity of solids was determined to be 2.65 as the mean value from two tests. The G_s was obtained by [ASTM D854-14 \(2014\)](#) standard method; modifications were made to the [ASTM D854-14](#) procedure by adding steps as suggested by [Bardet \(1997\)](#), [Das \(1997\)](#), [Kalinski \(2006\)](#), [Liu et al. \(2013\)](#) and [Ruffatto \(2013\)](#). The testing procedure included several steps. The samples were air dried. The samples were placed dry in a pycnometer #3; this pycnometer was calibrated complying with a volume's standard deviation of 0.05 mL as required by the [ASTM D854 – 14](#) standard. De-aired water was added to the pycnometer to form a slurry; water was added until two thirds of the pycnometer was filled. The water was de-aired in a Nold DeAerator for 3 hours under 29 in Hg vacuum. The water was placed into the pycnometer's bottom with a plastic hose coming from the deaerator's tank; this was done to avoid getting air bubbles in the water. After preparation, the slurry was de-aired by applying 29 in Hg of vacuum with a hose connected to a rubber stopper on the top of the pycnometer. Slurry de-airing by vacuum application was done during 3 hours while having the pycnometer on top of a heating apparatus; the apparatus was set up to keep a constant temperature of 30° C during the whole de-aeration process. After de-airing the slurry was brought down to room temperature. De-aired water was added until the bottom of the water meniscus touched the 500 ml mark. The water excess was dried from the surface of the pycnometer. The pycnometer was weighed and the slurry temperature was measured.

The specific gravity of solids herein is compared to other investigators in Table 2.2. The mean value is 2.660 and the median value is 2.669 for all the tests results from different researchers. The coefficient of variation is 0.4%. Small variations in the results might be due to different procedures to remove the air from the samples; entrapped air is a common source of error in measuring G_s .

2.4 Minimum Dry Density

The minimum dry density ($\rho_{d \text{ min}}$) and maximum void ratio (e_{max}) were determined to be 1446 kg/m³ and 0.83 respectively based on the [ASTM D4254-00 \(2000\)](#) method and using an aluminum mold with the same dimensions as the DSS rings and caps assembly (DSS); the same values were also obtained by Ruffatto's (2013) method. e_{max} corresponds to the value calculated from $\rho_{d \text{ min}}$ and from $G_s=2.65$. However, tests by two methods were conducted by Ruffatto's (2013) method and by [ASTM D4254-00 \(2000\)](#) method. Ruffatto's method was a modification by the method proposed by Lade (1988). This method consisted in placing around 411 g of air dried sand in a glass 1000 ml graduate glass cylinder. The top of the cylinder was cover with a latex membrane and was rotated 180° (turned up -side down) in 45 seconds. The reported value of $\rho_{d \text{ min}}$ obtained by Ruffatto's method corresponds to the mean value from 7 measurements. The [ASTM D4254-00](#) method consisted in filling a mold by pouring sand using a funnel or a rigid pipe and allowing the sand to freely fall inside the mold. Two tests with 9 measurements per test were run to determine the influence of mold size on the results. One test was run using a steel calibration mold with the same dimensions as the DSS rings and caps assembly (DSS). Another test was run using the vessel used for the one-dimensional compression tests (1DC). The test run with the DSS mold was run using procedure A stated in the [ASTM D4254-00](#) standard; this procedure consisted in placing the spout of a plastic funnel on the bottom of the mold, filled the funnel with enough sand to guarantee that the mold will be filled up to 13 to 25 mm above the top of the mold, raised up the funnel quickly to guarantee a zero height drop of the sand, and trimming the excess of sand with a straight edge in two passes. The test run with the DSS mold was run using procedure B stated in the [ASTM D4254-00](#)

standard; this procedure consisted in placing a rigid aluminum pipe on the bottom of the mold and filled it with sand using the plastic funnel, the pipe was filled with air dried sand until the height of sand was within 3 to 6 mm below the top of the soil, the pipe was quickly lifted to allow sand to freely fall and fill the mold and the excess of sand was trimmed with a straight edge in two passes. The pipe had a volume 1.25 times greater than the volume of the vessel and a diameter that was 0.7 time the diameter of the vessel. The dimensions of the IDC vessel are described in further detail in Chapter 4.

The $\rho_{d \min}$ and e_{\max} herein are compared to other investigators in Table 2.3. Ranges of $\rho_{d \min}$ are between 1413 to 1515 kg/m³ and ranges of e_{\max} are between 0.734 and 0.83, which were obtained by different testing methods and using different testing molds. The value obtained by Ruffatto (2013) is the same as the values obtained in this work by the ASTM D4254-00 using the DSS mold and by the Ruffatto's (2013) method; however, the value obtained by Ruffatto (2013) showed a smaller void ratio standard deviation (e SD), whereas the values of e SD obtained in this project by Ruffatto's (2013) method coincide with the values of e SD obtained by Vasko et al. (2014) using the same testing method. The $\rho_{d \min}$ and e_{\max} herein obtained by the ASTM D4254-00 (2000) method are compared to other investigator's results obtained using the same method in Table 2.4. The highest density using the ASTM D4254-00 method is reported by Cooper Lab and was done using a bigger mold. The coefficient of variation from results from Cooper Lab and from this projects is 2%. The $\rho_{d \min}$ and e_{\max} herein obtained by the Ruffatto's (2013) method only are compared to other investigators in Table 2.6. Variations in the results might be due to differences in the mold size and in the testing procedure.

2.5 Maximum Dry Density

The maximum dry density ($\rho_{d \max}$) and minimum void ratio (e_{\min}) were determined to be 1446 kg/m³ and 0.51 respectively based on the Japanese test method for minimum density of sand JIS A 1224 (JIS 2009) testing method. e_{\min} corresponds to the value calculated from $\rho_{d \max}$ and from $G_s=2.65$. Tests by two methods were conducted by the JIS A 1224 (2009) and by Ruffatto's (2013) method. The Japanese

method consisted of filling a steel mold with 240 g of air dried sand. The mold has an inner diameter of 60 mm and a height of 40 mm. Sand was placed inside the mold in 10 lifts. Each lift was vibrated by rotating the mold while hitting it 100 times with a rubber hammer. The hammer had a diameter of 40 mm. The collar of the mold was removed after the mold was filled and the excess of sand was trimmed with a knife in two passes. The mass of the specimen was measured. Likewise, Ruffatto's (2013) method consisted on placing 411 g of air dried sand into the 1000-ml graduated plastic cylinder in increments of about 25 g. Each increment was poured into the cylinder with a 50-ml glass graduated beaker filled with air dried sand up to about 20-ml, which was approximately 25 g of sand. The 1000-ml graduated cylinder was tapped 8 times after placing each layer. Two tests were conducted using different tools to tap the cylinder to determine the effect of different energy levels in the results. During test one a rubber hammer with a 45 mm diameter was used and during test two a wood rubber-headed pestle with a diameter of 25 mm was used. The cylinder was tap twice on each side. Then, the final volume was measured.

The $\rho_{d \max}$ and e_{\min} obtained in this project are compared to results obtained by other investigators in Table 2.6. Ranges of $\rho_{d \max}$ are between 1676 to 1788 kg/m³ and ranges of e_{\min} between 0.48 and 0.58, which were obtained by different testing methods and using different testing molds. The highest minimum void ratio's standard's deviation ($e_{\min} SD$) is from the test conducted by Ruffatto's (2013) method using the biggest hammer, whereas the lowest $e_{\min} SD$ is for the test conducted by Ruffatto (2013); the $e_{\min} SD$ value from Ruffatto's test is very similar to the value obtained in this project following the exact same procedure and using the rubber-headed pestle as Ruffatto (2013) did. Furthermore, the $\rho_{d \max}$ obtained by Ruffatto (2013) and the $\rho_{d \max}$ obtained in this project by Ruffatto's (2013) method using the rubber-headed pestle are compared in Table 2.7. The coefficient of variation for these results is 0.4 %. Variations in the results might be due to differences in the mold size, the testing procedure and the energy imposed when hitting the molds.

Table 2.1 Summary of grain size distribution data for Ottawa F-65 sand (Carey et al. 2015)

Author	Method	D₆₀	D₁₀	D₃₀	C_u	C_c	Fines	USCS
(--)	(--)	(mm)	(mm)	(mm)	(--)	(--)	(%)	(--)
Parra 1 2015	Dry sieving	0.22	0.13	0.17	1.61	0.96	0.2	SP
Parra 2 2015	Dry sieving	0.22	0.14	0.17	1.60	0.96	0.0	SP
Cerna 2014	Dry sieving	0.22	0.14	0.17	1.54	0.99	0.2	SP
Vasko et al. 2014	Dry sieving	0.21	0.13	0.17	1.62	1.06	0.6	SP
Cooper Lab 2013	Dry sieving	0.23	0.13	0.18	1.82	1.07	0.9	SP
Ruffatto 1 2013	Dry sieving	0.24	0.14	0.19	1.68	1.02	0.53	SP
Ruffatto 2 2013	Dry sieving	0.23	0.13	0.18	1.72	1.10	0.9	SP
Ruffatto 3 2013	Dry sieving	0.24	0.14	0.19	1.76	1.07	0.9	SP
US Silica 2013	Dry sieving	0.21	0.14	0.17	1.55	1.01	0.1	SP

Table 2.1 (cont'd) Summary of grain size distribution data for Ottawa F-65 sand (Carey et al. 2015)

Author	Method	D ₆₀	D ₁₀	D ₃₀	C _u	C _c	Fines	USCS
(--)	(--)	(mm)	(mm)	(mm)	(--)	(--)	(%)	(--)
Zhou 2014	Dry sieving	0.18	0.11	0.14	1.71	0.96	0.1	SP
Stringer 2015	Particle laser	0.22	0.13	0.17	1.65	1.01	0.36	SP
Mean		0.23	0.13	0.17	1.71	1.00	0.46	--
Median		0.22	0.13	0.17	1.68	1.02	0.53	--
Standard Deviation		0.01	0.01	0.01	0.17	0.09	0.33	--
Coefficient of variation		5%	7%	8%	10%	9%	73%	--

D₆₀ = Grain size corresponding to 60% finer by weight, *D₁₀* = Grain size corresponding to 10% finer by weight, *D₃₀* = Grain size corresponding to 30% finer by weight, *C_u* = Coefficient of uniformity, *C_c* = Coefficient of curvature, *USCS* = Unified Soil Classification System, *SP* = Poorly graded sand

Table 2.2 Summary of specific gravity of solids data for Ottawa F-65 sand (Carey et al. 2015)

Author	Method	G _s @ 20 °C	N	G _s SD
(--)	(--)	(--)	(--)	(--)
Parra 2015	ASTM D854-14	2.650	2	0.002
Cerna 2014	ASTM D854	2.669	2	0.011
Cooper lab 2013	ASTM D855	2.673	NR	NR
Vasko et al. 2014	ASTM D855	2.648	5	0.012
Zhou 2014	NR	2.671	NR	NR
Mean (--)		2.660		
Median (--)		2.669		
Standard Deviation (--)		0.011		
Coefficient of variation (%)		0.4%		

G_s@ 20 °C = Specific gravity of solids at 20 Celsius degrees, *N* = Number of measurements, *NR* = Not reported, *G_sSD* = Specific gravity of solids standard deviation

Table 2.3 Summary minimum dry density and maximum void ratio data for Ottawa F-65 sand

(Carey et al. 2015)

Author	Type of test	Mold	Mold vol.	$\rho_{d \text{ min}}$	N	$\rho_{d \text{ min}}$ SD	Gs	e_{max}	e SD
(--)	(--)	(--)	(cm ³)	(kg/m ³)		(kg/m ³)	(--)	(--)	(--)
Parra 2015	ASTM D4254, method A	DSS	62	1446	9	8.8	2.65	0.83	0.011
Parra 2015	ASTM D4254, method B	1DC	130	1463	9	1.6	2.65	0.81	0.002
Parra 2015	Ruffato's 2013	Graduated cylinder	1000	1446	7	17.5	2.65	0.83	0.022
Cerna 2014	Lade's 1988	Glass cylinder	2000	1452	NR	NR	2.65	0.83*	NR
Cerna 2014	Pouring with zero drop height with hopper	NR	NR	1413	NR	20.0	2.65	0.88*	NR
Cooper lab 2013	ASTM D4254	ASTM standard	28317	1515	4	0	2.65	0.75*	NR
Geocomp 2014	NR	NR	NR	1494	NR	NR	2.65	0.77*	NR

Table 2.3 (cont'd) Summary minimum dry density and maximum void ratio data for Ottawa F-65 sand

Author	Type of test	Mold	Mold vol.	$\rho_{d \min}$	N	$\rho_{d \min}$ SD	G _s	e_{\max}	e SD
(--)	(--)	(--)	(cm ³)	(kg/m ³)		(kg/m ³)	(--)	(--)	(--)
Ruffato 2013	Ruffato's 2013	Graduated cylinder	1000	1452	5	4.0	2.650	0.825	0.005
Vasko et. al 2014	ASTM D4254	NR	NR	NR	1	0	2.648	0.754	0
Vasko et. al 2014	Ruffato's 2013	NR	NR	NR	8	NR	2.648	0.734	0.020
Hung 2014	NR	NR	NR	1480	NR	NR	2.65	0.79*	NR
Zhou 2014	NR	NR	NR	1456	NR	NR	2.671	0.83	NR

$\rho_{d \min}$ = Minimum dry density, N = Number of measurements, $\rho_{d \min}$ SD = Minimum dry density's standard deviation, G_s = Specific gravity of solids, e_{\max} = Maximum void ratio, e_{\max} SD = Maximum void ratio's standard deviation, * estimated value using G_s from this project, IDC = One-dimensional compression, DSS = Direct simple shear, NR = Not reported

Table 2.4 Summary minimum dry densities obtained by the ASTM D4254 method for Ottawa F-65 sand (Carey et al. 2015)

Author	Type of test	Mold	Mold Volume	$\rho_{d \min}$
(--)	(--)	(--)	(cm ³)	(kg/m ³)
Parra 2015	ASTM D4254	1DC	130	1463
Parra 2015	ASTM D4254	DSS	62	1446
Cooper lab 2013	ASTM D4254	ASTM standard	28317	1515
Mean (kg/m³)				1475
Median (kg/m³)				1463
Standard Deviation (kg/m³)				29.6
Coefficient of variation (%)				2.0%

$\rho_{d \min}$ = Minimum dry density, IDC = One-dimensional compression, DSS = Direct simple shear

Table 2.5 Summary minimum dry densities obtained by the Ruffatto's method for Ottawa F-65 sand
(Carey et al. 2015)

Author	Type of test	Mold	Mold Volume	$\rho_{d \text{ min}}$
(--)	(--)	(--)	(cm³)	(kg/m³)
Parra 2015	Ruffatto's 2013	Cylinder	1000	1446
Ruffatto 2013	Ruffatto's 2013	Cylinder	1000	1452
Mean (kg/m³)				1435
Median (kg/m³)				1435
Standard Deviation (kg/m³)				16.7
Coefficient of variation (%)				1.2%

$\rho_{d \text{ min}}$ = Minimum dry density

Table 2.6 Summary maximum dry density and minimum void ratio data for Ottawa F-65 sand

(Carey et al. 2015)

Author	Type of test	Mold	Mold vol.	$\rho_{d \max}$	N	$\rho_{d \max}$ SD	G _s	e_{\min}	e_{\min} SD
(--)	(--)	(--)	(cm ³)	(kg/m ³)		(kg/m ³)	(--)	(--)	(--)
Parra 2015	Ruffatto's, 2013	Hydrometer cylinder, big hammer	1000	1788	9	25.2	2.65	0.48	0.021
Parra 2015	Ruffatto's, 2013	Hydrometer cylinder	1000	1689	7	15.4	2.65	0.57	0.014
Parra 2015	JIS 1224	JIS	140	1759	3	13.9	2.65	0.51	0.017
Cooper lab 2013	ASTM D4253	ASTM mold	2832	1736	2	NR	2.65	0.53*	NR
GeoComp 2014	NR	NR	NR	1758	NR	NR	2.65	0.51*	NR
Ruffatto 2013	Ruffatto's, 2013	Hydrometer cylinder	1000	1676	8	14.2	2.65	0.581	0.013
Vasko et al. 2014	ASTM D4253	ASTM mold	NR	NR	1	NR	NR	0.4915	0.0
Vasko et al. 2014	Ruffatto's, 2013	Hydrometer cylinder	1000	NR	8	NR	2.648	0.494	0.017

$\rho_{d \max}$ = Maximum dry density, N = Number of measurements, $\rho_{d \max}$ SD = Maximum dry density's standard deviation, G_s = Specific gravity of solids, e_{\min} = Maximum void ratio, * estimated value using G_s from this project, e_{\min} SD = Minimum void ratio's standard deviation, IDC = One-dimensional compression, DSS = Direct simple shear, NR = Not reported

Table 2.7 Summary maximum dry densities obtained by the Ruffatto's method for Ottawa F-65 sand (Carey et al. 2015)

Author	Type of test	Mold	Mold Volume	$\rho_{d \max}$
(--)	(--)	(--)	(cm ³)	(kg/m ³)
Parra 2015	Ruffato's 2013	Cylinder	1000	1689
Ruffato 2013	Ruffato's 2013	Cylinder	1000	1676
Mean (kg/m³)				1683
Median (kg/m³)				1683
Standard Deviation (kg/m³)				6.5
Coefficient of variation (%)				0.4 %

$\rho_{d \max}$ = Maximum dry density

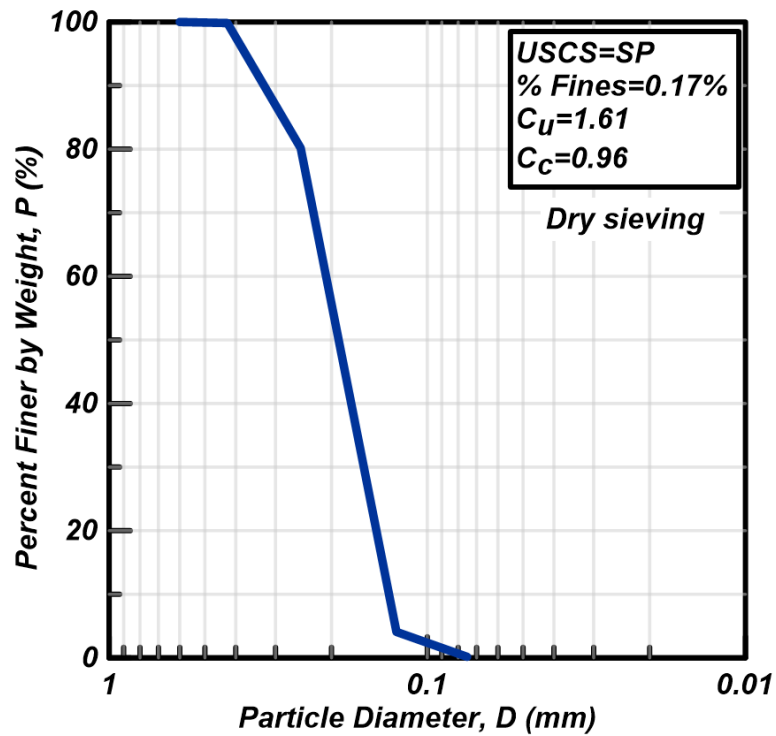


Figure 2.1 Grain size distribution

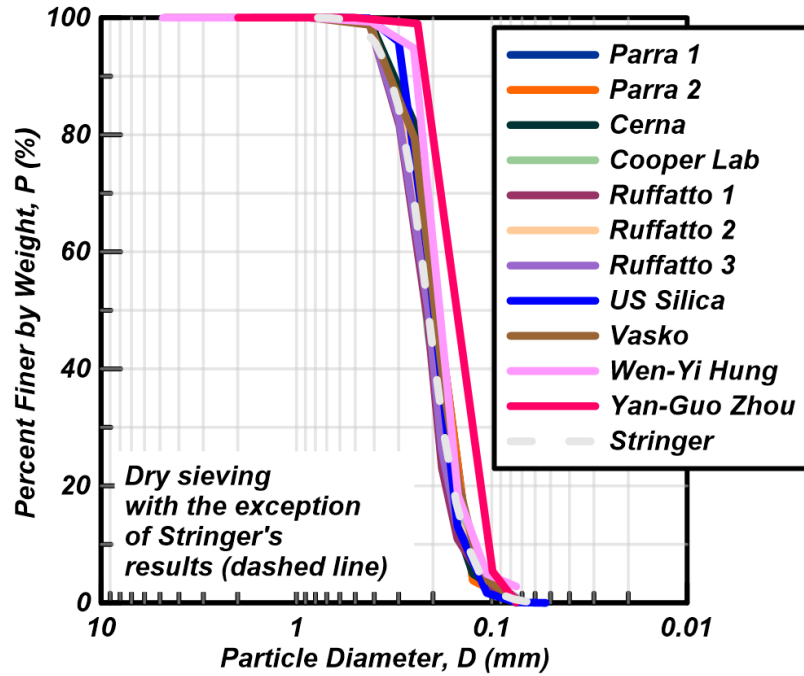


Figure 2.2 Grain size distribution from this project compared to those obtained by several other researchers

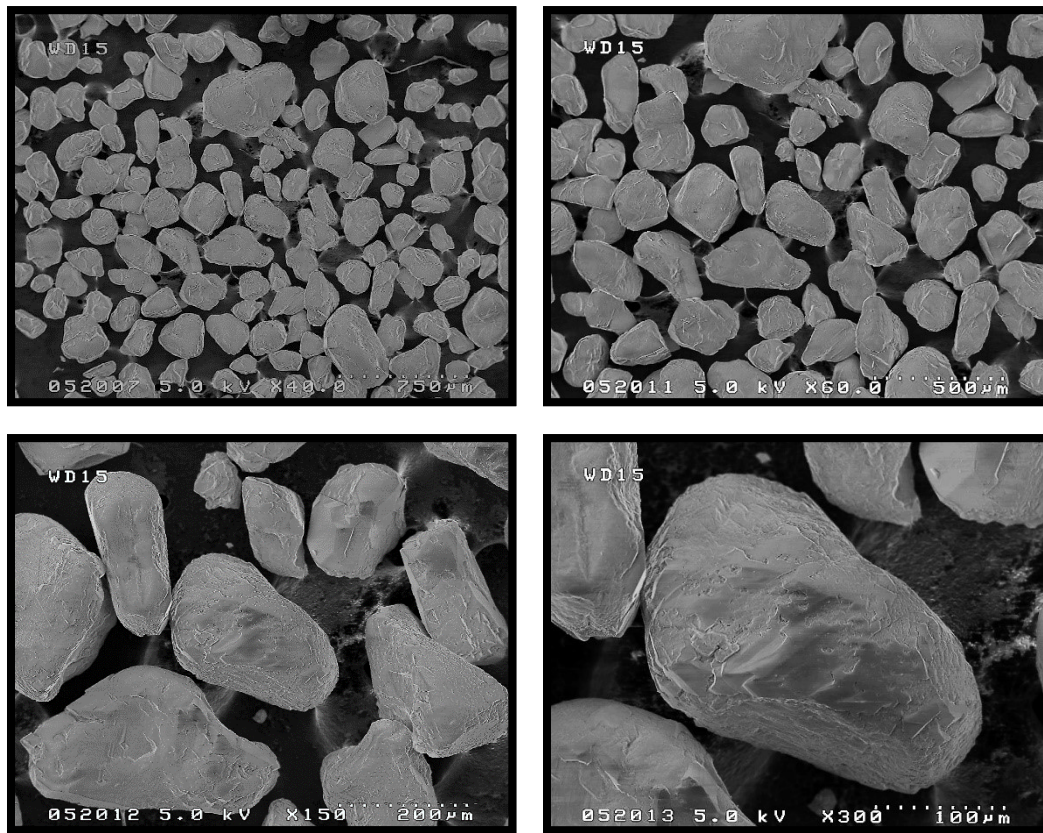


Figure 2.3 SEM images of Ottawa F-65 sand (images obtained by Michael Gomez)

Chapter 3

Hydraulic Conductivity

3.1 Introduction

This chapter summarizes the hydraulic conductivity results for Ottawa F-65 sand including: results on specimens prepared to different densities, comparison with results obtained by others, and comparison with results predicted from empirical correlations.

3.2 Hydraulic Conductivity Measurements

Hydraulic conductivity was measured using constant head tests following the [ASTM D2434 – 68 \(2000\)](#) standard. Modifications to the procedure described on the standard were made to follow steps suggested by [Bardet \(1997\)](#), [Das \(1997\)](#), [Head \(1988\)](#), [Kalinski \(2006\)](#) and [Liu et al. \(2013\)](#). The testing setup consisted of a permeameter cell placed inside a bucket filled with water as shown in Figure 3.1. The permeameter cell configuration is shown in Figure 3.2 and consists of a transparent Plexiglas cell, which rests over an assembly of a PVC pipe and two rubber collars that rest on a Plexiglas pedestal. Circular wire screens with diameters of 75, 300 and 2000 μm are placed in the top of the pedestal to prevent sand movement. The bottom rubber collar is placed on top of the pedestal and the PVC pipe is placed inside the collar, so the bottom part of the pipe rests on top of the screens. Specimens were dry deposited inside the PVC pipe. Loose specimens were prepared dry funnel deposited whereas dense specimens were prepared air pluviated. The dry funnel deposition method consists in placing the spout of a plastic funnel in the bottom of the PVC pipe, pouring dry sand into the funnel until it is full, and lifting the funnel slowly

as described by Erickson (2013). Dense specimens were air pluviated using a plastic pluviator with a screen and 3 openings, which could be graduated to open with different sizes. This method consists in raining the sand through the screen and the openings; the density of the specimen depends on the size of the opening where the sand is rained through and the falling height of the sand. The dense specimens were prepared by raining sand inside the PVC pipe with a height drop of 40 cm and were dropped through a 7 degrees opening as described by Ziotopoulou et al. (2013). Then, the top rubber collar was attached, the configuration was placed very carefully inside the bucket and the permeameter cell was placed so the bottom part rested inside the top rubber collar. The bottom tap was closed. The bucket was filled with tap water. The bottom tap was opened and water was allowed to flow upwards slowly through the pedestal's opening, to saturate the specimens in the permeameter cell, under a vacuum of 10 kPa that was applied during 10 minutes through the top tap of the cell until no air bubbles were released inside the water indicating the specimen was fully saturated.

The results of tests on one specimen tested over a range of hydraulic gradients (i) are shown in Figure 3.3. Three measurements were taken per each hydraulic gradient and three hydraulic gradients were used per test. The reported permeability for each specimen was the mean of the hydraulic conductivities calculated from the 9 measurements. Three hydraulic gradients were used to verify a linear variation of the hydraulic gradient with the discharge velocity (v). This was done verify that the selected hydraulic gradients guaranteed a sufficiently slow flow of water inside the specimen; the flow needs to slow enough to be in the laminar flow regime, this is verified when the variation of v versus i is linear as described by Bardet (1997). By guaranteeing the flow of water is laminar, the compliance of Darcy's law was guaranteed. Furthermore, a linear regression model using a least-squares fit to the i and v data confirmed that the measurements were performed within the laminar flow regime during each test as shown in Figure 3.3. The linear regression model used confidence bounds calculated with a confidence level of 95% using MATLAB®. The data, the linear fit and the confidence bounds are included on a plot for each test's results that are presented on the online database at NEESHUB.org.

The hydraulic conductivities for specimens at different initial dry densities are presented in Table 3.1. Figure 3.4 shows that k reduces as D_R increases. Figure 3.5, Figure 3.6, Figure 3.7 and Figure 3.8 presents the variation of k with void ratio, the square of void ratio divided by one plus void ratio and the cube of void ratio divided by one plus void ratio, respectively. The three relationships fit the data well making it difficult to distinguish whether one relationship provides a better fit than the others.

The results herein compared to results obtained by others are presented in Table 3.1 and in Figure 3.8. The hydraulic conductivities obtained in this study and a linear fit are in good agreement with the results obtained by [Cimini \(2015\)](#). This could be due to the fact that [Cimini \(2015\)](#) used the same equipment, the same testing procedure and the same analysis procedure to obtain his results. The hydraulic conductivities obtained in this study are higher than those obtained by [Vasko et al. \(2014\)](#).

The obtained hydraulic conductivities are consistent with values reported in the literature. [Head \(1988\)](#) describes that hydraulic conductivities for clean sands should be measured with a constant head permeameter and their hydraulic conductivities range from 10^{-5} to 10^{-2} m/s. The difference between the results obtained by [Vasko et al. \(2014\)](#) and those results obtained in this project might be due to ([Head 1988](#)): degree of saturation, fabric and type of flow. The degree of saturation would depend on the method use to saturate the samples, and degrees of saturation smaller than 85% can lead to continuous voids inside the sample that would reduce the permeability and invalidate the validity of Darcy's law ([Head 1988](#)). The fabric of the specimens is highly dependent on the preparation method and would lead to different values of hydraulic conductivities. The type of flow depends on the selected hydraulic gradients used to run the tests. Discharge velocities versus hydraulic gradients relationships that are not linear are not within a laminar flow regime and thus do not comply with Darcy's law; tests run with these hydraulic gradients would lead to invalid values of hydraulic conductivities.

3.3 Hydraulic Conductivity Comparisons to Empirical Equations

The results herein are compared to predictions obtained by empirical equations in arithmetic scale plot in Figure 3.9 and in semi-logarithmic scale plot in Figure 3.10. Hazen's equation's prediction is close to the lowest value of the experimental hydraulic conductivity obtained. Cozeny – Karman's equation lowest value predicts the same k as the lowest value of k from the experimental results obtained in this project; however, Cozeny – Karman's equation overestimates the values of k at higher e as shown in Figure 3.9 and Figure 3.10.

Hazen's equation relates the effective particle size (D_{10}) with hydraulic conductivity as follows:

$$k = CD_{10} \quad (3.1)$$

C can be assumed equal to 100 for uniform sands when D_{10} is in cm and k is in cm/s. $D_{10}=0.014$ cm (0.14 mm) for Ottawa F-65 sand. This relationship was developed with experimental results from tests on fine sands specimens and should provide a reasonable estimation of the magnitude of the hydraulic conductivities (Head 1988) as observed in Figure 3.9 and Figure 3.10; however, it does not take into account the effect of e in k . Head (1988) suggests that the range of hydraulic conductivities should be between $k/2$ and $2k$ with k obtained with Hazen's equation, or between 0.009 – 0.036 cm/s when $C=100$ for k and D_{10} in cm, which is close to the range of hydraulic conductivities obtained experimentally in this project.

Cozeny – Karman's equation relates k with the cube of e over e plus one, with the specific surface (S) and with the angularity factor (f) of the sand grains within the specimen as follows:

$$k = \frac{2}{fS^2} \frac{e^3}{1+e} \quad (3.2)$$

$$S = \frac{6}{\sqrt{d_{max}d_{min}}} \quad (3.3)$$

The maximum diameter (d_{max}) for Ottawa F-65 sand is 0.42 mm and the minimum diameter (d_{min}) for this sand is 0.085 mm; these values were obtained from dry sieving results that are explained in further detail in Chapter 2. S is 32 for the values of d_{max} and d_{min} obtained for this sand. f is 1.1 for rounded grains according to Loudon (1952).

Table 3.1 Summary of hydraulic conductivity measurements by different researchers

Author (--)	Type of test (--)	Loose ρ_d (kg/m ³)	Dense ρ_d (kg/m ³)	$k_{loose @ 20^\circ C}$ (cm/s)	$k_{dense @ 20^\circ C}$ (cm/s)
Parra 2015	ASTM D3424	1480	1722	0.022	0.016
Cimini 2015	ASTM D3424	NR	1654	NR	0.017
Vasko et al. 2014	ASTM D3424	1537	1617	0.0164	0.0118

ρ_d = Dry density, $k_{loose @ 20^\circ C}$ = hydraulic conductivity on a loose specimens at 20 Celsius degrees, $k_{dense @ 20^\circ C}$ = hydraulic conductivity on a loose specimens at 20 Celsius degrees



Figure 3.1 Permeameter cell

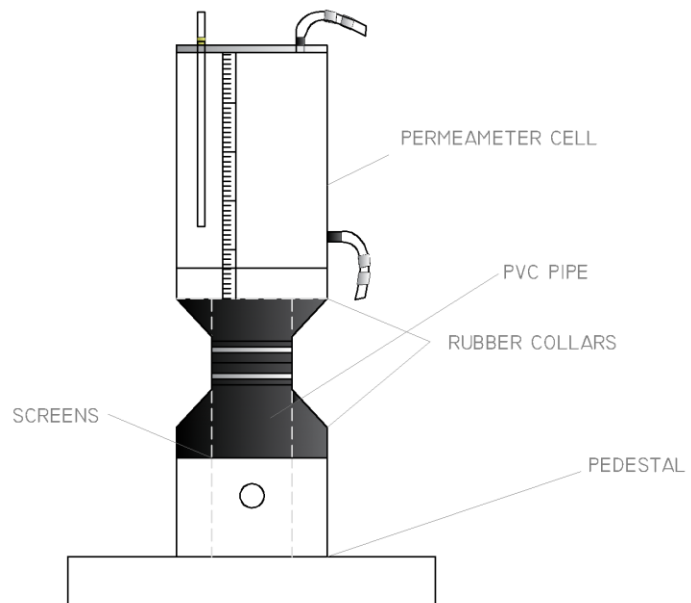


Figure 3.2 Permeameter configuration

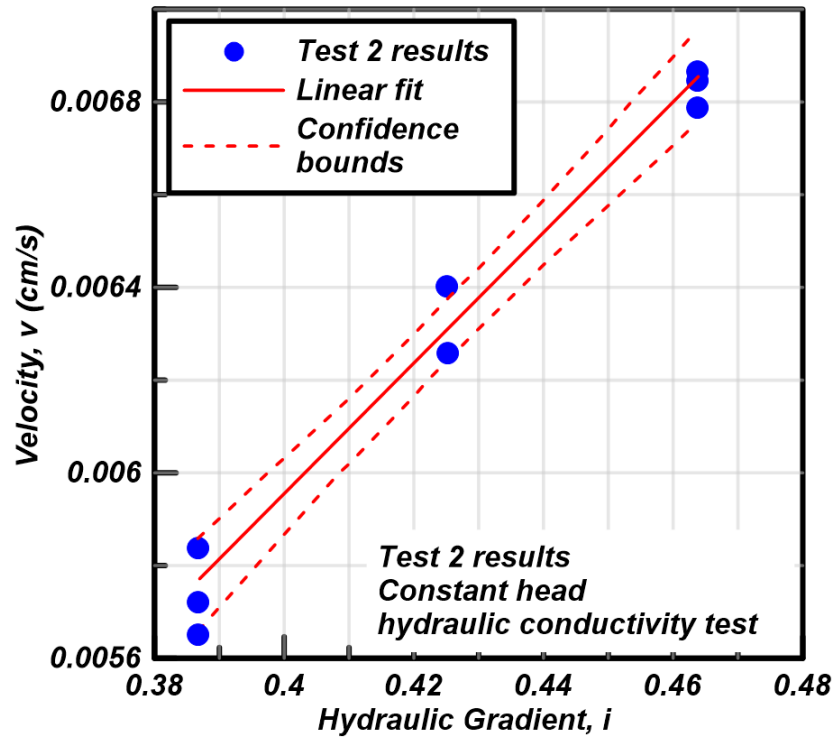


Figure 3.3 Velocity vs. hydraulic gradient test # 2

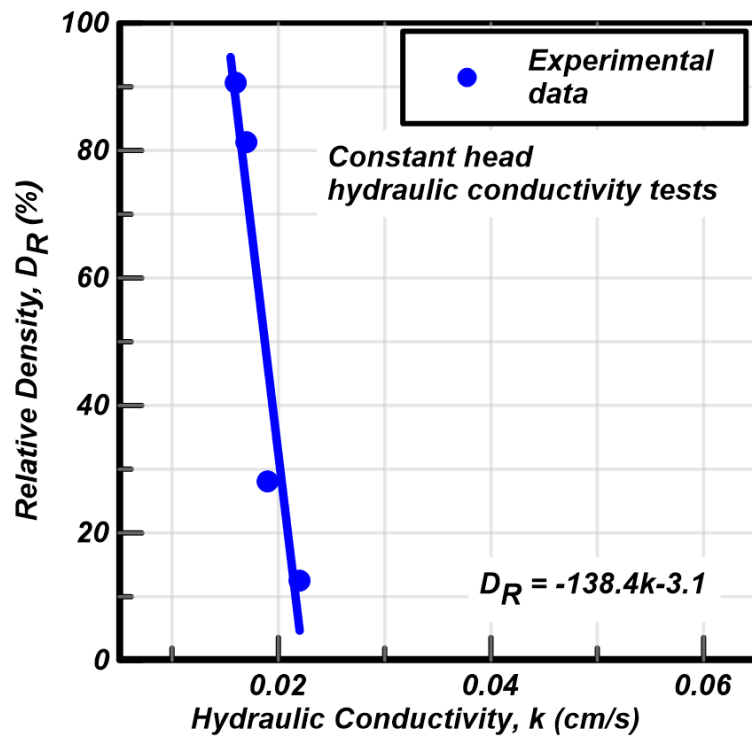


Figure 3.4 Relative density vs. hydraulic conductivity

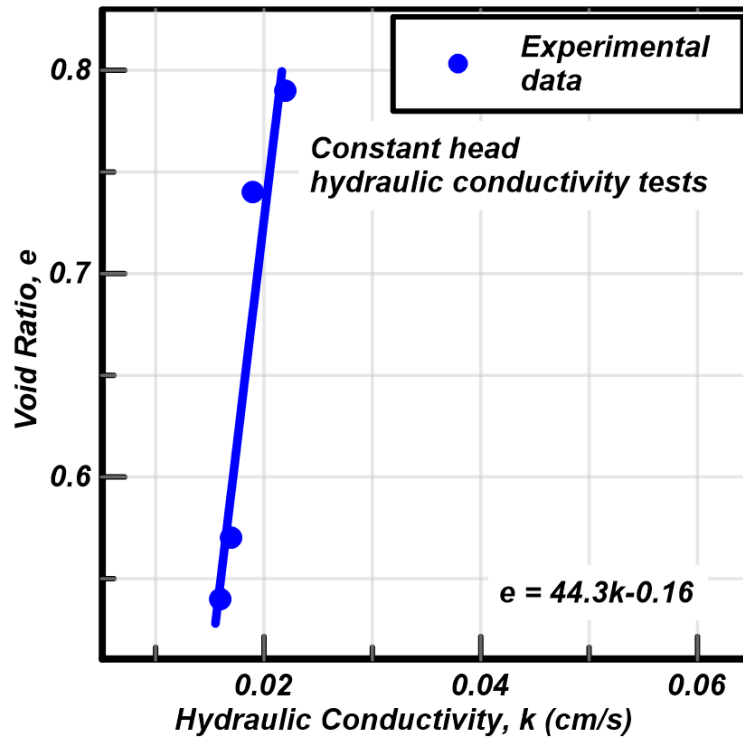


Figure 3.5 Void ratio vs. hydraulic conductivity

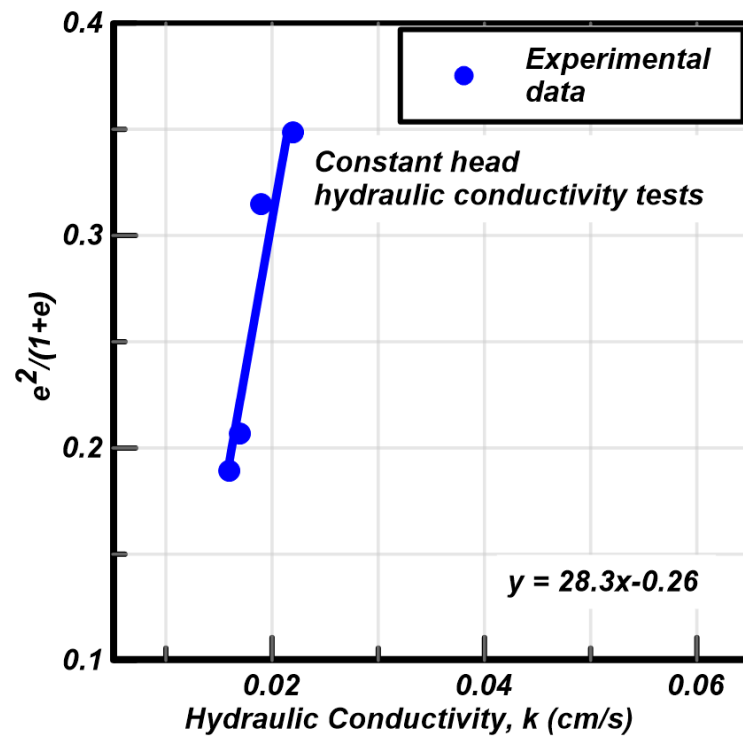


Figure 3.6 Square of void ratio vs. hydraulic conductivity

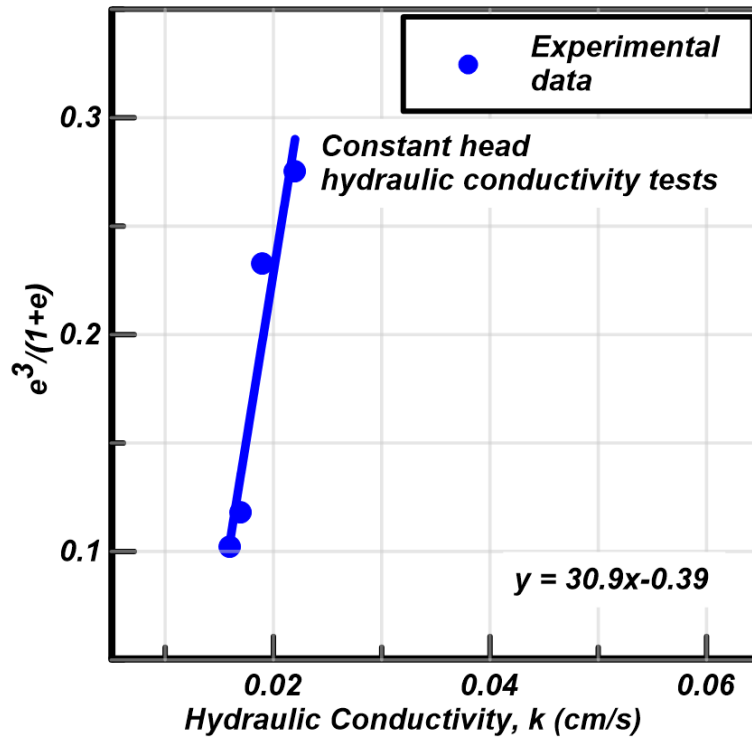


Figure 3.7 Cube of void ratio vs. hydraulic conductivity

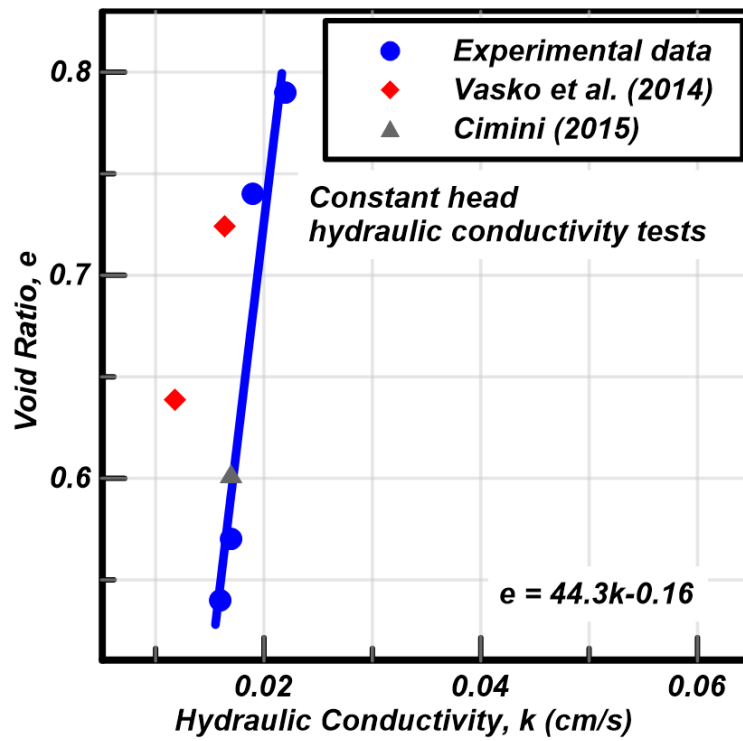


Figure 3.8 Void ratio vs. hydraulic conductivity comparison to data from other researchers

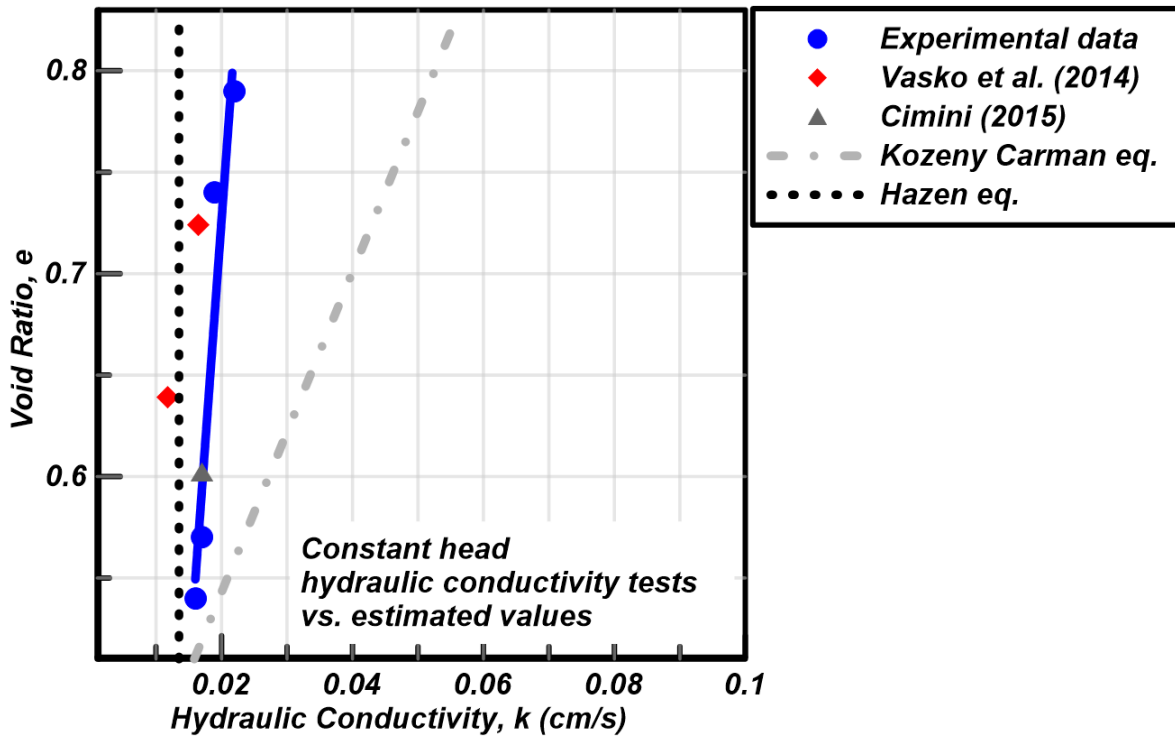


Figure 3.9 Void ratio vs. hydraulic conductivity comparison to empirical equations

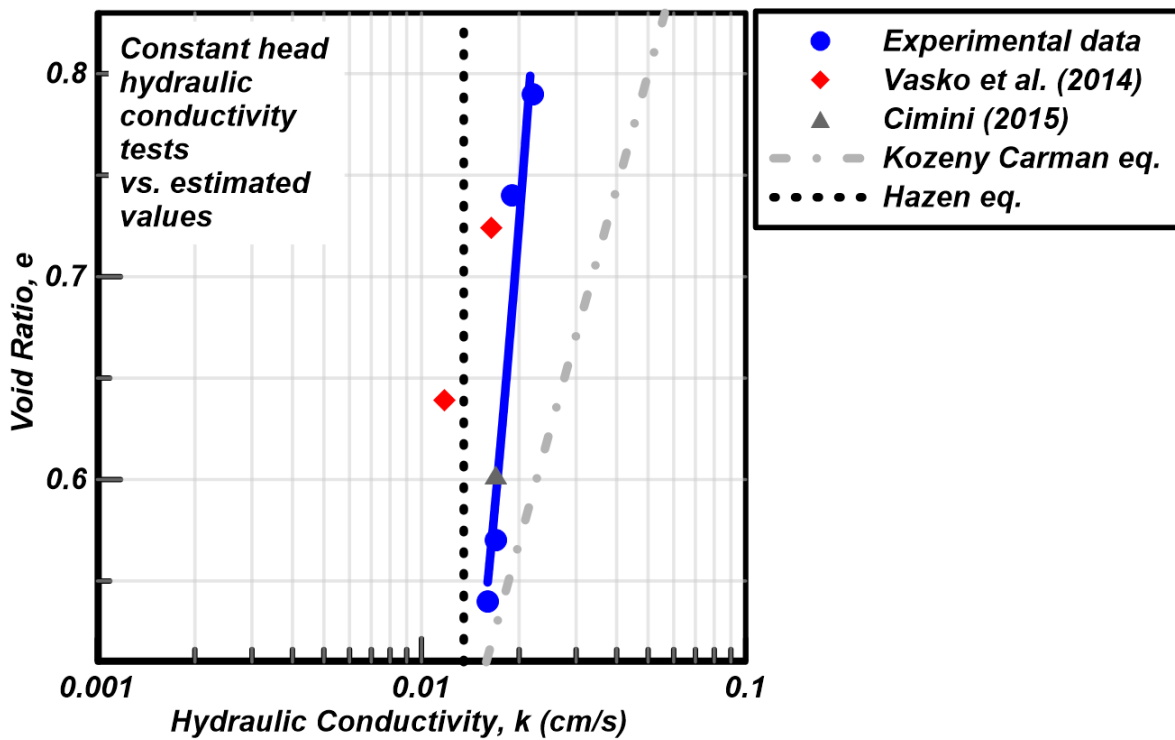


Figure 3.10 Void ratio vs. hydraulic conductivity comparison to empirical equations semi-log

Chapter 4

One-dimensional Compression Characteristics

4.1 Introduction

This chapter summarizes the one-dimensional compression (1DC) results for Ottawa F-65 sand including: compression stress strain responses on loose and dense specimens compressed to maximum vertical effective stresses (σ'_v) of 30, 70 and 140 MPa and particle size analysis to determine stress level and density effects on particle crushing magnitude.

4.2 1DC testing procedures

The tests were performed using two compression frames: one pneumatic frame with a 2.2 kN (500 lb) maximum capacity used for placement of the top cap under $\sigma'_v=100$ kPa and for pre-consolidating the specimens, and one MTS hydraulic frame with a 445 kN (100 kips) maximum capacity for compressing the tests to the desired elevated stresses. The pneumatic frame was custom made and is shown in Figure 4.1. The plans of the pneumatic frame is shown in Figure 4.2, Figure 4.3, Figure 4.4. The MTS hydraulic frame is shown in Figure 4.5.

The tests were performed using a custom-made assembly including a steel 4140 vessel, a steel top cap, an aluminum collar and two Linear Position Transducers (LPTs) as shown in Figure 4.6, Figure 4.7, Figure 4.8, Figure 4.9, and Figure 4.10. The mold was constructed so the diameter of the mold matched with the internal diameter of an aluminum trimming ring already available in the SIL Lab, so kaolin samples could be extruded directly from the mold. The height of the mold vessel was chosen so the mold could use

LPT's with a defined range of 25 mm. The mold was made of high resistance steel 4140 to reduce the size and weight of the mold, to permit the use of a scale with a 0.01g resolution. A previous mold made of regular steel was bigger and had perforated screens on the bottom of the mold instead of porous disks, which caused sufficient compliance that affected the void ratio measurements. In addition, the screens in the earlier mold were difficult to remove after testing. After construction of the vessel, two screws were attached on the outside of the vessel's walls and a hole was made on the flat face of each screw, so the tips of the LPTs could be attached to these screws with nuts as shown in Figure 4.6. The mold cap length was designed so it allowed the aluminum collar to be placed on top of the O-ring grooves but also allowed the use of the LPT's with a defined range of 25 mm when testing kaolin. The top cap has a threaded hole on the top, to allow easier removal of the top cap after testing, by means of forming a lever with the screw and a Vise-grip wrench. The top cap height was also selected to accommodate a drainage line on the top to allow water to drain when testing kaolin.

Two types of porous disks were used. The mold was initially designed using a miniature porous stone, which was custom made to fit the size of the groove shown in Figure 4.7 and with a tolerance of +0.002-0.000 in. However, after some initial tests, it was found that the top porous stone would break after one test and the bottom one would break after 2 or 3 tests; all these tests were subjected to a maximum applied $\sigma'_v=138$ MPa. These porous stones were replaced by miniature custom-made porous 316 L 0.2 media grade stainless steel disks (Mott Corporation). These disks worked well for all the tests, but will deform and get stuck inside the grooves after several tests; so they need to be changed periodically after some tests.

The friction between the top cap and the mold was found to be sensitive to the clearance between the top cap and the vessel and the size of the O-Rings, because the O-Rings would sometimes stick to the top cap during the pre-consolidation phase and this created an error in the height measurements. The mold cap was initially designed with a tolerance of +0.000" -0.002" and using thicker O-Rings. However, the Buna-N AS568 size 141 O-rings size was selected after testing different O-Rings sizes; the dimensions of

this type of O-Ring are shown in Figure 4.10. The clearance between the mold and the top cap was increased to 0.010” by sanding the vessel.

The LPTs were configured so that they provided continuous measurements of height from the time each specimen was loaded in the pneumatic frame up to time the specimen was unloaded in the MTS hydraulic frame. The process of installing the LPTs and acquiring data continuously included the following steps: the LPTs were attached to the mold cap to take a zero height before starting the preparation of the specimen. The specimen was then placed inside the vessel. The vessel was placed on top of two steel disks underneath the vertical actuator of the pneumatic frame. The steel disks serve as spacers so the actuator’s stroke was enough to load the specimen. The specimen was centered below the actuator. The O-rings were soaked with silicon oil and were placed on the mold cap, Penzol 705 multipurpose lubricant was placed on the sides of the top cap. The top cap, with the attached collar and LPTs, was placed inside the vessel. Only the bottom of the top cap was inserted inside the vessel while taking care that the tips of the LPTs were placed inside the holes of the screws on the sides of the vessel. An aluminum spacer was placed on the mold cap and the vertical actuator of the pneumatic frame was moved downwards so it barely touched the spacer. The data acquisition was started with recording using the RESDAQ software provided by [D. Wilson \(2012, personal communication\)](#). The air pressure was increased so the actuator applied a force that would result in $\sigma'_v=100$ kPa applied to the top cap inside the vessel; this was done with care and while watching the readings from the LPTs in the data acquisition system (RESDAQ) to guarantee that the top cap was placed level inside the vessel. The specimen was consolidated in the pneumatic frame during 20 minutes under $\sigma'_v=100$ kPa. Then, the vertical actuator of the pneumatic frame was lifted, and the tips of the LPTs were secured to the bottom screws of the sides of the vessel by tightening a nut. Then, the assembly was carefully moved to the MTS frame and was centered below a steel cylinder spacer attached to the bottom of the top plate of the MTS frame. The actuator was moved upwards very slowly until the spacer on the top of the MTS machine was very close to the top cap of the mold. Then the MTS machine was set up to start

the high-pressure loading phase of the test. Data was recorded continuously during the pre-consolidation phase and during the loading and unloading portions of the high pressure test.

The process of attaching the LPTs before taking their zeros was modified several times when developing the testing procedures. This process was crucial to obtain reliable height measurements. Attaching the LPTs included the following steps: the top cap without O-Rings was placed inside the vessel so the bottom of the top cap would touch the bottom of the vessel. The aluminum collar was attached to the top cap so the bottom of the collar would be in contact with the surface of the vessel's wall; this was done to guarantee the collar was always attached at the same position on the cap. Then, the LPTs were attached to the collar while having the top cap inside the vessel, with the LPT position set so their voltage reading was higher than 1 Volt; this was to guarantee the LPTs were measuring in their linear range. One LPT would be attached first by placing the groove on its side inside the holding bracket in the collar and tightening the bolts in the brackets with a wrench; then, the second LPT was attached repeating the process while ensuring that the voltage reading from RESDAQ of the second LPT matched the reading from the first LPT; this was to guarantee that they were placed at the same height. The assembly was placed in the pneumatic frame and a force causing a $\sigma'_v=100$ kPa was applied in the frame to take zeros of the test. Readings of voltages were recorded for 1 minute from the two LPTs, and the zero reading was selected as the average of those readings.

Loose specimens were prepared by the dry funnel deposition method and dense specimens were prepared by the air pluviation method as shown in Figure 4.11. The dry funnel deposition procedure consisted of placing a rigid aluminum pipe on the bottom of the mold's vessel and filling it with air dried sand using the plastic funnel. The pipe was filled until with the height of sand was within 3 to 6 mm below the top of the pipe. The pipe was quickly lifted to allow sand to freely fall and fill the mold, and the excess of sand was trimmed with a straight edge in two passes. The pipe had a volume 1.25 times greater than the volume of the vessel and a diameter that was 0.7 time the diameter of the vessel. The height of the sand inside the vessel was reduced by vacuuming the excess of sand with a small aluminum pipe

connected to plastic hose that vacuumed the sand into a flask. In contrast, the air pluviation method consisted in raining sand through an aluminum plate that had three circular openings as shown in Figure 4.12. The openings could be closed or opened by loosening a bolt and rotating the plate. The dry density of the specimen at preparation depended on the falling height and on the sand's drop velocity which is controlled by the openings. All the specimens were pluviated directly inside the vessel by placing the pluviator bottom end on top of the vessel; the drop height of the sand was 40 cm and the opening of the pluviator plate was 10 degrees.

Tests were run in controlled deformation mode at a constant rate of deformation of 0.025 in/min. Tests were stopped when the compression force reached 436 kN (98 kips). The MTS hydraulic frame loaded the specimens by moving the bottom plate upwards at the constant rate of deformation. The machine was programmed to stop automatically once the load cell would read 98 Kips by using the DC2 Up option in the limit levels menu in the machine's controller. Once the load cell reported 98 Kips the machine moved the bottom plate downwards at a rate of 1.0257 in/min.

The specimens were removed from the mold with care to prevent contamination with the lubricant on the top cap. Care was taken to recover as much as possible of the specimen from the vessel. Recovery was done by hitting the specimen with a spatula to release the specimen from the mold, due to the sand grains sticking together tightly after being compressed with such high pressures. Then, the specimen was poured into a plastic bag by turning the vessel upside down. The vessel was brushed with a small foam brush to remove the remaining particles inside the plastic bag. The plastic bag was carefully labeled with the mass of the specimen, the details of the test and the details of the specimen preparation. Then, the air dried specimen was dry sieved and the masses recorded. The specimens were prepared for hydrometer tests after sieving. Approximately 15 g from each of these specimens was separated to measure their moisture content following the [ASTM D2216 – 10 \(ASTM 2010\)](#) standard; the remaining material from each sample was soaked over-night in 125 ml of a solution of 40g of $(\text{NaPO}_3)_6$ per liter of solution. After

this, hydrometer testing was done on the soaked samples; hydrometer tests were conducted following the [ASTM D422 – 63 \(ASTM 2007\)](#) and using calibrated 152H hydrometers.

Other specimens were removed and prepared for SEM imaging. Sample preparation and SEM images were performed by Michael Gomez. The preparation of the specimens for SEM imaging included the following steps ([Gomez 2016](#)). The air dried crushed sand samples were mixed thoroughly to obtain a uniform sample. The pedestal was prepared by placing a black carbon double sided tape including the white protective layer. A triangular segment of the carbon tape and the white protective layer were removed to expose a small portion of the aluminum; this was used as a location reference during imaging. A small but representative soil sample was placed on the adhesive surface of the imaging aluminum pedestal Figure 4.13. The pedestal was tapped to remove weakly attached particles after placing the samples on top of the pedestal. Then, further sections of the white protective layer were cut and removed for placing subsequent samples on the pedestal, which can accommodate up to four samples concurrently. Then additional samples were placed carefully in pre-determined segments of the pedestal being sure to describe their location for reference during the imaging process. After this, the pedestal was stored inside a glass beaker with a foil cover and was placed in a drying oven with temperature of 110° C for 2 days before imaging. This process was performed to remove excess of moisture which could distort the SEM images. The images were taken using the HITACHI S-4100T Field Emission Scanning Electron Microscope (FE-SEM) with an OXFORD INCA Energy Dispersive X-ray Spectrometer (EDS). The microscope is show in Figure 4.14. The HITACHI S-4100T has a functional resolution less than 2 nm and a resolution of 132 eV ([Hicklin and Liu 2012](#)).

4.3 Stress strain response in compression

1DC curves are shown in Figure 4.15 for both loose and dense specimens loaded up to maximum σ'_v of 30, 70 and 140 MPa. The three curves for the loose specimens and for the dense specimens largely overlap. Both curves for loose and dense specimens loaded up to $\sigma'_v = 140$ MPa reached the limiting compression

curve (LCC) regime where their compression behavior is essentially independently of the initial density of the specimens. This behavior was expected in the high stress regime due to particle crushing at this stress level for Ottawa sand as described in Figure 4.16 (Pestana and Whittle 1995). The overlap of the curves for specimens with similar initial densities at $\sigma'_v < 10$ MPa and the overlap of the curves from the loose and dense specimens at high stresses, indicate that the tests results for all the loose specimens and for all the dense specimens are consistent. The void ratio for these curves is calculated from the average void ratio obtained from the height readings from each of the LPTs. The consistency of the LCC curves from tests on specimens with different initial densities suggests that the final procedures used to obtain height measurements from the LPTs for these tests are repeatable and reliable.

The IDC curve for the dense specimen is flatter than for the loose specimen for σ'_v from 0.1 to 10 MPa. The volumetric strain at 10 MPa was 2.9% for the loose specimen and it was 1.8% for the dense specimen as shown in Figure 4.17. The greater volumetric strain for the loose specimen over this stress range is expected because the particles within the specimen start in a looser arrangement than the particles in the dense specimen; thus, the particles within the loose specimen are able to move and rotate more when subjected to the IDC loading.

The stress strain curves in arithmetic scale present three portions with different slopes as shown in Figure 4.18. The first portion for curves for loose and dense specimens is for σ'_v from 0.1 to 10 MPa and presents non-linear behavior with the steepest secant slope of all the three portions. The second portion of the curves is between 10 and 35 MPa for the loose specimens and between 10 and 60 MPa for the dense specimens, and corresponds to flatter and approximately linear slopes. The third portion corresponds to stresses that are higher than 35 MPa for the loose specimens and higher than 60 MPa for the dense specimens, and corresponds to a non-linear slope that shows a progressive reduction at very high stresses. The slopes in all portions of the stress strains curves in arithmetic scale are greater for loose specimens than for dense specimens. Hagerty et al. (1993) conducted tests on Ottawa sand and showed a very similar stress strain behavior in linear scale. They attributed the first portion of the curve to a pseudo elastic compression.

They attributed the second portion of the curve to a transition phase associated with the onset of particle crushing. They attributed the third portion of the curve to extensive particle crushing, which created a very stiff material with the crushing rate diminishing with stress and approaching a second pseudo elastic compression stage at elevated stresses. During this third phase, intact and crushed particles quickly rearrange causing a rapid reduction in void ratio.

The IDC curves for the loose specimens remain flat up to σ'_v at about 10 MPa after which they curve strongly to a steeper limiting compression curves. The IDC curves for the dense specimens remain flat at to σ'_v at about 30 MPa after which they start to curve to a steeper limiting compression curves. The data show the maximum curvature point in the IDC curve of the loose specimen is 35 MPa and the maximum curvature point in the IDC curve of the dense specimens is at about 60 MPa; these stresses are consistent with the stresses at the initiation of the third portion of the stress strain curves in Figure 4.17. [Nakata et al. \(2001\)](#) describe the point of maximum curvature on the IDC curves as a “yield point” of the sand associated with particle crushing consistent with the critical pressure point definition ([DeSouza 1958](#)). [DeSouza \(1958\)](#) defined that the critical pressure for sand is a stress level in IDC where grain size distributions showed significant particle breakage and the slope of the IDC curves increases significantly.

The IDC curves from loose and dense specimens come together at the LCC portion of the IDC curve which is consistent with the expectations for stress levels within the LCC regime. The slope of the LCC portion of the IDC curve (ρ_c) is 0.48. This value of ρ_c is close to the estimated value of $\rho_c=0.45 \pm 0.015$ from results from [DeSouza \(1958\)](#) and [Roberts \(1964\)](#) as reported by [Pestana and Whittle \(1995\)](#). Their values of ρ_c corresponds to tests on specimens with three different gradations of uniform Ottawa sand with rounded grains, $C_u=1.5$, $G_s=2.66$, $0.14 \text{ mm} < D_{50} < 0.60 \text{ mm}$, $0.75 < e_{\max} < 0.82$ and $0.48 < e_{\min} < 0.65$.

The reference stress (σ'_r) is defined by [Pestana and Whittle \(1995\)](#) as the vertical effective stress at a void ratio of 1.0 on the extension of the LCC line (in $\log e$ versus $\log \sigma'_v$ space). σ'_r is about 14 MPa for the IDC curves from the loose specimens and 15 MPa for IDC curves of the dense specimens. [Pestana and](#)

Whittle (1995) reported $\sigma_r = 15 \pm 1$ MPa for Ottawa sand with $D_{50} = 0.14$ mm from the tests from DeSouza (1958) and Roberts (1964).

There are several other studies presenting IDC results for Ottawa sand including: Roberts and DeSouza (1958), Hagerty et al. (1993), Christoph (2005), and Mesri and Vardhanabhuti (2009). These tests examined behavior of different gradations of Ottawa sand with different loading paths and different vertical effective stresses. The tests results obtained in the present study are generally consistent with those from other studies. The IDC results presented here are for the Ottawa F-65 sand batches used at the CGM.

4.4 Particle crushing variation with stress levels

The amount of particle crushing is not evident in the SEM images on samples taken from loose or dense specimens after compression to a maximum IDC σ'_v of 30 MPa as shown in Figure 4.19 the SEM images from the loose specimens show some particles that appear to have breaks at some small asperities. The grain size distribution (GSD) results from dry sieving analysis on samples taken from loose or dense specimens after the tests to a maximum IDC σ'_v of 30 MPa, show almost no particle crushing evidence in Figure 4.20; however, a very small amount of fines generation in the loose specimen is indicated in the log-log scale plot in Figure 4.21. The absence of fines generation is consistent with their IDC curves not exceeding the point of maximum curvature (i.e., σ'_v of 30 MPa for the loose specimens). A small amount of asperity breakage for the loose specimens would be consistent with the σ'_v of 30 MPa being at the point of maximum curvature as shown in Figure 4.22. No apparent fines are shown in the SEM images, although this might be due to the fines being lost during sample removal and specimen preparation for SEM imaging. A similar situation has been described by Nakata et al. (2001) who conducted tests with uniformly graded silica sand with particle diameter between 1.4 to 1.7 mm. They observed that just 20% of particles had their asperities broken when they were loaded with a IDC σ'_v 4.4 MPa smaller than the σ'_v at the maximum curvature point on the IDC curve. They showed almost no fines creation on a semi-log scale grain size distribution graph, but did show that 0.8% of fines were generated in a log-log grain size distribution plot.

For the tests presented herein, no particle crushing is evident for the dense specimen's grains on the SEM images or on their grain size distributions, which is consistent with the applied stresses being smaller than the maximum curvature point at σ'_v of 60 MPa. The observations on the dense specimens are consistent with the observations from [DeSouza \(1958\)](#), who observed that when the IDC σ'_v is much smaller than the yield point, particle crushing is not extensive enough to observe changes in the grain size distributions.

Particle crushing is evident on the SEM images on samples taken from loose or dense specimens after compression to a maximum IDC stress of 70 MPa as shown in Figure 4.22. The GSD results from dry sieving analysis after testing to a maximum IDC stress of 70 MPa show that particle crushing occurred as shown in Figure 4.23. Significant particle crushing is expected for both loose and dense specimens because they are in the LCC regime at σ'_v of 70 MPa. The amount of particle crushing indicated by the GSD results show that particle crushing was greater in loose than in dense specimens. These results were expected due to sand grains within the loose specimens being arranged in looser arrangements that cause lower coordination numbers, prompting higher contact stresses at interparticle contacts. On the other hand, sand grains within dense specimens are in tighter arrangements that cause higher coordination numbers, prompting lower contact stresses at interparticle contacts.

Particle crushing is evident on the SEM images on samples taken from loose or dense specimens after the tests to a maximum IDC stress of 140 MPa as shown in Figure 4.24. The GSD results from dry sieving analysis after testing to a maximum IDC stress of 140 MPa show that particle crushing occurred as shown in Figure 4.25. The amount of particle crushing indicated by the GSD results show that particle crushing was greater in loose than in dense specimens. Again greater particle crushing is expected in the grains from the loose specimens due to lower coordination numbers. The SEM images show that the sample from the dense specimen has bigger grains whereas the sample from the loose specimen has a wider range of particle sizes.

The effect of using dry versus wet sieving on the GSD for specimens loaded to different stress levels was also examined. The results presented and discussed above were all for GSD obtained by

combining dry sieving and hydrometer tests. Additional tests were performed with GSD determined by wet sieving on portions of the test specimens. The results for specimens tested at 30 MPa are compared in Figure 4.26 and Figure 4.27. The curves from loose specimens are essentially the same for grain sizes greater than the grain size of the 10th percentile, but the wet sieved specimen had 2.8% more fines. The curves from dense specimens are essentially the same for grain sizes greater than the grain size of the 9th percentile, but the wet sieved specimen had 2.7 % more fines. The results for specimens tested at 70 MPa are compared in Figure 4.28 and Figure 4.29. The curves from loose specimens are essentially the same for grain sizes greater than the grain size of the 25th percentile, but the wet sieved specimen had 2.3% less fines. The curves from dense specimens are essentially the same for grain sizes greater than the grain size of the 15th percentile, but the wet sieved specimen had 3.3% more fines. The results for specimens tested at 140 MPa are compared in Figure 4.30 and Figure 4.31. The curves from loose specimens are essentially the same for size greater, but the wet sieved specimen had 1.1% less fines. The curves from dense specimens are essentially the same for grain sizes greater than the grain size of the 50th percentile, but the wet sieved specimen had 1.5% more fines. Overall, wet sieving did produce a slightly greater amount of fines for almost all the specimens with the exception of the loose specimens compressed to 70 and 140 MPa, but the differences are small enough to not affect the general conclusions and observations discussed previously based on the GSD results obtained by dry sieving and hydrometer.

SEM images, GSDs, and IDC stress-strain responses are in good agreement with the variation of particle crushing with stress level and placement density. Figure 4.32 and Figure 4.33 show that the amount of particle crushing increases with the maximum σ'_v , which is consistent with the evidences from the SEM images, GSDs, and IDC stress strain curves. The GSDs show that the amount of particles with diameters bigger than 0.20 mm show very little variation, even after the specimens were compressed with IDC maximum stresses of 140 MPa in loose and dense specimens. This is shown in the SEM images where the larger particles are still observed in the specimens subjected to IDC maximum stresses of 140 MPa. Some larger particles or large pieces of the larger particles might survive when they start to be surrounded by

smaller crushed particles, due to the coordination number increasing as the material becomes more well graded.

Particle crushing stages as described by [Nakata et al. \(2001\)](#) and shown in Figure 4.34 were observed in SEM images as shown in Figure 4.35 and agree with the inferred behaviors from the GSDs and 1DC stress-strain responses. Picture (1) in Figure 4.35 shows some sand grains from a loose specimen which was compressed to a maximum σ'_v of 30 MPa; some grains appear to have grinded surfaces as described in stage 2 from Figure 4.34. Picture (2) in Figure 4.35 shows some grains from a dense specimen which was compressed to a maximum σ'_v of 70 MPa; some grains appear to have broken asperities as described in stage 3 from Figure 4.34. Picture (3) in Figure 4.35 shows some grains from a dense specimen which was compressed to a maximum σ'_v of 70 MPa; some grains appear to have broken asperities and some of the asperities appear to have been part of bigger asperities which split in the middle, as described in stage 4 from Figure 4.34. Picture (4) in Figure 4.35 shows some grains from a loose specimen which was compressed to a maximum σ'_v of 70 MPa; the grain split in the middle and one of the middle parts split again, as described in stage 5 from Figure 4.34.

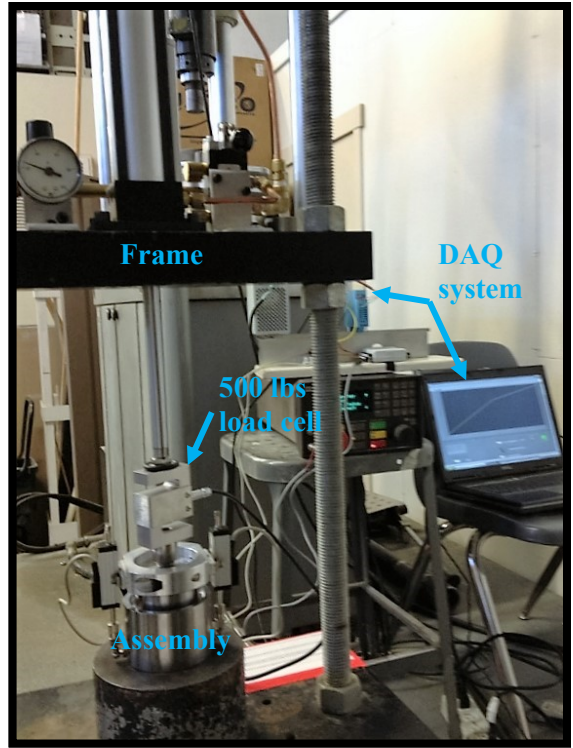


Figure 4.1 500 lbs capacity consolidation frame

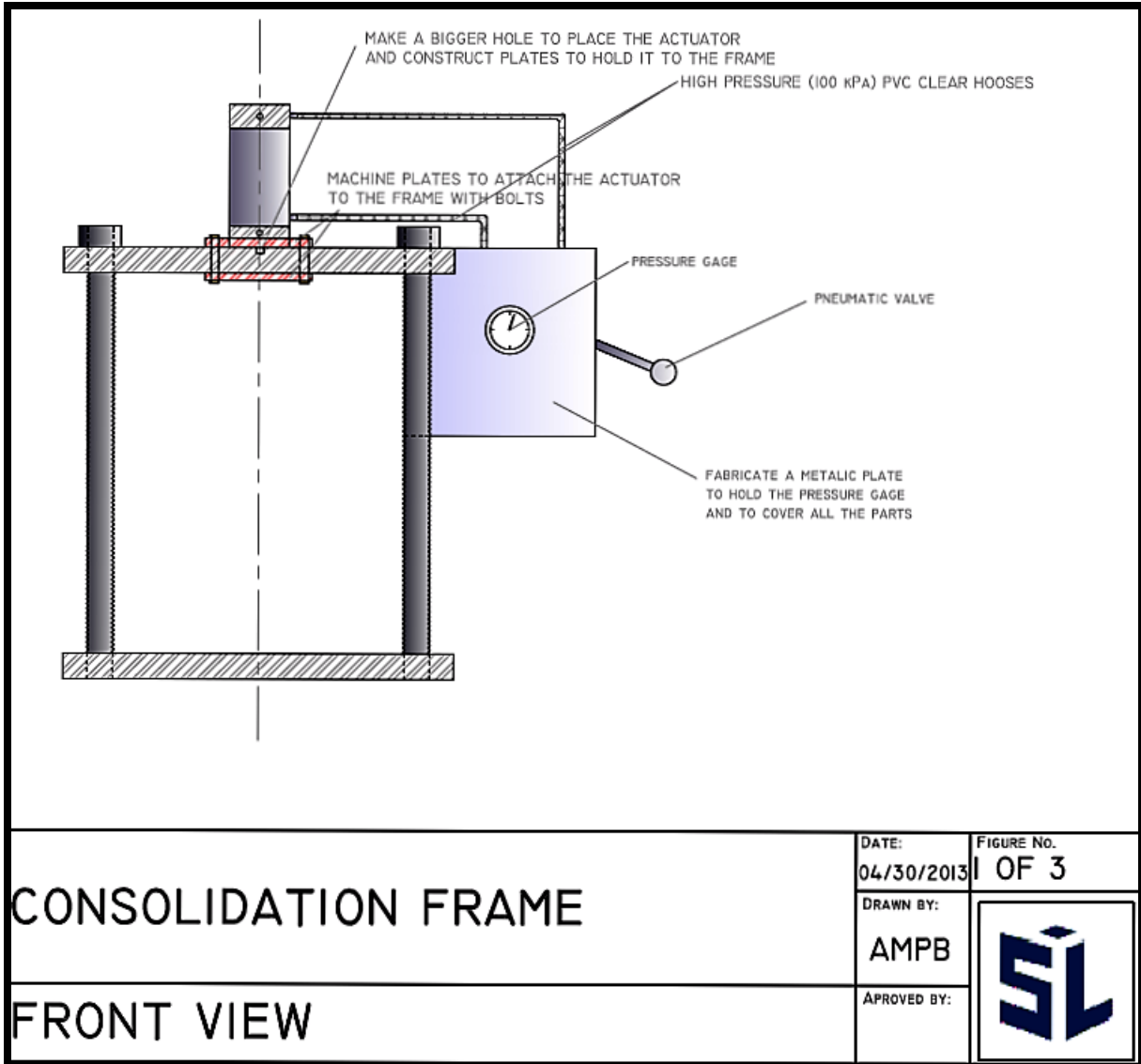


Figure 4.2 Pneumatic consolidation frame front view

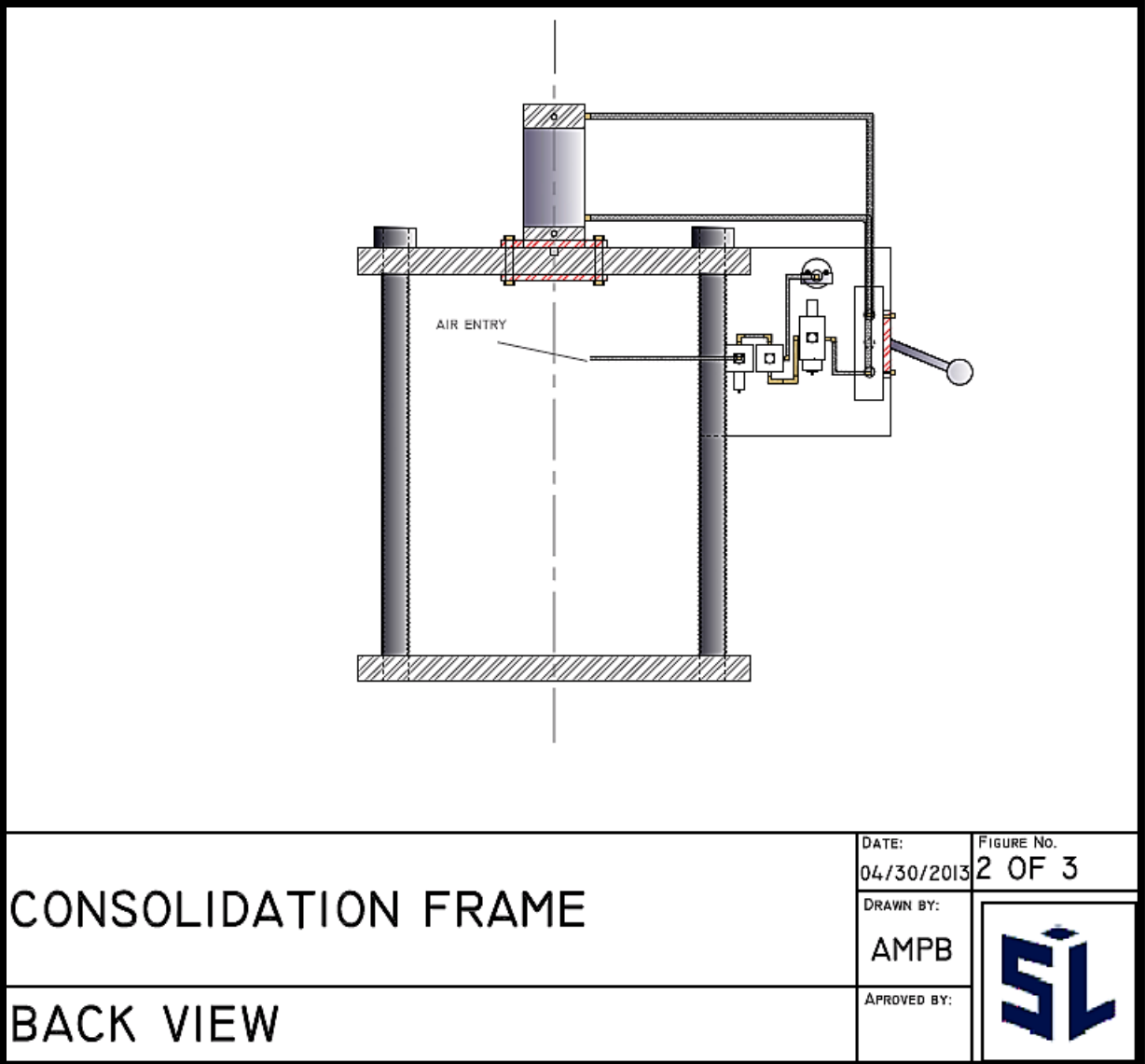


Figure 4.3 Pneumatic consolidation frame back view

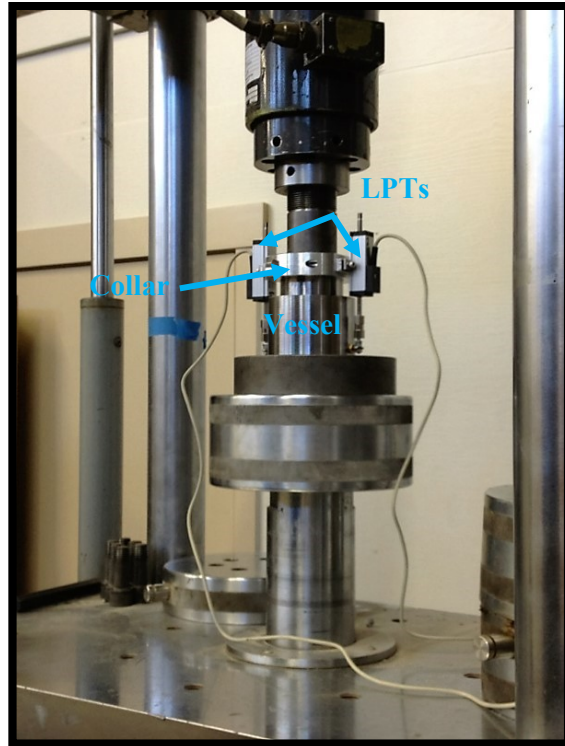


Figure 4.5 100 Kips capacity MTS load frame

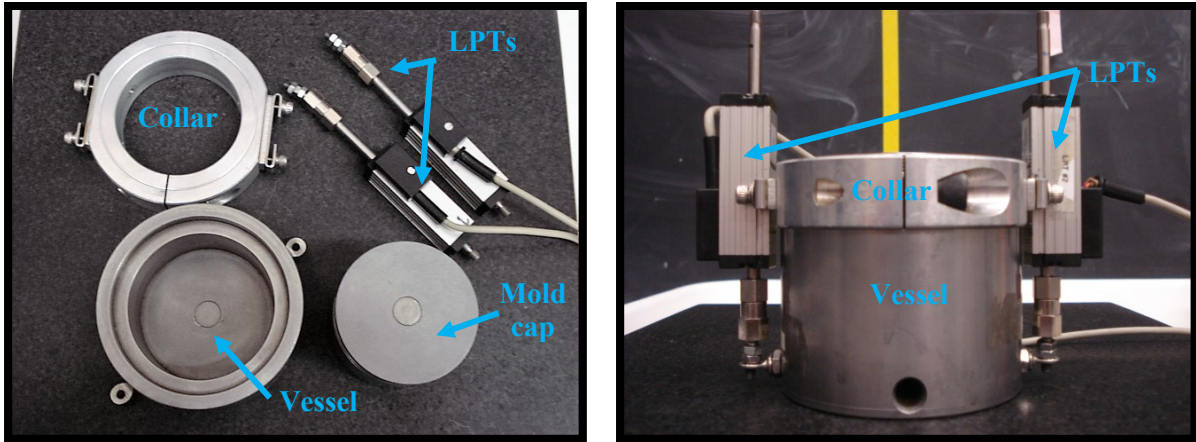


Figure 4.6 1DC mold components (left) and assembly (right)

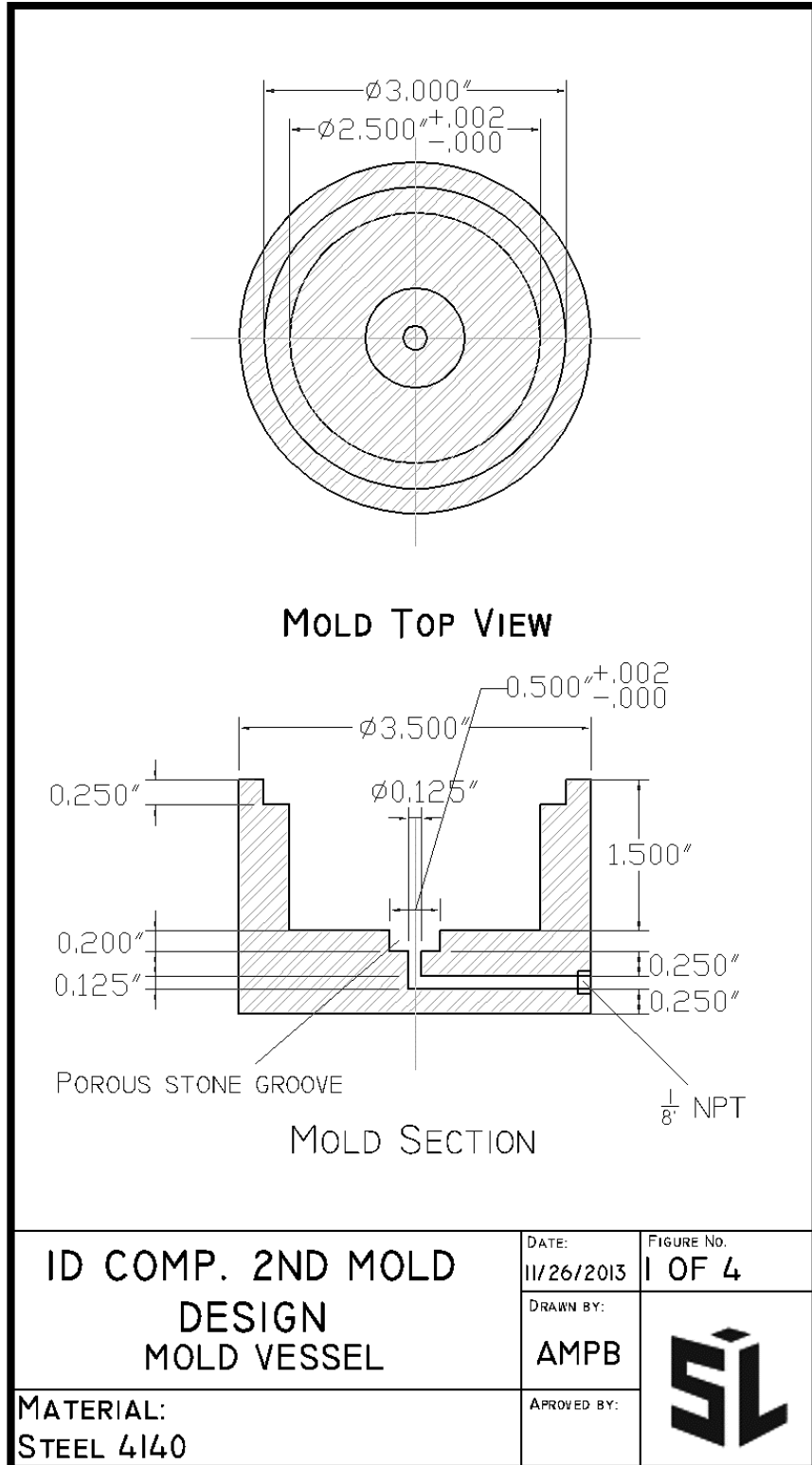


Figure 4.7 IDC mold vessel plans

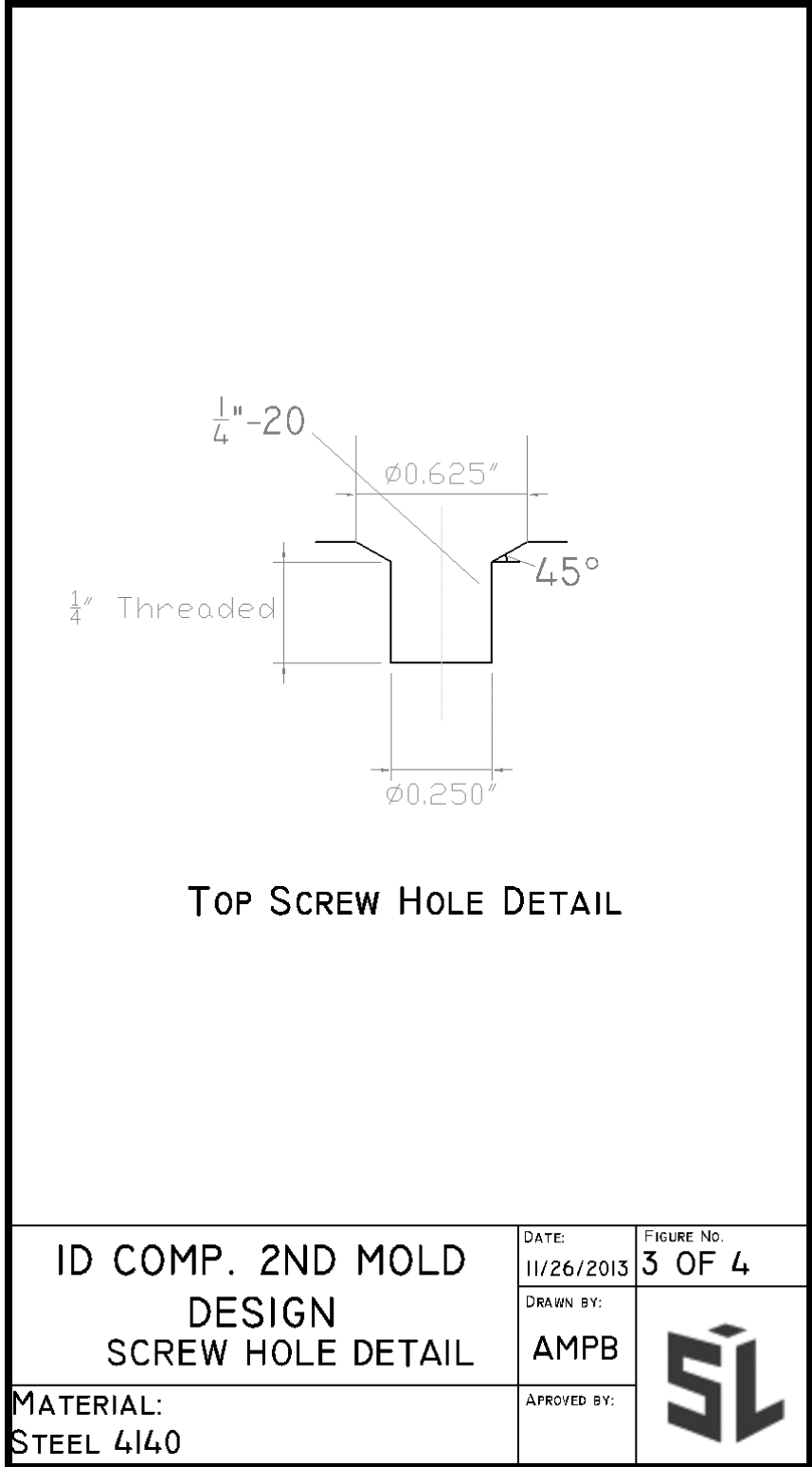


Figure 4.9 IDC mold cap's top screw hole detail plans

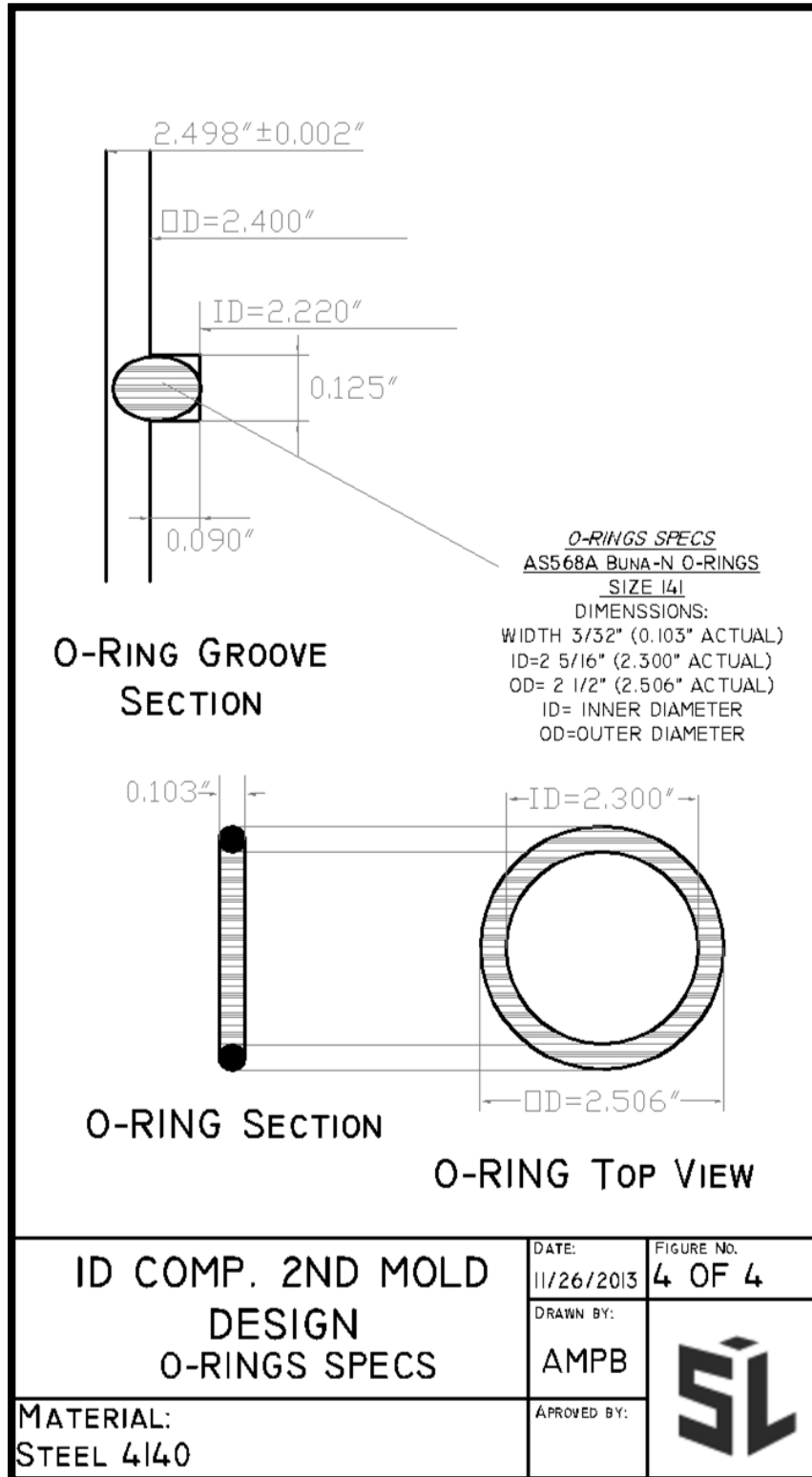


Figure 4.10 IDC mold O-Rings specifications

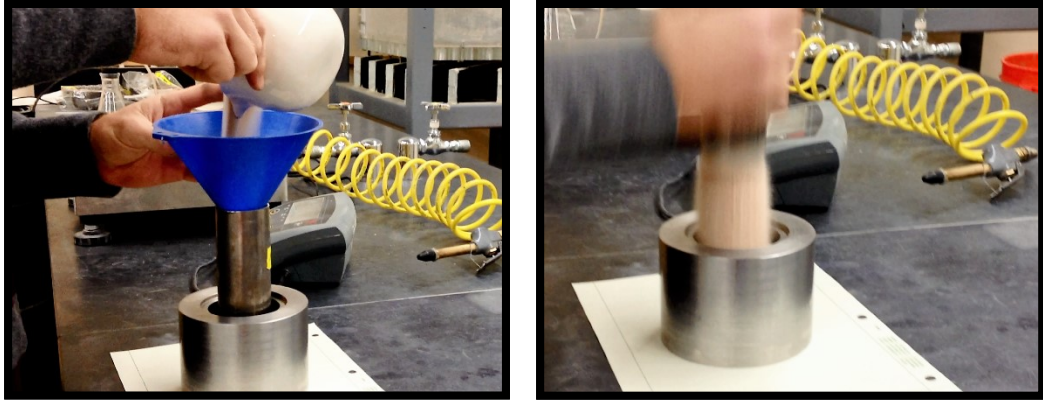


Figure 4.11 Dry funnel deposition method

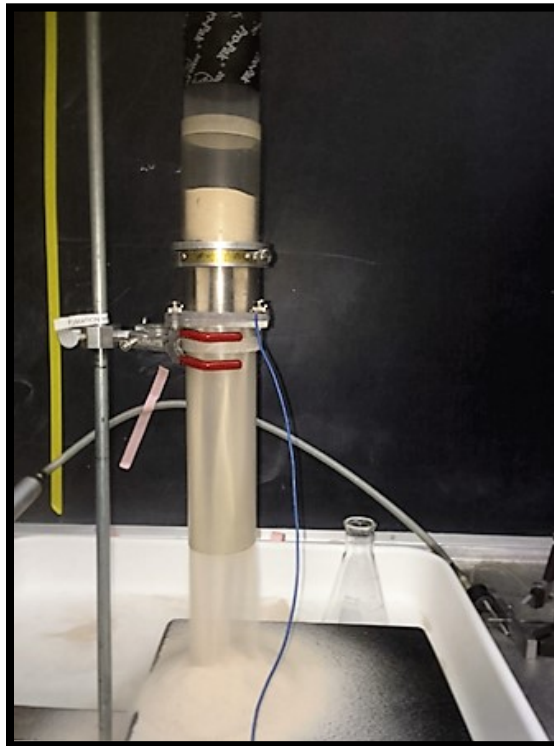


Figure 4.12 Air pluviation method



Figure 4.13 Aluminum pedestal for placing samples for SEM imaging



Figure 4.14 SEM microscope

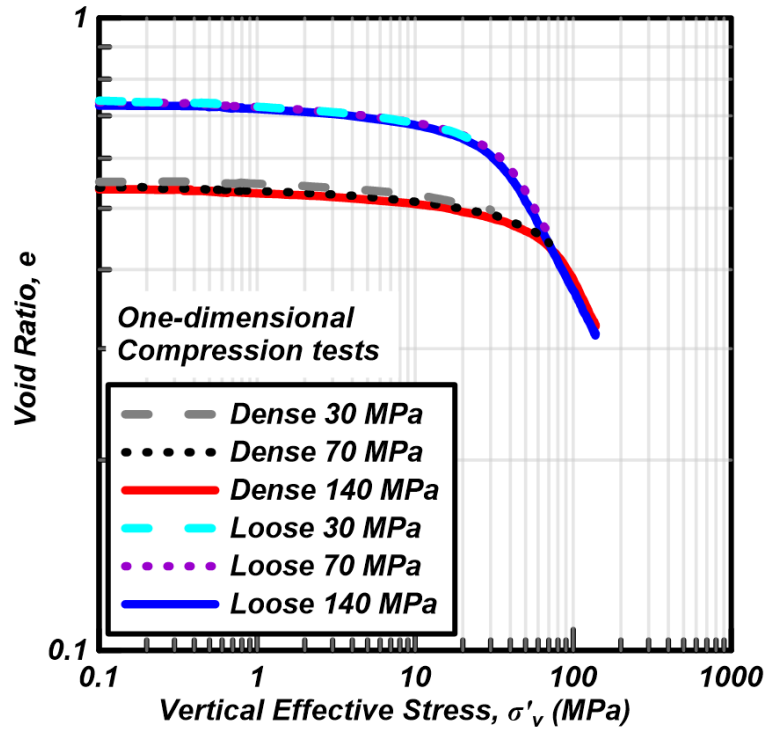


Figure 4.15 Compression curve

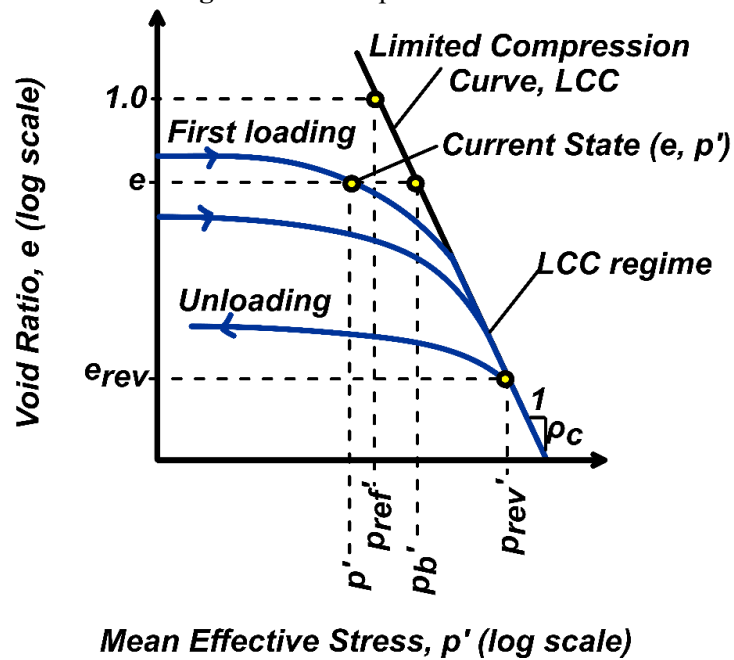


Figure 4.16 Limited Compression Curve (redrawn from Pestana and Whittle 1995)

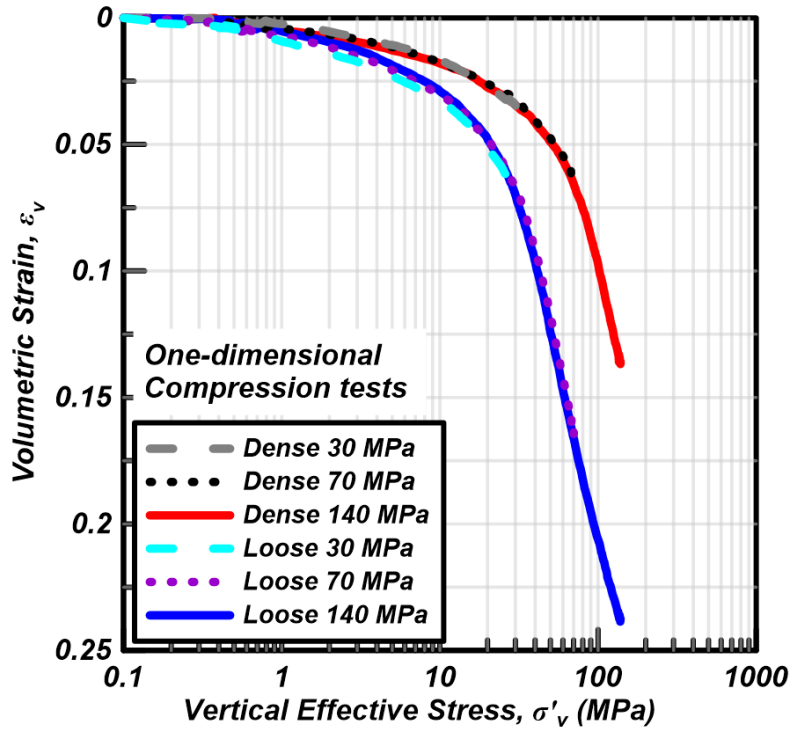


Figure 4.17 Volumetric strain vs. vertical effective stress (semi-log scale)

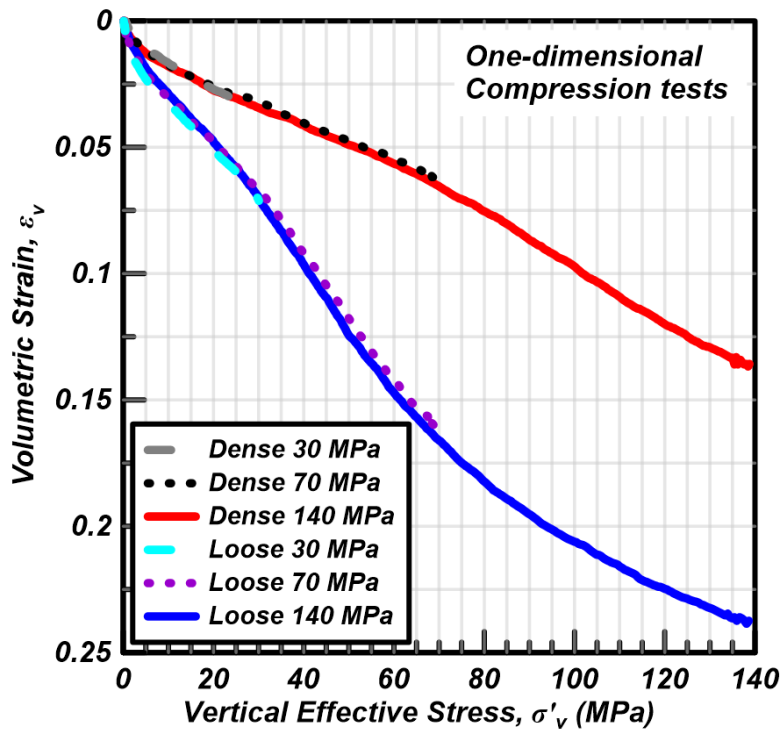


Figure 4.18 Volumetric strain vs. vertical effective stress (arithmetic scale)

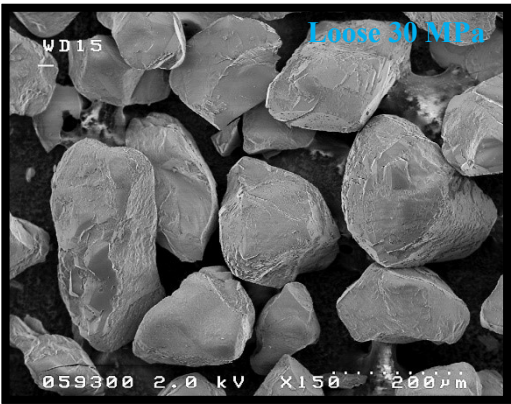
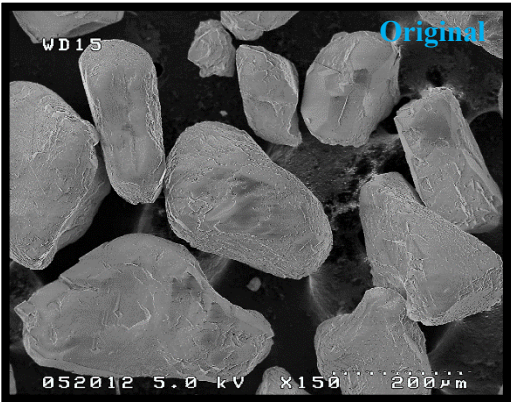


Figure 4.19 From top to bottom: original sand, grains from loose specimen and grains from dense specimen loaded to $\sigma'_{vmax}=30$ MPa

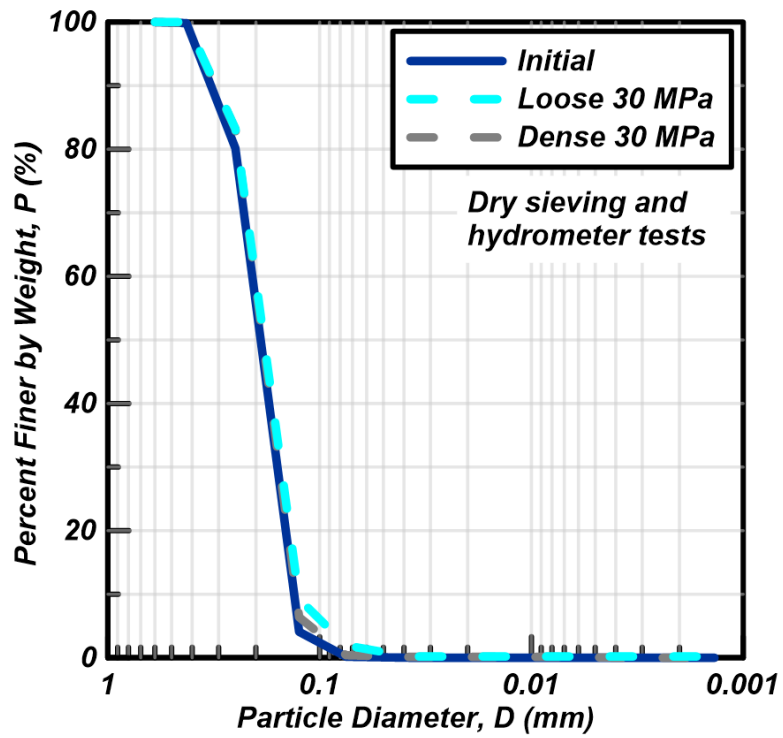


Figure 4.20 GSD after 1DC with $\sigma'_{vmax}=30$ MPa

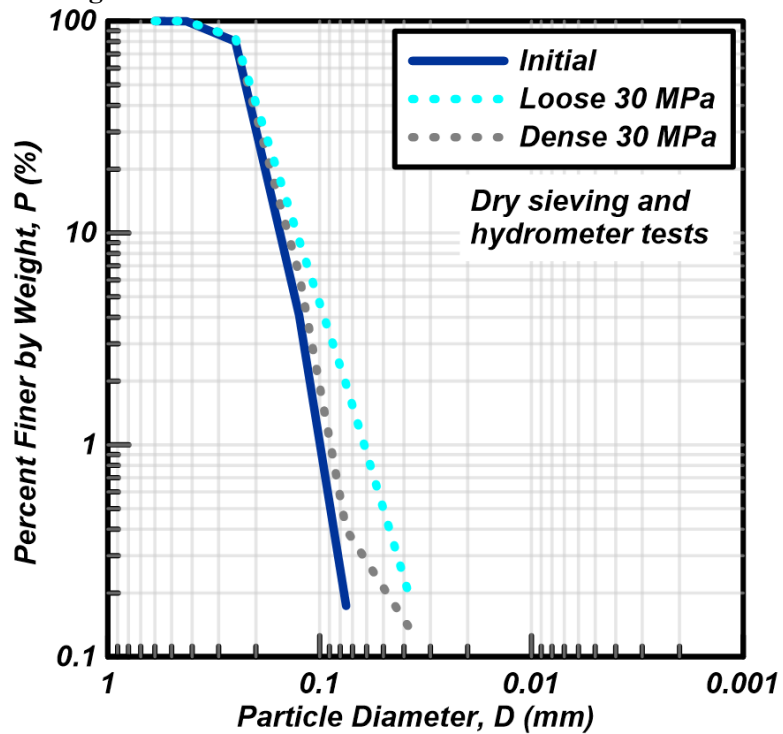


Figure 4.21 GSD after 1DC with $\sigma'_{vmax}=30$ MPa (log-log scale)

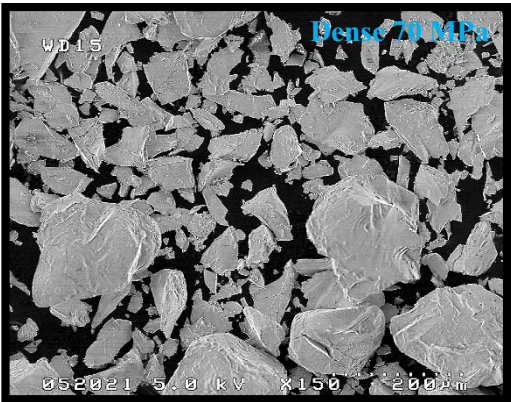
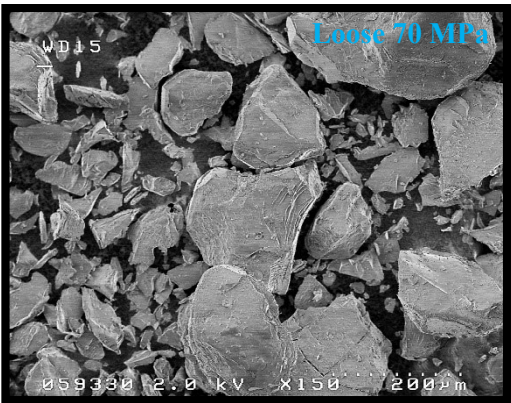
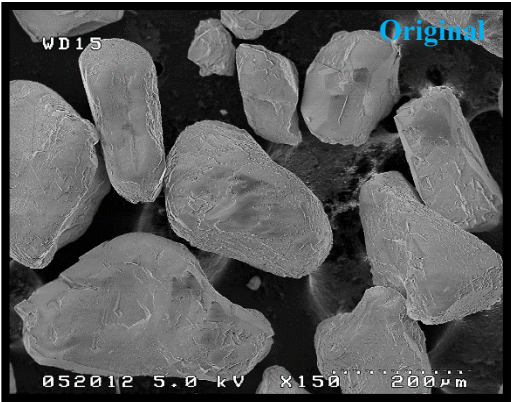


Figure 4.22 From top to bottom: original sand, grains from loose specimen and grains from dense specimen loaded to $\sigma'_{vmax}=70$ MPa

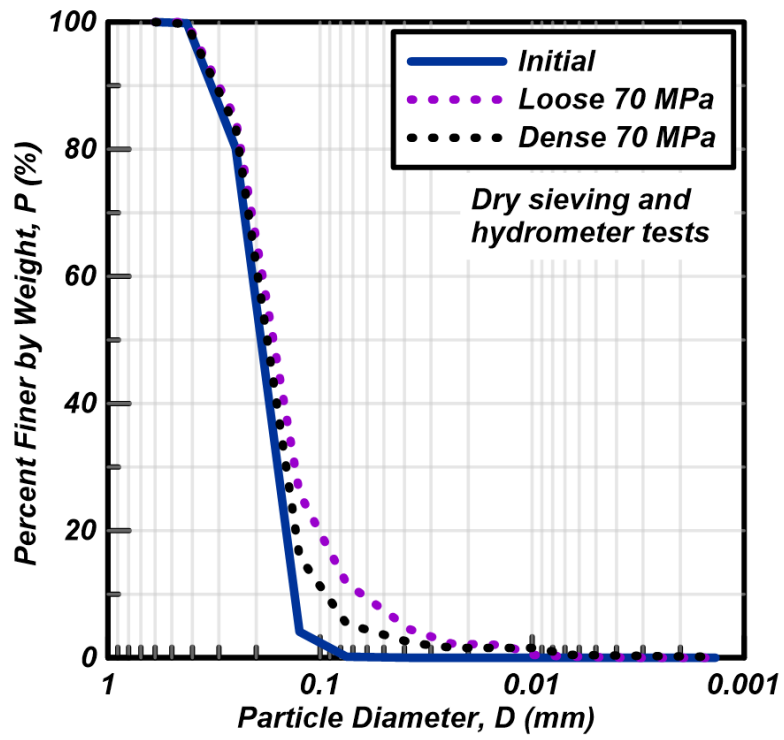


Figure 4.23 GSD after 1DC with $\sigma'_{vmax}=70$ MPa

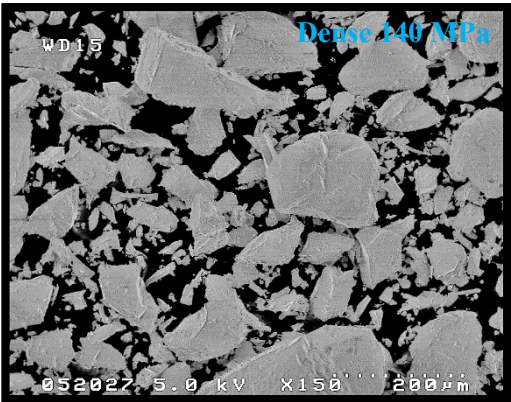
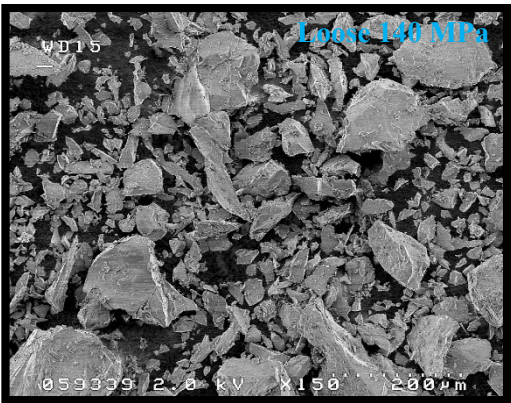
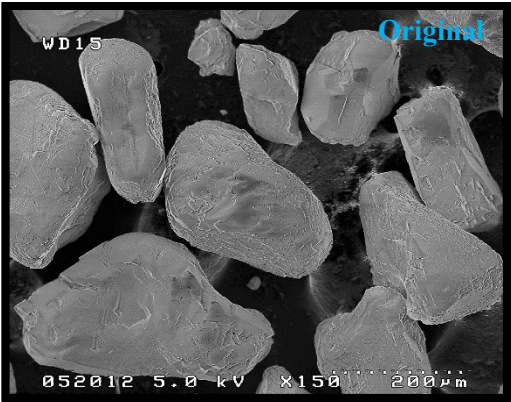


Figure 4.24 From top to bottom: original sand, grains from loose specimen and grains from dense specimen loaded to $\sigma'_{\text{vmax}}=140$ MPa

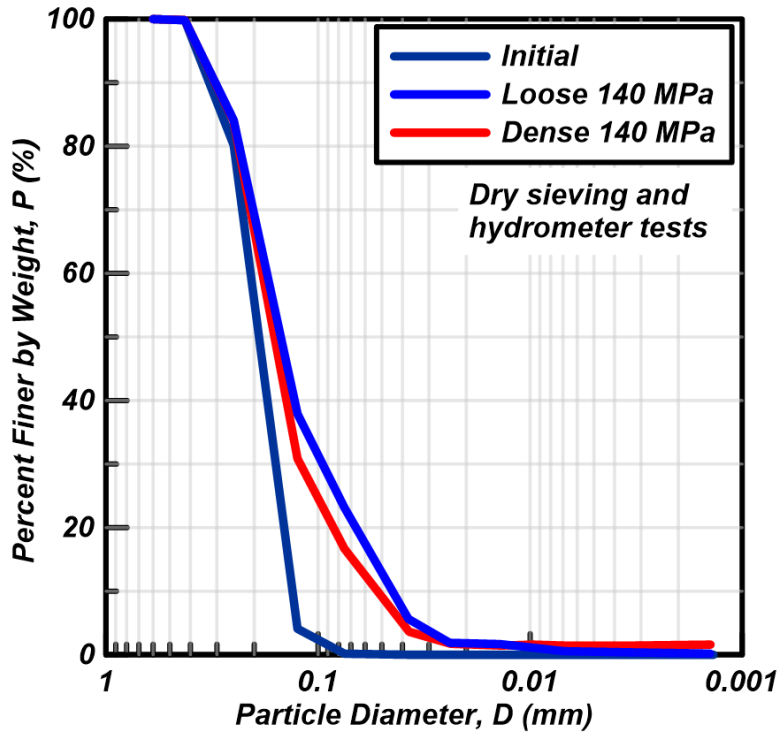


Figure 4.25 GSD after 1DC with $\sigma'_{vmax}=140$ MPa

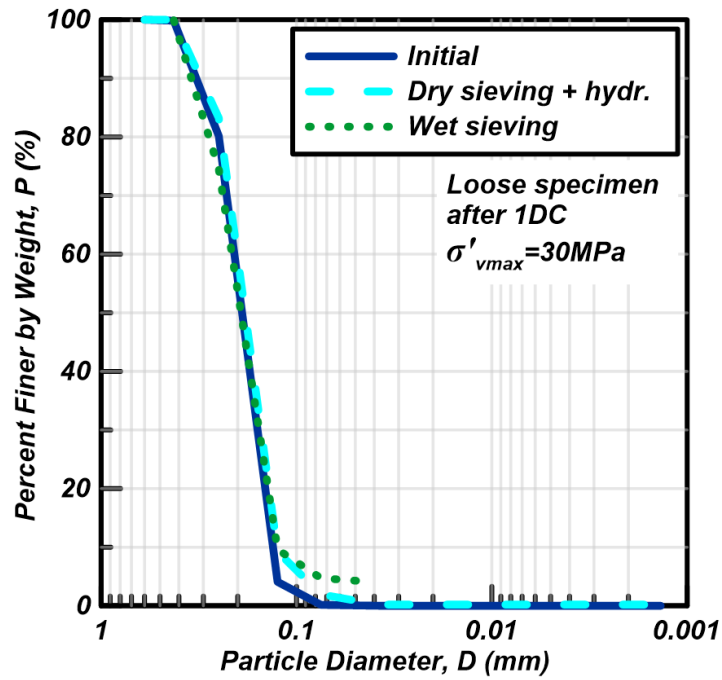


Figure 4.26 GSD from dry sieving and hydrometer vs. wet sieving tests results on loose specimens after 1DC with $\sigma'_{vmax}=30$ MPa

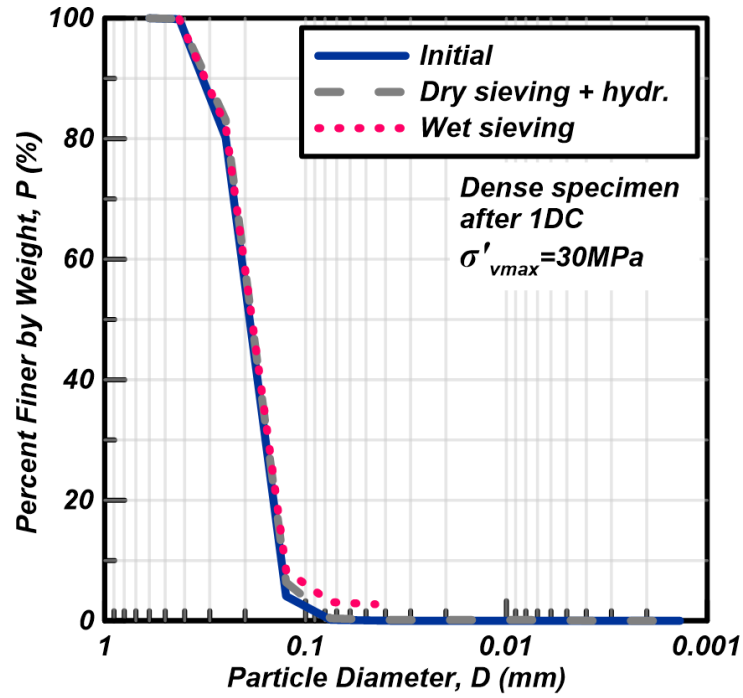


Figure 4.27 GSD from dry sieving and hydrometer vs. wet sieving tests results on dense specimens after 1DC with $\sigma'_{vmax}=30$ MPa

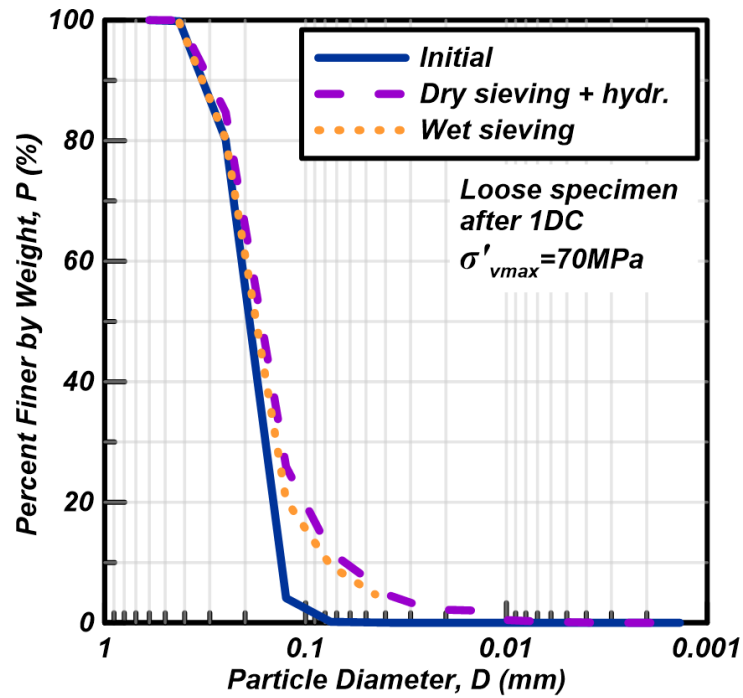


Figure 4.28 GSD from dry sieving and hydrometer vs. wet sieving tests results on loose specimens after 1DC with $\sigma'_{vmax}=70$ MPa

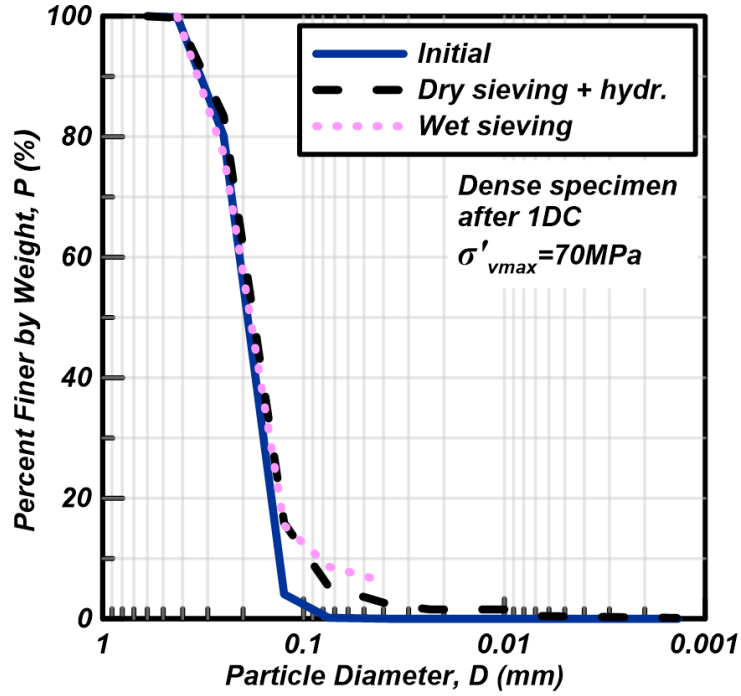


Figure 4.29 GSD from dry sieving and hydrometer vs. wet sieving tests results on dense specimens after 1DC with $\sigma'_{vmax} = 70 \text{ MPa}$

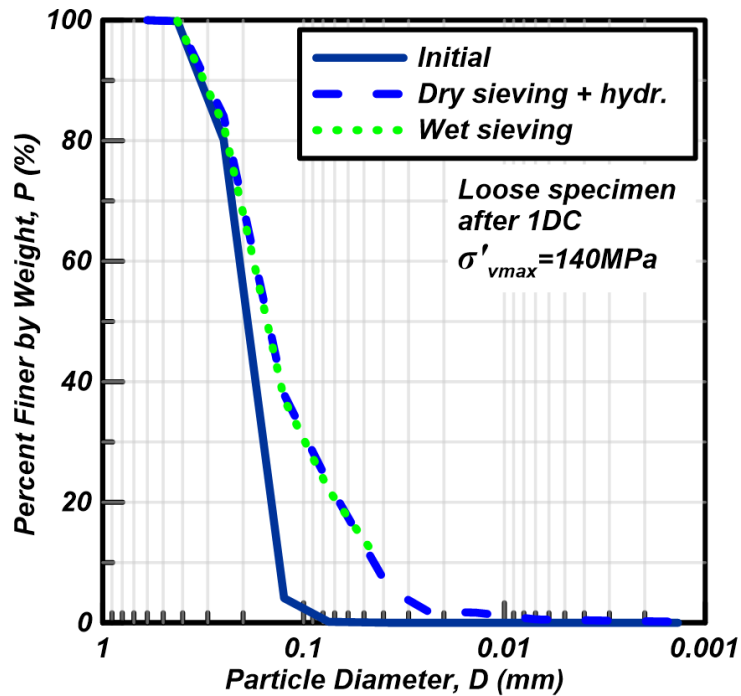


Figure 4.30 GSD from dry sieving and hydrometer vs. wet sieving tests results on loose specimens after 1DC with $\sigma'_{vmax} = 140 \text{ MPa}$

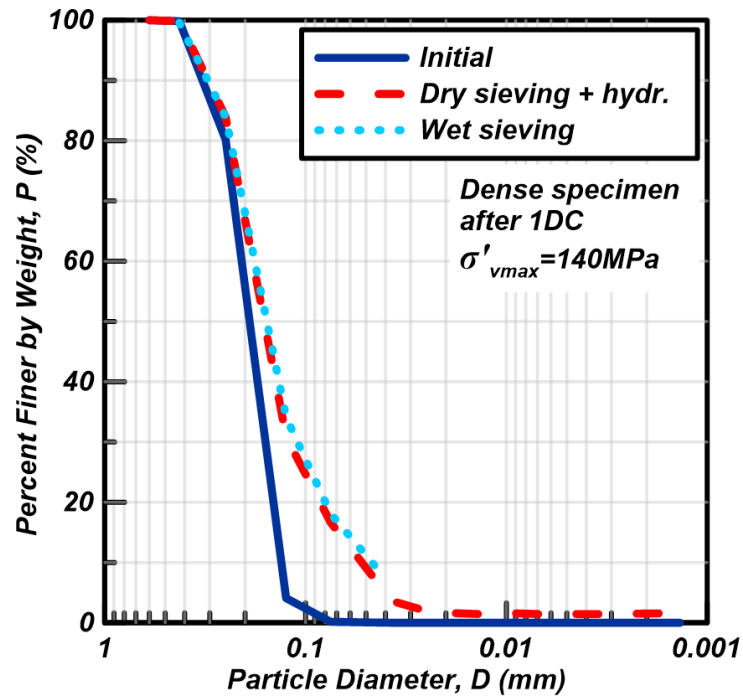


Figure 4.31 GSD from dry sieving and hydrometer vs. wet sieving tests results on dense specimens after 1DC with $\sigma'_{vmax} = 140$ MPa

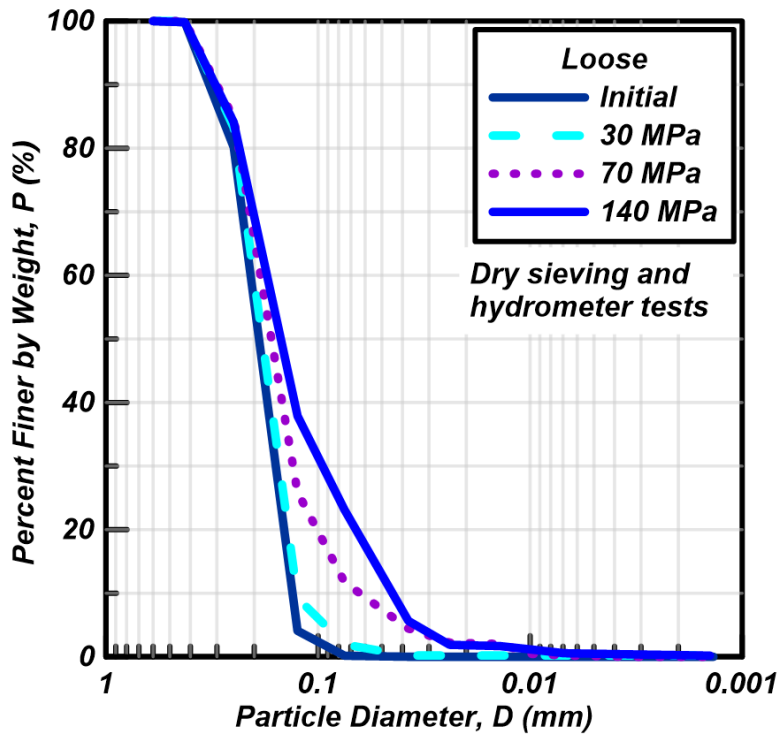


Figure 4.32 GSD after 1DC from loose specimens

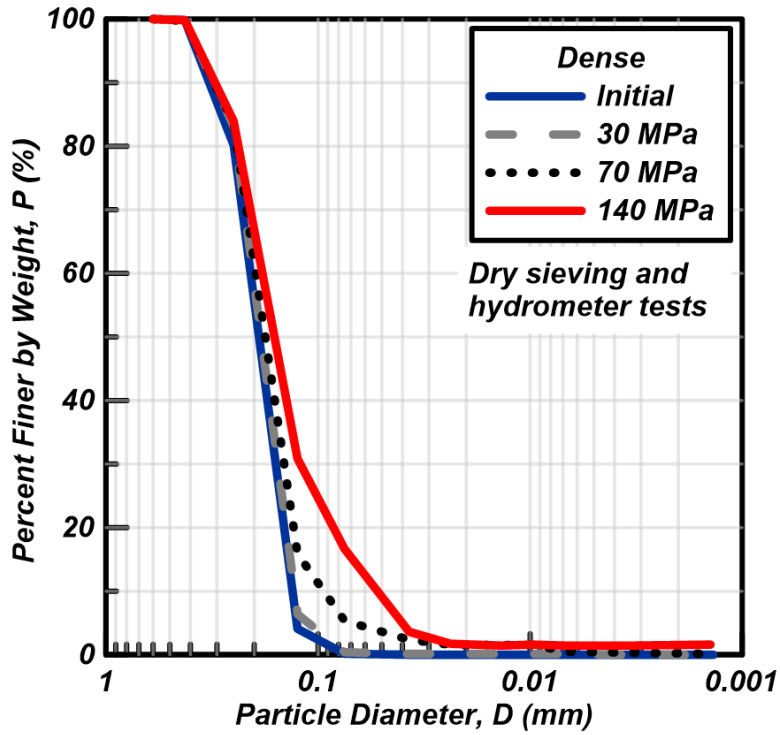


Figure 4.33 GSD after IDC from dense specimens

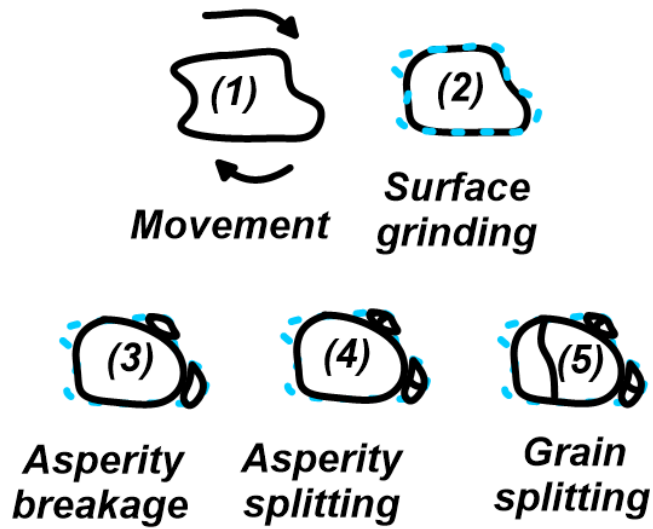


Figure 4.34 Particle breakage stages (described by Nakata et al. 2001)

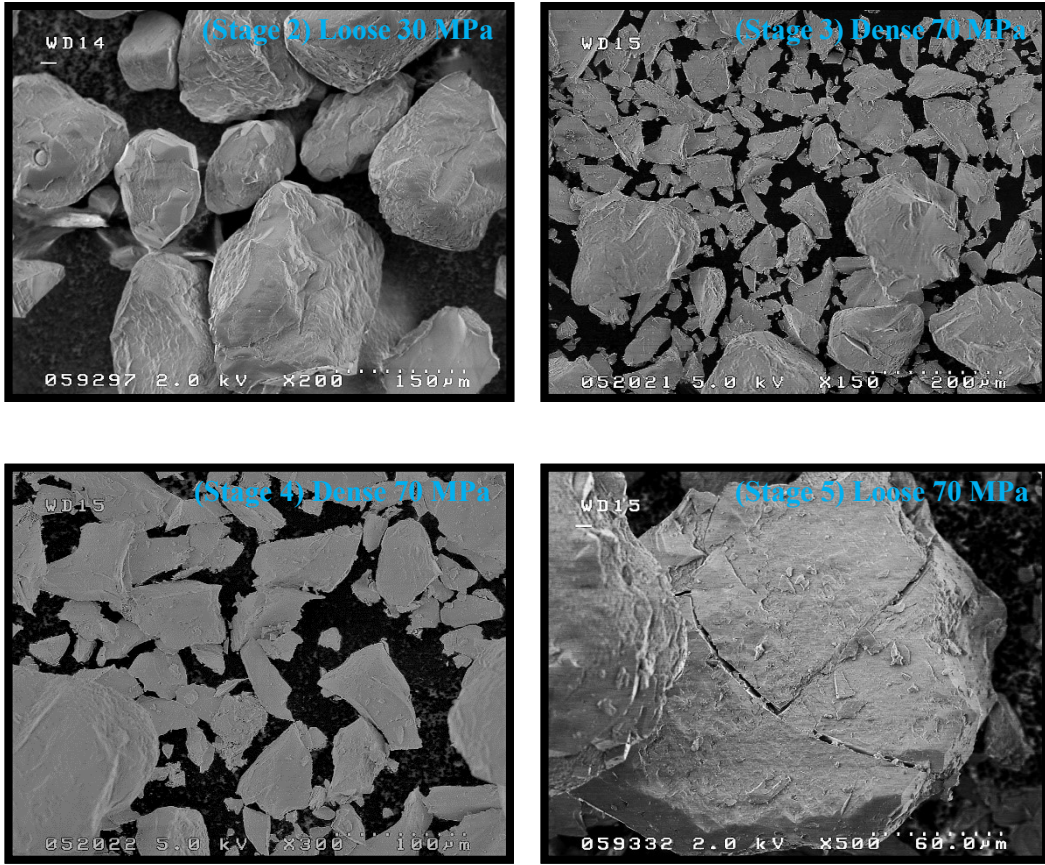


Figure 4.35 Particle breakage stages examples, from top left to bottom right: (1) surface grinds, (2) asperities break, (3) asperities split, (4) particles split

Chapter 5

Monotonic Direct Simple Shear Characteristics

5.1 Introduction

This chapter summarizes the undrained monotonic Direct Simple Shear (DSS) results for Ottawa F-65 sand including: stress strain and stress path responses on normally consolidated specimens consolidated to σ'_{vc} of 100 kPa, 400 kPa and 800 kPa, the critical state friction angle (ϕ'_{cr}) and the inferred critical state line (CSL) position. The cyclic and pre-strain DSS tests are described in following chapters.

5.2 Monotonic DSS testing procedures

Monotonic, cyclic and pre-strain DSS tests were performed using a GEOTAC Direct Simple Shear apparatus as shown in Figure 5.1. The apparatus consist of a loading frame with two servo modules controlling motors of vertical and horizontal actuators as shown in Figure 5.2. The servo modules are connected to a computer by a network module and all the system is controlled by a computer with the Digishear software. The horizontal actuator pushes a horizontal travelling plate and the vertical actuator directly pushes the top cap inside the assembly that contains the specimen. The actuators have load cells that measure the force they apply to the specimen. The vertical servo module has a deformation rod which has a DCDT position transducer on top that allows measuring the vertical position of the vertical actuator. The travelling plate touches a Linear Variable Displacement Transducer (LVDT) that measures the horizontal position of the travelling plate.

Loose specimens were prepared by the dry funnel deposition method and dense specimens were prepared by the air pluviation method as described in further detail in Chapter 4 and in the online database

at NEESHUB.org. The specimens were placed inside an assembly, which consisted of the bottom cap overtopped with confining rings surrounding a latex membrane. The rings were kept together with clamping screws as shown in Figure 5.3. The top cap was placed on top of the specimens and inside the inner latex membrane after the specimen was placed inside the membrane. The top cap was attached to the inner latex membrane with three O-rings. Details of the top and bottom caps are shown in Figure 5.4. The assembly containing the specimens and the top cap was placed in the DSS device. The assembly was affixed to the apparatus by attaching the bottom cap to the travelling plate of the apparatus by means of a bolt. Then, the specimens were subjected to a seating load to impose σ'_v of 10 kPa to level the top cap, while affixing the top cap of the assembly to the vertical actuator of the DSS apparatus with a bolt. Then, the load application was stopped and the specimens were saturated with approximately 100 ml of deionized water; the load was stopped to allow the water to flow inside the specimen by gravity. Loose specimens were saturated in approximately 25 minutes while dense specimens were saturated in approximately 35 minutes. Specimens were saturated until the remaining volume of water on the saturation tank was 10 ml, at this point no air bubbles came out from the drainage line inside the beaker. The process did not include percolation with CO₂ to avoid the disturbance of the specimen's fabric and to reduce the time of the saturation process. Achieving 100% saturation was not the main concern in the saturation process due to all the specimens were sheared under a constant volume condition; Finn and Vaid (1977) showed no practical differences in the results from constant volume cyclic DSS tests on dry and saturated specimens of Ottawa C-109 sand. After saturation, the saturation lines that went into the specimens were closed, the clamping screws that kept the rings together were removed and the specimens were consolidated. The drainage line that went from the specimen to a collection beaker for water to exit the specimen remained open during consolidation.

Consolidation was done using Incremental Load Consolidation (ICL). Load increments started with a consolidation stress of 25 kPa and the stress increased with a Load Increment Ratio (LIR) of 2 up to the desired consolidation stress for each test. Each load increment was applied for 5 minutes with the exception of the last load increment, which was applied from the end of the preceding load increment to one hour

after the starting point of the first load increment. The last consolidation load increment lasted longer than the other load increments to allow the specimen to consolidate and creep before shearing. Then, the horizontal actuator was moved until the horizontal load cell started to touch the side of the travelling plate. After touching the travelling plate, the horizontal load cell was connected to the travelling plate with a bolt while maintaining the consolidation load. Then, the consolidation load control was stopped and the constant height bolts were tightened to ensure a constant height condition during the shearing stage of the test. The vertical load sometimes increased a little during the tightening of the bolts. The excess of load was allowed to freely reduce to a value closer to the consolidation load by waiting 15 to 25 minutes before starting the shearing of the specimen; longer times were required for the dense specimens due to the increment in the load while tightening the bolts sometimes being greater.

Specimens were sheared under a constant height condition which is equivalent to an undrained shearing condition in the DSS (Dyvik et al 1987). All of the tests with $\sigma'_{vc}=100$ kPa and some of the tests with $\sigma'_{vc}=400$ kPa showed a mean volumetric strain (ϵ_v) $<0.05\%$ as recommended by ASTM D6528 – 07 (2007), with the exception of test 6 and 15 ($\sigma'_{vc}=400$ kPa) and all the tests with $\sigma'_{vc}=800$ kPa. Tests were run in deformation controlled mode with a deformation controlled rate equivalent to 50% shear strain per hour and were stopped at a maximum shear strain of 25% to comply with recommendations provided by ASTM D6528 – 07 (2007). Results are presented up to a maximum shear strain of 15%; ring slippage and significant localization within the specimen sometimes occurred after shear strains exceeded 15% as described by Doygun (2009), indicating an increase of the non-uniformity of the stresses within the specimen. This situation diminishes the reliability of the results at shear strains higher than 15%.

5.3 Stress strain and stress path responses

Stress path and stress-strain responses from specimens consolidated to a vertical effective stress (σ'_{vc}) of 100 kPa are shown in Figure 5.5 and Figure 5.6 respectively. Results show that the dilative tendencies increased with relative density in the specimens consolidated to 100 kPa as expected. Specimen from test

3 reached a critical state (CS) condition after achieving a shear strain of approximately 3%. Specimen from test 5 reached a quasi-steady state (QSS) condition after achieving a shear strain of approximately 3%, but continued to have a dilative tendency under higher shear strains. Specimen from test 12 did not show a quasi-steady state and showed a strong dilative tendency during most of the test.

Stress path and stress-strain responses from tests on specimens consolidated to $\sigma'_{vc}=400$ kPa are shown in Figure 5.7 and Figure 5.8 respectively. Results show that the dilative tendencies increased with relative density in the specimens consolidated to $\sigma'_{vc}=400$ kPa as expected. Specimens from tests 6 and 8 reached a quasi-steady state at a shear strain of 7.5% approximately, but continued to dilate under higher shear strains up to the end of the test. Specimens from tests 13 and 15 did not show a quasi-steady state and showed a strong dilative tendency during most of the test.

Stress path and stress-strain responses from tests on specimens consolidated to $\sigma'_{vc}=800$ kPa are shown in Figure 5.9 and Figure 5.10 respectively. Results shown that the dilative tendencies increased with relative density in the specimens consolidated to $\sigma'_{vc}=800$ kPa as expected. Specimens from tests 2 and 7 reached a quasi-steady state at a shear strain of 4% approximately, but continued to dilate under higher shear strains up to the end of the test. Specimens from tests 4, 11 and 9 did not show a quasi-steady state and showed a strong dilative tendency during most of the test.

The dilative tendencies across all tests generally increased with increasing density and decreased with increasing consolidation stress. Stress paths from tests on specimens with $D_R < 35\%$ are shown in Figure 5.11. Dilative tendencies decreased with increasing confining stress for the tests on specimens consolidated to $\sigma'_{vc}=100$ and $\sigma'_{vc}=400$ kPa with $D_R < 35\%$. The dilative tendencies appear to increase for the tests consolidated to $\sigma'_{vc}=800$ kPa with $D_R < 35\%$, but these specimens had slightly greater as-consolidated densities. Dilative tendencies of these specimens are controlled by the D_R . However, the increment of dilative tendencies in the specimens consolidated to $\sigma'_{vc}=800$ might have been caused by compliance. The specimens consolidated to $\sigma'_{vc}=800$ kPa experienced higher compliance ($\epsilon_v=0.223\%$ and $\epsilon_v=0.206\%$ was the maximum compliance for the tests with $D_R=34\%$ and $D_R=35\%$ respectively, when shear strain was

between 5% and 15%) during the constant volume phase than the specimens consolidated to $\sigma'_{vc}=100$ kPa and $\sigma'_{vc}=400$ kPa (All the tests had a maximum compliance smaller than $\epsilon_v = 0.05\%$ with the exception of test 6 which had a maximum compliance of $\epsilon_v = 0.14\%$, when shear strain was between 5% and 15%).

Stress paths from tests on specimens with $35\% < D_R \leq 69\%$ are shown in Figure 5.12. Dilative tendencies were very similar for the tests on specimens consolidated to $\sigma'_{vc}=400$ and $\sigma'_{vc}=800$ kPa with $D_R=58\%$ and $D_R=54\%$ respectively. The specimen consolidated to $\sigma'_{vc} = 800$ kPa has a greater dilative tendency, but it also had the greater $D_R=69\%$ among all the tests with $35\% < D_R \leq 69$. Overall dilative tendencies of these specimens are controlled by the D_R . Specimens consolidated to $\sigma'_{vc}=400$ and $\sigma'_{vc}=800$ kPa with $D_R=58\%$ and $D_R=54\%$ showed more initial contraction than the specimens consolidated to $\sigma'_{vc}=800$ kPa with $D_R=69\%$. However, these specimens did not show a clear quasi-steady state.

Stress paths from tests on specimens with $69\% < D_R$ are shown in Figure 5.13. Dilative tendency was the smallest for the test on the specimen consolidated to $\sigma'_{vc}=100$ with $D_R=78\%$. Dilative tendencies were very similar for the tests on specimens consolidated to $\sigma'_{vc}=400$ and $\sigma'_{vc}=800$ kPa with $D_R=81\%$ and $D_R=78\%$ respectively. The specimen consolidated to $\sigma'_{vc}=100$ kPa with $D_R=78\%$ showed the highest initial contractive tendency followed by the specimen consolidated to $\sigma'_{vc}=400$ kPa with $D_R=81\%$ and by the specimen consolidated to $\sigma'_{vc}=800$ kPa with $D_R=78\%$ respectively. Dilatancy tendencies increasing with consolidation stress is the opposite behavior compared to the expected behavior. Compliance had an influence on the observed behaviors. Loose specimens consolidated to $\sigma'_{vc}=400$ and $\sigma'_{vc}=800$ kPa experienced higher compliance ($\epsilon_v=0.052\%$ and $\epsilon_v=0.1\%$ was the maximum compliance respectively, when shear strain was between 5% and 15%) during the constant volume phase than the specimen consolidated to $\sigma'_{vc}=100$ kPa ($\epsilon_v=0.02\%$ was the maximum compliance respectively, when shear strain was between 5% and 15%).

A compliance test was run to determine the amount of compliance during compression and the effectiveness of the constant height bolts mechanism to reduce compliance. The test was run with different loading increments while having the constant height bolts tight in some stages and released in other stages.

An aluminum puck with a height of 12.68 mm and a diameter of 64.52 mm was loaded and unloaded to evaluate the compliance on the equipment. Two DCDTs were placed to measure compliance, one was placed on the top of the vertical actuator piston as is usually placed during a regular DSS tests and another one was placed on a plate attached below the load cell of the equipment. The puck was loaded to 600 and unloaded 400 kPa while maintaining the constant height bolts released, then the constant height bolts were tightened and the loading sequence was repeated. This loading process was repeated but the load increments were changed to 800 kPa and 400 kPa. Differences in the strains measured by the two DCDTs were observed. The DCDT on the top of the piston did move during the loading stages when having the constant height bolts tight, whereas the DCDT on top of the plate did not move when having the constant bolts tight. Both DCDTs moved when the constant height bolts were released and any of the DCDTs measured zero strain during unloading of the zeroing load which corresponded to a stress of 10 kPa. These results indicate that the actuator on the top is being held in position.

The compliance effect on the results of the tests that showed significant compliance is difficult to be determined with certainty because it depends on the amount of tightening that was put on the constant height bolts and the actuator being stuck during the test; the amount of compliance observed in the specimens consolidated to $\sigma'_{vc}=400$ and $\sigma'_{vc}=800$ kPa increased with reducing relative density, which might indicate that in the case of the looser specimens the bolts were not tight enough to avoid the disturbance of the specimens. Thus, a rough estimation of the error on the results of the tests consolidated to $\sigma'_{vc}=800$ kPa caused by the compliance can be made assuming the constant height bolts were loosened, by obtaining the compliance from the unloading stage of the compliance test when the puck was unloaded from 800 kPa to 400 kPa and comparing this stiffness with the stiffness from a loose specimen. The compliance of the equipment is 3×10^{-4} m/kN. The compliance from the specimen was determined using the Young's modulus relationship presented in Figure 6.13 presented on Chapter 6. The compliance for the specimen from test 7 ($D_R=34\%$) is 2.75×10^{-5} m/kN. The ratio of the compliances is 9% and corresponds to the error on the

vertical effective stresses on test 7, which is the test that presented the highest compliance and was done in the loosest specimen of the tests consolidated to 800 kPa.

5.4 Critical state friction angle

Figure 5.14 shows envelopes that were developed by drawing a tangent of ϕ'_{DSS} that would match the inferred critical state points from the results. The plots show the corresponding ϕ'_{CV} , which corresponds to the arc sine of the tangent of ϕ'_{DSS} , based on the following interpretation method. To interpret DSS results an assumption regarding the state of stress is required because the lateral stresses are unknown. Two common assumptions include that the horizontal plane is the plane of maximum shear stress ($\phi'_{mob} = \alpha$) or that the horizontal plane is the plane of maximum stress obliquity ($\phi'_{mob} = \beta$).

$$\phi'_{mob} = \alpha = \sin^{-1} \left(\frac{\tau}{\sigma'_v} \right) \quad (5.1)$$

$$\phi'_{mob} = \beta = \tan^{-1} \left(\frac{\tau}{\sigma'_v} \right) \quad (5.2)$$

Wijewickreme et al. (2013) conducted simulations of elements within a specimen tested on the DSS apparatus using the Discrete Element Method (DEM) implemented in the code PCF3D. They modeled a sand specimen with a diameter of 15 cm and a height of 4.5 cm, confined by a top cap, a bottom cap and 23 confining rings 2 mm thick. Specimens were consolidated to of $\sigma'_{vc}=100$ kPa. The results from their simulations of a soil element at the center of the specimen (MS1), which was subjected to constant volume monotonic shearing up to $\gamma=20\%$ are as follows: they suggested for $12\% < \gamma < 15\%$ ϕ'_{mob} becomes approximately equal to α , whereas for $\gamma=20\%$ ϕ'_{mob} reaches a value between α and β and shows a decreasing trend indicating that ϕ'_{mob} could reach values closer to β at higher values of γ . On the other hand, Powrie (1997) states that at critical state the sine of ϕ'_{PS} is equal to the tangent of ϕ'_{DSS} because the angle of dilation is zero. For Powrie (1997), ϕ'_{PS} corresponds to the actual friction angle in plane strain whereas ϕ'_{DSS} corresponds to the horizontal plane being the plane of maximum stress obliquity. Powrie (1997) states that using ϕ'_{DSS} leads to an underestimation of the mobilized friction angle at critical state under plain strain

loading conditions. This argument is consistent with the experimental observations from this project and with reported values of effective critical state friction angles on Ottawa sand published by others as shown in Table 5.1. Figure 5.15 shows the friction angle at the Quasi-Steady State ($\phi'_{DSS QSS}$). $\phi'_{DSS QSS}=24.6^\circ$ is smaller than ϕ'_{DSS} and ϕ'_{CV} . [Kutter and Chen \(1997\)](#) described that the mobilized friction angles under constant p' and under constant volume conditions are different and that the angles under constant volume conditions are smaller than under constant p' . The value of the friction angle at the Quasi-Steady State might be a better approximation of the angle at critical state due to the localization that the specimens arise after shear strains exceed 12%. The $\phi'_{DSS QSS}$ is smaller than the ϕ'_{CV} and is consistent with the observations from [Kutter and Chen \(1997\)](#). Thus, the recommended value of the effective mobilized friction angle at critical state is $\phi'_{DSS QSS}=24.6^\circ$ instead of $\phi'_{CV}=30^\circ$ or $\phi'_{DSS}=26.5^\circ$.

5.5 Critical state line

The above experimental results provide only limited constraints on the position of the critical state line (CSL) because many of the tests were trying to dilate at the end the test. The approximate position of the CSL can be inferred by tracking those few tests (tests 3, 6 and 8) that reached a condition close to critical state as shown in Figure 5.16. The shape and position of the CSL was inferred by using [Boulanger's \(2003\)](#) empirical relationship between D_R and the mean effective stress (p'). This relationship uses [Bolton's \(1986\)](#) dilatancy relationship to define the shape and position of the CSL with the parameters Q and R . The parameters Q and R were selected so the CSL position tracked with the initial state of the specimens from the monotonic DSS tests in D_R vs. p'/p_a space, so those initial states agreed with the observed stress strain responses. $Q=10$ and $R=1$ were proposed by [Bolton \(1986\)](#) to provide an adequate fit for quartzitic sands. These values of Q and R result on a CSL with a position that makes the initial state of all the monotonic DSS tests to be below the CSL, with the exception of the initial state of test 3 as observed in Figure 5.16. The position of the initial states of the specimens with respect to the position of the inferred CSL agree with the observed dilative tendencies of the majority of the specimens, and with the contractive tendency of the specimen in test 3.

Table 5.1 Effective friction angles at critical state measured by others

Author	Material	ϕ'_{cv}	Method	D₆₀	D₁₀	e_{min}	e_{max}
(--)	(--)	(°)	(--)	(mm)	(mm)	(--)	(--)
Carraro et al. (2009)	Ottawa sand	29.5	ICD triaxial compression	0.35	0.18	0.495	0.767
Sukumaran and Ashmawy (2001) and Ashmawy et al. (2003)	Ottawa #20/70 sand	28	ICD triaxial compression	NR D ₅₀ =0.53	NR	0.470	0.780
Sukumaran and Ashmawy (2001) and Ashmawy et al. (2003)	Ottawa #45 sand	33	ICD triaxial compression	NR D ₅₀ =0.57	NR	0.750	1.110
Sukumaran and Ashmawy (2001) and Ashmawy et al. (2003)	Ottawa #60/80 sand	30	ICD triaxial compression	NR D ₅₀ =0.21	NR	0.550	0.850
Sukumaran and Ashmawy (2001) and Ashmawy et al. (2003)	Ottawa #90 sand	32	ICD triaxial compression	NR D ₅₀ =0.27	NR	0.730	1.100

NR= Not reported

Table 5.1 (cont'd) Effective friction angles at critical state measured by others

Author	Material	ϕ'_{cv}	Method	D₆₀	D₁₀	e_{min}	e_{max}
(--)	(--)	(°)	(--)	(mm)	(mm)	(--)	(--)
Santamarina and Cho (2001)	Ottawa F20-30 sand	27	ICD triaxial compression	0.75	0.65	0.502	0.742
Santamarina and Cho (2001)	Ottawa F20-30 sand	28	Simplified method, using the angle of repose of by rotating a cylinder filled with sand and water	0.75	0.65	0.502	0.742
Santamarina and Cho (2001)	Ottawa F110 sand	31	Simplified method, using the angle of repose of by rotating a cylinder filled with sand and water	0.13	0.081	0.535	0.848
Sasitharan et al. (1993 and 1994)	Ottawa sand C109	30.6	ICD triaxial compression	NR D ₅₀ =0.34	NR	0.50	0.82
Dennis (1988)	Ottawa banding sand	30	ICU triaxial compression	NR D ₅₀ =0.19	NR	0.51	0.82
Lee and Seed (1967)	Ottawa sand	30	ICD triaxial compression	0.76	0.65	0.49	≈0.80

NR= Not reported

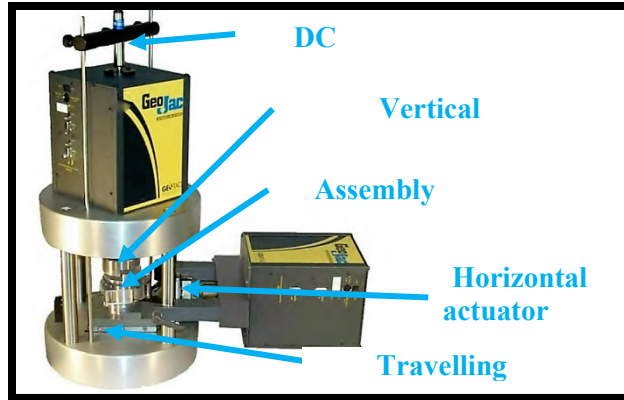


Figure 5.1 Direct simple shear apparatus (Brandon 2013)

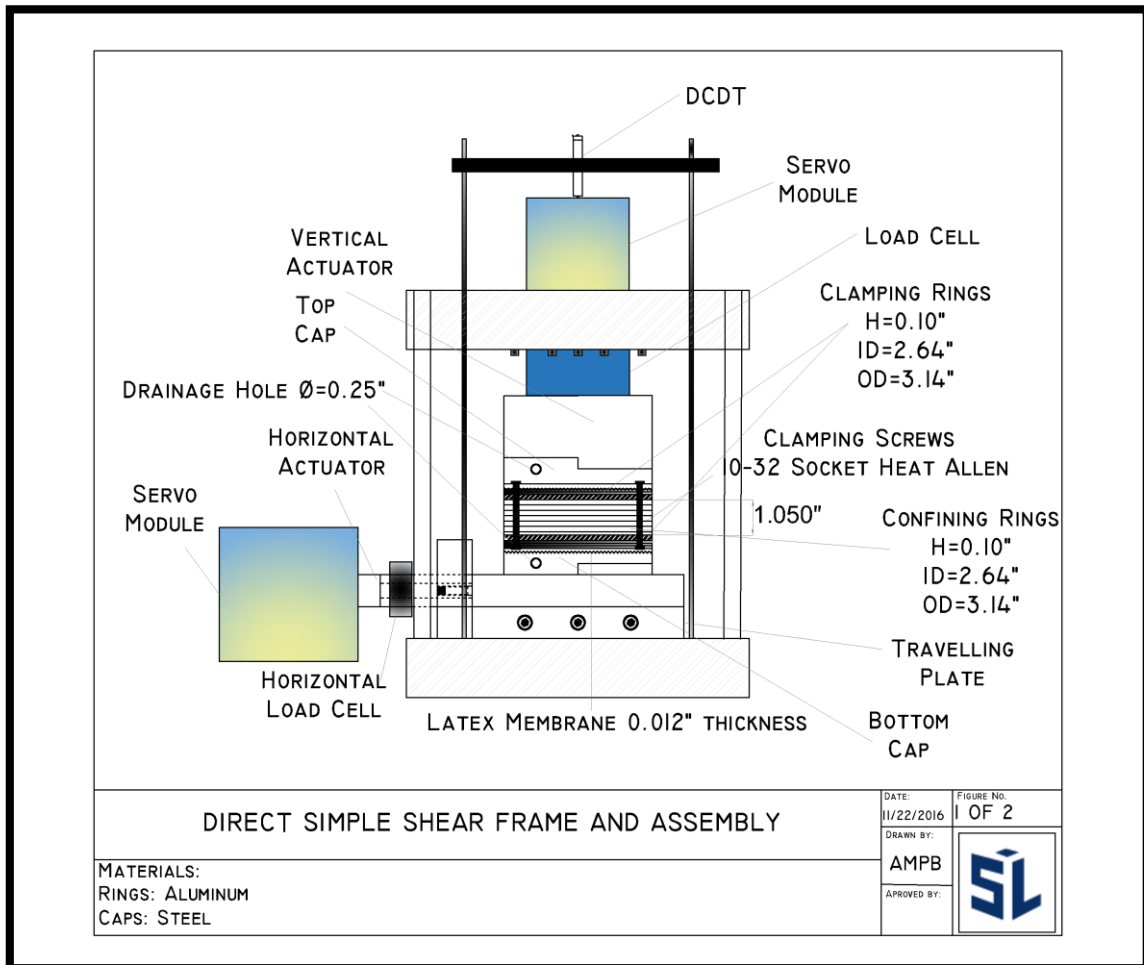


Figure 5.2 DSS Frame including assembly

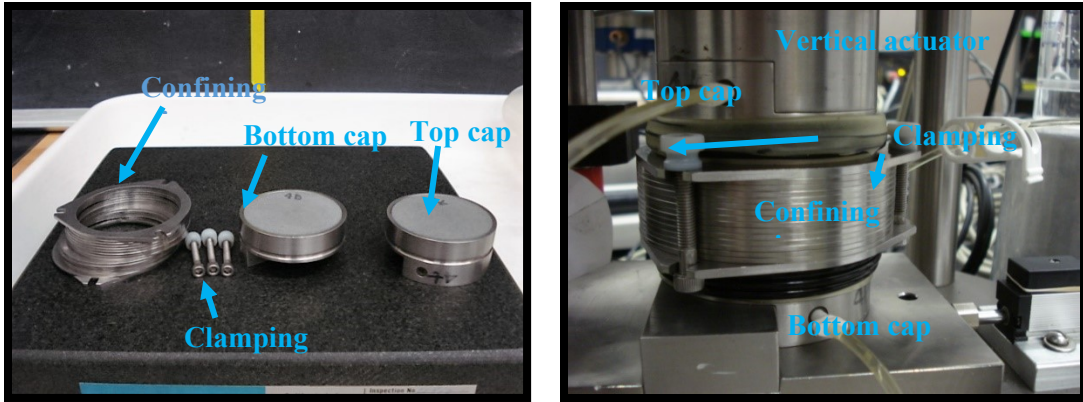


Figure 5.3 Direct simple shear assembly components (left) and assembly (right)

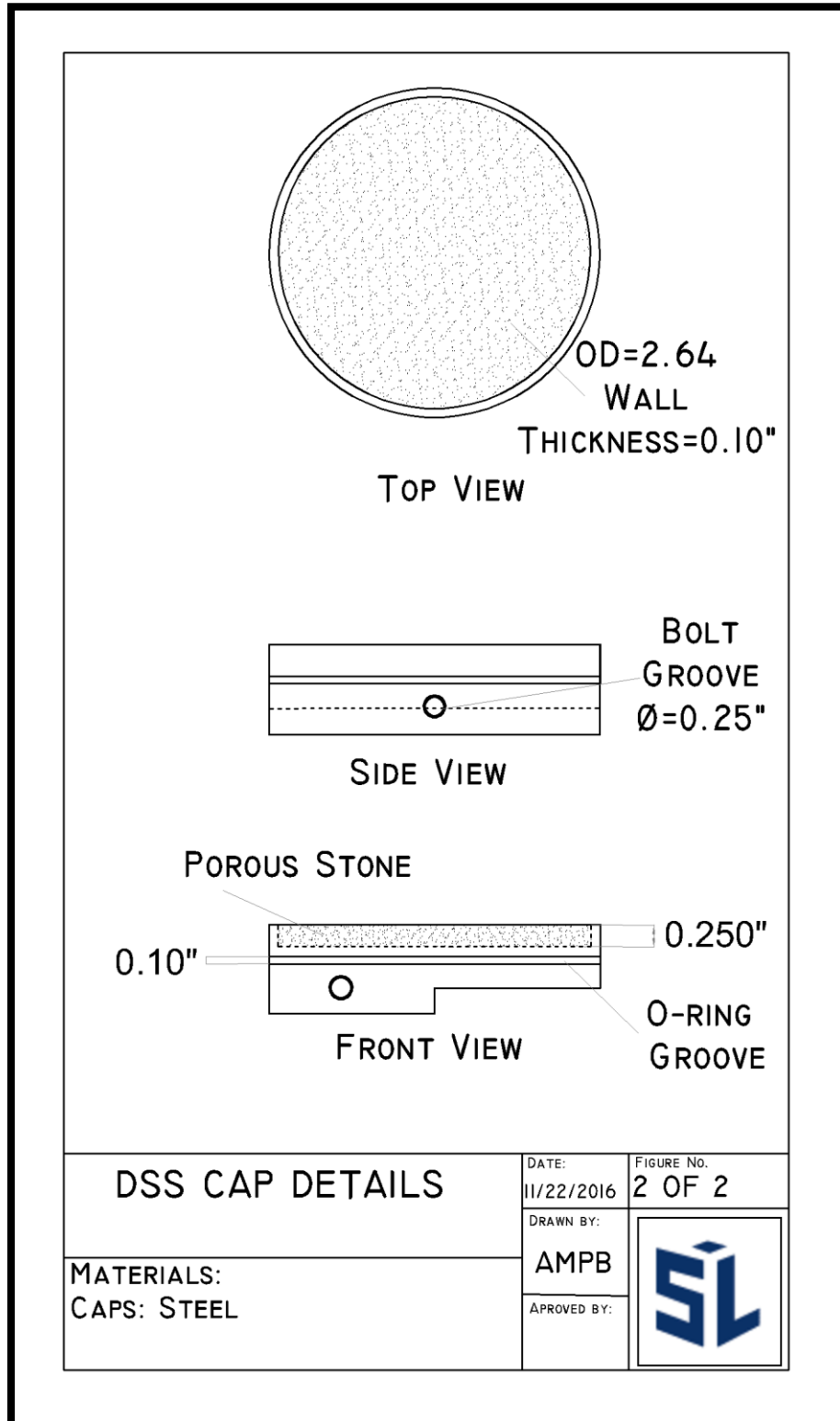


Figure 5.4 DSS mold details

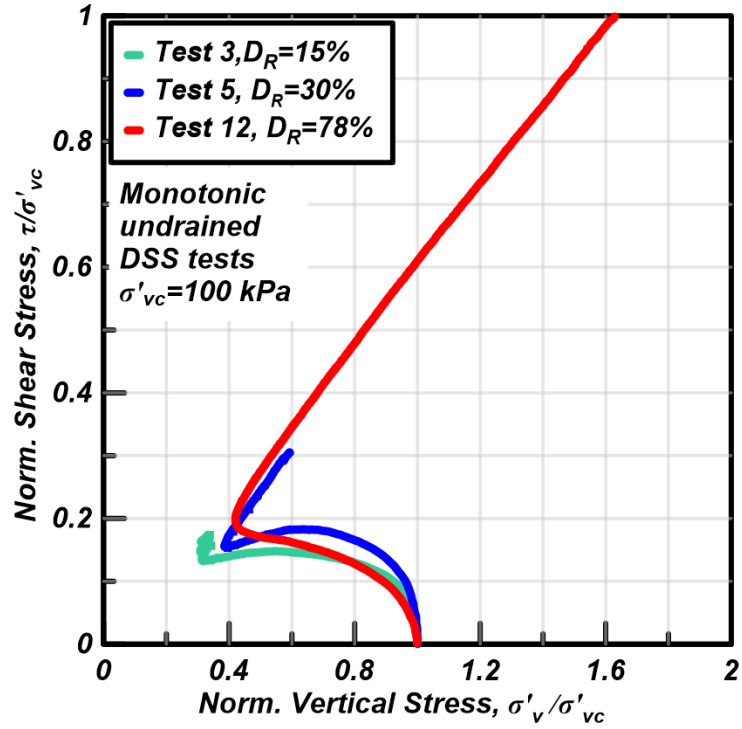


Figure 5.5 Stress path for $\sigma'_{vc}=100$ kPa DSS monotonic tests

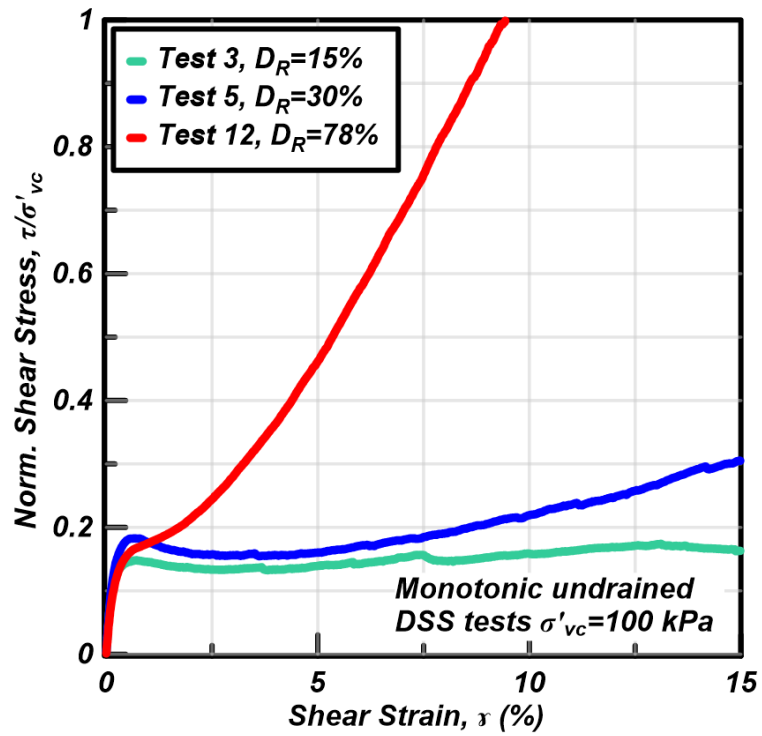


Figure 5.6 Stress strain response for $\sigma'_{vc}=100$ kPa DSS monotonic tests

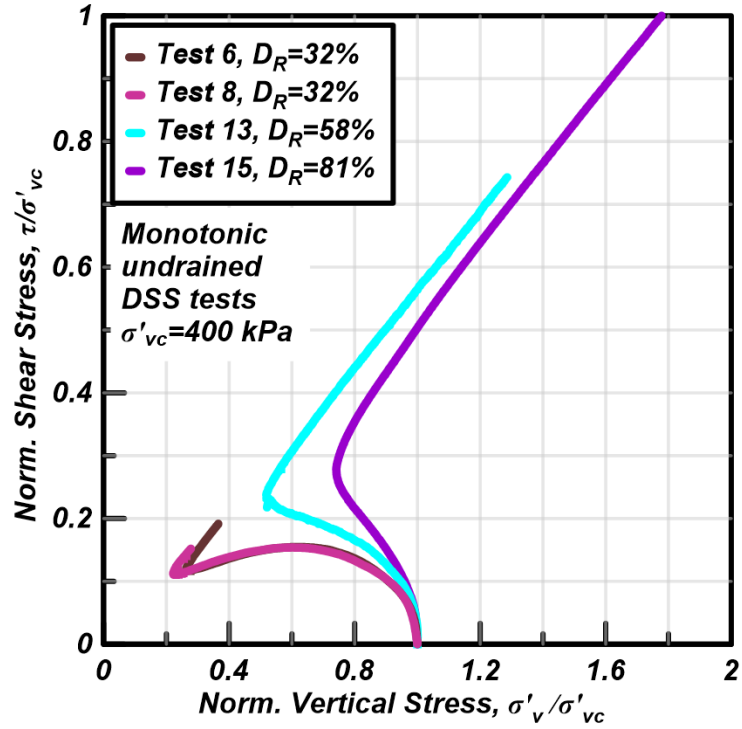


Figure 5.7 Stress path for $\sigma'_{vc}=400$ kPa DSS monotonic tests

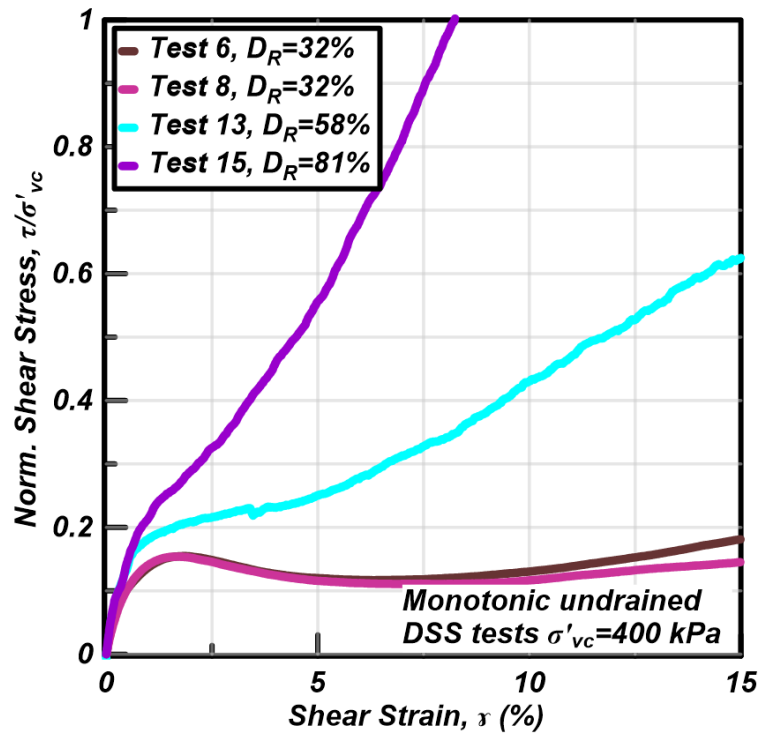


Figure 5.8 Stress strain response for $\sigma'_{vc}=400$ kPa DSS monotonic tests

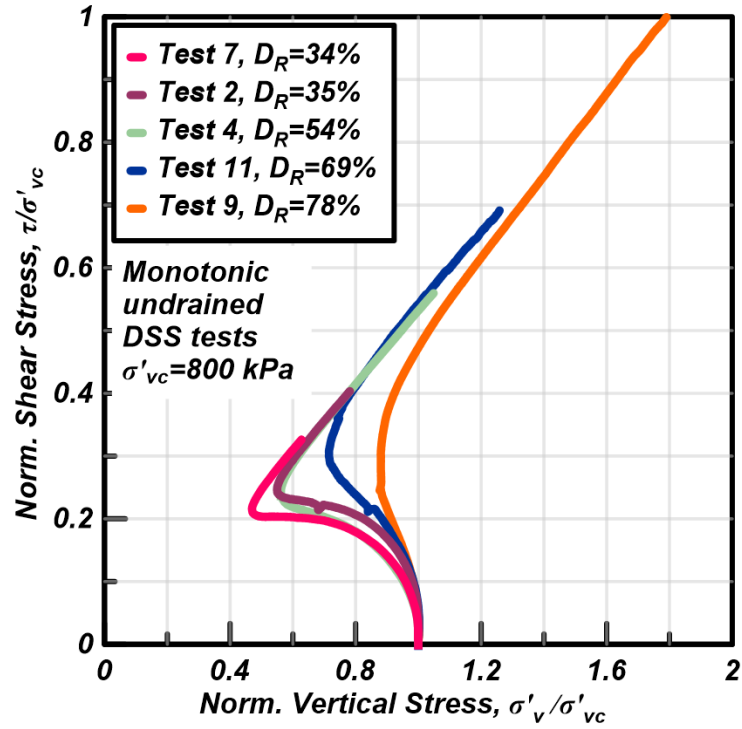


Figure 5.9 Stress path for $\sigma'_{vc}=800$ kPa DSS monotonic tests

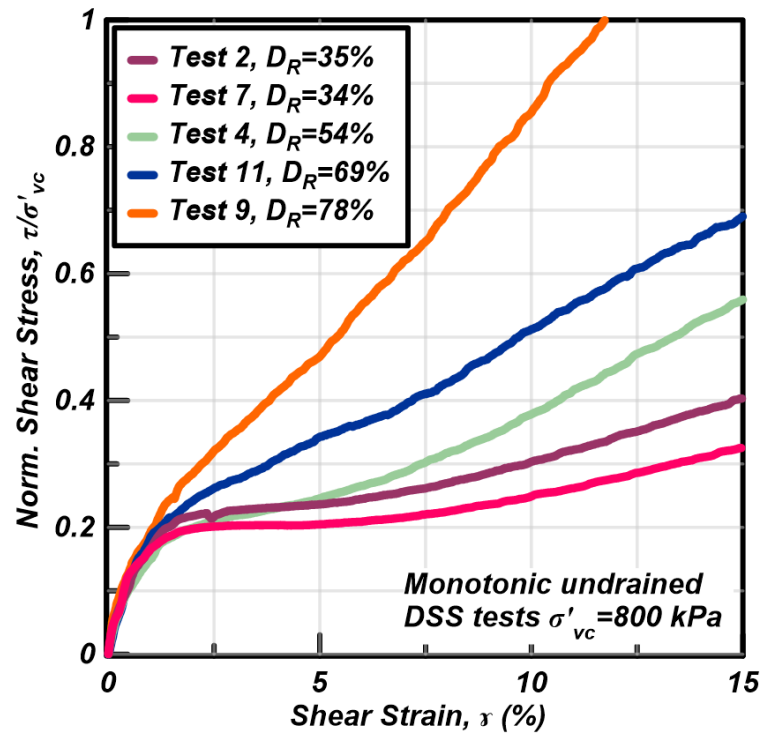


Figure 5.10 Stress strain response for $\sigma'_{vc}=800$ kPa DSS monotonic tests

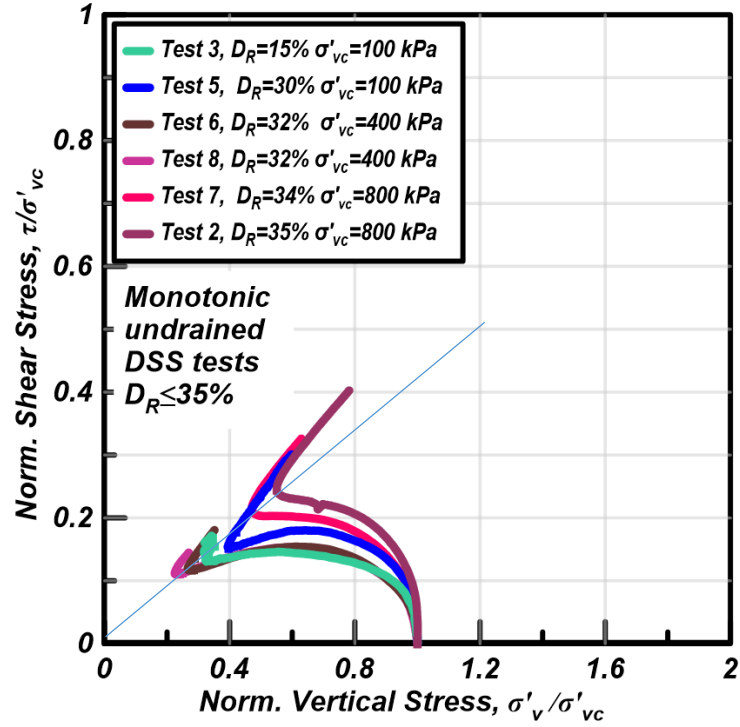


Figure 5.11 Stress path for tests on specimens with $D_R < 35\%$

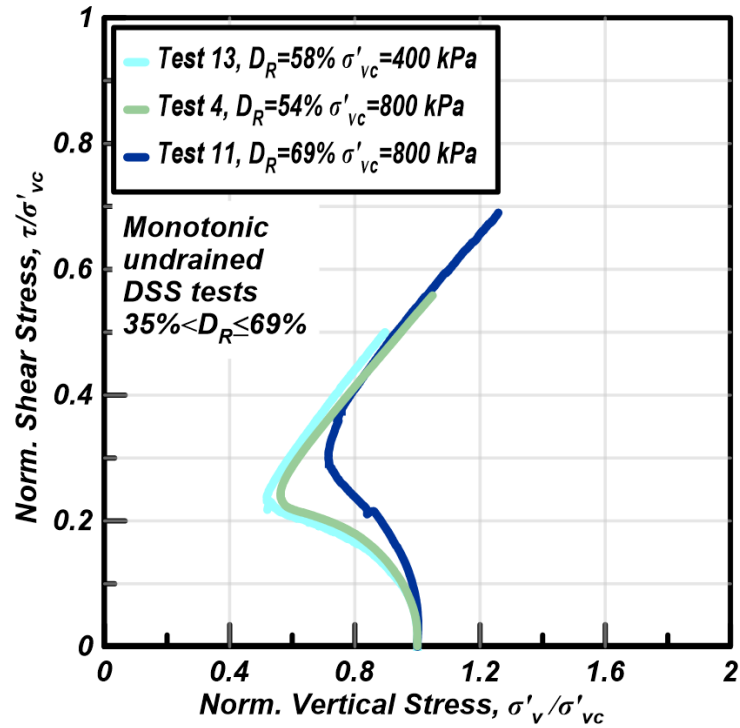


Figure 5.12 Stress path for tests on specimens with $35\% < D_R \leq 69\%$

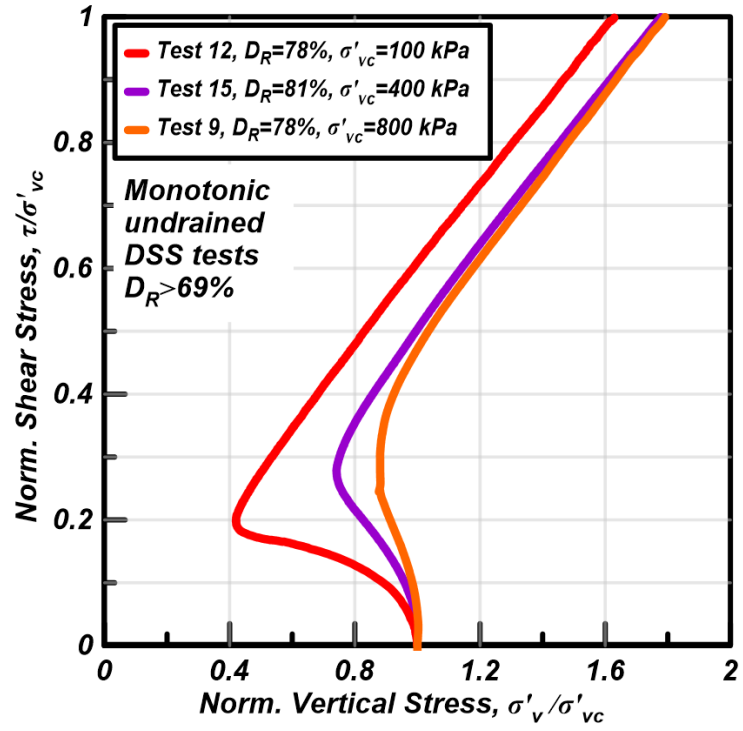


Figure 5.13 Stress path for tests on specimens with $69\% < D_R$

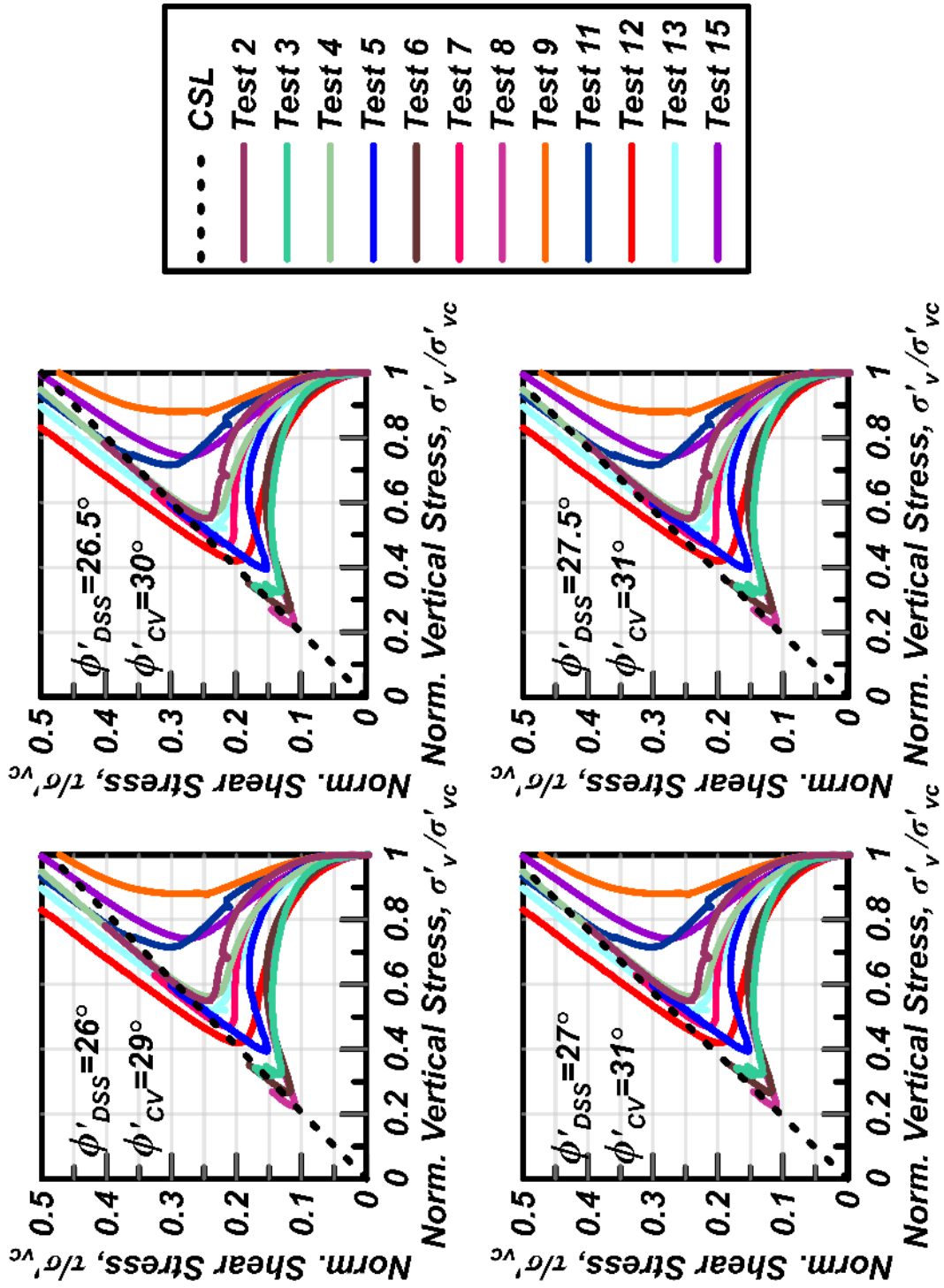


Figure 5.14 Constant volume friction angle selection

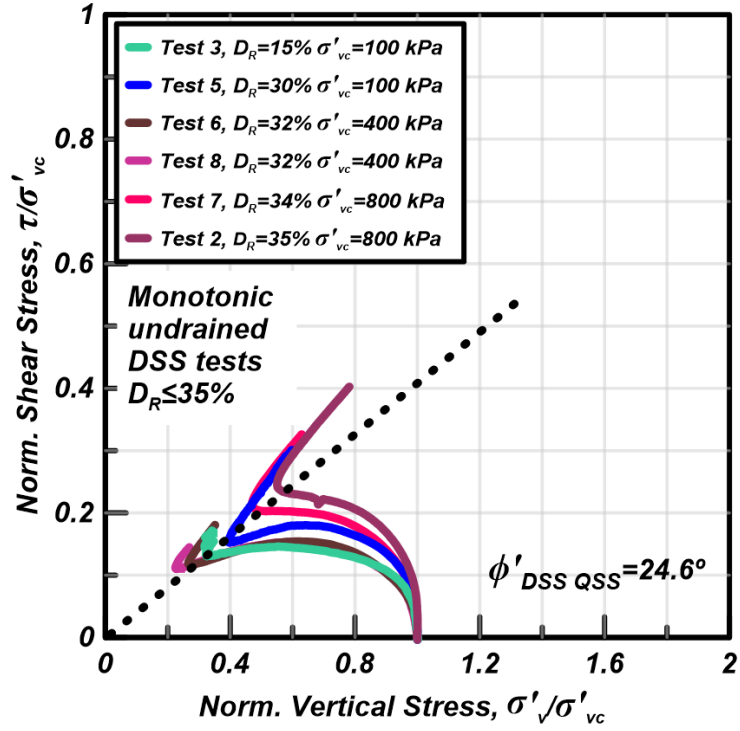


Figure 5.15 Constant volume from the quasi-steady state

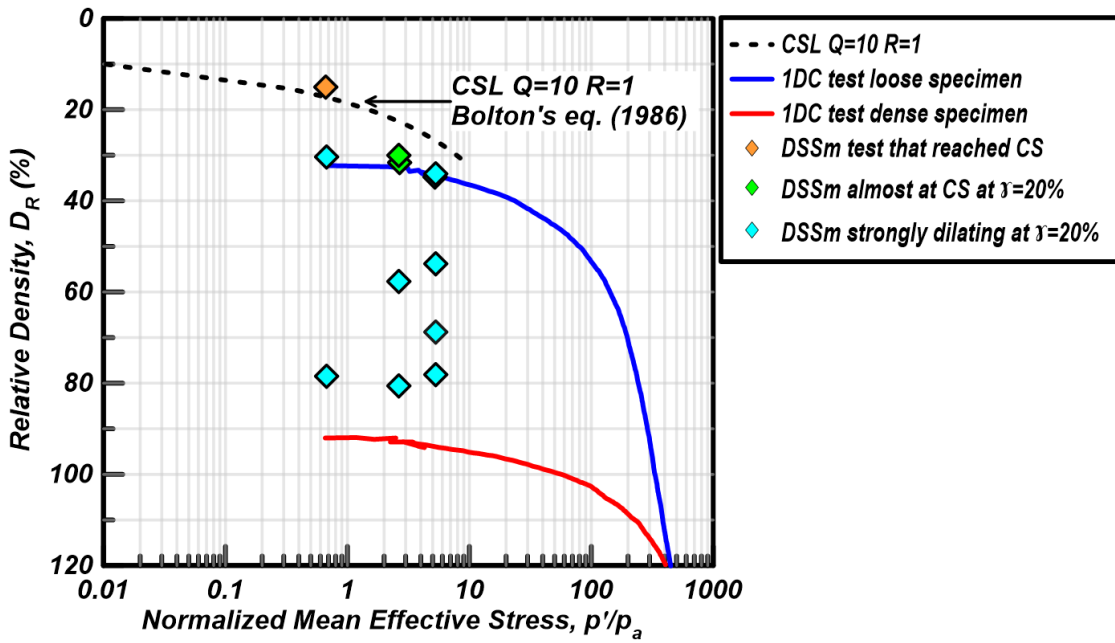


Figure 5.16 Critical state line and monotonic tests results

Chapter 6

Cyclic Direct Simple Shear Characteristics

6.1 Introduction

This chapter summarizes the undrained cyclic Direct Simple Shear (DSS) results for Ottawa F-65 sand specimens including: cyclic resistance curves from tests on Normally Consolidated (NC) specimens consolidated to 50 kPa, 100 kPa and 400 kPa, cyclic resistance curves for tests on Over-Consolidated (OC) loose specimens with an Over-Consolidation Ratio (OCR) of 4 and an initial confining stress of 100 kPa, reconsolidation results from tests on the NC specimens consolidated and reconsolidated to 50 kPa, 100 kPa and 400 kPa, post-cyclic monotonic tests results from tests on the NC specimens consolidated to 50 kPa, 100 kPa and 400 kPa, and stress strain responses from tests sheared to large single amplitude shear strains.

6.2 Cyclic DSS Testing Procedures

The procedures for the cyclic DSS tests were the same as used for the monotonic DSS tests. Tests were run using a GEOTAC Direct Simple Shear apparatus, specimens were sheared with a constant height condition. Loose specimens were prepared dry funnel deposited and dense specimens were prepared air pluviated, and tests were run under a deformation controlled rate equivalent to a 50% shear strain per hour.

Cyclic tests were run under a deformation-controlled mode using stress-controlled criteria for reversal of loading directions. For some cyclic tests on loose specimens, the specimen was loaded to a peak shear strain of approximately 20%. For some cyclic tests on dense specimens, the specimen was loaded to

a peak shear strain of approximately 10%. For all the other cyclic tests on loose and dense specimens, the cyclic loading was continued up to a peak shear strain of approximately 5%, after which the specimen was subjected to one of the following post cyclic tests: post-cyclic monotonic shearing or post-cyclic reconsolidation.

For post-cyclic monotonic shearing tests, the cyclic shearing phase of the test stopped at 5% and the travelling plate was re-centered to the position of absolute zero strain. The constant height bolts stayed tight and the specimen was monotonically shear under constant height condition to strains of up to 15%.

For post-cyclic reconsolidation tests, the cyclic part of the test stopped at 5% and the travelling plate was re-centered to the position of absolute zero strain. The constant height bolts were then loosened to allow drainage and the specimen was reconsolidated using the same loading increments used in the virgin consolidation phase.

6.3 Cyclic Stress-Strain Responses

The cyclic loading responses of a loose specimen consolidated under $\sigma'_{vc} = 100$ kPa is shown in Figure 6.1. Normalized shear stress (τ/σ'_{vc}) vs. number of loading cycles (N), pore pressure ratio (r_u) vs. N, shear strain (γ) vs. N, τ/σ'_{vc} vs. γ and τ/σ'_{vc} vs. normalized vertical effective stress (σ'_v/σ'_{vc}) are shown in the figure. The peak r_u exceeds 0.75 and the peak γ exceeds 1% after 3.5 loading cycles as shown in both γ vs. N and τ/σ'_{vc} vs. γ plots. Before this point, the shear strain accumulation rate is very low and seems constant, whereas after this point the shear strain accumulation rate increases rapidly with every cycle of loading because the specimen had lost a significant amount of vertical effective stress. The value of σ'_v/σ'_{vc} reduces to about 0.70 during the first loading cycle, to about 0.44 during the 2 following loading cycles, and to about 0.10 in the fourth cycle. At the same point, γ starts to increase rapidly. The values of σ'_v/σ'_{vc} then show transient increases and decreases with each loading cycle, forming loops in the stress path plot.

The cyclic loading responses of a dense specimen under $\sigma'_{vc} = 100$ kPa is shown in Figure 6.2. The τ/σ'_{vc} vs. N , r_u vs. N , γ vs. N , τ/σ'_{vc} vs. γ and τ/σ'_{vc} vs. σ'_v/σ'_{vc} are shown in the figure. The responses of the dense specimen are similar to that of the loose specimen, in that the dense specimen starts to accumulate γ greater than 1% after an r_u of 0.75 has been reached. On the other hand, the responses of the dense specimen differ from the responses of the loose specimen in the following: once the r_u of 0.75 is reached and γ exceeds 1%, the strain accumulation rate is smaller than for the loose specimen and it decreases with each loading cycle. The denser specimens required higher cyclic stress ratios (CSR) to trigger various strain levels than the looser specimens, so the differences in other responses are larger attributable to the different imposed loadings.

The cyclic stress-strain response for a loose specimen with peak shear strains reaching up to 20% is shown in Figure 6.3. Once the value of r_u exceeds 0.75 and γ peak exceeds 1%, the shear strains start to grow rapidly as shown in both γ vs. N and τ/σ'_{vc} vs. γ plots. The shear strain accumulation rate is similar in the first 3 loading cycles and then it reduces with each additional loading cycle. The reduction of σ'_v/σ'_{vc} during the first loading cycle is greater for this specimen than for the loose specimen shown in Figure 6.1 because this specimen has been sheared with a higher CSR and the effect of having a higher CSR is governing given the D_R of this specimen is 3% higher than the D_R of the specimen shown in Figure 6.1.

The cyclic stress-strain response for a dense specimen is shown in Figure 6.4 for peak shear strains reaching up to 9%. The response of this specimen differs from the response of the specimen in Figure 6.2. The specimen accumulated $\gamma=5\%$ in a smaller number of cycles than the specimen in Figure 6.2 because this specimen has been sheared with a higher CSR and the D_R of this specimen is 4% lower than the D_R of the specimen in Figure 6.2. The shear strain accumulation rate decreases after the 2nd loading cycle and up to γ of approximately 5% and then it seems to increase again; this trend is similar to the trend observed in the test in Figure 6.2 up to γ of approximately 5%.

The general features of the excess pore pressure evolution for these tests are consistent with those in the literature for silica sands. The excess pore pressure evolution pattern has three stages as shown in the stress paths from Figure 6.1, Figure 6.2, Figure 6.3 and Figure 6.4: an initial stage where the excess of pore pressure rises more rapidly, a second stage where the excess pore pressure continues to increase but in a smaller proportion during each cycle of loading, and a final stage where the excess pore pressure rises to levels equal to the consolidation stress, followed by alternating cycles of incremental contraction and dilation. This excess pore pressure evolution pattern is similar to those described by [Alarcon-Guzman et al. \(1988\)](#) for specimens that experienced limited flow deformation and from specimens tested in cyclic undrained torsional shear tests. They described that sand specimens might experience structural collapse during undrained shearing, which leads to a sudden increase of the excess pore pressure. Structural collapse happens early in loading due to the rolling of some grains that are within loose portions of the specimens. Structural collapse happens again when the specimens starts to try to contract, so grains are re-arranged allowing the collapse of the grain's structure when the direction of the shearing is reversed, causing the excess pore pressure to rise due to the loss of particle to particle contact points ([Alarcon-Guzman et al. 1988](#)). Undrained DSS tests results from tests on Nevada sand air pluviated specimens, which were conducted before this project and from tests results on similar specimens from [Ziotopoulou \(2014\)](#) show a similar excess pore pressure evolution pattern. Undrained bidirectional cyclic simple shear tests conducted by [Boulanger and Seed \(1995\)](#) on loose Sacramento River sand moist tamped specimens showed similar excess pore pressure evolution pattern. Undrained cyclic torsional tests with lateral confinement at $K_0=0.5$ conducted by [Ishihara and Li \(1972\)](#) conducted on Toyoura sand loose specimens showed similar excess pore pressure evolution patterns as well.

The general features of the stress-strain accumulation evolution are consistent with the cyclic response shown in the available literature for silica sands. The specimen's stress-strain accumulation evolution depends on the relative density. For almost all the loose specimens, the accumulated peak shear strains were smaller than 1% while r_u was less than 70%, after which shear strain accumulation increased

rapidly and the loose specimens usually reached peak shear strains of 3% and 5% within the next one or two loading cycles, as shown in the stress-strain plots from Figure 6.1 **Error! Reference source not found.** and Figure 6.3. This is consistent with the strain accumulation pattern observed by others, as noted above.

6.4 Cyclic Resistance Ratio vs. Number of Cycles

The cyclic stress ratio (CSR) vs. number of loading cycles to reach several failure criteria (N) was evaluated for loose specimens with D_R of about 42% and dense specimens with D_R of about 80% consolidated to a range of vertical effective stresses and over-consolidation ratios. Consolidation vertical effective stresses (σ'_{vc}) of 50, 100 and 400 kPa were used for NC specimens. OC loose specimens with D_R of about 35% with an OCR=4 and consolidated to σ'_{vc} of 100 kPa were also tested.

The CSR vs. number of loading cycles to reach 3% peak shear strain ($N_{V=3\%}$) for the loose specimens is shown in Figure 6.5 for consolidation effective stresses of 50, 100 and 400 kPa. The curves are shifted up with increasing consolidation stress, with the results for $\sigma'_{vc} = 400$ kPa being the highest curve and the one with the greatest difference of position for the NC specimens. The slope b of the CSR vs. $N_{V=3\%}$ is 0.15 and was selected by fitting the results from the loose tests consolidated to $\sigma'_{vc}=100$ kPa to a power law using the least squares fitting method. The curves were assumed to be parallel so the same b was set for the other curves.

The slope b is in the range of slopes for other silica sands, recognizing differences in b values may arise from differences in the type of sand tested, the specimen type, the specimen preparation technique, the testing technique and the type and magnitude of the failure criteria (Tatsouka et al. 1986). CSR curves for loose specimens in the literature are described as follows. Yoshimini et al. (1989) presented results of CSR vs. number of cycles to failure with b values of 0.15 from undrained cyclic triaxial tests on isotropically consolidated specimens from frozen samples of fine silica sand No. 6 from a hydraulic fill strata; the specimens had $D_R=56\%$. Pillai and Stewart (1994) presented results of CSR vs. number of cycles to failure

with $b=0.08$ from curves from cyclic DSS tests on specimens from frozen samples from Duncan dam. Okamura et al. (2003) presented results of CSR vs. number of cycles to 5% double amplitude axial strain ($N_{\text{EDA}=5\%}$) with $b=0.13$, 0.15 and 0.21, for loose sand from a site in Niigata Japan treated with compaction piles, the curves are from undrained triaxial cyclic triaxial tests on specimens from frozen samples and the D_R of the specimens were 59.9%, 59.7% and 66% respectively. Toki et al. (1986) presented results of CSR vs. $N_{\text{EDA}=5\%}$ with $b=0.10$ from cyclic undrained triaxial tests on air pluviated specimens of Toyoura sand with $D_R=50\%$. Boulanger and Seed (1995) presented results of CSR vs. $N_{V=3\%}$ with b values of 0.17 for $D_R=35\%$, of 0.15 for $D_R=45\%$ and of 0.27 for $D_R=55\%$ from curves from cyclic DSS tests on Sacramento river sand moist tamped specimens. De Alba et al. (1976) presented results of CSR vs. number of cycles to cause initial liquefaction with $b=0.23$, from curves from shaking table tests on specimens with $D_R=54\%$. Tatsouka et al. (1986) presented results of CSR vs. number of cycles to 15% double amplitude axial strain ($N_{\text{EDA}=15\%}$) with $b=0.20$ from curves from undrained cyclic torsional shear tests on air pluviated specimens on Sengenyama sand with $D_R=40\%$; they also conducted undrained cyclic triaxial tests and found that triaxial results produce steeper cyclic resistance curves. Carraro et al. (2003) presented results of CSR vs. $N_{\text{EDA}=5\%}$ with $b=0.14$ from curves from undrained cyclic triaxial tests on Ottawa sand C-109 on slurry deposited specimens with $D_R=40\%$. Towhata et al. (2014) presented results of CSR vs. number of cycles to 5% peak shear strain ($N_{VDA=3\%}$) with $b=0.10$ from curves from undrained cyclic torsional shear tests on Tokyo bay sand ejecta on air pluviated specimens prepared with a constant energy placement method.

The effective failure criterion on the CSR vs. number of loading cycles for the loose specimens is shown in Figure 6.6 for peak shear strains of 1%, 3% and 5% and a consolidation effective stress of 100 kPa. It is difficult to distinguish the curves that corresponds to each failure criteria due to the effect of the failure criteria being very small. The loose specimens reached the three failure criteria within the same cycle of loading in most of the tests. This is consistent with the stress-strain responses shown in Figure 6.1 and Figure 6.3.

The CSR vs. number of loading cycles for the dense specimens is shown in Figure 6.7 for shear strain of 3% and consolidation effective stress of 50, 100 and 400 kPa. The curve for $\sigma'_{vc} = 50$ kPa is the highest one and the one with the greatest difference of position compared to the other curves. The slope b of the CSR vs. $N_{v=3\%}$ is 0.17 and was selected by fitting the results from the loose tests consolidated to $\sigma'_{vc}=100$ kPa to a power law using the least squares fitting method. The curves were assumed to be parallel so the same b was set for the other curves; however, there is significant scatter in the data corresponding to tests with $\sigma'_{vc}=50$ kPa. The scatter in the results from specimens consolidated to $\sigma'_{vc}=50$ kPa is due to the initial confinement being relatively small, so any disturbance of the specimen due to tightening the constant height bolts generates an increment in the vertical load that can cause some over consolidation on a material that has already a higher dilatant tendency.

The slope b for dense specimens is lower than the slopes obtained by other researchers for dense silica sands, with some exceptions. The same b was reported by Carraro et al. (2003) for CSR vs. $N_{\epsilon_{DA}=5\%}$ with $b=0.17$ from curves from undrained cyclic triaxial tests on Ottawa sand C-109 on slurry deposited specimens with $D_R=67\%$. Other CSR curves from cyclic tests on dense specimens available in the literature are described as follows. Yoshimini et al. (1989) presented results of CSR vs. number of cycles to failure with b values of 0.41 and 0.34 from undrained cyclic triaxial tests on isotropically consolidated specimens from frozen samples of fine silica sand No. 6 from a hydraulic fill strata; the specimens had $D_R=78\%$ and $D_R=87\%$ respectively. Okamura et al. (2003) presented results of CSR vs. number of cycles to 5% double amplitude axial strain ($N_{\epsilon_{DA}=5\%}$) with $b=0.45$, 0.54 and 0.50 for frozen samples of loose sand from a site in Niigata Japan treated with compaction piles; the D_R for the specimens were 77.4%, 73.7% and 79.4% respectively. Yoshimini et al. (1984) presented results of CSR vs. $N_{\epsilon_{DA}=5\%}$ with $b=0.34$ from cyclic undrained triaxial tests on specimens from frozen samples of sand from Niigata with $D_R=87\%$. De Alba et al. (1976) presented results of CSR vs. number of cycles to cause initial liquefaction with $b=0.21$, 0.21 and 0.25, from curves from shaking table tests on specimens with $D_R=68\%$, 82% and 90% respectively. Tatsouka et al. (1986) presented results of CSR vs. number of cycles to 15% double amplitude axial strain

($N_{\epsilon_{DA}=15\%}$) with $b=0.30, 0.31$ and 0.39 from curves from undrained cyclic torsional shear tests on air pluviated specimens on Sengenyama sand with $D_R=80\%, 90\%$ and 95% respectively; they also conducted undrained cyclic triaxial tests and found that triaxial results produce steeper curves. Carraro et al. (2003) presented results of CSR vs. $N_{\epsilon_{DA}=5\%}$ with $b=0.28$ and 0.23 from curves from undrained cyclic triaxial tests on Ottawa sand C-109 on slurry deposited specimens with $D_R=77\%$ and 82% respectively.

The effective failure criteria on the CSR vs. the number of loading cycles for the dense specimens with $\sigma'_{vc}=100$ kPa to reach shear strains of 1%, 3% and 5% is shown in Figure 6.8. The curves shift upward with increasing shear strain failure criterion. Almost all the specimens reached $\gamma=1\%$ within the first loading cycle. All the specimens reached $\gamma=5\%$ after 8 loading cycles or more. The reduction in the strain accumulation rate with increasing loading cycles for shear strains bigger than 5% is consistent with the stress-strain responses shown in Figure 6.2 and Figure 6.4.

The effect of OCR on the CSR vs. $N_{\gamma=3\%}$ of loose specimens is shown in Figure 6.5 for specimens having an OCR = 4. The curve for the over-consolidated specimens plots above from curves from the normally consolidated (NC) specimens. The cyclic resistance curve for the OC specimens was assumed to be parallel to the curves of the NC specimens; $b=0.15$ was used in the curve fitting process. The OCR = 4 provides an increase of 86% in the CSR to reach $\gamma=3\%$ in 20 loading cycles for loose specimens consolidated to $\sigma'_{vc}=100$ kPa as expected. Several authors including Ishihara and Takatsu (1979) have observed that overconsolidation causes an increase in the ratio of lateral to vertical effective stress (K_o) when compared to the K_o in the normally consolidated states. They also proposed an equation to predict the increment in the CRR at 20 cycles to cause initial liquefaction due to OCR and K_o at consolidation; using this equation and assuming K_o increases from approximately 0.5 to 1 and with OCR=4, the expected increment in the CRR at 20 cycles is 200% which is higher than the observed increment in the CRR. Several authors have described that overconsolidation increases the undrained cyclic strength of clean sands including Seed and Peacock (1971), Lee and Focht (1975), Ishihara, Sodekawa and Tanaka (1978), Ishihara

and Okada (1978), Ishihara and Takatsu (1979), Nagase et al. (1996) and Nagase et al. (2000), however Seed and Peacock (1971), Lee and Focht (1975), and Ishihara, Sodekawa and Tanaka (1978) reported lower increments in the ratio of CRR to initial mean effective stress with OCR, which is consisted with the DSS results shown in Figure 6.5.

6.5 Reconsolidation after Liquefaction

Post-cyclic reconsolidation vertical strains (ϵ_v) were measured for some of the loose and dense specimens. Values of ϵ_v were measured after the cyclic shearing stage of the tests stopped for the specimens that reached $\gamma_{\text{peak}} = 5\%$ in less than 10 loading cycles. Two tests on loose specimens were the exception, in that the specimens reached $\gamma_{\text{peak}} = 5\%$ in less than 10 loading cycles and were allowed to reach $\gamma_{\text{peak}} = 7\%$ and $\gamma_{\text{peak}} = 8\%$. The specimens were re-centered to the position of zero shear strain after they reached the desired γ_{peak} . The constant height bolts were loosened and the reconsolidation stage started. The reconsolidation was done in the same fashion as the consolidation of the virgin specimen. Both stages were done with ICL consolidation with a LIR of 2.

Post-cyclic reconsolidation results for the loose specimens are shown in **Error! Reference source not found.** Figure 6.9 ϵ_v vs. σ'_{vc} are presented from data from the consolidation of the virgin specimens and from the reconsolidation of the pre-sheared specimens. The virgin specimens began with as-placed D_R of 18-39%, whereas the reconsolidation specimens began with as-consolidated D_R of 38-50%. The ϵ_v increased with consolidation stress in all specimens, as expected. For the specimens consolidated to $\sigma'_{vc} = 50$ kPa, the ϵ_v was greater for the reconsolidation test (as-consolidated $D_R = 38\%$) than for the virgin consolidation process (as-placed $D_R = 33\%$). During the consolidation process a sudden increase in the vertical strain of this specimen was observed while applying the last loading increment. For the specimens consolidated to $\sigma'_{vc} = 100$ kPa and $\sigma'_{vc} = 400$ kPa, the ϵ_v during reconsolidation tests (as-consolidated $D_R = 37-50\%$) were smaller than for the virgin consolidation process (as-placed $D_R = 18-39\%$); the greater ϵ_v during virgin

consolidation is attributed to the as-placed D_R being significantly smaller than the as-consolidated D_R for the reconsolidation test specimens.

Post-cyclic reconsolidation results in semi-logarithmic scale for the loose specimens are shown in Figure 6.11 Consolidation and reconsolidation after cyclic shearing results from tests on loose specimens in semi-log scale Figure 6.11. The same data presented in Figure 6.9 is presented in semi-logarithmic scale to show the initial vertical effective stress before the reconsolidation process started (σ'_{vco}). The specimen consolidated to $\sigma'_{vc}=50$ kPa started its reconsolidation at $\sigma'_{vco}=2.65$ kPa and showed a reconsolidation ϵ_v of 1.6%, the specimen consolidated to $\sigma'_{vc}=100$ kPa started its reconsolidation at $\sigma'_{vco}=28$ kPa showed a reconsolidation ϵ_v of 0.48%, the loosest specimen consolidated to $\sigma'_{vc}=400$ kPa started its reconsolidation at $\sigma'_{vco}=21$ kPa showed a reconsolidation ϵ_v of 1.74% and the densest specimen consolidated to $\sigma'_{vc}=400$ kPa started its reconsolidation at $\sigma'_{vco}=17$ kPa showed a reconsolidation ϵ_v of 1.15%. The combination of the difference in σ'_{vco} and the D_R influenced the results.

Post-cyclic reconsolidation results for the dense specimens are shown in Figure 6.10 ϵ_v vs. σ'_{vc} are presented from data from the consolidation of the virgin specimen and from the reconsolidation of the pre-sheared specimen. The virgin consolidation ϵ_v increases with decreasing D_R , the virgin consolidation ϵ_v increases with increasing σ'_{vc} in the specimens consolidated to $\sigma'_{vc}=100$ and 400 kPa. All the specimens showed lower ϵ_v during their reconsolidation process than during their virgin consolidation process. This is attributed to the fact the pre-sheared specimens were denser (as-consolidated $D_R = 66-84\%$) than the virgin specimens (as-placed $D_R = 59-72\%$).

Post-cyclic reconsolidation results in semi-logarithmic scale for the dense specimens are shown in Figure 6.12 Figure 6.11 Consolidation and reconsolidation after cyclic shearing results from tests on loose specimens in semi-log scale. The same data presented in Figure 6.10 is presented in semi-logarithmic scale to show the initial vertical effective stress before the consolidation process started (σ'_{vco}). The specimen consolidated to $\sigma'_{vc}=50$ kPa started at $\sigma'_{vco}=14.4$ kPa and showed a reconsolidation ϵ_v of 0.35%, the

specimen consolidated to $\sigma'_{vc}=100$ kPa started at $\sigma'_{vco}=5.8$ kPa and showed a reconsolidation ϵ_v of 0.29 and the specimen consolidated to $\sigma'_{vc}=400$ kPa started at $\sigma'_{vco}=19.7$ kPa and showed a reconsolidation ϵ_v of 0.39%. The combination of the difference in σ'_{vco} and the D_R influenced the results.

The effect of re-centering on the reconsolidation ϵ_v observed in the specimens was evaluated. All the loose specimens gained vertical effective stress during re-centering. The change in the vertical effective stress increased the observed ϵ_v compared to the expected ϵ_v value without re-centering. The observed reduction in ϵ_v due to re-centering was estimated to be in the range 0.001% (test 8, for the increasing of vertical effective stress of 0.7 kPa during re-centering) to 0.05% (test 7, for the increasing of vertical effective stress of 26 kPa during re-centering). In contrast, all the dense specimens lost vertical effective stress during re-centering. The change in the vertical effective stress increased the observed ϵ_v compared to the expected ϵ_v value without re-centering. The observed reduction in ϵ_v due to re-centering was estimated to be in the range 0.01% (test 47, for the reduction of vertical effective stress of 4 kPa during re-centering) to 0.08% (test 7, for the reduction of vertical effective stress of 88 kPa during re-centering). The reduction of ϵ_v was calculated using a Young's modulus and vertical effective stress relationship obtained from the unloading portion of the OCR=4 specimens from tests 55, 56 and 59 as shown in Figure 6.13. Tests 55, 56 and 59 provided best consolidation curves from all OCR=4 specimens. The values of Young's modulus obtained by this correlation are within the range of 40 MPa ($\sigma'_{vc}=50$ kPa) to 113 MPa ($\sigma'_{vc}=400$ kPa). These values are consistent with the value of 55 MPa presented by [Lambe and Whitman \(1969\)](#) for secant modulus to half peak deviator stress from specimens of hard, rounded particles confined to 100 kPa under triaxial loading.

The post-cyclic ϵ_v are compared with results from reconsolidation volume change and shear strain curves proposed by [Ishihara and Yoshimine \(1992\)](#) in Figure 6.14. The values of ϵ_v were corrected by the ϵ_v changes caused by the changes in vertical effective stress due to re-centering of the traveling plate after the cyclic shearing stage. The curves [Ishihara and Yoshimine \(1992\)](#) proposed are based on results from

multi and uni-directional simple shear tests on Fuji River sand specimens. The experimental results show that the effect of γ_{peak} is stronger than the effect of D_R on the ϵ_v due to reconsolidation. The reconsolidation ϵ_v in the present tests are lower compared to the range of values predicted by the curves proposed by [Ishihara and Yoshimine \(1992\)](#). The same curves were redrawn by [Idriss and Boulanger \(2008\)](#) including the experimental data points; this curve shows significant variability in the results, as can be seen in Figure 6.15. The experimental results obtained in this work are within the scatter range of the results depicted in Figure 6.15.

6.6 Post-Cyclic Monotonic Strengths

Post-cyclic monotonic tests on loose and dense specimens under initial consolidation effective stresses of 50, 100 and 400 kPa are presented. The results are shown for consolidation effective stresses of 50, 100 and 400 kPa in Figure 6.16, Figure 6.17, Figure 6.18, Figure 6.19, Figure 6.20 and Figure 6.21. In each figure the cyclic loading response is shown in blue and the post-cyclic monotonic is shown in red. For the tests at 100 and 400 the results of a monotonic undrained tests on a virgin specimens are shown in grey.

The monotonic stress-strain responses of loose virgin and pre-strained specimens show the following behaviors. The post-cyclic monotonic stress-strain responses of the loose specimens are softer compared to the responses of the virgin specimens; the post-cyclic specimens show a stress-strain response that is essentially like one more loading cycle up till the CSR level is reached, after which it continues to show dilative tendencies at a similar rate of hardening as the virgin specimens. The virgin specimen consolidated to $\sigma'_{vc}=100$ kPa shows a monotonic response with a stronger dilative tendency compared to the response of the post-cyclic specimen up to a shear strain of about 13%; then, the post-cyclic specimen shows a response with a stronger dilative tendency. This might be because the virgin specimen has a lower D_R than the post-cyclic specimen, or reflect the differences in fabric at these different strain levels. The virgin specimen consolidated to $\sigma'_{vc}=400$ kPa shows a monotonic response with a stronger dilative tendency

compared to the response of the post-cyclic specimen. Similarly, this might be in part because the virgin specimen has a higher D_R than the post-cyclic specimen, or to differences in fabric at these different strain levels.

The stress-strain monotonic responses of dense virgin and pre-strained specimens show the following behaviors. The monotonic stress-strain responses of the dense pre-strained specimens are softer compared to the responses of the virgin specimens; the pre-strained specimens show a stress-strain response that follows curve that mimics the beginning of a cyclic stress-strain loop before reaching the CSR from the cyclic test; then, the specimens continue to show dilative tendencies at a similar rate of hardening as the virgin specimens. The differences in the responses of the virgin and pre-strained specimens consolidated to $\sigma'_{vc}=400$ kPa are in part due to the lower D_R of the pre-strained specimen.

These post cyclic responses are consistent with the expectations. The virgin specimen and the pre-strained specimens have different states and different fabrics even if they have the same D_R . The virgin specimens start at a state where they have some mean effective stress due to consolidation under the selected vertical effective stress and with a K_o condition, whereas the post-cyclic specimen starts at a condition with a much lower vertical effective stress but with higher K_o due to the evolution of the fabric caused by the prior cyclic loading. As a result, the post-cyclic specimens mobilize a lower shear strength than the virgin specimen at the same level of shear strain under monotonic undrained loading; this is due to the post-cyclic specimen starting with a lower vertical effective stress. This difference in shear strength among the virgin and the post-cyclic specimens is also dependent on the initial D_R and consolidation stresses of the specimens. Additionally, the stress-strain uniformities that develop inside the DSS specimens at large shear strains might have influenced the dilatant tendencies observed in the responses of the pre-strained and virgin specimens at large levels of shear strains, as described in Chapter 5. In contrast, the hardening rate of the virgin and the post-cyclic specimens is similar taking into account that the virgin specimen starts with a stiffer response when starting the test while having a higher vertical effective stress.

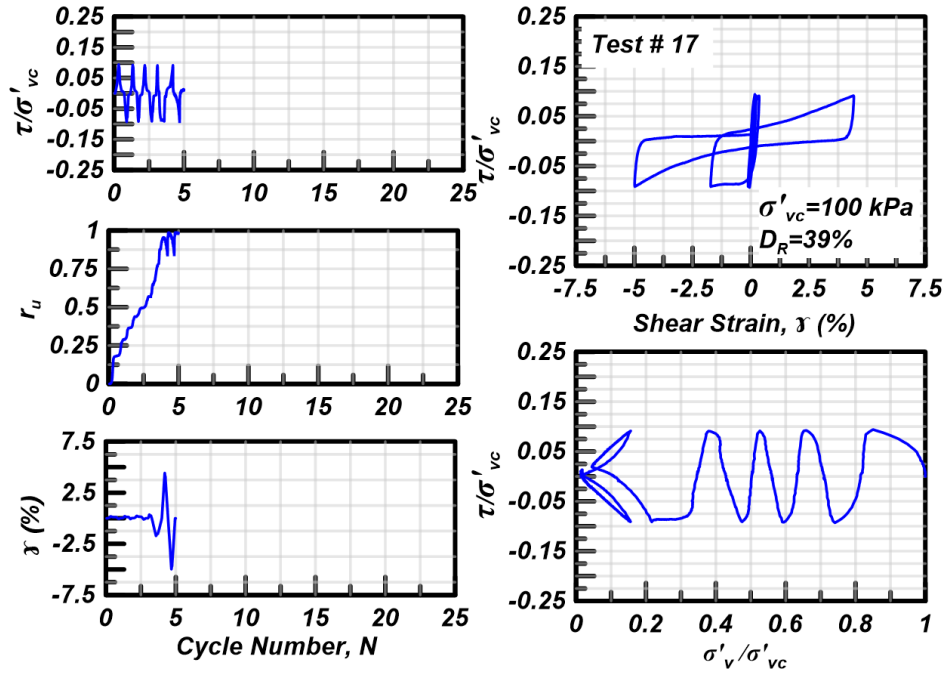


Figure 6.1 Cyclic loading responses of a loose specimen under a 100 kPa sheared up to $\gamma_{\text{peak}} = 5\%$

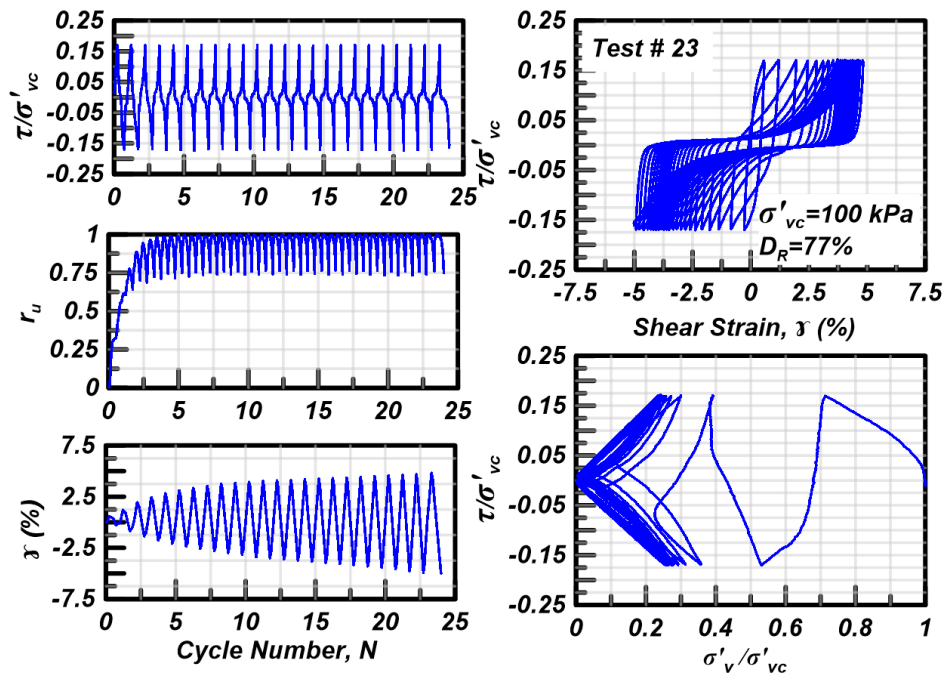


Figure 6.2 Cyclic loading responses of a dense specimen under a 100 kPa sheared up to $\gamma_{\text{peak}}=5\%$

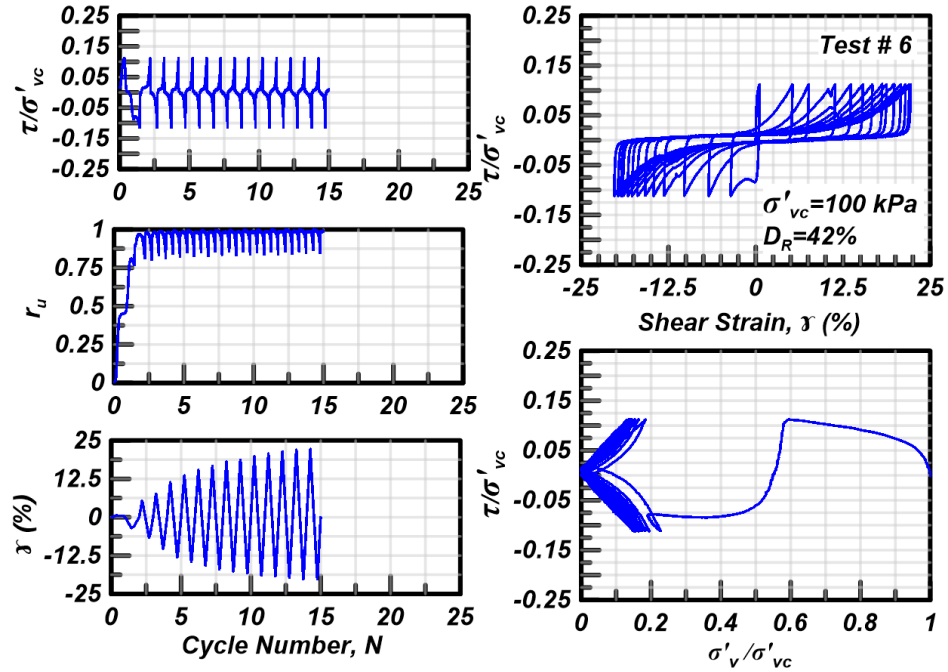


Figure 6.3 Cyclic loading responses of a loose specimen under a 100 kPa sheared up to $\gamma_{\text{peak}}=20\%$

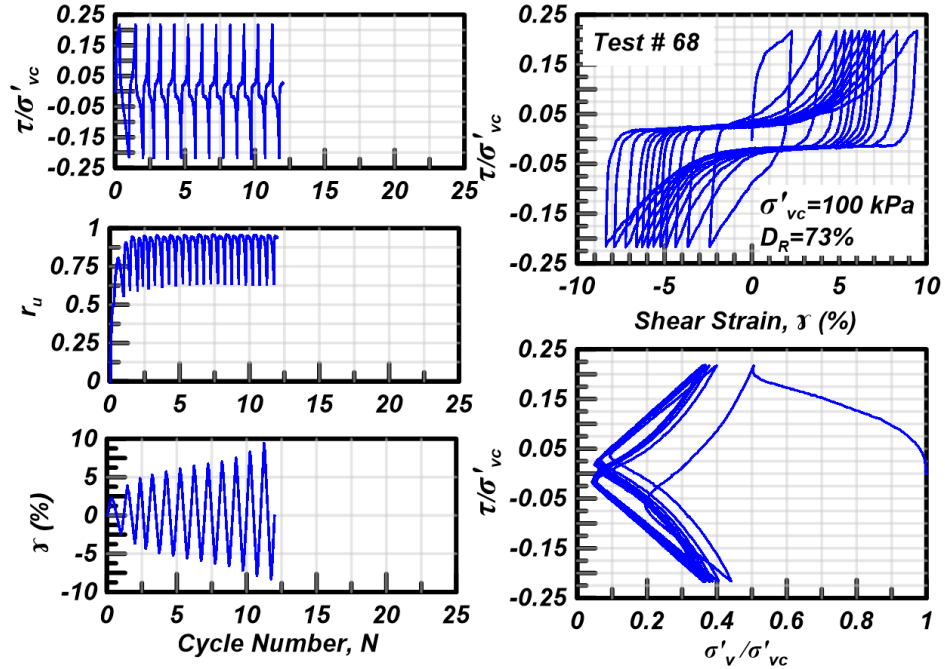


Figure 6.4 Cyclic loading responses of a dense specimen under a 100 kPa sheared up to $\gamma_{peak}=9\%$

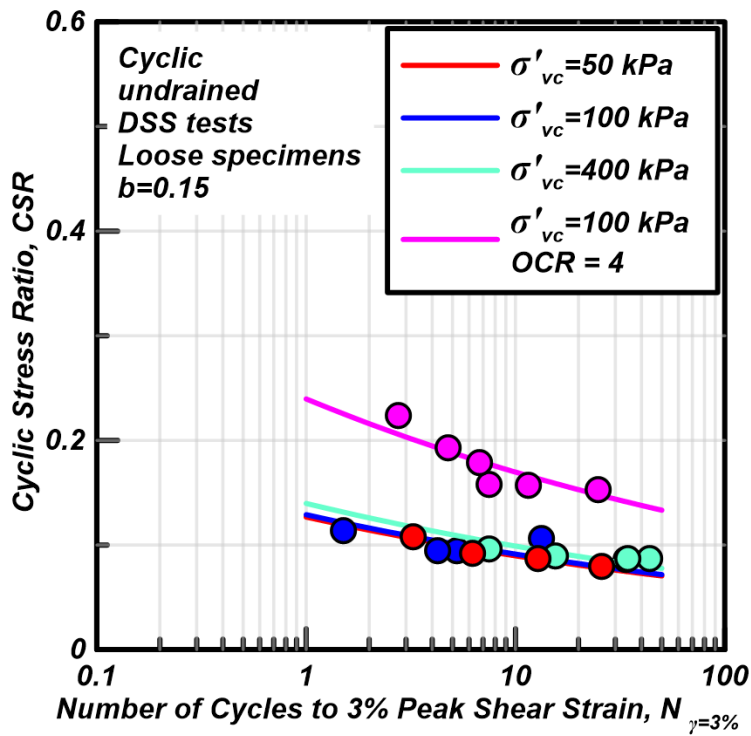


Figure 6.5 CRR vs. $N_{\gamma=3\%}$ curves from DSS tests on loose specimens

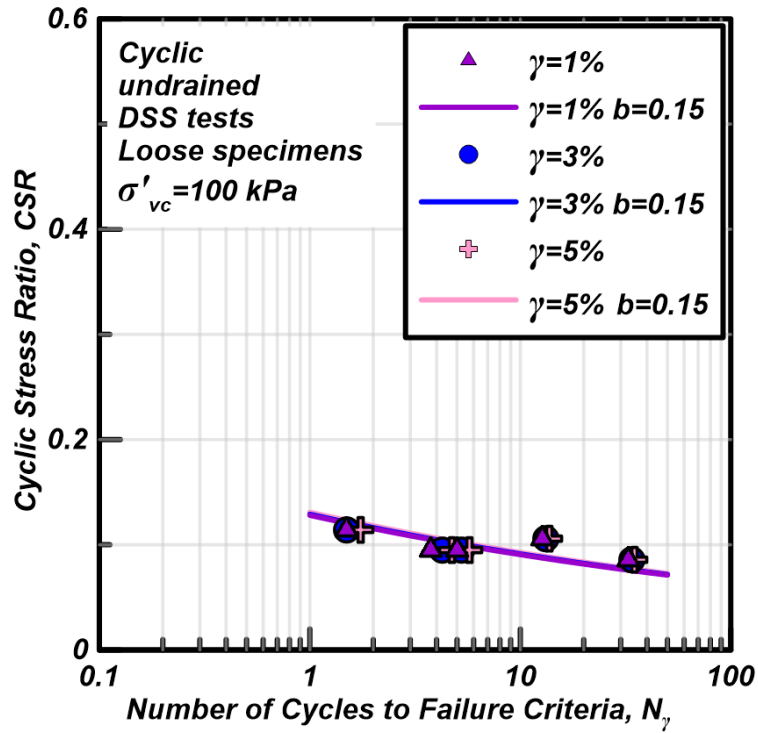


Figure 6.6 CRR vs. N_γ curves from DSS tests on loose specimens for failure criteria of $\gamma = 1, 3$ and 5%

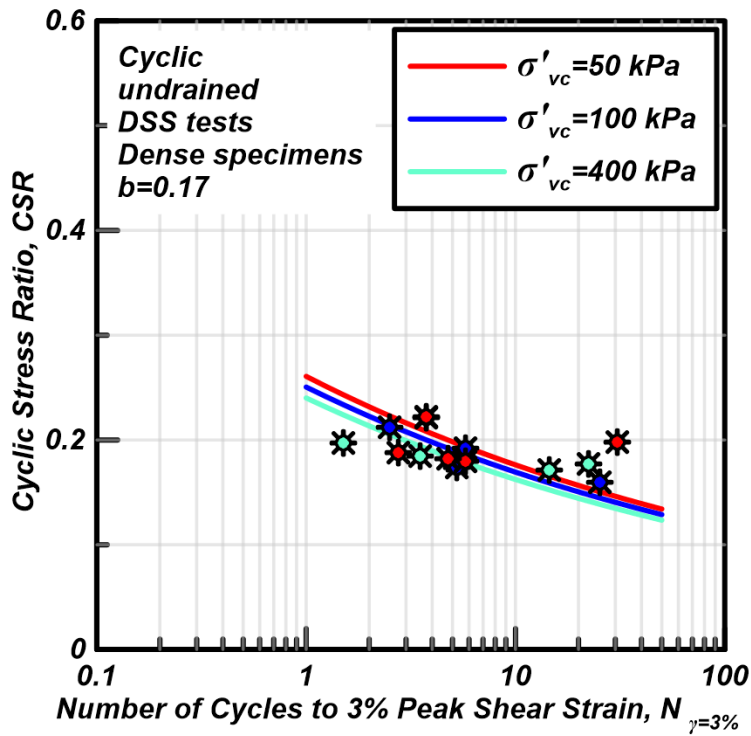


Figure 6.7 CRR vs. $N_{\gamma=3\%}$ curves from DSS tests on dense specimens

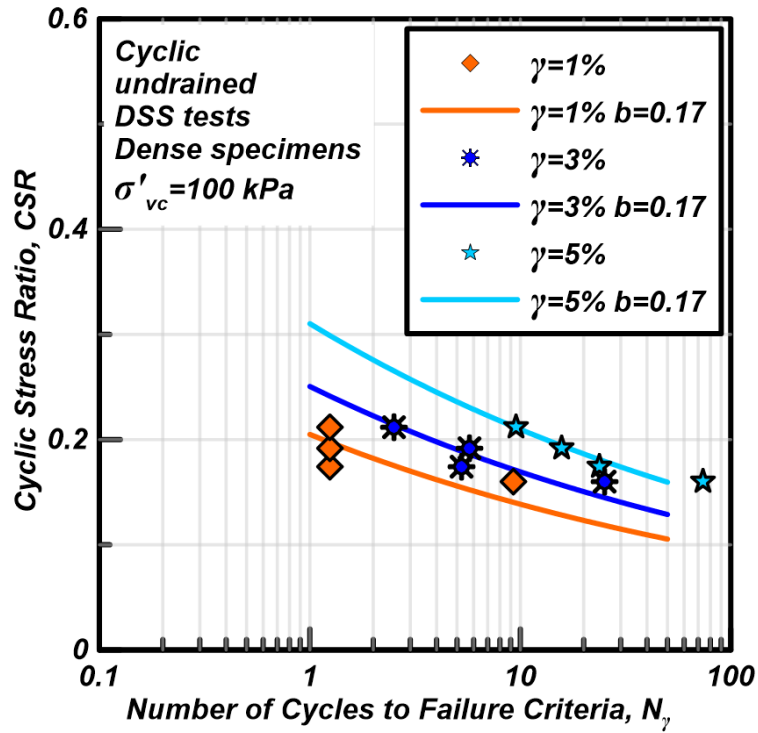


Figure 6.8 CRR vs. N_γ curves from DSS tests on dense specimens for failure criteria of $\gamma = 1, 3$ and 5%

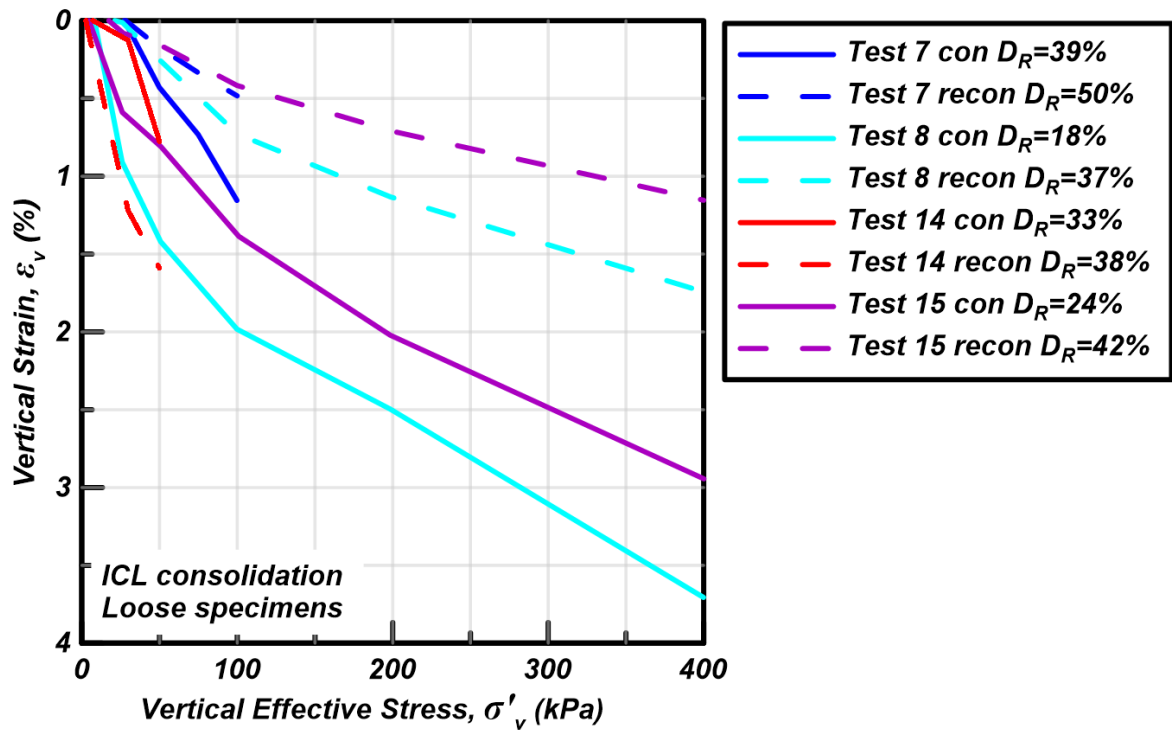


Figure 6.9 Consolidation and reconsolidation after cyclic shearing results from tests on loose specimens

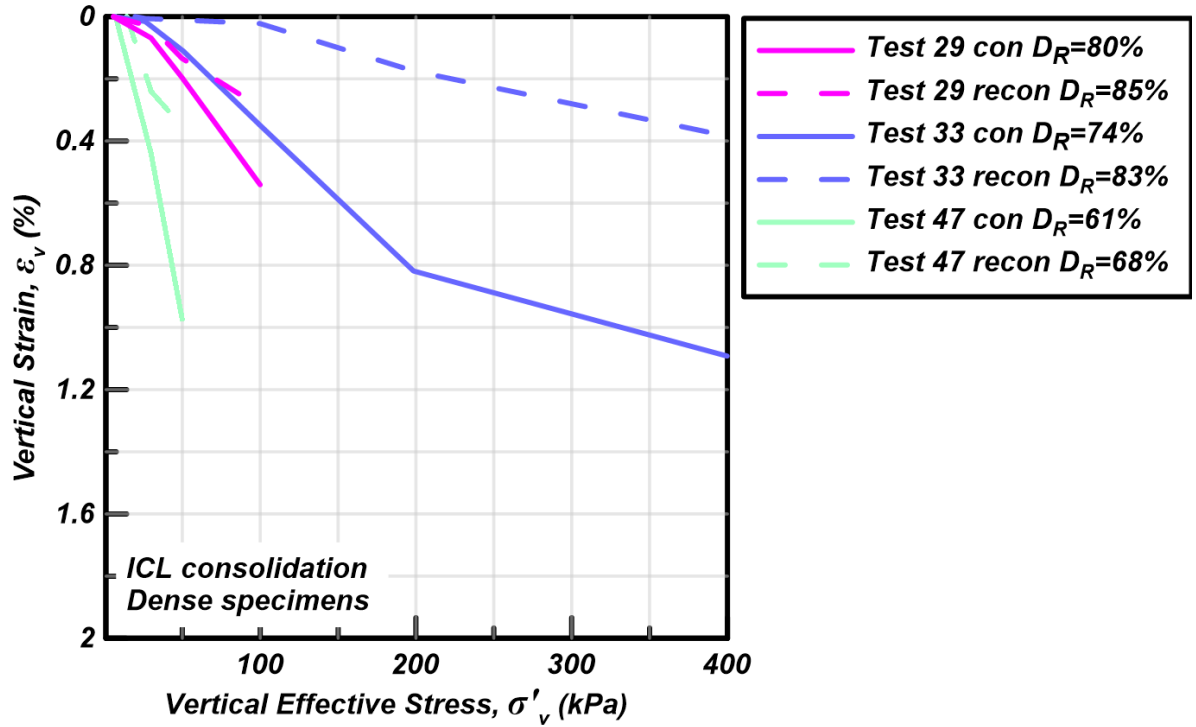


Figure 6.10 Consolidation and reconsolidation after cyclic shearing results from tests on dense specimens

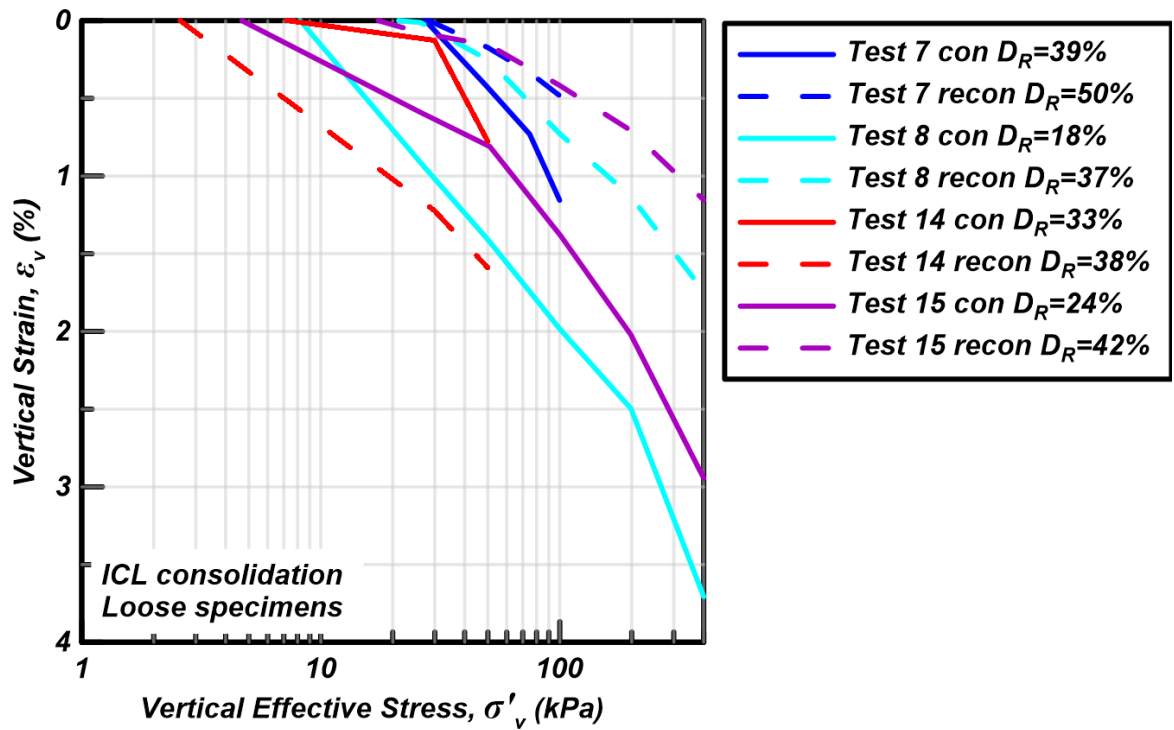


Figure 6.11 Consolidation and reconsolidation after cyclic shearing results from tests on loose specimens in semi-log scale

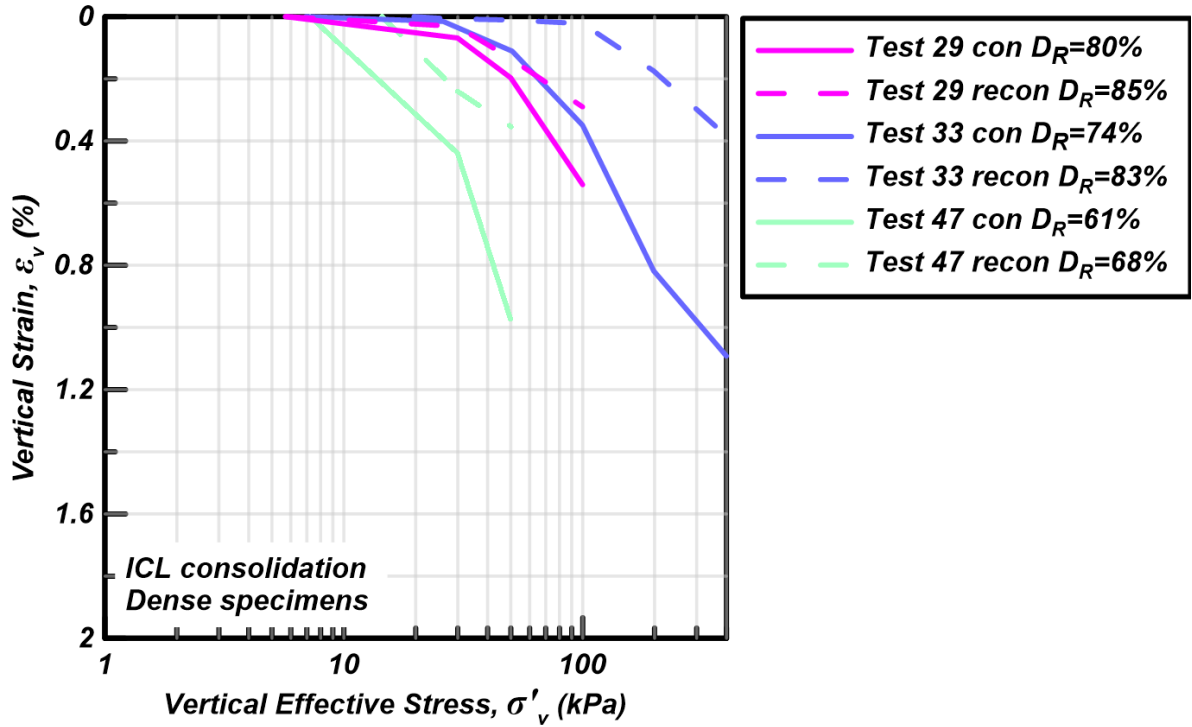


Figure 6.12 Consolidation and reconsolidation after cyclic shearing results from tests on dense specimens in semi-log scale

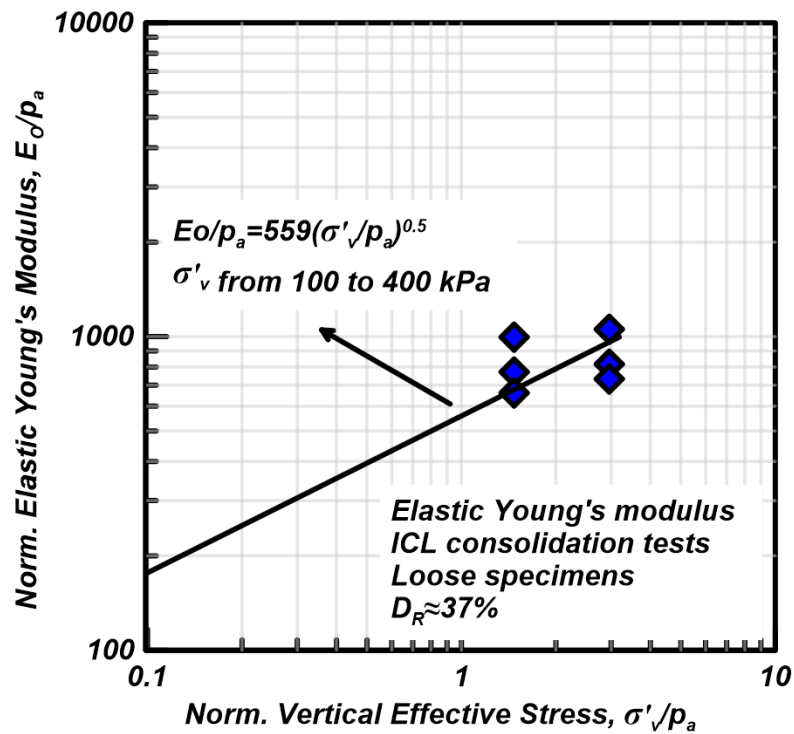


Figure 6.13 Young's modulus relationship from unloading portion from tests on OCR=4 specimens

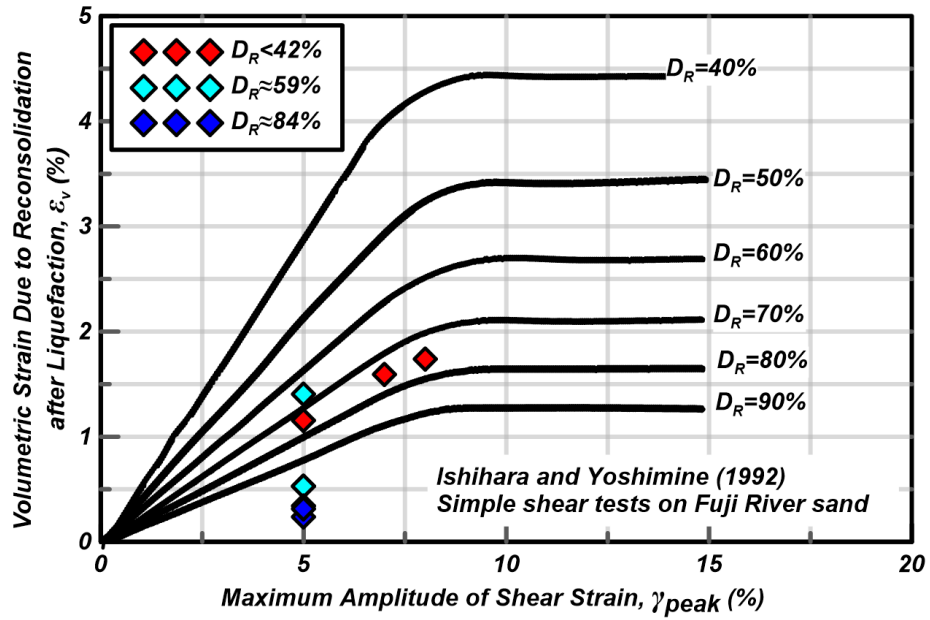


Figure 6.14 Reconsolidations results compared to Ishihara and Yoshimine's (1992) reconsolidation curves

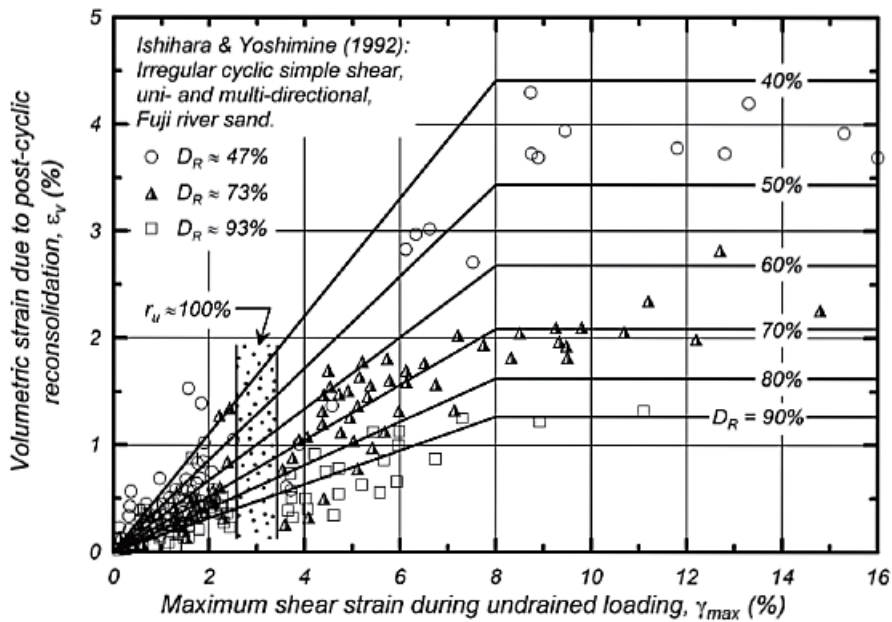


Figure 6.15 Ishihara and Yoshimine's (1992) reconsolidation curves redrawn by Idriss and Boulanger (2008) to include experimental results

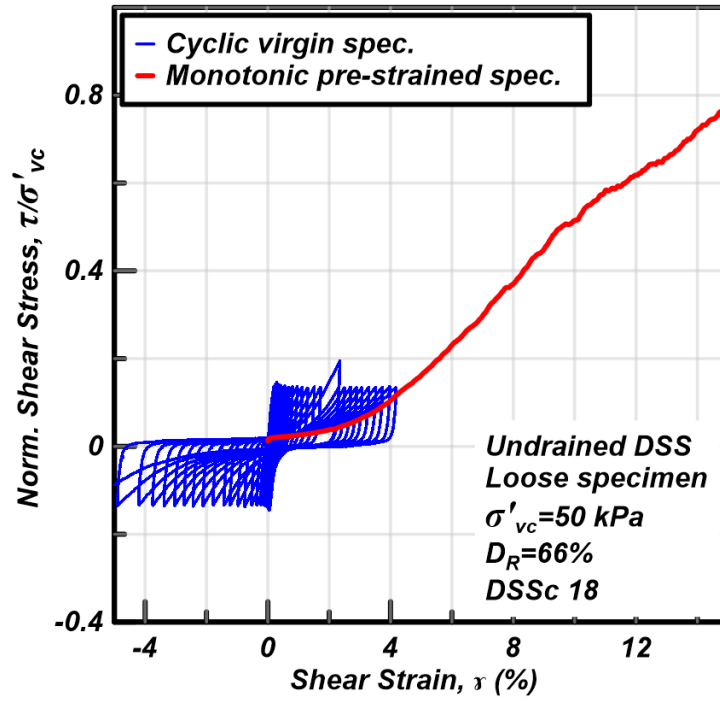


Figure 6.16 Results from a DSS cyclic test and from a DSS monotonic test performed after the cyclic test on a loose specimen consolidated under 50 kPa

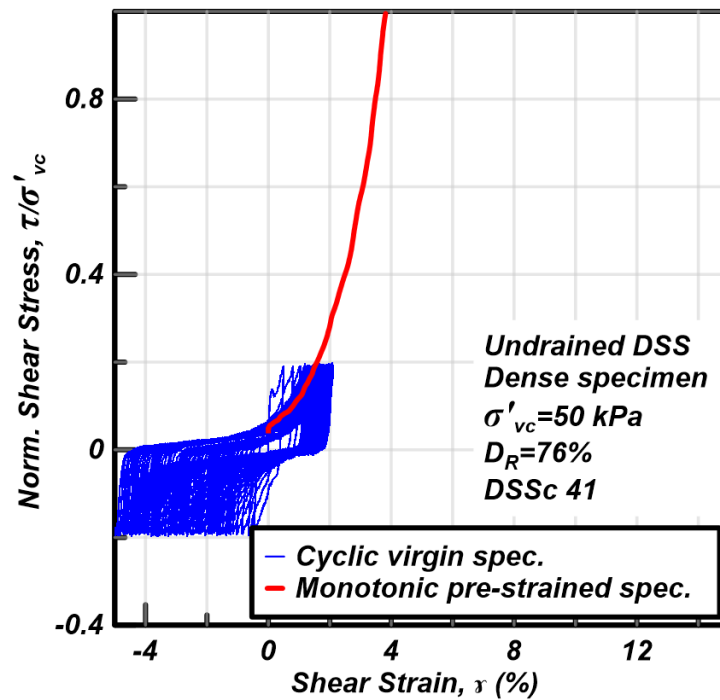


Figure 6.17 Results from a DSS cyclic test and from a DSS monotonic test performed after the cyclic test on a dense specimen consolidated under 50 kPa

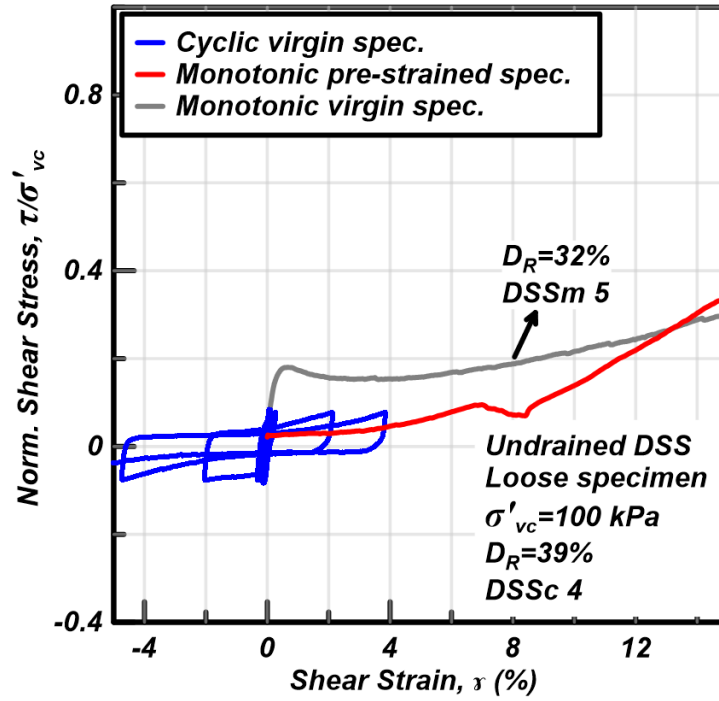


Figure 6.18 Results from a DSS cyclic test, from a DSS monotonic test performed after the cyclic test and from a DSS monotonic test on a virgin specimen. Tests are from loose specimens consolidated under 100 kPa

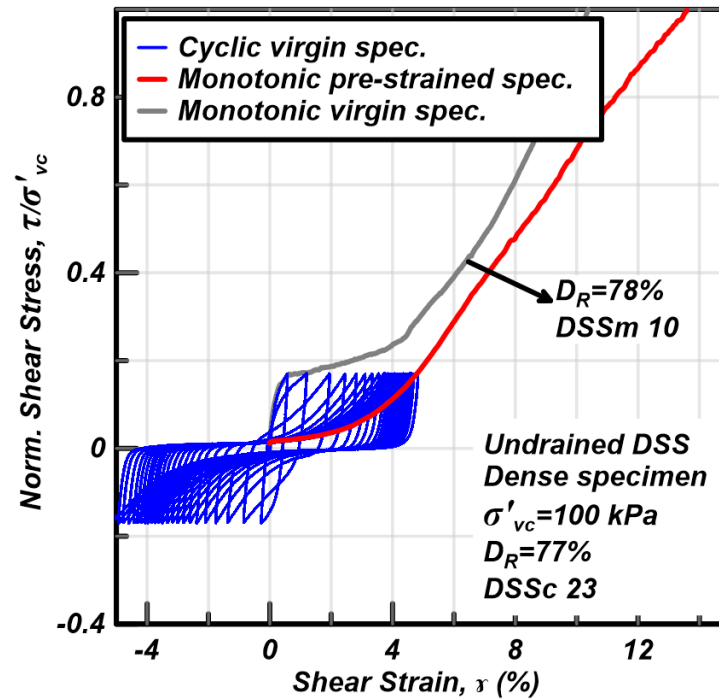


Figure 6.19 Results from a DSS cyclic test, from a DSS monotonic test performed after the cyclic test and from a DSS monotonic test on a virgin specimen. Tests are from dense specimens consolidated under 100 kPa

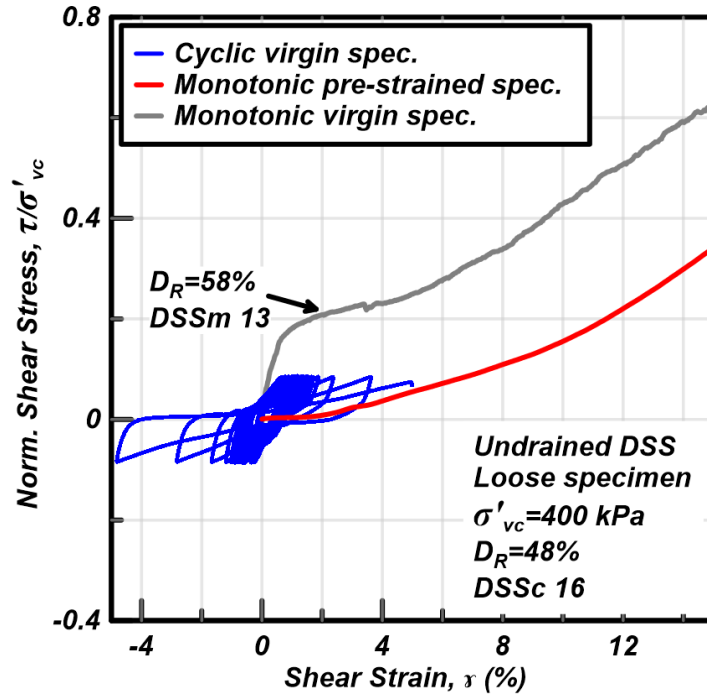


Figure 6.20 Results from a DSS cyclic test, from a DSS monotonic test performed after the cyclic test and from a DSS monotonic test on a virgin specimen. Tests are from loose specimens consolidated under 400 kPa

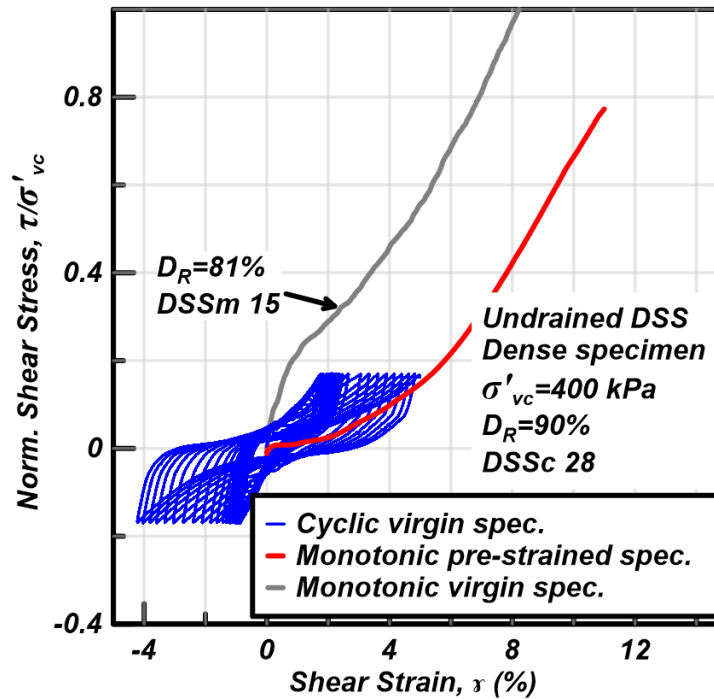


Figure 6.21 Results from a DSS cyclic test, from a DSS monotonic test performed after the cyclic test and from a DSS monotonic test on a virgin specimen. Tests are from dense specimens consolidated under 400 kPa

Chapter 7

Pre-Straining Cyclic Direct Simple Shear Characteristics

Original Publication: Parra Bastidas A. M., Boulanger R. W., DeJong J. T. and Price A. B. (2016): Effects of Pre-Strain History on the Cyclic Resistance of Ottawa F-65 Sand, 16th World Conference on Earthquake Engineering (WCEE), to be presented in Santiago de Chile, Chile 2017.*

**Original text has been modified relative to the published paper for consistency in notation and terminology used in the other chapters of the present Dissertation.*

7.1 Abstract

The cyclic strength of a saturated sand can be expected to evolve in response to the cumulative effects of multiple earthquake events over geologic time. Prior laboratory studies have demonstrated that cyclic pre-straining can significantly increase or decrease the cyclic strength for future events, depending on the sand's properties and state variables (e.g., relative density, stress history), effective confining stresses, and dynamic strains (e.g., amplitudes and numbers of cycles). For example, prior studies have shown that small amplitude cyclic pre-straining tends to increase cyclic strength whereas large amplitude cyclic pre-straining can decrease cyclic strength for dense sand. The cumulative effect of repeated recurrent liquefaction and pre-straining events on the correlation between cyclic strength and void ratio have not, however, been examined. The present study examines the effects of repeated recurrent liquefaction and cyclic pre-straining on the cyclic strength of clean Ottawa F-65 sand. Cyclic direct simple shear tests are performed for a range of initial relative densities subjected to sequences of cyclic loading events. Each cyclic loading event consisted of uniform cyclic stress controlled loading to a maximum shear strain or

maximum number of loading cycles, after which the specimen was allowed to reconsolidate prior to the next cyclic loading event. The evolution of cyclic loading behavior through these sequences of loading events are described. Recurrent liquefaction (i.e., $r_u = 100\%$ or $\gamma_{\max} = 3\%$) and cyclic pre-straining without causing liquefaction caused significant increases in cyclic strength relative to virgin specimens across a range of loose to dense conditions, with the effects being greater for denser specimens. The observed responses and their implications for liquefaction triggering correlations in practice are discussed.

Keywords: Pre-strain history, Cyclic strength, Liquefaction, Laboratory testing

7.2 Introduction

Recurrent soil liquefaction has been observed at many sites during different earthquake events. Recent examples include the recurrence of liquefaction in natural deposits in the Christchurch, New Zealand area during the 2010-11 Canterbury Earthquake Sequence (Lees et al. 2015) and in artificial fills in the Tokyo area during the 2011 Tohoku earthquake (Wakamatsu 2012). Field studies have attempted to quantify the effects that liquefaction has on in-situ test results or a site's performance in subsequent earthquake events, but noticeable effects have been difficult to discern relative to the effects of spatial variability and other sources of uncertainty.

The repeated recurrence of liquefaction would be expected to produce a progressive evolution of soil properties throughout a soil profile. The schematic in Figure 7.1 illustrates how the accumulation of densification from repeated events would be expected to produce a state with greater resistance to liquefaction. The progression may be different at different depths in the soil profile, perhaps even with some loosening or weakening near the surface or beneath lower permeability layers that can impede upward water flow. Overall, however, the expectation would be that a sufficient number of strong shaking events would eventually improve the resistance of a site to liquefaction.

Laboratory element testing has shown that cyclic pre-straining can increase or decrease the cyclic strength of sand depending on a number of factors (Singh et al. 1982, Goto et al. 1988, Seed et al. 1977, and Oda et al. 2001). For example, Singh et al. (1982) performed undrained cyclic triaxial tests in reconstituted sand specimens with $D_R = 48\%$, some of the specimens were virgin specimens whereas other specimens were subjected to small amplitude cyclic shear strains; some of the specimens were subjected to freeze and thawed cycles. They found out that all the pre-strained specimens had CRRs that were 30 to 40% higher than the virgin specimens even when all the specimens had similar D_R values (Figure 7.2a). Goto et al. (1988) performed similar tests to those by Singh et al. (1982), however, the pre-strained specimens were extensively pre-strained (with approximately 10,000 cycles with an axial strain amplitude of 0.05%) and the specimens had $D_R = 90\%$. Their findings were similar to those from Singh et al. (1982), however the increase in CRR was much higher (80-100%) as shown in Figure 7.2b. Seed et al. (1977) conducted shaking table tests on air pluviated sand specimens, in which the specimens were first subjected to short-duration cyclic loading events (2½-3 cycles with reconsolidation between events) followed by long-duration cyclic loading. The short-duration cyclic loading (or pre-straining events) caused excess pore pressure ratios of 0.3 to 0.05 with little change in dry density during reconsolidation, but still caused an increase in cyclic strength (Figure 7.3) and a decrease in the rate of excess pore water pressure generation during the long-duration cyclic loading. Oda et al. (2001) performed undrained cyclic triaxial tests on air pluviated, dense Toyoura sand specimens that had been reconsolidated after being cyclically loaded undrained to different levels of peak axial strain ($\epsilon_{a,pre}$). They observed that the cyclic strength of these dense specimens was reduced when the value of $\epsilon_{a,pre}$ was greater than 1% (Figure 7.4); this was observed even when the prior cyclic loading and reconsolidation caused the relative density (D_R) of the specimens to increase. They associated the reduction of liquefaction resistance with the development of specimen anisotropy, with sand particles envisioned to have formed column-like structures (even if the global void ratio did not change significantly) which were less stable when the specimen was stressed perpendicular to the elongation direction.

Centrifuge tests have also been used to study the effect of prior cyclic loading on the cyclic strength of sands. [El-Sekelly et al. \(2015\)](#) subjected a centrifuge model of a level silty sand profile to 91 shaking events that included events with 5 cycles of loading with a maximum acceleration of about 0.035 g and events with 15 cycles of loading with a maximum acceleration of about 0.040 g and 0.12 g; events were followed by full pore water pressure dissipation. They concluded that pre-shaking with small acceleration events reduced the maximum excess pore pressure ratios and the depths at which liquefaction was triggered within the model; however, this effect was reset when the model was shaken with events with higher accelerations, and this resetting effect diminished towards the end of the experiments. Overall, pre-shaking increased the cyclic strength of a silty sand deposit over the progression of shaking events. [El-Sekelly et al. \(2016\)](#) performed similar tests with clean Ottawa F#55 sand and obtained similar findings. [Darby et al. \(2016\)](#) conducted a centrifuge test with multiple shaking events and inflight cone penetration resistance measurements in Ottawa F-65 sand. The model was subjected to sixteen shaking events of 15 cycles of sinusoidal acceleration followed by full pore pressure dissipation; the peak base acceleration was between 0.018 to 0.09 g. They concluded that the cumulative effect of these sixteen events, of which five triggered liquefaction, resulted in about a 160% increase in the average cone tip resistance from about 2.5 MPa to 6.5 MPa and an associated modest increase in cyclic strength.

The results of the above laboratory and centrifuge testing studies demonstrate that the effect of cyclic pre-straining on the cyclic strength of sands depends on: the amplitude and number of prior strain cycles; the initial D_R and the changes in D_R due to prior cyclic loading; the changes in fabric due to recurrent cyclic loading, with the changes depending on the amplitude of the cyclic strains; and any destruction of prior ageing, cementation, over-consolidation, or cyclic pre-straining effects if the most recent pre-strains are of large enough amplitude.

The purpose of this paper is to examine the effect of repeated recurrent liquefaction and cyclic pre-straining on the cyclic strength of clean Ottawa F-65 sand. The results serve two purposes. First, this sand is a standard reference sand used in centrifuge model studies, including at the Center for

Geotechnical Modeling at the University of California at Davis. Centrifuge models are frequently subjected to multiple shaking events, such that the evolution of cyclic strengths with pre-straining is an issue that requires attention in the calibration of nonlinear numerical models. Second, the results provide further insights on the evolution of cyclic strengths with multiple pre-straining stages. This paper describes the characteristics of Ottawa F-65 sand, the experimental procedures used to conduct direct simple shear (DSS) tests with repeated loadings, results from monotonic and cyclic DSS tests on virgin specimens, results from cyclic pre-straining DSS tests, and discussion of the effects that cyclic pre-straining had on cyclic strengths and cyclic loading behaviors. Finally, some of the implications of the findings are discussed.

7.3 Experimental Approach

The effect of repeated recurrent liquefaction and cyclic pre-straining on the cyclic loading behavior of Ottawa F-65 sand was evaluated using DSS tests. The characteristics of the sand, the specimen preparation procedures, and the DSS testing procedures are described in this section. Additional test data are in [Parra Bastidas et al. \(2016\)](#).

Ottawa F-65 sand is a quartzitic uniform sand with rounded grains produced by mining of fine-grained St. Peter sandstone deposits near Ottawa, Illinois. The silica content of this sand is 99.5% ([US Silica 2016](#)). The coefficient of uniformity (C_u) is 1.61, the coefficient of curvature (C_c) is 0.96, the fines content is 0.17% and the specific gravity of solids (G_s) is 2.65. The maximum dry density is 1759 kg/m³ by the Japanese Method [JIS A 1224 \(JIS 2009\)](#) standard method and the minimum dry density is 1446 kg/m³ by [ASTM D4254-00 \(ASTM 2000\)](#) standard method. The corresponding minimum and maximum void ratios are 0.507 and 0.833, respectively.

Specimens were prepared dry and were placed in a GEOTAC DSS apparatus for saturation, consolidation and shearing. Loose specimens were prepared by the dry funnel deposition (DFD) method

and dense specimens were prepared by the air pluviation (AP) method. Specimens were subjected to a seating load of 10 kPa in the DSS apparatus. Specimens were saturated in the DSS apparatus with approximately 100 ml of de-ionized water which flowed by gravity. Specimens were consolidated using load increment ratios of about 2.0 until the final consolidation stress was reached. Each intermediate load increment was applied for 5 minutes, whereas the final load was maintained for one hour to allow the specimen to consolidate and creep before shearing.

Undrained simple shear tests were performed under a constant height condition that is equivalent to an undrained shearing condition on the DSS apparatus (Dyvik et al. 1987). Monotonic tests on virgin specimens were performed at a shear strain rate of 50% per hour and to a maximum shear strain (γ_{\max}) of approximately 15%. Cyclic tests on virgin specimens were performed at a shear strain rate of 50% per hour, but with a stress criterion for reversal of loading directions to produce uniform cyclic stress ratio loadings. Cyclic loading was continued to a γ_{\max} of approximately 5% in all tests of virgin specimens.

The loading procedures for pre-strained specimens is similar to the process followed by Price et al. (2016). Each cyclic loading stage consisted of uniform cyclic stress ratio loading until a γ_{\max} of approximately 3% or a maximum of 100 loading cycles was reached. The specimen was then re-centered to the position of absolute zero shear strain, the constant-height restraints were released, and the specimen was reconsolidated using the same procedures used for virgin consolidation. This process was followed for all cyclic loading stages. The cyclic stress ratio for the cyclic loading stages was increased in a sequence of steps, with several cyclic loading stages being performed at each step. At each value of cyclic stress ratio, cyclic loading stages were repeated until the specimen resisted 100 cycles of loading without reaching $\gamma_{\max} = 3\%$. The cyclic stress ratio was then increased for the next series of cyclic loading stages. The cyclic stress ratios applied to the loose specimens were 0.12, 0.18, 0.25, 0.40 and 0.80. The cyclic stress ratios applied to the dense specimens were 0.25, 0.40 and 0.80.

7.4 Monotonic and Cyclic DSS Results for Virgin Specimens

Monotonic undrained DSS responses for loose and dense normally consolidated (NC) virgin specimens consolidated to a vertical effective consolidation stress (σ'_{vc}) of a 100 kPa are shown in Figure 7.5. Dilative tendencies increase with relative density (D_R). The specimen with a $D_R = 15\%$ shows little change in shear stress and vertical effective stress after a shear strain (γ) of approximately 2%, indicating this specimen is approximately at a critical state condition. The specimen with a $D_R = 30\%$ shows an initial contractive tendency, followed by a quasi-steady state behavior (Alarcon-Guzman et al. 1988) at a γ of approximately 3 to 5%, followed by a dilatant tendency after approximately 5% γ . The specimen with a $D_R = 78\%$ shows a smaller initial contractive tendency followed by a strong dilatant tendency with no quasi-steady behavior.

The cyclic resistance ratio (CRR) is plotted versus the number of loading cycles (N) to $\gamma_{max} = 3\%$ for loose and dense NC virgin specimens consolidated to $\sigma'_{vc} = 100$ kPa in Figure 7.6. The loose specimens had a D_R of about 40% and the dense specimens a D_R of about 80%. The CRR to cause $\gamma_{max} = 3\%$ in a certain number of cycles increases with D_R . The CRR versus N curves were each fit with a power law and the exponent b (which defines the negative slope of the curve) was determined to be 0.15 ($CRR_{\gamma_{max} = 3\%} = 0.14N^{-0.15}$) for the loose specimens and 0.17 ($CRR_{\gamma_{max} = 3\%} = 0.26N^{-0.17}$) for the dense specimens.

7.5 Cyclic DSS with pre-straining

Undrained cyclic DSS with pre-straining tests were conducted on loose and dense NC specimens consolidated to $\sigma'_{vc} = 100$ kPa. An example loading sequence is illustrated in Figure 7.7 for test PS6, showing the CSR that was applied during each cyclic shearing stage, the corresponding number of cycles to $\gamma_{max} = 3\%$ and the D_R of the specimen at the start of each loading. This specimen was subjected to 9 stages of cyclic loading and reconsolidation with $CSR = 0.12$ (stages A1 to A9), 1 stage of cyclic loading

and reconsolidation with $CSR = 0.18$ (stage B1), 1 stage of cyclic loading and reconsolidation with $CSR = 0.25$ (stage C1), 2 stages of cyclic loading and reconsolidation with $CSR = 0.40$ (stage D1 to D2) and 3 stages of cyclic loading and reconsolidation with $CSR = 0.80$ (stages E1 to E3). The D_R progressively increased throughout the sequence from its initial value of 25% to its final value of 83%. The number of cycles required to reach $\gamma_{max} = 3\%$ increased in each loading stage with the same CSR . Note that γ_{max} did not reach 3% in the loading stages that stopped at 100 cycles (stages A9, B1, C1, D2, and E3).

The cyclic loading responses of test PS6 for select cyclic loading stages are shown Figure 7.8; this figure shows normalized shear stress versus shear strain (top row), stress paths (middle row) and normalized vertical effective stress versus shear strain (bottom row) for the cyclic loading stages A3 (1st column), A6 (2nd column), B1 (3rd column) and D1 (4th column) (Figure 7.8). The specimen exhibited increased dilative tendencies as the specimen became denser with each loading stage. The rate of shear strain accumulation after strains exceeded about 1% became progressively smaller with each loading stage at the same CSR and sometimes smaller even when the CSR was increased to the next level.

The behaviors evident in Figure 7.7 and Figure 7.8 are representative of those observed in other tests on NC specimens independent of their initial D_R . Specimens that began with a higher initial D_R took fewer loading stages to develop a given level of cyclic strength, but the cyclic loading behavior at any one stage was dependent on the prior loading history as well as the current value of D_R , as illustrated below.

The cyclic loading responses of a virgin specimen and a pre-strained specimen at similar D_R are presented in Figure 7.9; the response of the virgin specimen from test V23 with initial $D_R = 77\%$ is plotted in Figure 7.9a and the response of the pre-strained specimen from test PS6 in the loading stage D1 with a current $D_R = 74\%$ is plotted in Figure 7.9b. The pre-strained specimen had stronger dilative tendencies than the virgin specimen, even though the virgin specimen has a slightly higher initial D_R . The pre-strained specimen had a slower accumulation of shear strain per loading cycle after strains exceed about 1%. However, the pre-strained specimen accumulated approximately 1% shear strain during the first quarter of the first loading cycle whereas the virgin specimen accumulated only 0.5% shear strain during the first

quarter of the first loading cycle. Thus, the pre-strained specimen reached 1% strain more quickly than the virgin specimen, but then accumulated strains slower than the virgin specimen subsequently. The net effect was that the pre-strained specimen had a greater resistance to developing a maximum shear strain of 3% than the virgin specimen. The pre-strained specimen had a lower phase transformation angle ($\approx 20^\circ$) during the first quarter cycle of loading than the virgin specimen during its second loading cycle ($\approx 26^\circ$) or the virgin specimen from the monotonic test ($\approx 29^\circ$ on Figure 7.5). The lower transformation angle in the pre-strained specimen might be due to the more stable fabric that developed across the shearing stages, even though this specimen was prepared initially looser than the virgin specimen. The difference in the specimen's preparation methods might also have had some influence in the difference in the phase transformation angles mobilized by the virgin and the pre-strained specimens.

The evolution of the CRR with each loading stage on pre-strained specimens was evaluated by estimating the CRR for $\gamma_{\max} = 1\%$ or 3% in 15 cycles for each loading stage. The $\text{CSR}_{N=15}$ were obtained from converting the applied CSRs to equivalent $\text{CSR}_{N=15}$ using the process described by [Idriss and Boulanger \(2008\)](#). For those loading stages that did not reach $\gamma_{\max} = 3\%$ before the test was stopped at 100 cycles, the equivalent $\text{CSR}_{N=15}$ represents a lower bound estimate for the $\text{CRR}_{N=15}$ against $\gamma_{\max} = 3\%$. The above process applied to the pre-strained specimen in test PS6 and a failure criterion of $\gamma_{\max} = 3\%$ is shown in Figure 7.10. The parameter b , which is the slope of the $\log(\text{CRR})$ versus $\log(N)$ curves, was taken as 0.15 for both virgin and pre-strained specimens with $D_R < 60\%$ and 0.17 for all denser specimens. The parameter b was assumed to be equal for virgin and pre-strained specimens and for either failure criterion, although the potential evolution of b with cyclic pre-straining and its dependence on the failure criterion warrant further investigation.

The $\text{CRR}_{N=15}$ for $\gamma_{\max} = 1\%$ or 3% from test PS6 are plotted versus the average (global) void ratio (e) for each cyclic loading stage in Figure 7.11. The $\text{CRR}_{N=15}$ to $\gamma_{\max} = 1\%$ and 3% were about the same when the specimen was loose (i.e., $e > 0.65$). The $\text{CRR}_{N=15}$ for $\gamma_{\max} = 3\%$ then became progressively greater than for $\gamma_{\max} = 1\%$ as the void ratio progressively decreased to smaller values. At these lower void ratios,

high r_u values and $\gamma_{\max} = 1\%$ could generate fairly quickly, but the specimens were highly resistant to accumulating larger strains as evident in the stress-strain responses shown previously in Figure 7.8 and Figure 7.9. The $CRR_{N=15}$ for $\gamma_{\max} = 3\%$ became greater than unity when the average void ratio had decreased to about 0.56, corresponding to an average (global) D_R of about 83%.

The $CRR_{N=15}$ to $\gamma_{\max} = 3\%$ for virgin specimens in tests V4, V7, V19, V23, V25 and V62 and pre-strained specimens in tests PS3, PS6, PS10, PS11 and PS12 are plotted together versus average (global) void ratio in Figure 7.12. Loose virgin specimens ($0.68 < e < 0.73$) had about 10-50% lower $CRR_{N=15}$ values than pre-strained specimens over the same void ratio range. Dense virgin specimens ($0.56 < e < 0.58$) had 40-55% lower $CRR_{N=15}$ values than pre-strained specimens over the same void ratio range. The greater effect of pre-straining on the denser specimens could be partly due to the different sample preparation methods used to prepare the initially loose (dry funnel deposition) and dense (dry air pluviation) specimens. The cyclic strengths for virgin specimens would be expected to depend on preparation method (e.g., [Mulilis et al. 1977](#)), whereas the cyclic strengths for specimens after several cyclic loading stages would likely be less dependent on the preparation method. Nonetheless, it appears that pre-straining had a stronger effect on the rate of shear strain accumulation after $r_u > 0.90$ developed, regardless of initial placement method (e.g., Figure 7.11 and Figure 7.12).

7.6 Discussion

The repetition of multiple cyclic loading stages on single DSS specimens are likely to have produced non-uniform distributions of void ratio throughout the specimens. For example, [Gilbert \(1984\)](#) measured void ratio non-uniformities in triaxial specimens after a single stage of undrained cyclic loading to large axial strains. None of the specimens tested herein developed visible offsets in the stacked confining rings, which suggests that strong shear localizations did not develop in these tests. Nonetheless, it is reasonable to assume that certain zones in the DSS specimens will be denser and others looser than represented by the average, or global, void ratio. Evaluating these non-uniformities and their effects on

specimen behavior would benefit from quantitative measurements of local void ratios using techniques like those used by [Frost and Jang \(2000\)](#).

Evaluating the effect of pre-straining on liquefaction triggering correlations in sands will require parallel examination of how pre-straining affects both cyclic strengths and the results of in-situ test measurements. A promising approach to evaluate this issue is the use of centrifuge and shaking table tests, such as recently explored by [El-Sekelly et al. \(2016\)](#) and [Darby et al. \(2016\)](#). These studies are expected to provide improved understanding of how recurrent liquefaction triggering affects liquefaction resistance and our ability to evaluate liquefaction resistance in young, uncemented sands.

The effect of multiple earthquake events on a site's liquefaction resistance over geologic time will be further complicated by other mechanisms, including ageing, cementation, and stress history (e.g., over-consolidation). In this regard, individual earthquake events could decrease a site's liquefaction resistance by destroying any benefits from ageing, cementation, or over-consolidation since the prior event. For example, [Price et al. \(2016b\)](#) performed direct simple shear tests with multiple cyclic loading stages on initially over-consolidated non-plastic silt specimens, and showed that the cyclic strength of the over-consolidated specimens decreased after the first cyclic loading stage had triggered liquefaction. They further found that repeated recurrent liquefaction and reconsolidation stages eventually produced large net increases in cyclic strength. Thus, it appears reasonable to expect that the cumulative effect of multiple earthquake events would contribute, in general, to a progressive increase in a site's resistance to liquefaction-induced deformations over geologic time.

7.7 Conclusions

The cumulative effects of repeated recurrent liquefaction and cyclic pre-straining on the cyclic strength of clean Ottawa F-65 sand was evaluated using cyclic direct simple shear tests with multiple stages of uniform cyclic loading followed by reconsolidation. For example, the cyclic resistance ratio

against a peak shear strain of 3% in 15 uniform loading cycles was increased from about 0.06 for a virgin loose specimen (initial relative density of 25%) to greater than 0.6 after a sequence of 14 cyclic loading stages (9 of which triggered liquefaction) had increased the specimen's relative density to about 80%.

Recurrent liquefaction and cyclic pre-straining caused significant increases in cyclic strength relative to virgin specimens across a range of loose to dense initial conditions, with the effects being stronger for denser specimens. The pre-straining history was particularly effective at reducing the rate of shear strain accumulation during uniform cyclic loading after $r_u > 0.90$ developed (or after shear strains exceeded about 0.5-1.0%). The beneficial effects of recurrent liquefaction and cyclic pre-straining are attributed to a combination of densification and the evolution of a more stable fabric within the test specimens.

The results of the present study provide a basis for evaluating how the cyclic loading behavior of Ottawa F-65 sand may evolve in centrifuge or shaking table model tests subjected to multiple shaking events. The results also provide insights on the role that progressive densification and pre-straining may play in natural deposits subject to multiple earthquake events, although in-situ behaviors over geologic time will also be affected by other mechanisms such as ageing, cementation, and stress history (e.g., over-consolidation).

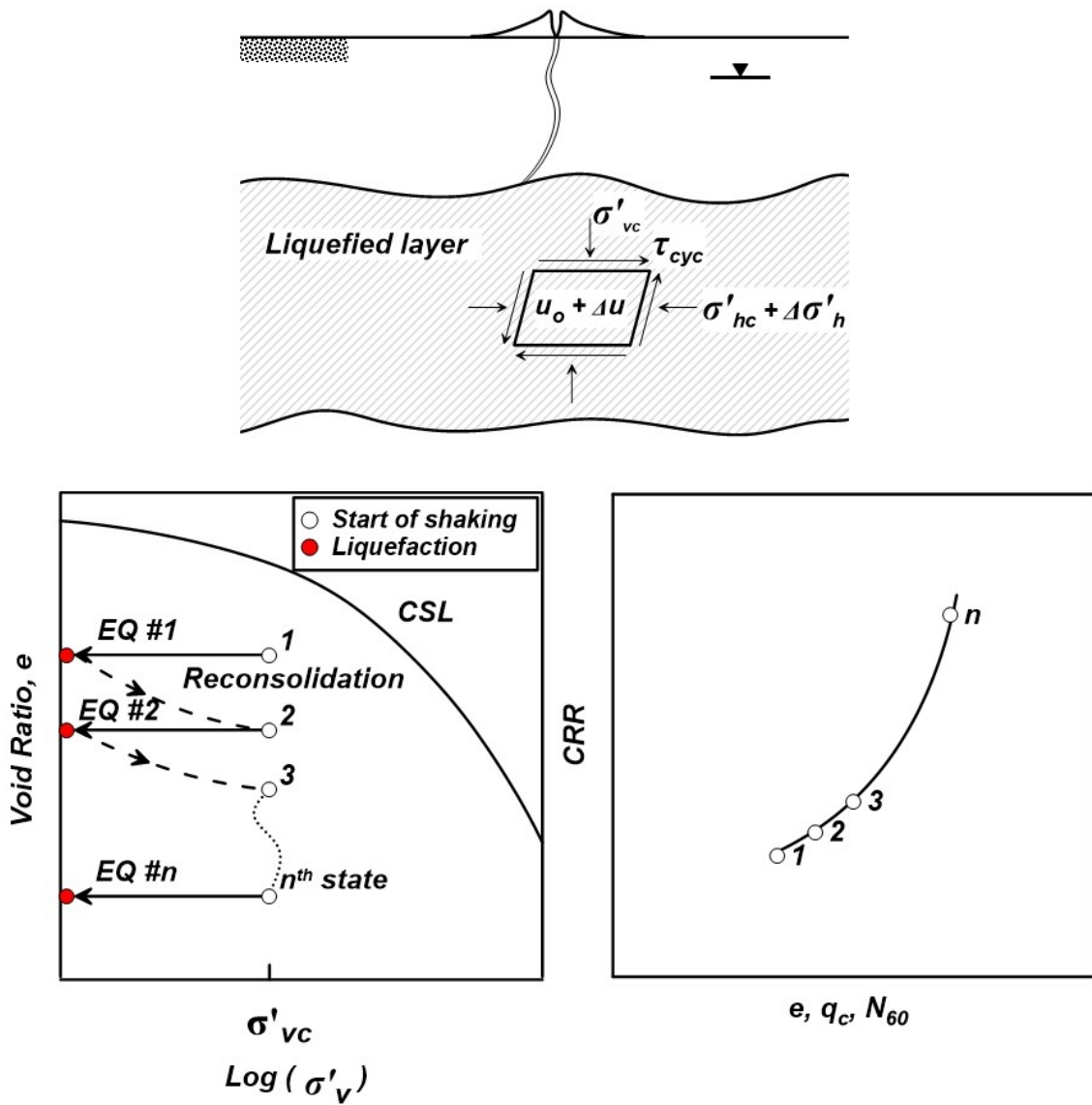


Figure 7.1 Conceptual effect of recurrent liquefaction events: (a) soil element in liquefied layer, (b) void ratio–vertical effective stress paths for a series of earthquake loadings causing liquefaction and subsequent reconsolidation, and (c) evolution of cyclic strength versus indices of density (after Price et al. 2016a)

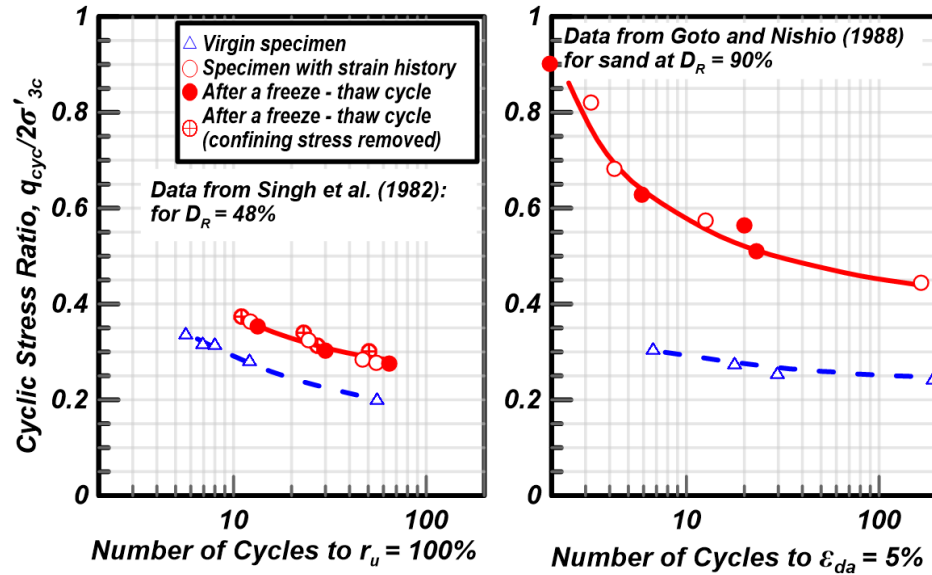


Figure 7.2 Effects of freeze-thaw cycle on the cyclic resistance of saturated clean sand undrained cyclic triaxial tests: Left: Data from Singh et al. (1982) for sand at $D_R=48\%$. Right: Data from Goto and Nishio (1988) for sand at $D_R=90\%$ (after Yoshimine et al. 1994 and Idriss and Boulanger 2008)

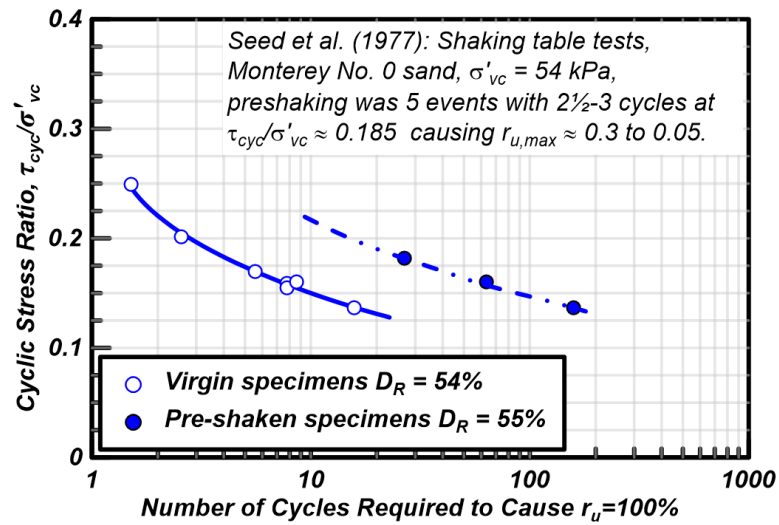


Figure 7.3 Cyclic stress ratio versus number of uniform load cycles to cause $r_u = 100\%$ from shake table tests on air pluviated sand specimens with and without pre-straining (after Seed et al. 1977)

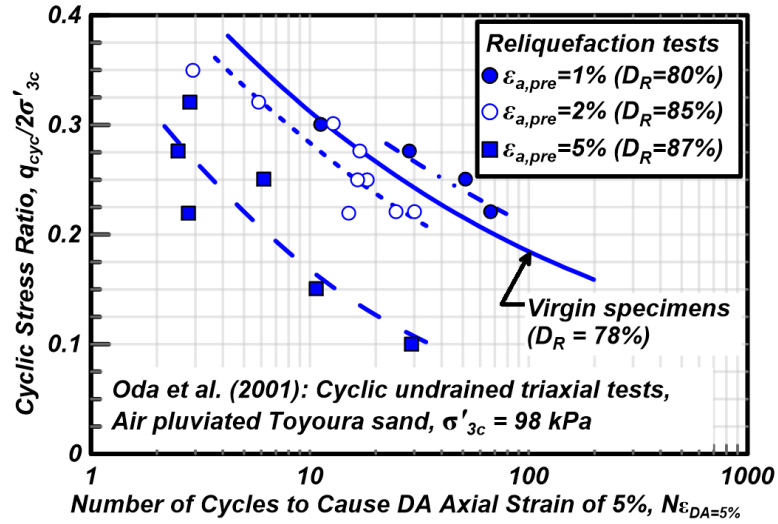


Figure 7.4 Cyclic stress ratio versus number of uniform load cycles to cause double amplitude (DA) axial strain of 5% from cyclic undrained triaxial tests results on air pluviated Toyoura sand specimens with pre-straining to different peak axial strains (after Oda et al. 2001)

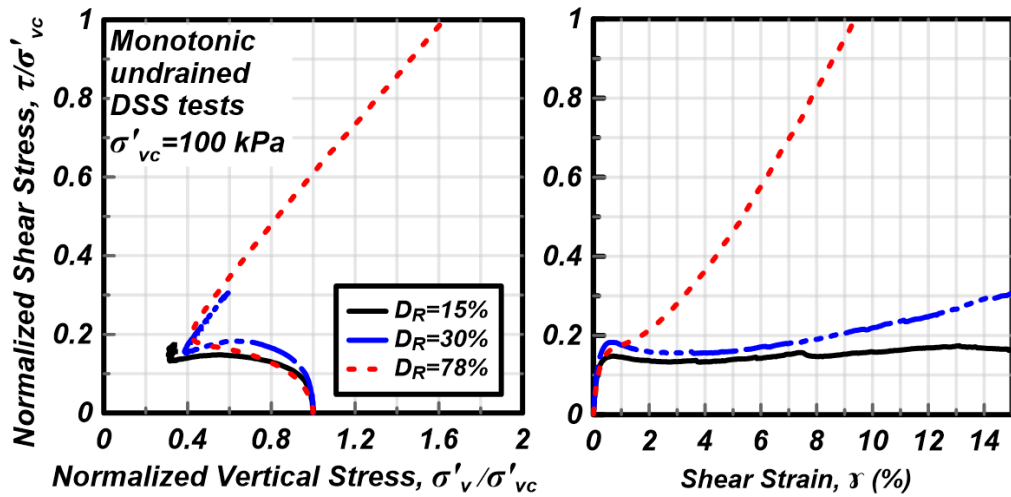


Figure 7.5 Monotonic responses for loose and dense virgin specimens of Ottawa F-65 sand

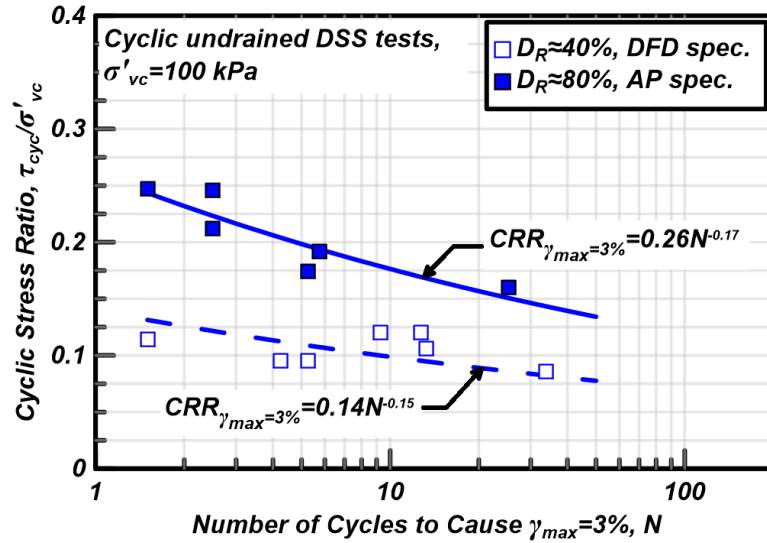


Figure 7.6 Cyclic resistance curves for loose and dense specimens of Ottawa F-65 sand

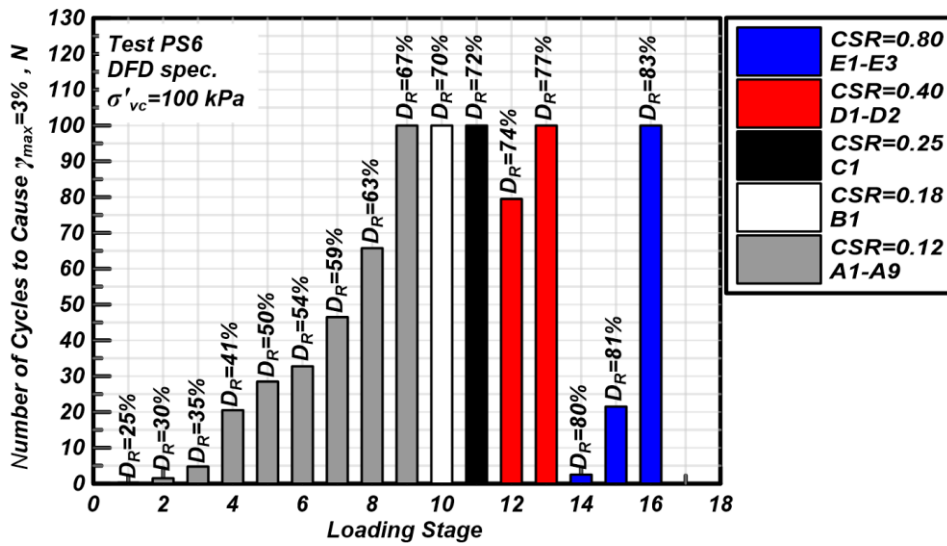


Figure 7.7 Number of cycles to peak 3% shear strain vs. loading stage on test PS6

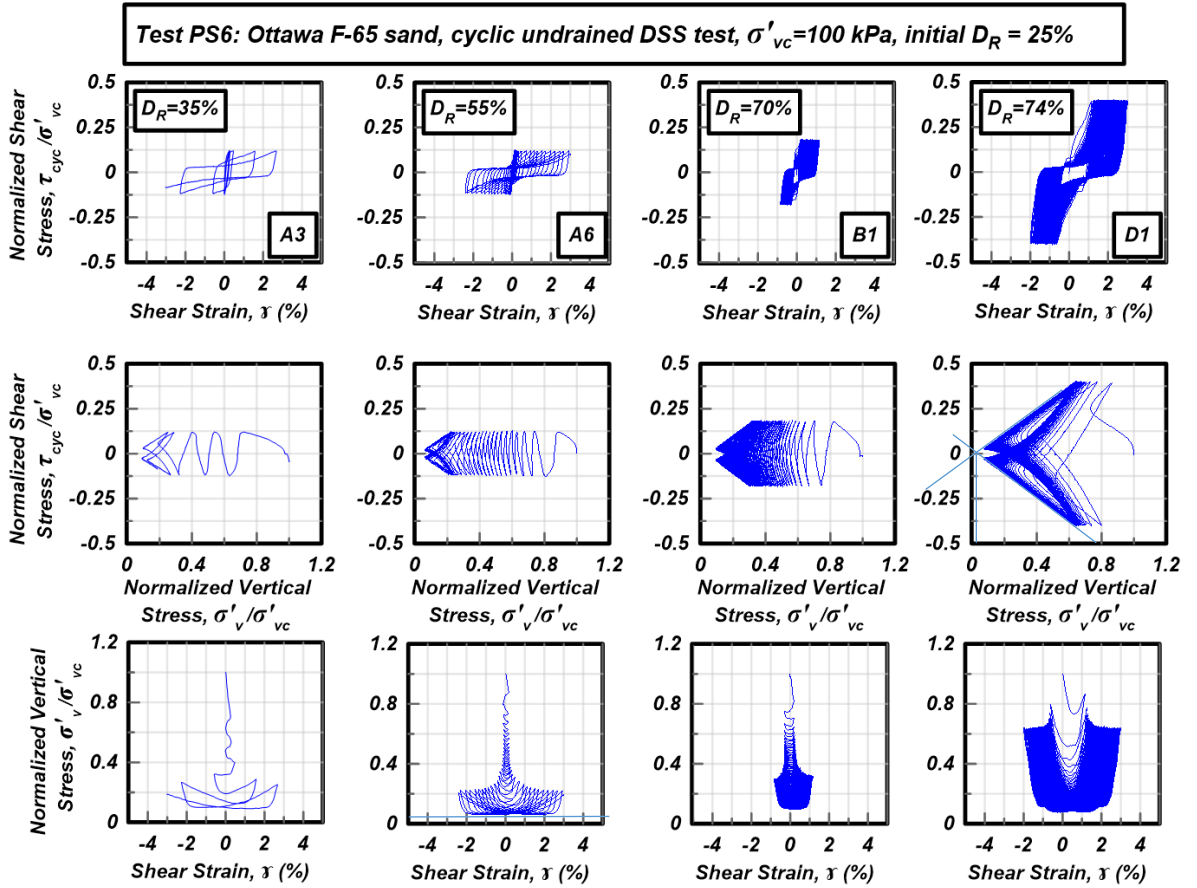


Figure 7.8 Undrained cyclic DSS test results from loading stages A3, A6, B1 and D1 for test PS6

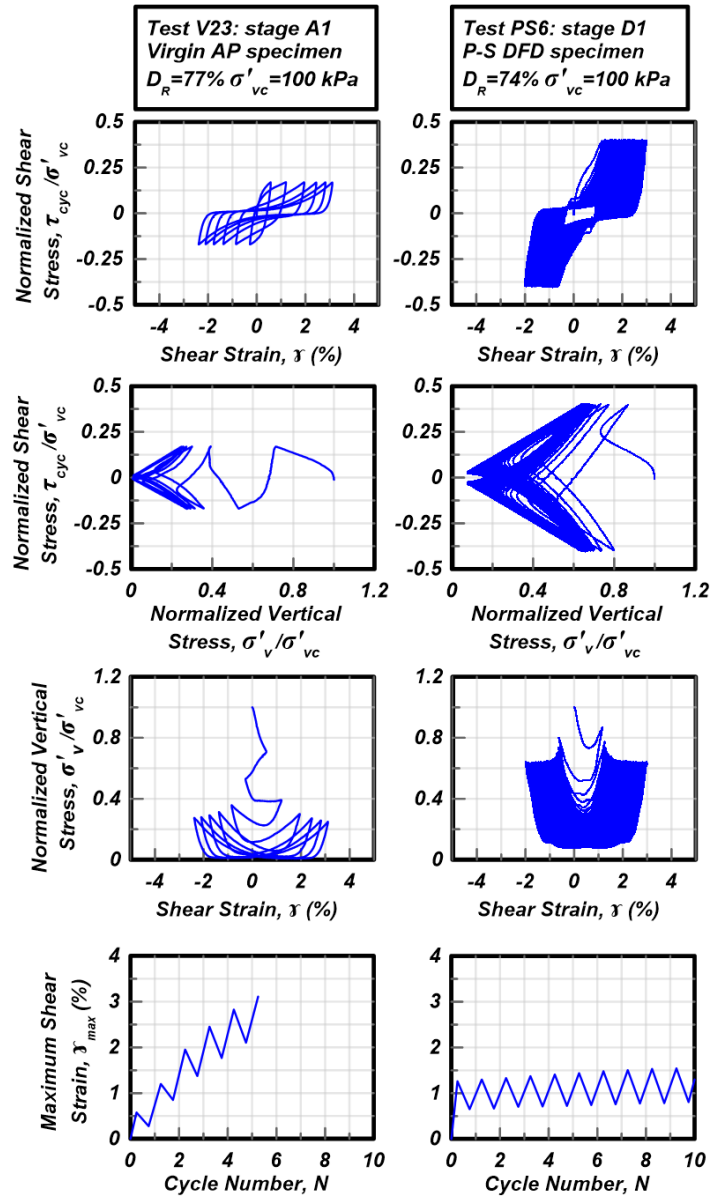


Figure 7.9 Undrained cyclic DSS test results on dense initially NC specimens: (a) virgin specimen from test V23, and (b) pre-strained specimen from test PS6 during loading stage D1

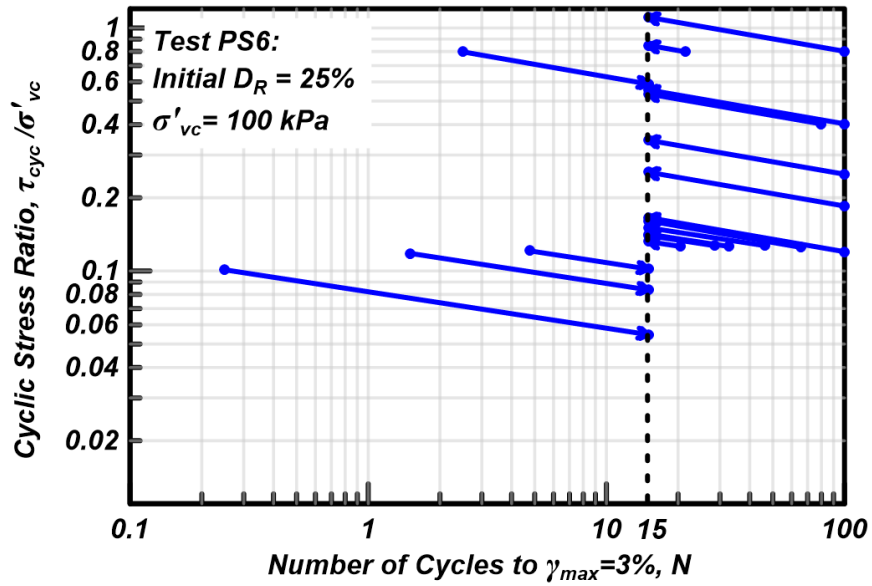


Figure 7.10 Conversion of applied CSR to CSR_{N=15} cycles for $\gamma_{max} = 3\%$ for each loading stage in test PS6

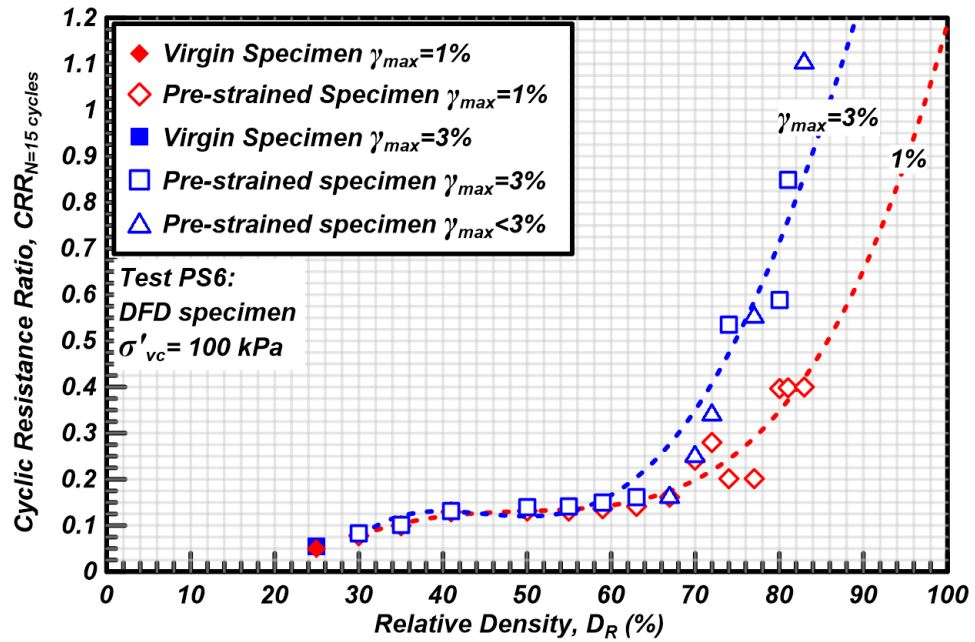


Figure 7.11 Evolution of the CRR_{N=15} for γ_{max} of 1% and 3% versus average void ratio for test PS6

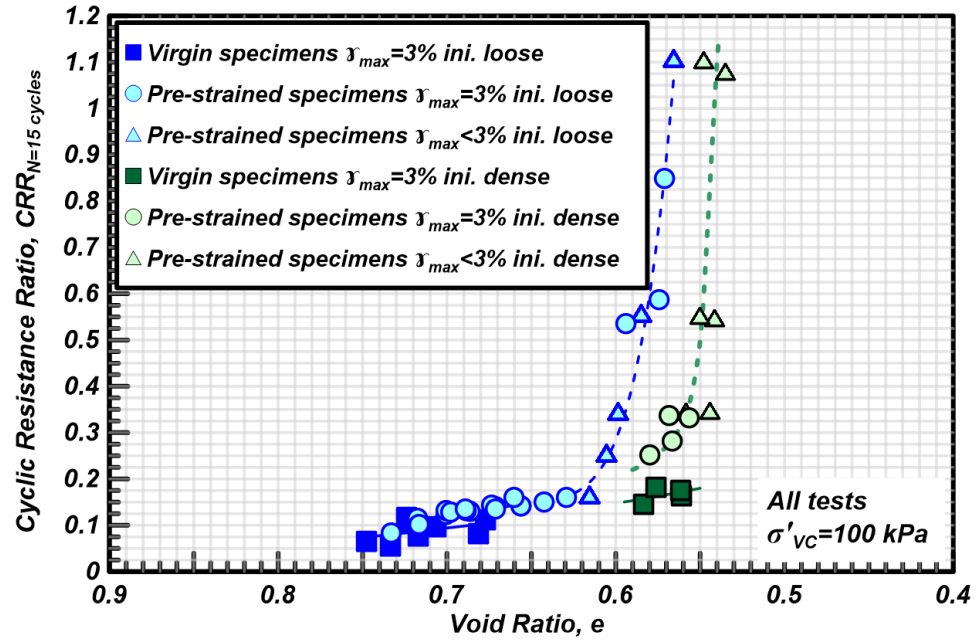


Figure 7.12 Evolution of the $CRR_{N=15}$ to $\gamma_{max} = 3\%$ versus average void ratio for virgin and pre-strain specimens

Chapter 8

Calibration of PM4Sand for Ottawa F-65 Sand

8.1 Introduction

A primary purpose for the experimental data presented in this thesis is the use for calibration of constitutive models being used to analyze centrifuge data. Constitutive models might not be able to recreate all the sand behaviors that are observed in centrifuge models. Thus, the selection of the constitutive model for centrifuge experiments data analysis should be done such that the chosen constitutive model is capable to recreate the behaviors of greatest interest to the modeler.

The calibration of the constitutive model usually requires compromises. Constitutive models have limitations and cannot reproduce all the characteristics of sand response observed in the laboratory or field. The user must decide what behaviors are most important for the problem in consideration in order to prioritize the behaviors to calibrate the constitutive model against. The Cyclic Resistance Ratio (CRR) against the number of cycles to trigger liquefaction and the shear-strain accumulation rate after liquefaction triggering are often key behaviors for liquefaction experiments and analyses. For such cases, the goal of an initial calibration might be to capture, as closely as possible, these two aspects as observed in the DSS laboratory experiments from Chapter 6 of this dissertation. Other behaviors of interest for calibration of constitutive models for analysis of centrifuge experiments include ([Ziotopoulou 2014](#)): dependence of CRR on vertical effective stresses, sand response to irregular cyclic loading histories, volumetric strains due to reconsolidation after the triggering of liquefaction, volumetric strains due to drained cyclic loading, strength loss caused by void redistribution, drained and undrained monotonic shear strengths, small strain shear modulus and shear modulus reduction and equivalent damping ratio relationships. For analyses of geotechnical structures in practice, many of these behaviors must be estimated using empirical correlations

to in-situ test and/or index test data. For analyses of centrifuge test data, these behaviors are best defined using laboratory element tests to reduce the uncertainty associated with use of empirical correlations for estimating properties.

The purpose of this chapter is to present two different calibrations of PM4Sand against the experimental data presented in Chapter 6. These calibrations will emphasize calibration against cyclic loading behaviors for relative densities of about 40 and 80% and confining stresses of 50 to 400 kPa, which envelopes the range of conditions for many of the centrifuge tests performed at UC Davis. At this range of stresses the sands will generally be dense of critical, which is the range of states at which cyclic mobility behavior is more significant to match the behaviors observed in centrifuge models. Calibration No.1 included varying the fewest set of parameters relative to the default calibration proposed by [Boulanger and Ziotopoulou \(2015\)](#). During this initial calibration h_{po} was changed to match the CRR to reach a peak shear strain of 3% at 15 of loading cycles from PM4Sand element tests with the CRR curves from cyclic DSS tests at a consolidation stress of 100 kPa. Simulations using this calibration are then compared to cyclic strengths, cyclic stress-strain responses, and monotonic stress-strain responses at other consolidation stresses. Calibration No. 2 included varying one additional secondary parameter (n_b which affects the dilatancy) and then recalibrating h_{po} to match the CRR at 15 loading cycles for each of the consolidation stresses (50, 100, and 400 kPa). Simulations using this calibration are then also compared to cyclic strengths, cyclic stress-strain, and monotonic stress-strain responses at the different consolidation stresses.

8.2 PM4sand constitutive model

The PM4Sand constitutive model is described by [Boulanger and Ziotopoulou \(2015\)](#). PM4Sand is a stress-ratio controlled, critical state compatible and bounding surface plasticity model for clean sand. The sand model was developed taking into account the sand bounding surface plasticity model developed by [Dafalias and Manzari \(2004\)](#). The last version of PM4Sand is version 3. This version of the model came from a modification from version 2 to improve “stress-strain responses important to geotechnical earthquake

engineering applications” (Boulanger and Ziotopoulou 2015). PM4Sand version 3 was calibrated at the equation level to: include dependence on fabric and fabric evolution with previous loading history by making the fabric formation/destruction to depend on the plastic volumetric strains, adding the fabric history and cumulative fabric formation terms and making the plastic modulus relationship to be dependent on fabric; increase control on the volumetric contractive over the expansive behavior; constrain the dilatancy during volumetric expansion to be consistent with Bolton’s (1986) dilatancy relationship; change the process to track initial back-stress ratios so it includes the effects of loading history; and include the effects of pre-strain history.

The model has six primary input parameters and eighteen secondary parameters. The six primary parameters include three soil properties, two flags and the atmospheric pressure. The three soil properties are the apparent relative density (D_R), the shear modulus coefficient (G_o) and the contraction rate parameter (h_{po}). The two flags are the FirstCall flag and the PostShake flag: the FirstCall flag is used to change the back stress ratio to its current stress ratio whereas the PostShake flag is used to reduce the elastic modulus at the end of the strong shaking to improve simulations of reconsolidation strains. The atmospheric pressure is specified to ensure consistent units, with the default being 101300 Pa. The eighteen secondary parameters include: coefficient to adjust the plastic modulus to the elastic modulus ratio (h_o), maximum void ratio (e_{max}), minimum void ratio (e_{min}), coefficient to control the dilatancy (n^b), coefficient that controls the stress ratio at where contraction transitions to dilation (n^d), coefficient based on Bolton’s dilatancy relationship (A_{do}), maximum value of the fabric tensor (Z_{max}), coefficient that controls the levels of strain at which the fabric effects become important (c_z), coefficient to adjust the strain rate accumulation during undrained cyclic loading (c_ε), constant volume effective friction angle (ϕ'_{CV}), Poisson’s ratio (ν_o), inverse of the maximum degradation of the small strain elastic shear modulus (C_{GD}), coefficient that controls the effect of static shear stress on plastic modulus (C_{ksf}), Q coefficient from Bolton’s relationship (1986) which indicates the normalized level of p' at what the critical state line starts to significantly bend due to significant particle crushing, R coefficient from Bolton’s relationship (1986), coefficient to define the diameter of the yield’s

surface cone in terms of stress ratio (m), the nominal plastic shear strength assigned when FirstCall flag is equal to zero (c_{hg}) and the nominal plastic shear strength ratio used to compute c_{hg} at the time when the FirstCall flag is equal to zero (cr_{hg}).

There are several parameters from the model that are well constrained by the data provided earlier in this thesis. Those parameters include: G_s , e_{max} , e_{min} and ϕ'_{CV} . Those parameters are discussed in sections 2.3, 2.4, 2.5 and 5.3 of this dissertation respectively. The G_o parameter presented in Figure 8.1 comes from algebraic manipulation of the G_{max} data/relationship from [Alarcon-Guzman et al. \(1989\)](#) shown in Figure 8.2. [Alarcon-Guzman et al. \(1989\)](#) performed triaxial compression tests combined with resonant column and torsional shear tests on air pluviated specimens of Ottawa 20-30 and Ottawa 50-70 sands, to study the effects of grain size distribution, initial stress ratio, and strain history on the shear modulus. They performed resonant column tests on saturated solid specimens with D_R between 18% and 95% to measure the specimen's maximum shear modulus at a shear strain of about 10^{-4} % (G_{max}). These data are shown in Figure 8.2. They found G_{max} to have little dependency on grain size distribution, fabric, initial stress ratio, monotonic and cyclic pre-straining. G_{max} from [Alarcon-Guzman et al. \(1989\)](#) has been compared with results from [Carraro et al. \(2009\)](#) in Figure 8.3, it can be observed little dependency of G_{max} on specimen preparation and grain size distribution. [Carraro et al. \(2009\)](#) conducted tests on slurry prepared specimens of Ottawa sand with $d_{60}=0.34$ mm, $d_{50}=0.31$ mm, $d_{10}=0.18$ mm, $e_{min}=0.495$, $e_{max}=0.767$, $C_u=1.89$ and $G_s=2.65-2.66$. [Carraro et al. \(2009\)](#) estimated G_{max} from triaxial compression tests with bender elements using the [Hardin and Richardt \(1963\)](#) relationship.

Other parameters were varied as part of developing two different calibrations. Calibration No.1 included varying the fewest set of parameters relative to the default calibration proposed by [Boulanger and Ziotopoulou \(2015\)](#). During this initial calibration h_{po} was changed to match the CRR to reach a peak shear strain of 3% at 15 uniform loading cycles from PM4Sand element tests with the CRR curves constructed with the cyclic DSS results at a consolidation stress of 100 kPa. Calibration No. 2 included varying one

additional secondary parameter (n_b) and then recalibrating h_{po} to match the CRR at 15 loading cycles for each of the consolidation stresses (50, 100, and 400 kPa).

8.3 Small strain modulus, Critical State Line and other fixed parameters

The G_o parameter for small strain shear modulus was based on the relationship presented in Figure 8.1 which comes from algebraic manipulation of the G_{max} relationship from [Alarcon-Guzman et al. \(1989\)](#) shown previously in Figure 8.2. This relationship was used for both calibrations.

The position of the critical state line was examined using monotonic undrained DSS test as described in Chapter 5. The position of the Critical State Line (CSL) appeared reasonably bounded using [Bolton's \(1986\)](#) relationship with two possible set of parameters as shown in Figure 8.4. The use of $Q=10$ and $R=1$ provides an estimate of the highest position of the CSL and the use of $Q=10$ and $R=1.5$ provides an estimate of the lowest position of the CSL. The calibrations presented later were based on $Q=10$ and $R=1.5$.

Other parameters common to both calibrations are as follows. ϕ'_{CV} is 30 degrees as presented in Chapter 5. G_s , e_{max} and e_{min} are 2.65, 0.83 and 0.51 respectively as presented in Chapter 2. There are several other parameters that have default values as presented in [Boulanger and Ziotopoulou \(2015\)](#) which will remained unchanged. These include the following: h_o , n^d , A_{do} , Z_{max} , c_z , c_ϵ , v_o , C_{GD} , C_{kaf} , m , c_{hg} and cr_{hg} .

8.4 Calibration No. 1

The first calibration used the parameter h_{po} to calibrate the model against the cyclic strength curve at a consolidation stress of 100 kPa, and to examine the model's ability to reproduce the other observed cyclic strength curves, cyclic stress-strain, and monotonic stress-strain responses at other consolidation stresses (50, 100 and 400 kPa).

The cyclic loading behavior for loose sands was best approximated by using an h_{po} of 0.32 to get a CRR at 15 cycles to reach 3% shear strain of 0.093 at a consolidation stress of 100 kPa. The simulated cyclic strength curves are compared to the data in Figure 8.5, Figure 8.6 and Figure 8.7 for tests with overburden stresses of 50, 100 and 400 kPa respectively. The simulations produce CRR curves that are steeper than the CRR from cyclic DSS tests. This effect is reduced with increasing confinement. The cyclic strength at 15 cycles for 50 kPa is overestimated by 26% and the cyclic strength at 15 cycles for 400 kPa is underestimated by 5%. These differences are attributed to the PM4Sand model having been formulated to produce a greater dependence of CRR on consolidation stress (i.e., K_σ behavior) than is observed in the experimental data.

The simulated and measured cyclic stress-strain responses are shown in Figure 8.8, Figure 8.9 and Figure 8.10 for loose sand specimens at overburden stresses of 50, 100 and 400 kPa. The experimental responses accumulate a higher r_u than the simulated response during the first two loading cycles and then accumulate r_u slower than the simulated responses after the first two loading cycles. The simulated responses accumulate cyclic strains more slowly than the experimental responses during the first loading cycles when r_u is small. The simulated responses accumulate higher cyclic strains per loading cycle than the experimental responses after an r_u of 100 % has been reached.

The simulated and measured monotonic stress-strain responses are shown in Figure 8.11, Figure 8.12, Figure 8.13 for loose sand specimens at overburden stresses of 100, 400 and 800 kPa. The simulated response for the loose specimen consolidated to 100 kPa shows very quick strain hardening compared with the experimental response. The closest simulated response for the loose specimens is the response from the specimen consolidated to 400 kPa. The simulated response for the loose specimen consolidated to 800 kPa shows much slower strain hardening, which is consistent with the experiments.

The cyclic loading behavior for dense sands was best approximated by using an h_{po} of 0.007 to get a CRR at 15 cycles to reach 3% shear strain of 0.164 at a consolidation stress of 100 kPa. The simulated cyclic strength curves are compared to the data in Figure 8.14, Figure 8.15 and Figure 8.16 for tests with

overburden stresses of 50, 100 and 400 kPa respectively. The simulations produce CRR curves that are steeper than the CRR from experimental results. This effect is reduced with increasing confinement. The cyclic strength at 15 cycles for 50 kPa is overestimated by 41% and the cyclic strength at 15 cycles for 400 kPa is underestimated by 8%. These differences are attributed to the PM4Sand model having been formulated to produce a greater dependence of CRR on consolidation stress (i.e., K_σ behavior) than is observed in the experimental data, even more so at this high relative density compared to the tests at about 40% relative density.

The simulated and measured cyclic stress-strain responses are shown in Figure 8.17, Figure 8.18 and Figure 8.19 for dense sand specimens at overburden stresses of 50, 100 and 400 kPa. The experimental responses accumulate a higher r_u than the simulated responses during the first loading cycle and then accumulate r_u slower than the simulated responses after the first loading cycle. The experimental responses accumulate more shear strain per loading cycle than the simulated responses of the specimens consolidated to 50 and a 100 kPa. The experimental response accumulates more shear strains per loading cycle during the first loading cycles than the simulated response of the specimen consolidated to 400 kPa; then, the experimental response accumulates less shear strain per loading cycle than the simulated response.

The simulated and measured monotonic stress-strain responses are shown in Figure 8.20, Figure 8.21 and Figure 8.22 for dense sand specimens at overburden stresses of 100, 400 and 800 kPa stresses. The simulated response for the dense specimens consolidated to 100 kPa shows very quick strain hardening compared with the experimental responses. The closest simulated response for the dense specimens is the response for the specimen consolidated to 400 kPa.

Overall, the first calibration produced simulations that roughly approximated some aspects of the measured behaviors but had significant differences for other aspects. Specifically, the simulations roughly approximated the pore pressure generation and cyclic mobility behavior observed for both the loose and dense specimens, but with the cyclic strength curves (CRR versus N cycles) being steeper and more

dependent on confining stress than was observed. The simulated monotonic undrained loading responses also generally exhibited an overly rapid strain hardening response relative to the measured responses.

8.5 Calibration No. 2

The second calibration used a reduced value for the secondary parameter n_b to improve the responses controlled by dilatancy, after which the value for h_{po} was recalibrated against the cyclic strength curve at each of the consolidation stresses of 50, 100 and 400 kPa. The value of n_b was reduced to 0.25 (default value was 0.50), which reduced the dilatancy by about a factor of 2 for a given relative state parameter. A lower dilatancy was needed to better approximate some of the observed cyclic strength curves and reduce the rate of strain hardening in undrained monotonic loading. The calibrated model was then evaluated for its ability to reproduce the observed cyclic strength curves, cyclic stress-strain, and monotonic stress-strain responses at other consolidation stresses (50, 100 and 400 kPa).

The cyclic loading behavior for loose sand specimens was best approximated by using an h_{po} of 0.145, 0.32, and 0.37 to get a CRR at 15 cycles to reach 3% shear strain of 0.085, 0.093, and 0.094 at consolidation stresses of 50, 100, and 400 kPa, respectively. The simulated cyclic strength curves are compared to the data on Figure 8.23, Figure 8.24 and Figure 8.25 for tests with overburden stresses of 50, 100 and 400 kPa respectively. The simulated responses from Calibration No. 2 are closer to the experimental responses when compared with the simulated responses from Calibration No. 1. The simulations produce CRR curves that are steeper than the CRR from experimental results, but less so than for calibration 1. This effect is reduced with increasing confinement. The steeper CRR curves are again attributed to the PM4Sand model having been formulated to produce a greater dependence of CRR on consolidation stress (i.e., K_σ behavior) than is observed in the experimental data.

The simulated and measured cyclic stress-strain responses are shown in Figure 8.26, Figure 8.27 and Figure 8.28 for loose sand specimens at overburden stresses of 50, 100 and 400 kPa. The simulated responses from Calibration No. 2 are closer to the experimental responses when compared with the

simulated responses from Calibration No. 1. The experimental responses accumulate a higher r_u than the simulated responses during the first loading cycle and accumulate r_u slower than the simulated responses after the first loading cycle. The experimental responses accumulate cyclic strains at a similar rate as the simulated responses before a shear strain of 1% has been reached, with the exception of the results from the specimen consolidated to 400 kPa on which the experimental response accumulate shear strains quicker than the simulated response. The simulated responses accumulate shear strains at roughly similar rates as the experimental responses after an r_u of 100 % has been reached.

The simulated and measured monotonic stress-strain responses are shown in Figure 8.29, Figure 8.30 and Figure 8.31 for loose sand specimens at overburden stresses of 100, 400 and 800 kPa. The simulated responses from Calibration No. 2 are closer to the experimental responses when compared with the simulated responses from Calibration No. 1. The simulated response for the loose specimen consolidated to 100 kPa shows very quick strain hardening compared with the experimental response. The closest simulated response for the loose specimens is the response from the specimen consolidated to 400 kPa. The simulated response for the loose specimen consolidated to 800 kPa shows a slower strain hardening compared with the experimental response.

The cyclic loading behavior for dense sand specimens was best approximated by using an h_{po} of 0.037, 0.016, and 0.020 to get a CRR at 15 cycles to reach 3% shear strain of 0.177, 0.165, and 0.152 at consolidation stresses of 50, 100, and 400 kPa, respectively. The simulated cyclic strength curves are compared to the data on Figure 8.32, Figure 8.33 and Figure 8.34 for tests with overburden stresses of 50, 100 and 400 kPa respectively. The simulations produce CRR curves that are steeper than the CRR from experimental results, but less so than for Calibration 1. This effect is reduced with increasing confinement. Again, this is because the PM4Sand model is formulated to produce a greater dependence of CRR on consolidation stress (i.e., K_σ behavior) than is observed in the experimental data.

The simulated and measured cyclic stress-strain responses are shown in Figure 8.35, Figure 8.36 and Figure 8.37 for dense sand at overburden stresses of 50, 100 and 400 kPa. The simulated responses

from Calibration No. 2 generate pore pressures more slowly than the experimental responses, but then accumulate shear strains more rapidly than the experimental responses once a high r_u level has been reached. This calibration, with a reduced parameter n^b , resulted in the faster strain rate accumulation after a high r_u level was reached, and this required a reduction in the rate of pore pressure generation (via calibration of h_{po}) to get the correct target CRR value.

The simulated and measured monotonic stress-strain responses are shown in Figure 8.38, Figure 8.39 and Figure 8.40 for dense sand specimens at overburden stresses of 100, 400 and 800 kPa. The simulated responses from Calibration No. 2 are closer to the experimental responses when compared with the simulated responses from Calibration No. 1. The simulated response for the dense specimen consolidated to 100 kPa and 400 kPa shows quicker strain hardening compared with the experimental response. The closest simulated response of the dense specimens is the response of the specimen consolidated to 800 kPa.

Overall, the second calibration produced improved approximations of some aspects of the measured behaviors but also poorer approximations for some other aspects. Specifically, the reduced dilation rates (via the reduced n^b parameter) improved the monotonic undrained loading responses and slightly reduced the slopes of the cyclic strength curves, but it resulted in simulated cyclic responses for the dense specimens that accumulated shear strains too rapidly after a high r_u was reached.

8.6 Summary remarks

Two calibrations for the constitutive model PM4Sand were presented. Calibration No. 1 retained all default parameters with the exception of the h_{po} parameter, which was used to calibrate the model to a specific CRR value at one overburden stress. Calibration No. 2 retained all default parameters with the exception of the n_b and the h_{po} parameters; the n_b parameter was reduced to half its default value to reduce the dilatancy by about a factor of 2 for a given relative state parameter. The h_{po} parameter was used to calibrate the model to a specific CRR value at each overburden stress.

The PM4Sand model with Calibration No. 1 was able to simulate the general features of cyclic mobility behavior but had significant differences for certain aspects of the monotonic and cyclic loading behaviors. The PM4Sand model fit the CRR to $\gamma=3\%$ curves for loose sand specimens better than the curves for dense sand specimens. However, the PM4Sand model over-predicted the steepness of the CRR curves, the dependence of the CRR on overburden stress, and the rate of strain hardening in monotonic undrained loading.

The PM4Sand model with Calibration No. 2 produced improved approximations of some aspects of the measured behaviors relative to Calibration No. 1, but also poorer approximations for some other aspects. The simulations with Calibration No. 2 produced CRR to $\gamma=3\%$ curves that were closer to the curves from the experimental results, with the agreement being better for loose sand specimens than for dense sand specimens. However, the PM4Sand model still over-predicted the steepness of the CRR curves and the rate of strain hardening in most undrained monotonic loading tests. In addition, the cyclic stress-strain response of the model for the dense sand specimens produced an overly rapid accumulation of shear strains after a high r_u was reached.

This comparison of simulated and measured responses for Ottawa sand illustrate some of the capabilities and limitations on the PM4Sand constitutive model. PM4Sand produces cyclic strength curves whose slopes are consistent with typical CRR curves for silica sands in the literature, but may not match the slopes for specific sands. PM4Sand recreates the dependence of the CRR on vertical effective stresses (K_σ) and horizontal static shear stresses (K_α) that are consistent with the [Idriss and Boulanger \(2008\)](#) and [Boulanger \(2003\)](#) relationships, respectively, but again these may not match with a specific sand. PM4Sand simulates the general characteristics of shear strain accumulation during cyclic undrained DSS loading and monotonic undrained DSS loading for typical sands. In applying PM4Sand specifically to Ottawa sand, it was observed that it: produced steeper-than-observed CRR curves particularly for small numbers of loading cycles and denser specimens, produced greater-than-observed rates of shear strain accumulation after high r_u values were reached in denser specimens, and tended to produce greater-than-observed rates of strain

hardening in undrained monotonic loading. The significance of these differences for simulating the response of geotechnical systems in centrifuge model tests are likely to depend on the specific conditions (e.g., soil densities, layer and slope geometries, input motions, structural configurations). In addition, the impact of uncertainty in the model calibrations (e.g., CRR values or calibration parameter sets) may be evaluated by sensitivity studies for the system level responses.

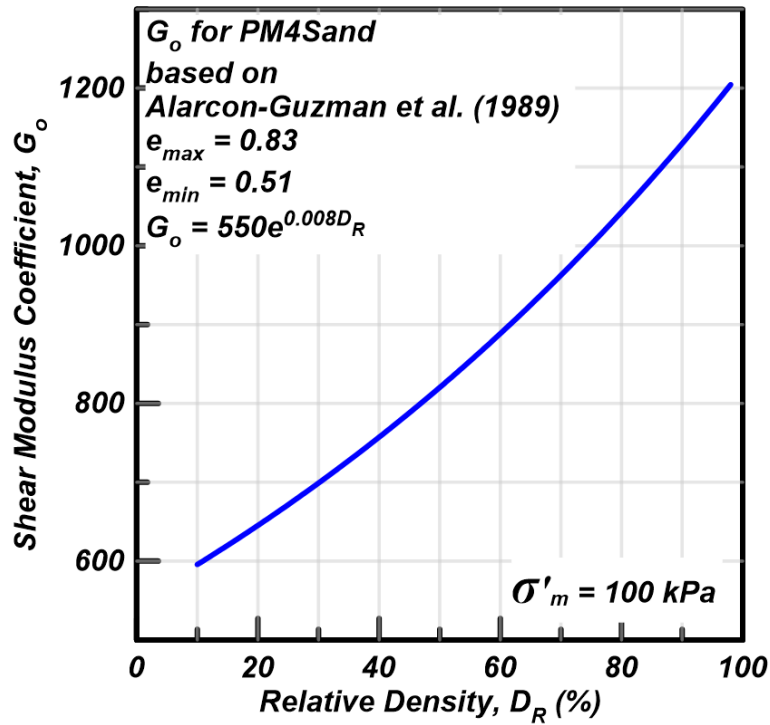


Figure 8.1 G_o vs. D_R for PM4Sand

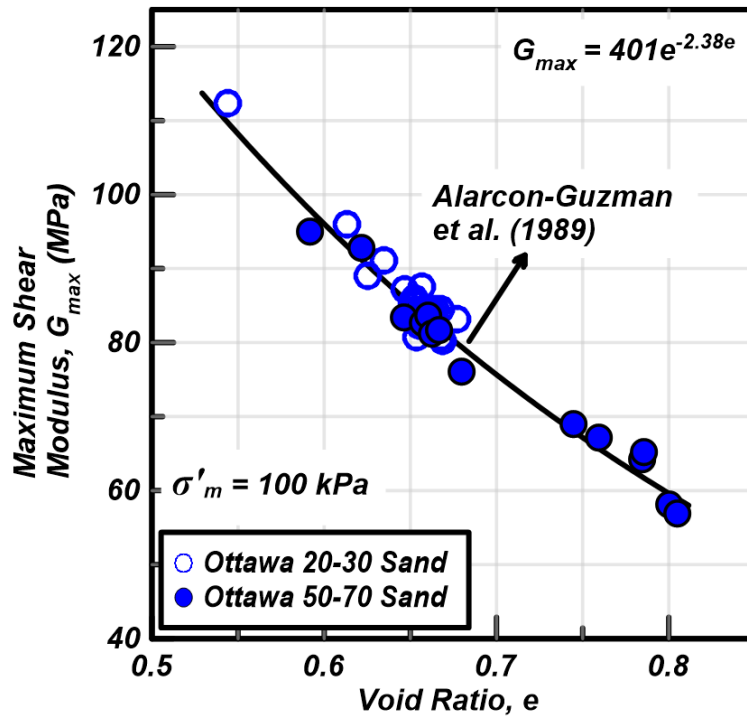


Figure 8.2 G_{max} vs. e from air pluviated specimens

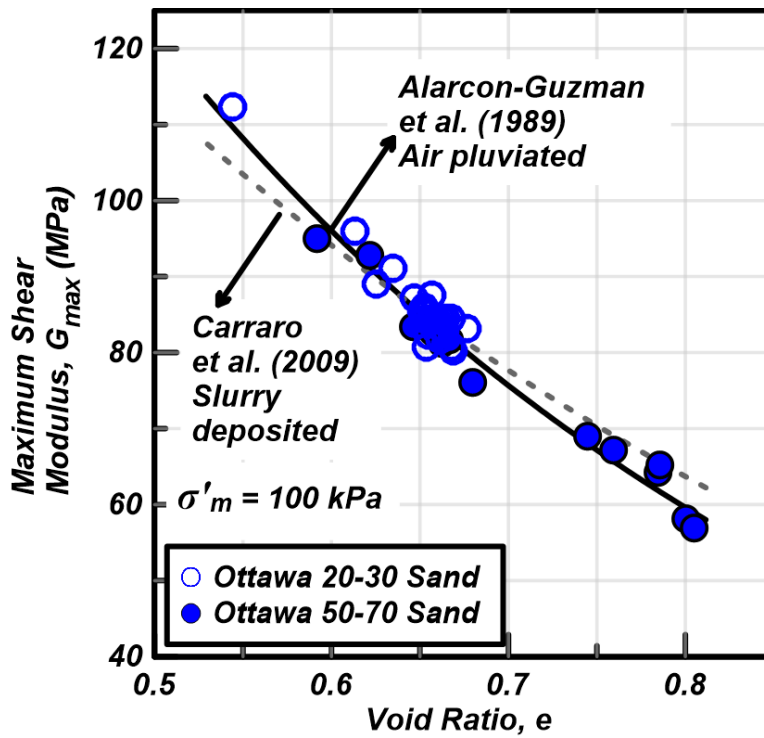


Figure 8.3 G_{max} vs. e

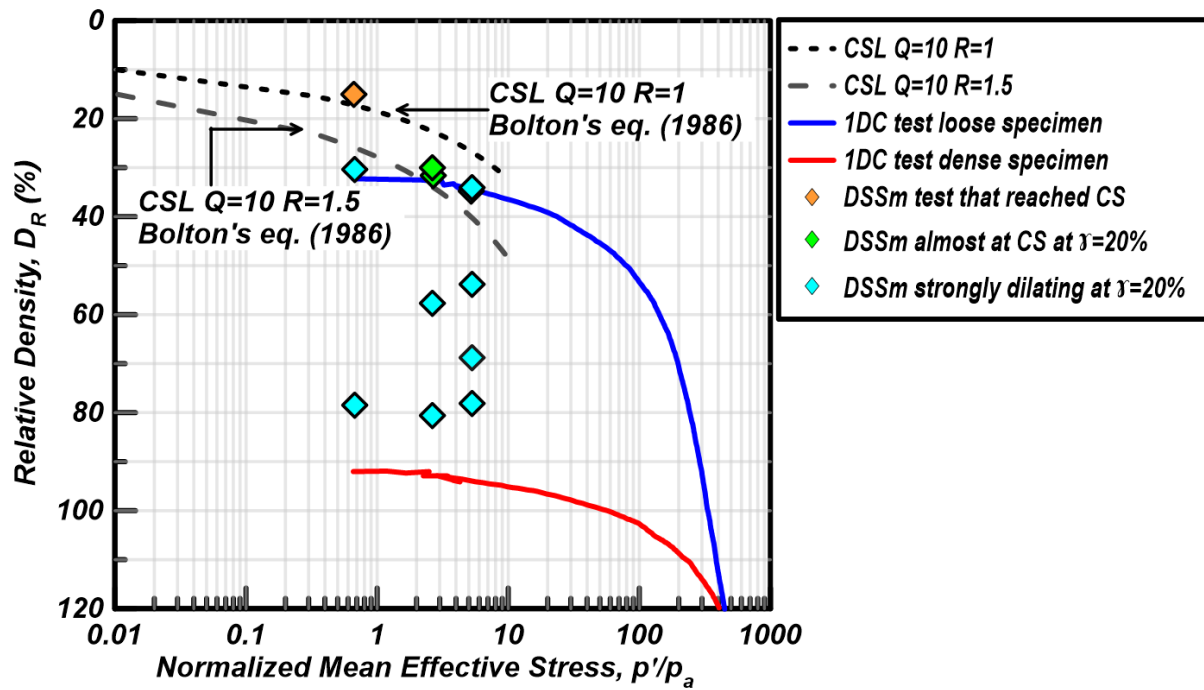


Figure 8.4 Critical state line position bounds and initial points from monotonic DSS tests

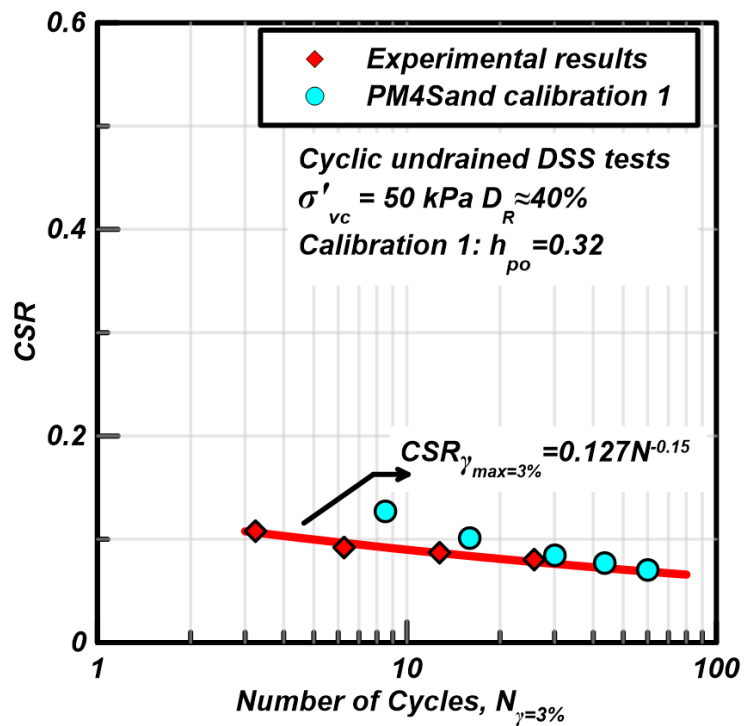


Figure 8.5 CRR curves from DSS tests and PM4Sand simulations for loose specimens consolidated to 50 kPa

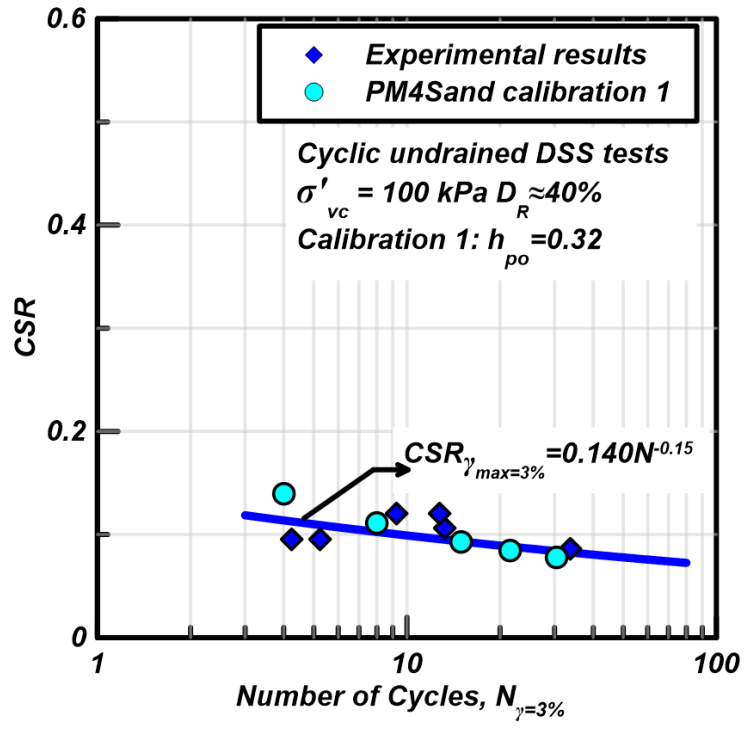


Figure 8.6 CRR curves from DSS tests and PM4Sand simulations for loose specimens consolidated to 100 kPa

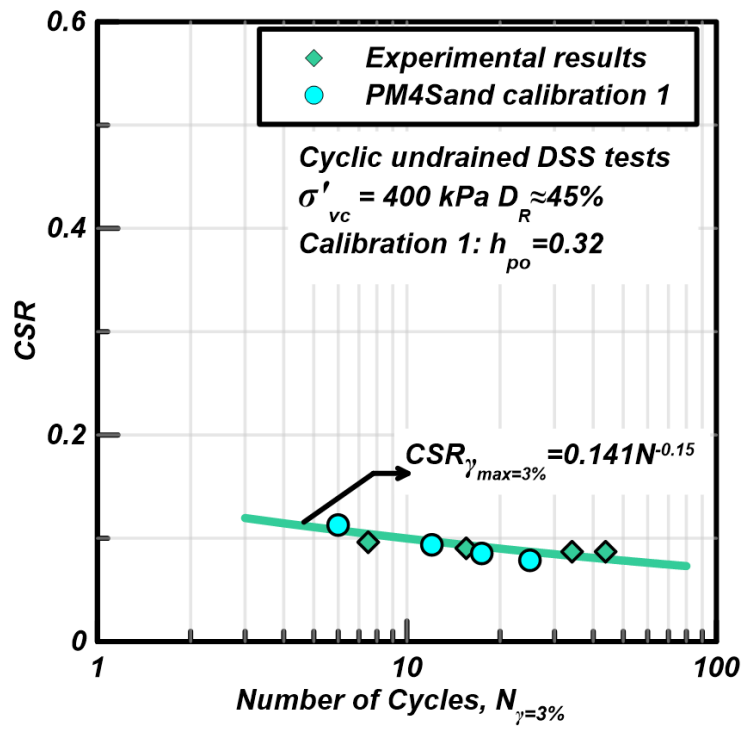


Figure 8.7 CRR curves from DSS tests and PM4Sand simulations for loose specimens consolidated to 400 kPa

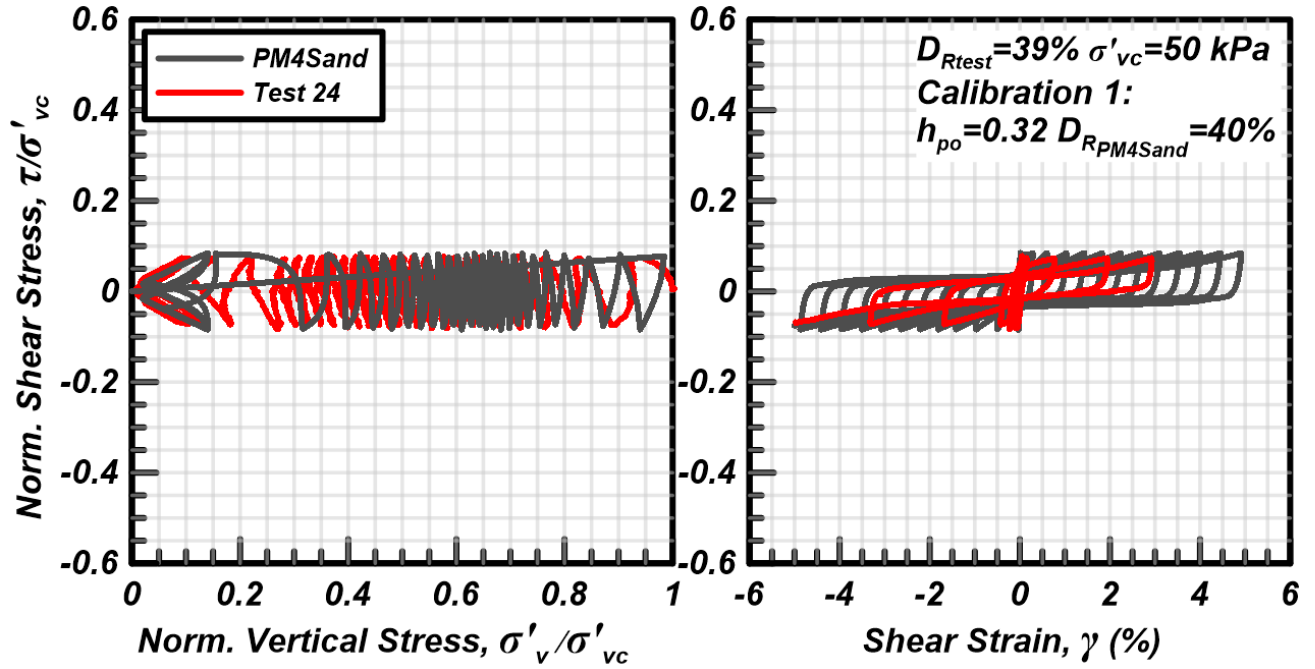


Figure 8.8 Stress-strain responses from cyclic DSS tests and PM4Sand calibration No. 1 simulations on a loose specimen consolidated to 50 kPa

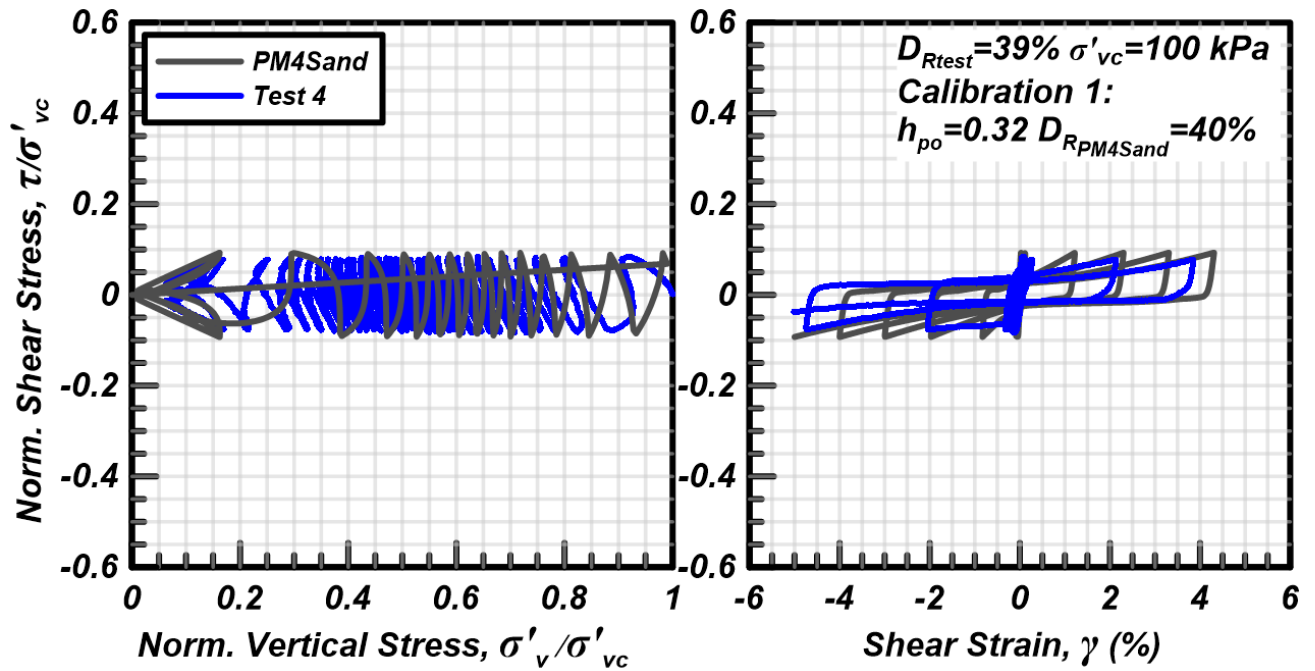


Figure 8.9 Stress-strain responses from cyclic DSS tests and PM4Sand calibration No. 1 simulations on a loose specimen consolidated to 100 kPa

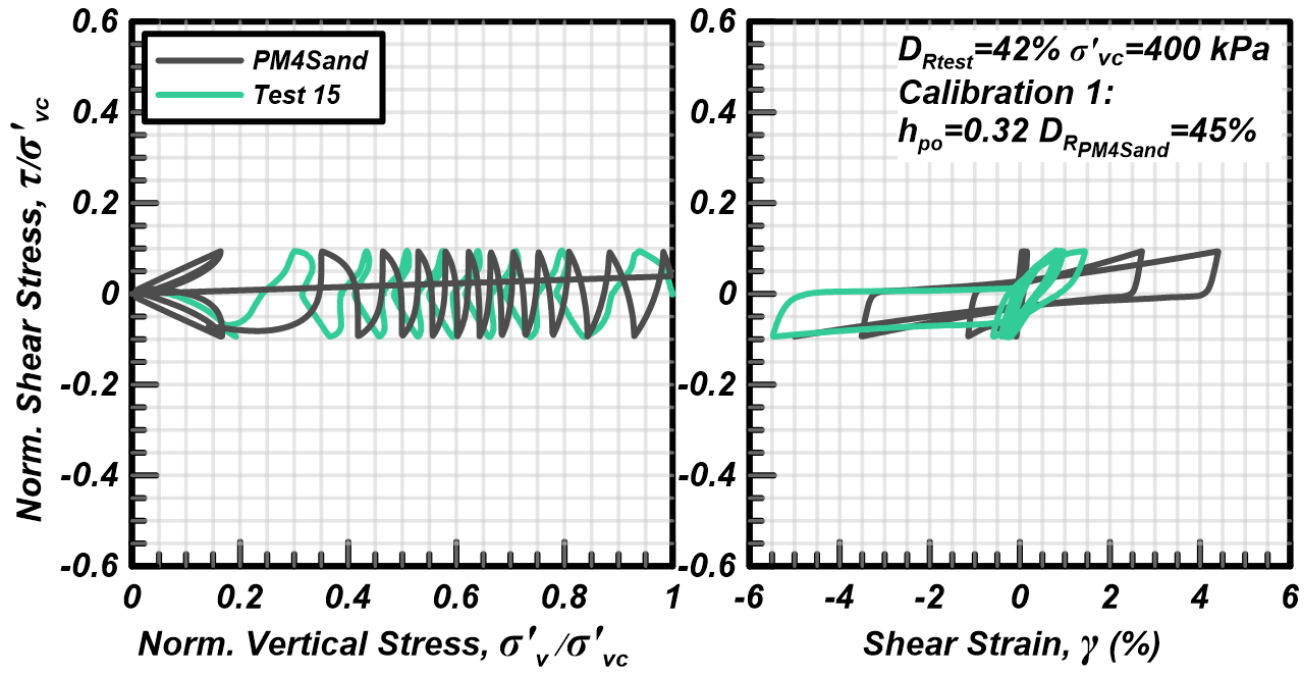


Figure 8.10 Stress-strain responses from cyclic DSS tests and PM4Sand calibration No. 1 simulations on a loose specimen consolidated to 400 kPa

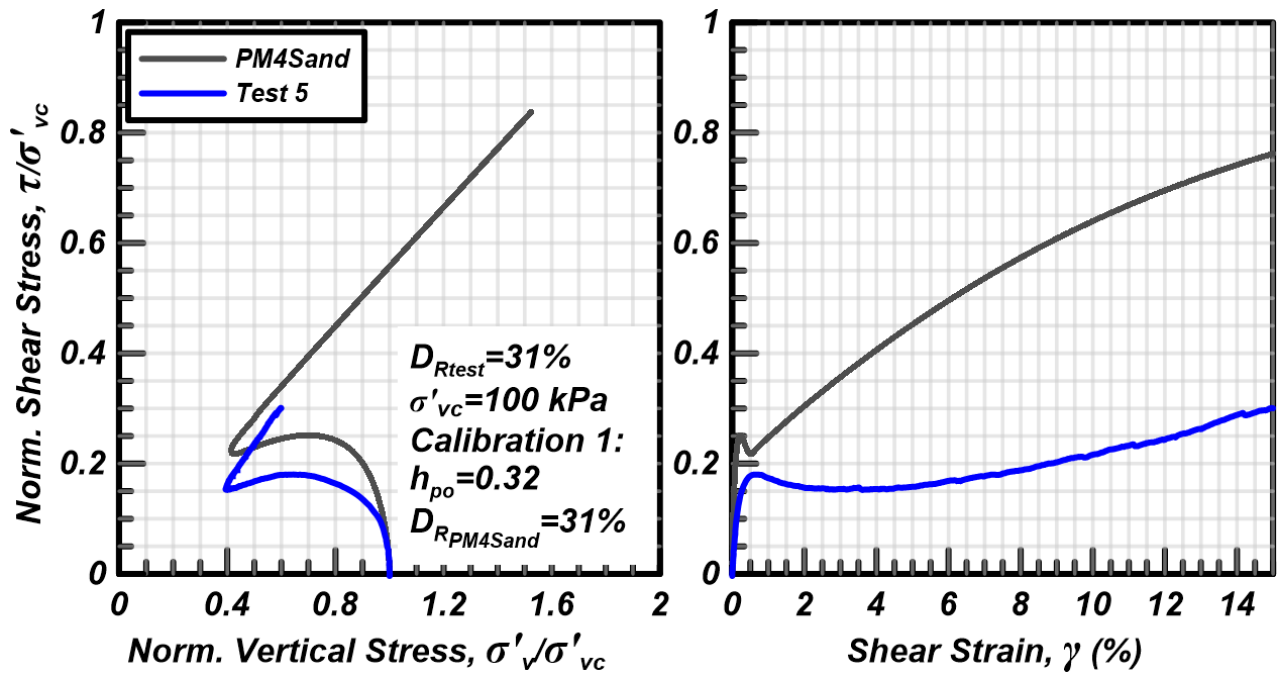


Figure 8.11 Stress-strain responses from monotonic DSS tests and PM4Sand calibration No. 1 simulations on a loose specimen consolidated to 100 kPa

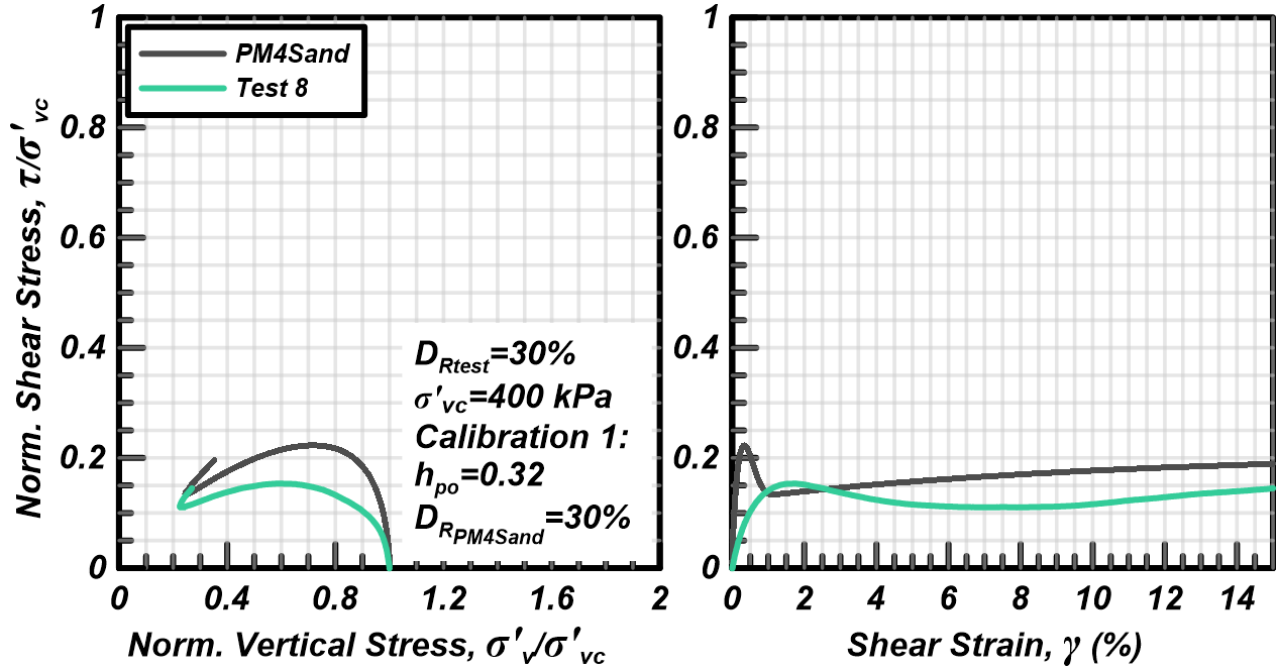


Figure 8.12 Stress-strain responses from monotonic DSS tests and PM4Sand calibration No. 1 simulations on a loose specimen consolidated to 400 kPa

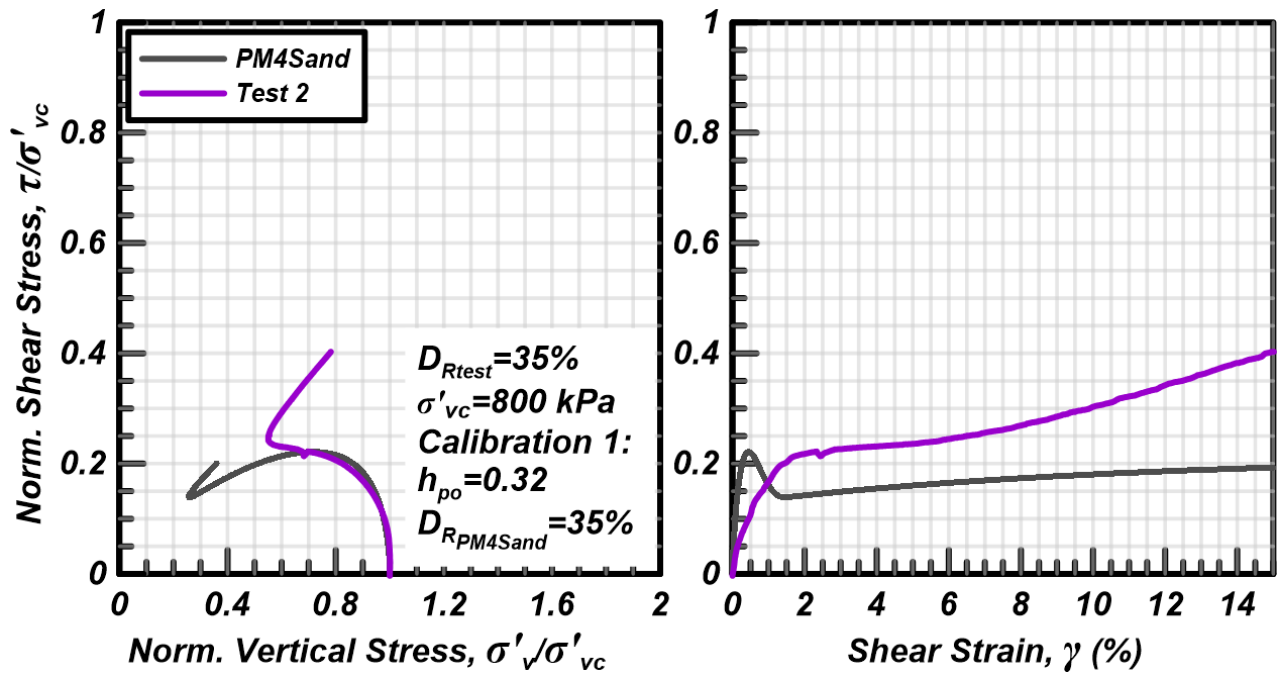


Figure 8.13 Stress-strain responses from monotonic DSS tests and PM4Sand calibration No. 1 simulations on a loose specimen consolidated to 800 kPa

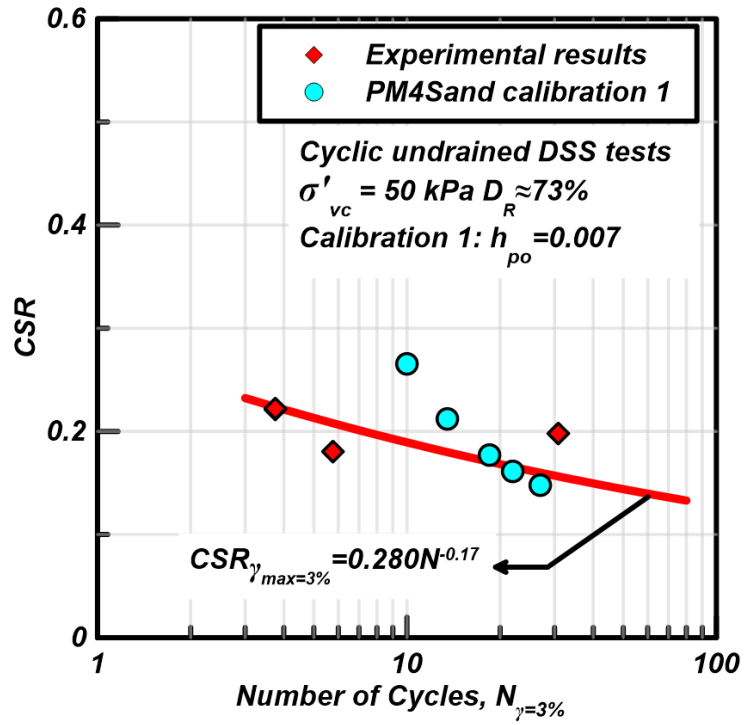


Figure 8.14 CRR curves from DSS tests and PM4Sand calibration No. 1 simulations for dense specimens consolidated to 50 kPa

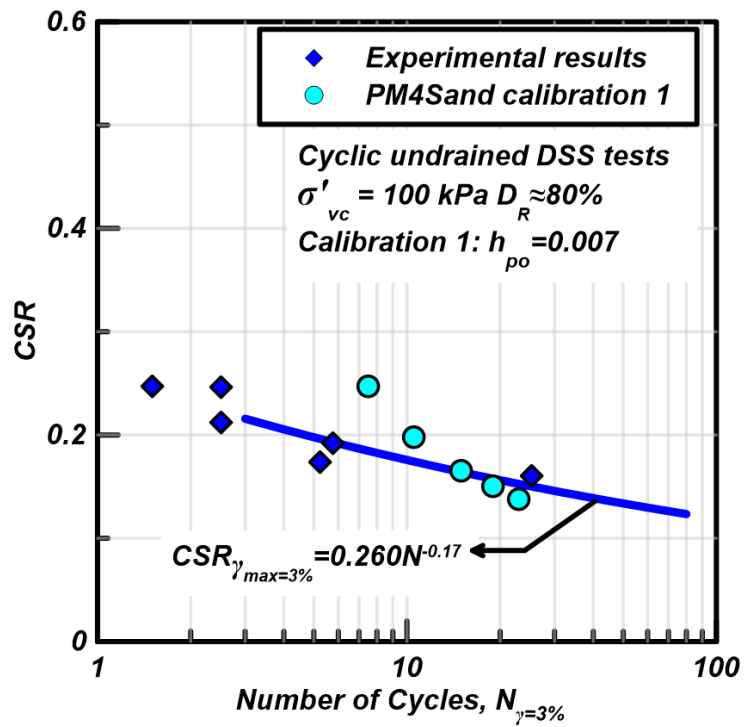


Figure 8.15 CRR curves from DSS tests and PM4Sand calibration No. 1 simulations for dense specimens consolidated to 100 kPa

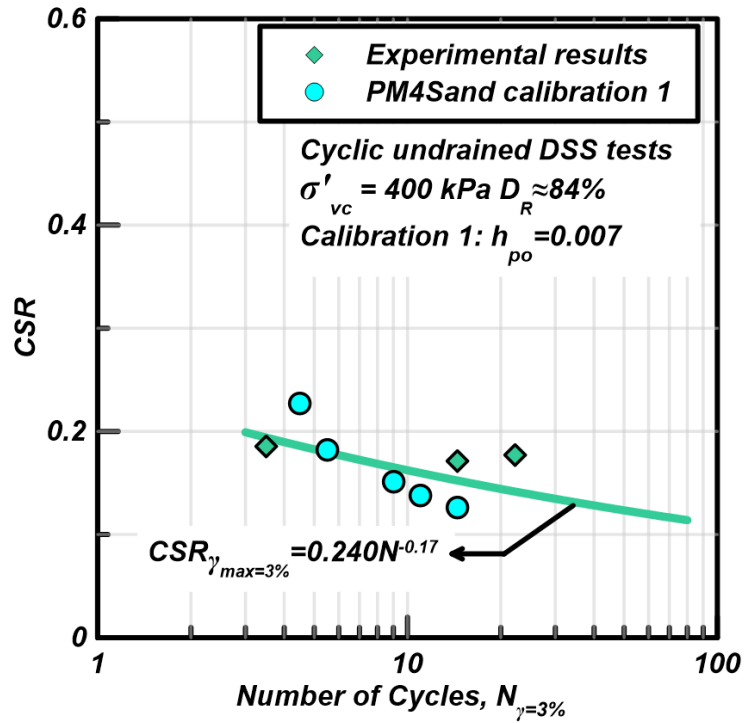


Figure 8.16 CRR curves from DSS tests and PM4Sand calibration No. 1 simulations for dense specimens consolidated to 400 kPa

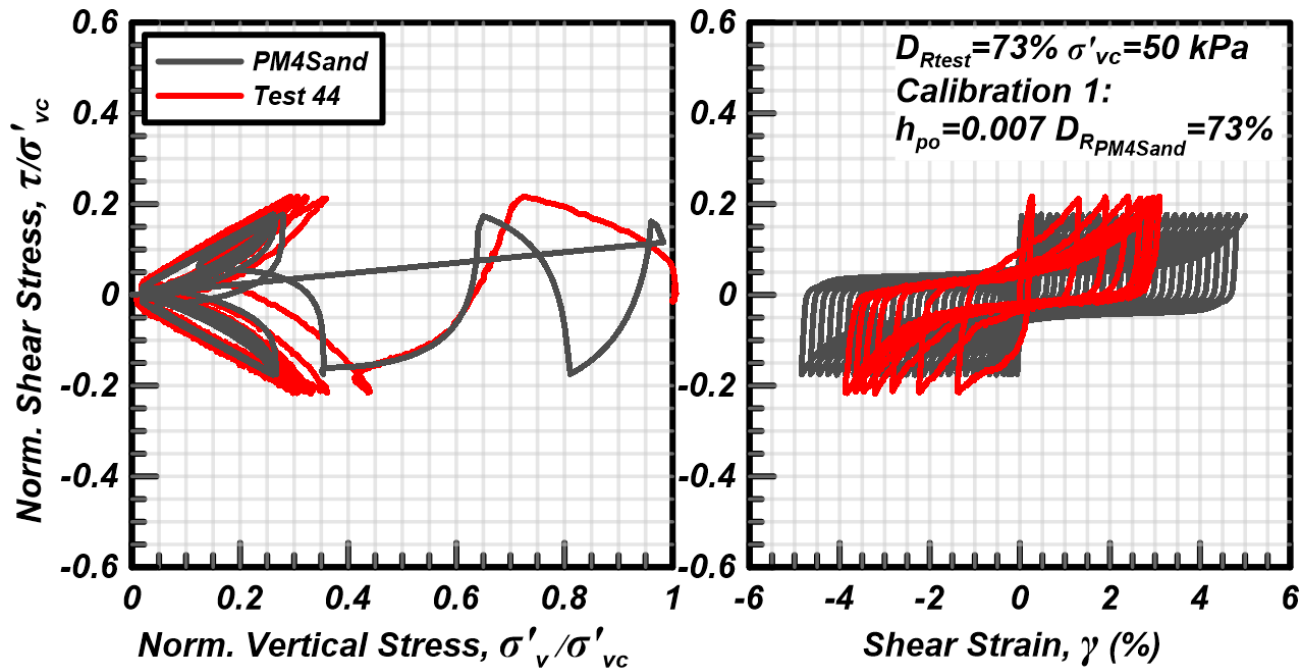


Figure 8.17 Stress-strain responses from cyclic DSS tests and PM4Sand calibration No. 1 simulations on a dense specimen consolidated to 50 kPa

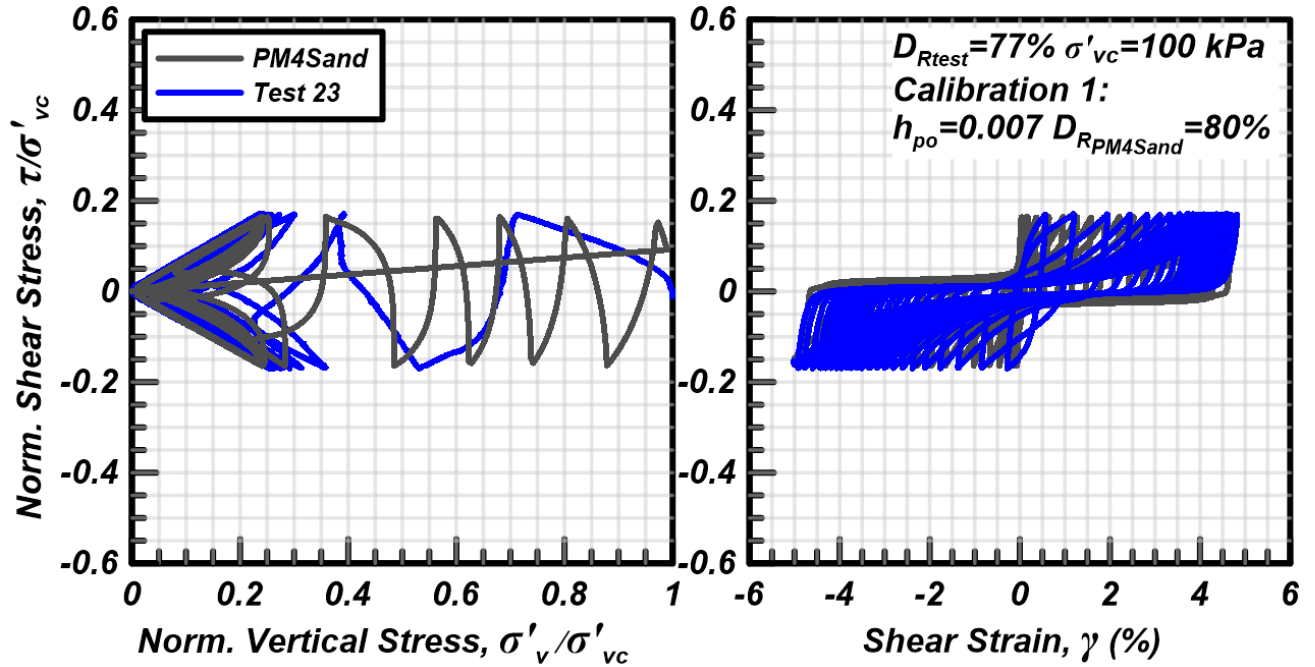


Figure 8.18 Stress-strain responses from cyclic DSS tests and PM4Sand calibration No. 1 simulations on a loose specimen consolidated to 100 kPa

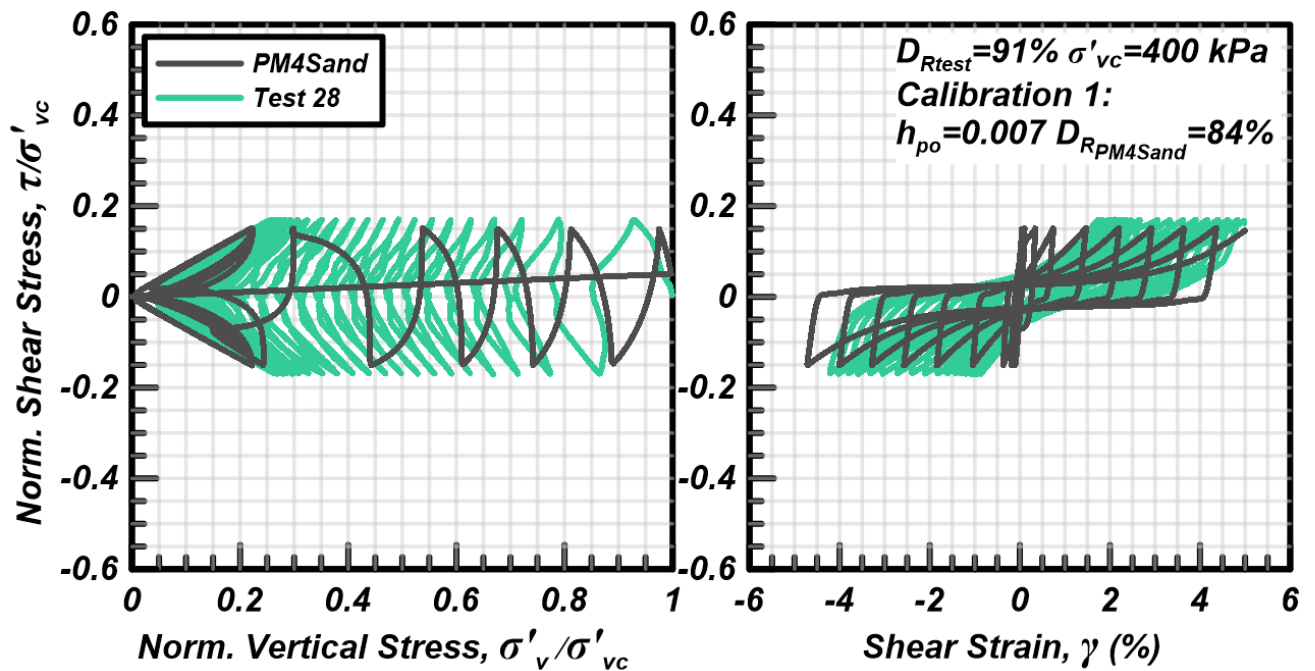


Figure 8.19 Stress-strain responses from cyclic DSS tests and PM4Sand calibration No. 1 simulations on a dense specimen consolidated to 400 kPa

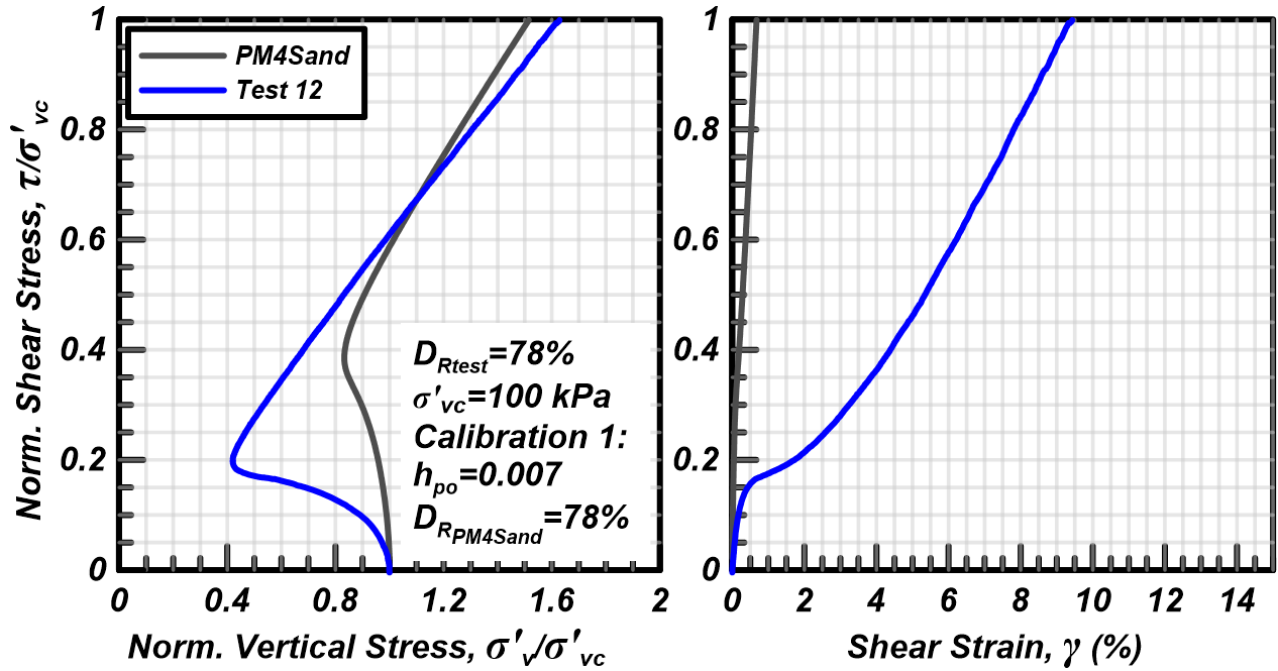


Figure 8.20 Stress-strain responses from monotonic DSS tests and PM4Sand calibration No. 1 simulations on a dense specimen consolidated to 100 kPa

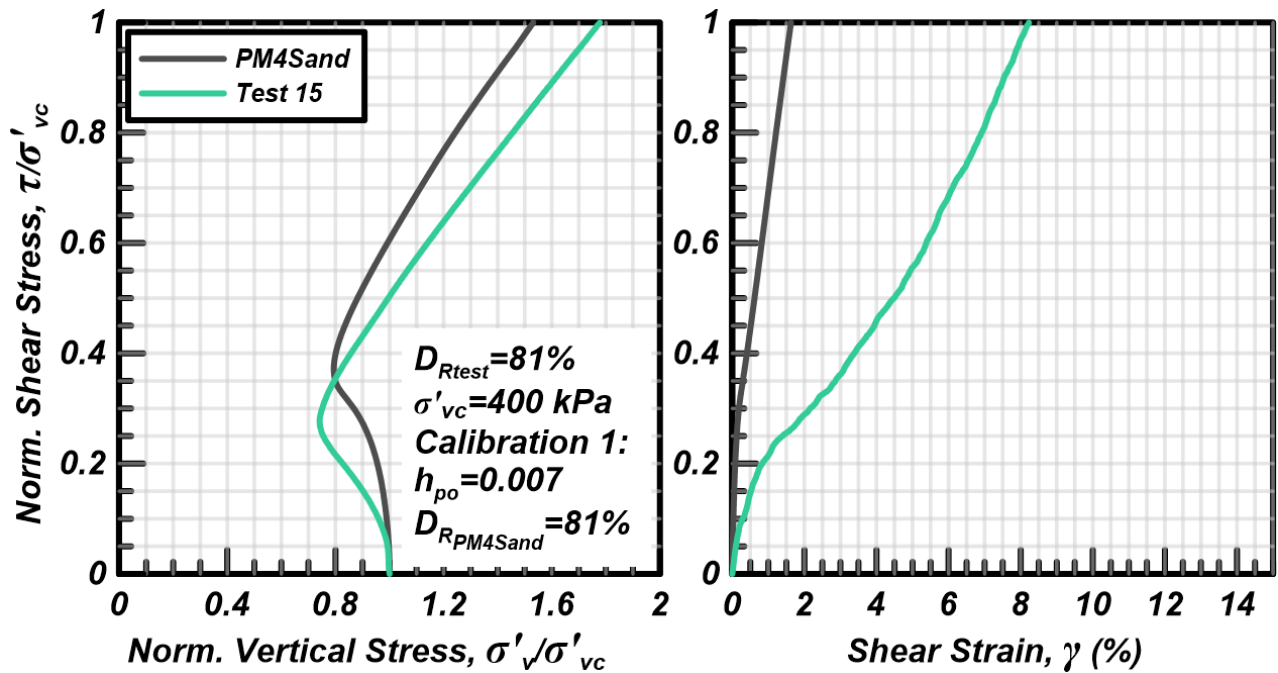


Figure 8.21 Stress-strain responses from monotonic DSS tests and PM4Sand calibration No. 1 simulations on a dense specimen consolidated to 400 kPa

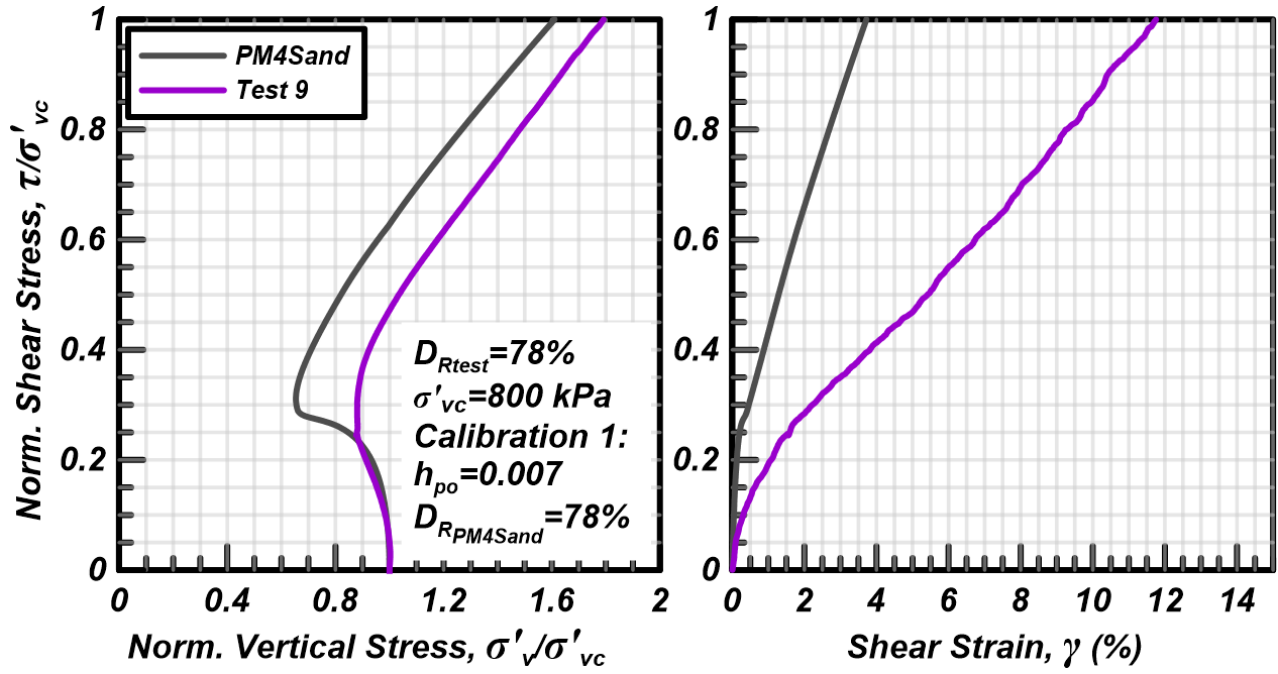


Figure 8.22 Stress-strain responses from monotonic DSS tests and PM4Sand calibration No. 1 simulations on a dense specimen consolidated to 800 kPa

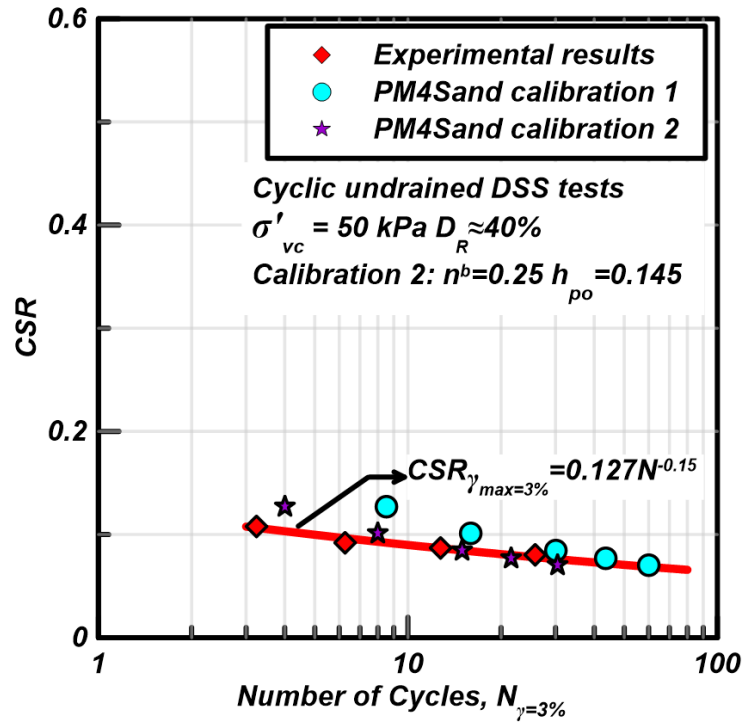


Figure 8.23 CRR curves from DSS tests and PM4Sand calibration No. 2 simulations for loose specimens consolidated to 50 kPa

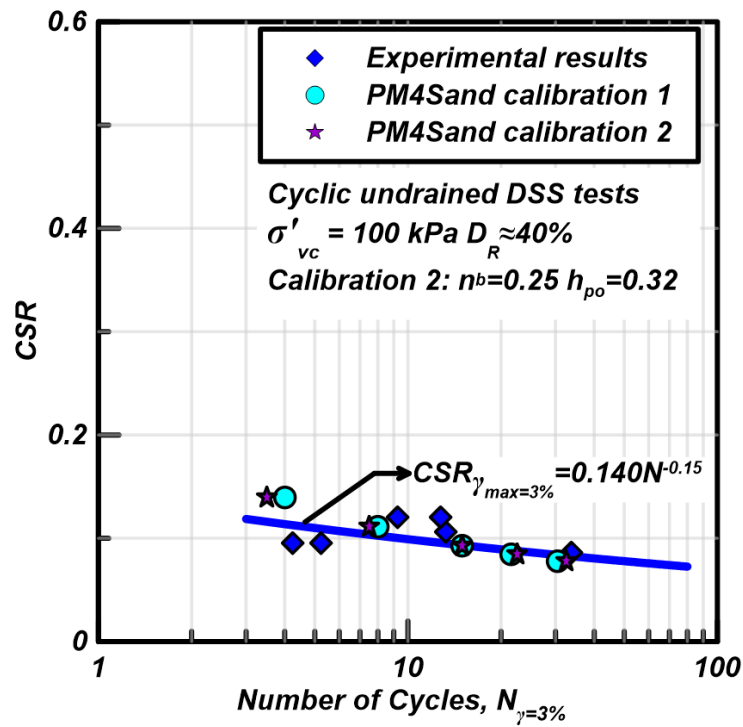


Figure 8.24 CRR curves from DSS tests and PM4Sand calibration No. 2 simulations for loose specimens consolidated to 100 kPa

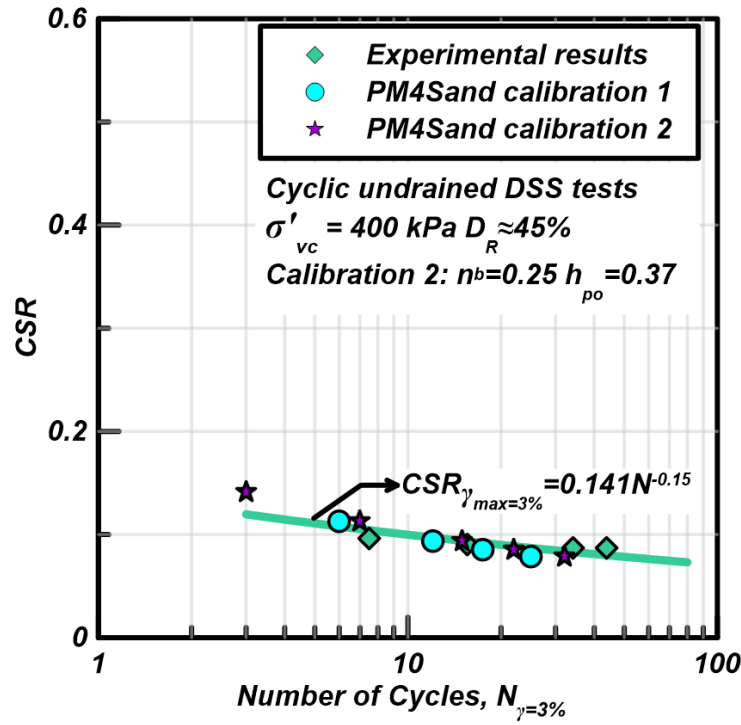


Figure 8.25 CRR curves from DSS tests and PM4Sand calibration No. 2 simulations for loose specimens consolidated to 400 kPa

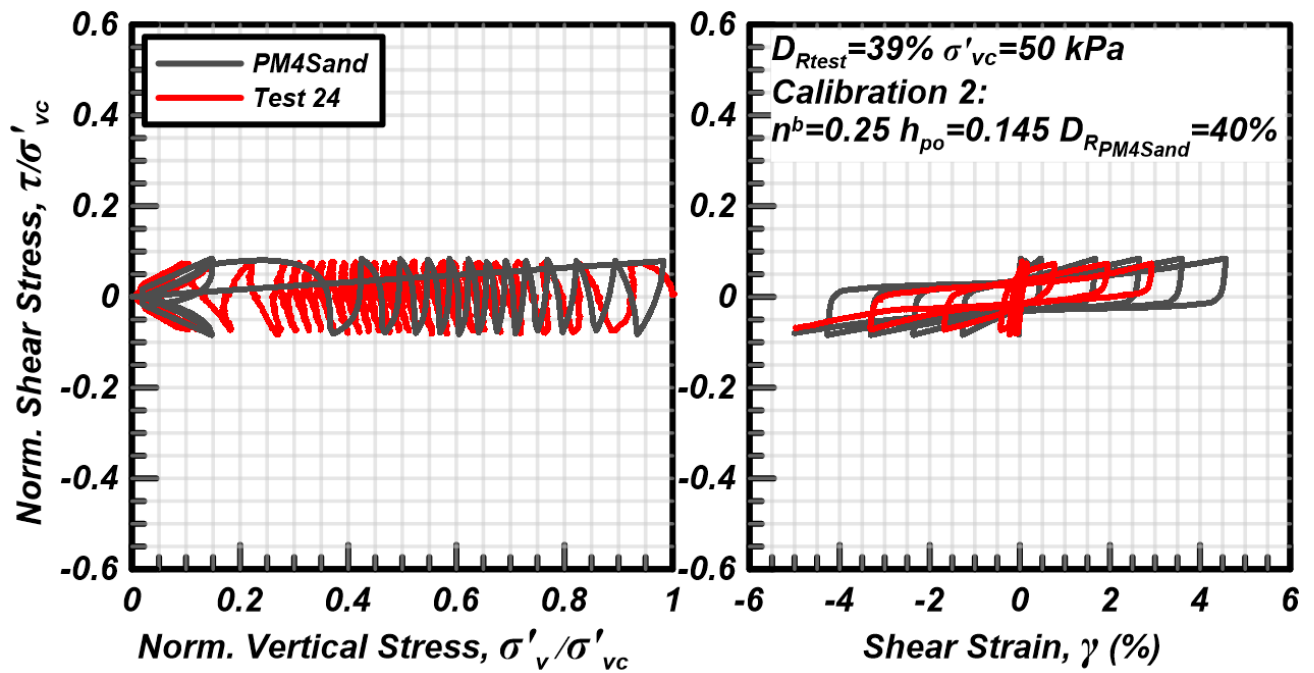


Figure 8.26 Stress-strain responses from cyclic DSS tests and PM4Sand calibration No. 2 simulations on a loose specimen consolidated to 50 kPa

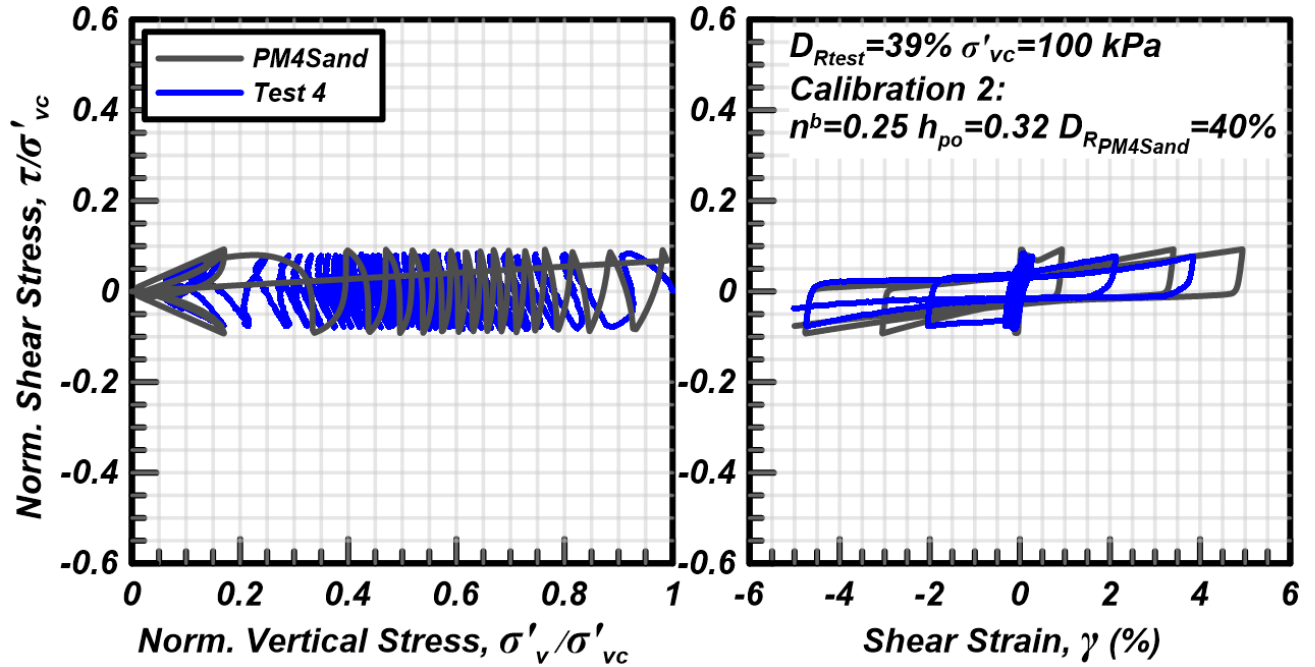


Figure 8.27 Stress-strain responses from cyclic DSS tests and PM4Sand calibration No. 2 simulations on a loose specimen consolidated to 100 kPa

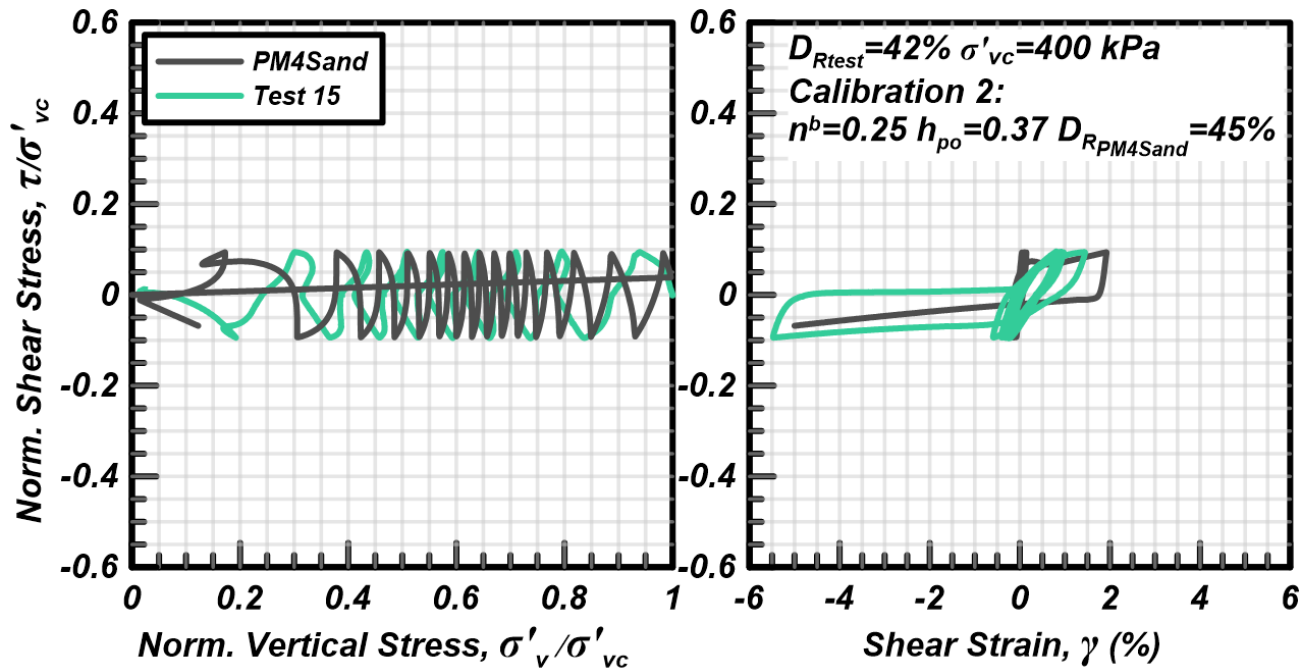


Figure 8.28 Stress-strain responses from cyclic DSS tests and PM4Sand calibration No. 2 simulations on a loose specimen consolidated to 400 kPa

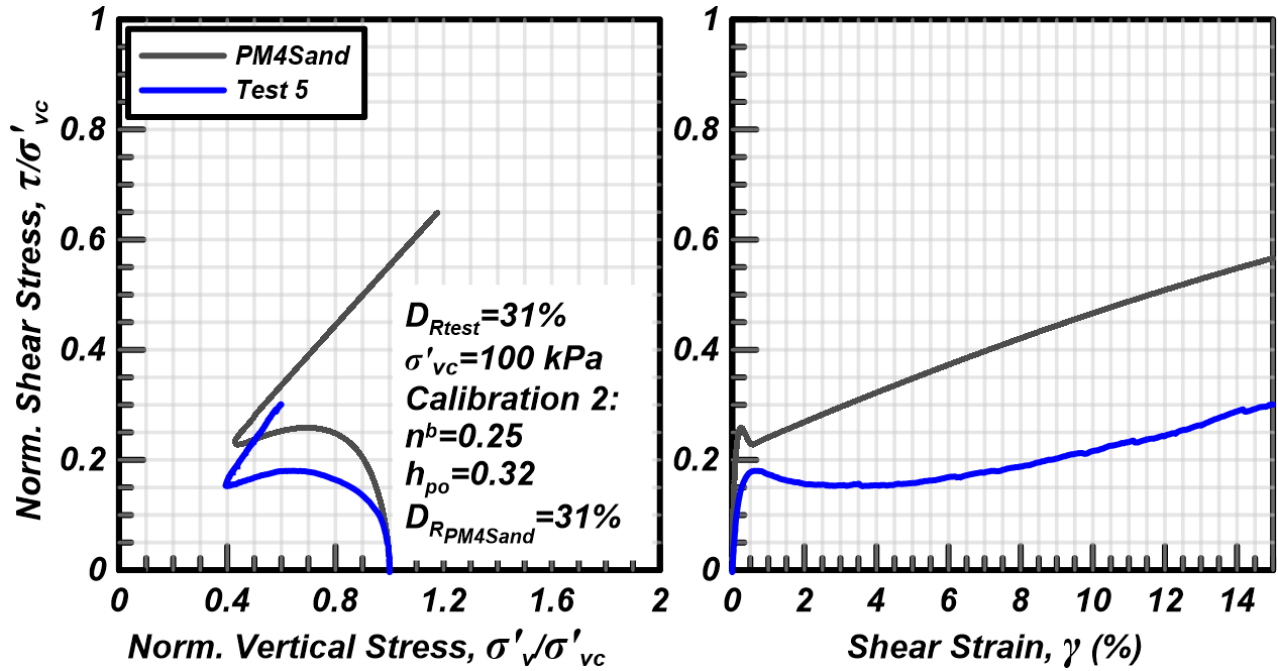


Figure 8.29 Stress-strain responses from monotonic DSS tests and PM4Sand calibration No. 2 simulations on a loose specimen consolidated to 100 kPa

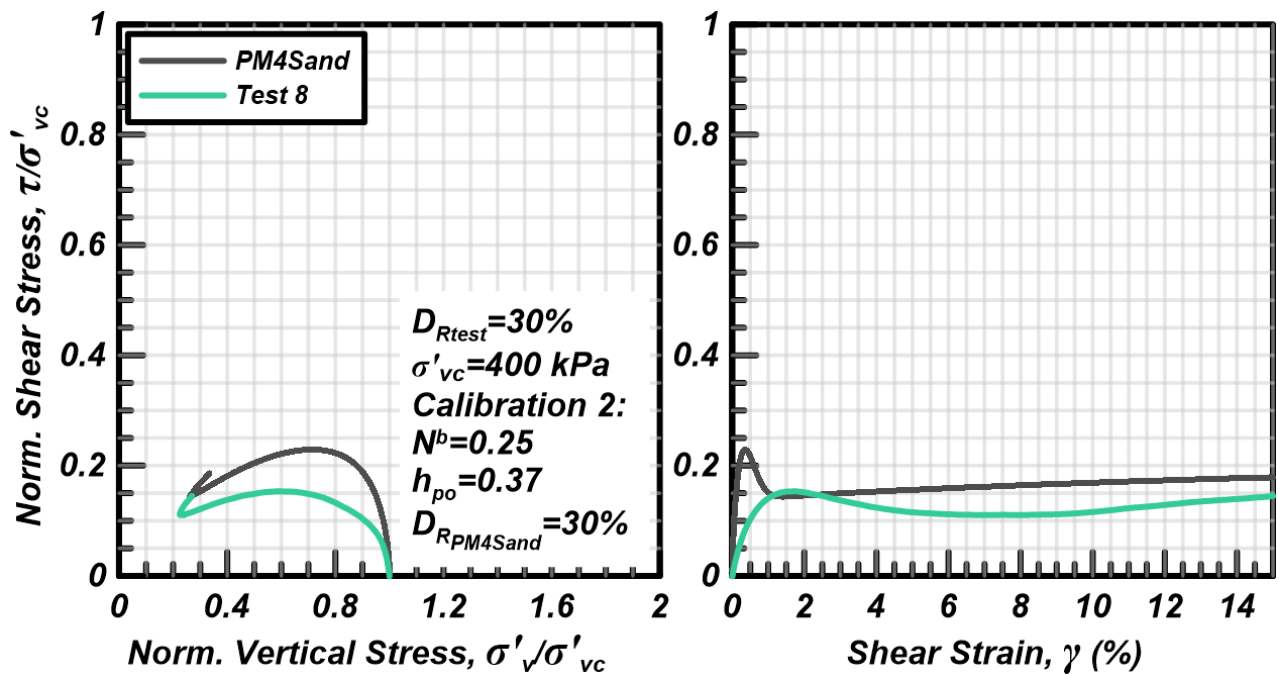


Figure 8.30 Stress-strain responses from monotonic DSS tests and PM4Sand calibration No. 2 simulations on a loose specimen consolidated to 400 kPa

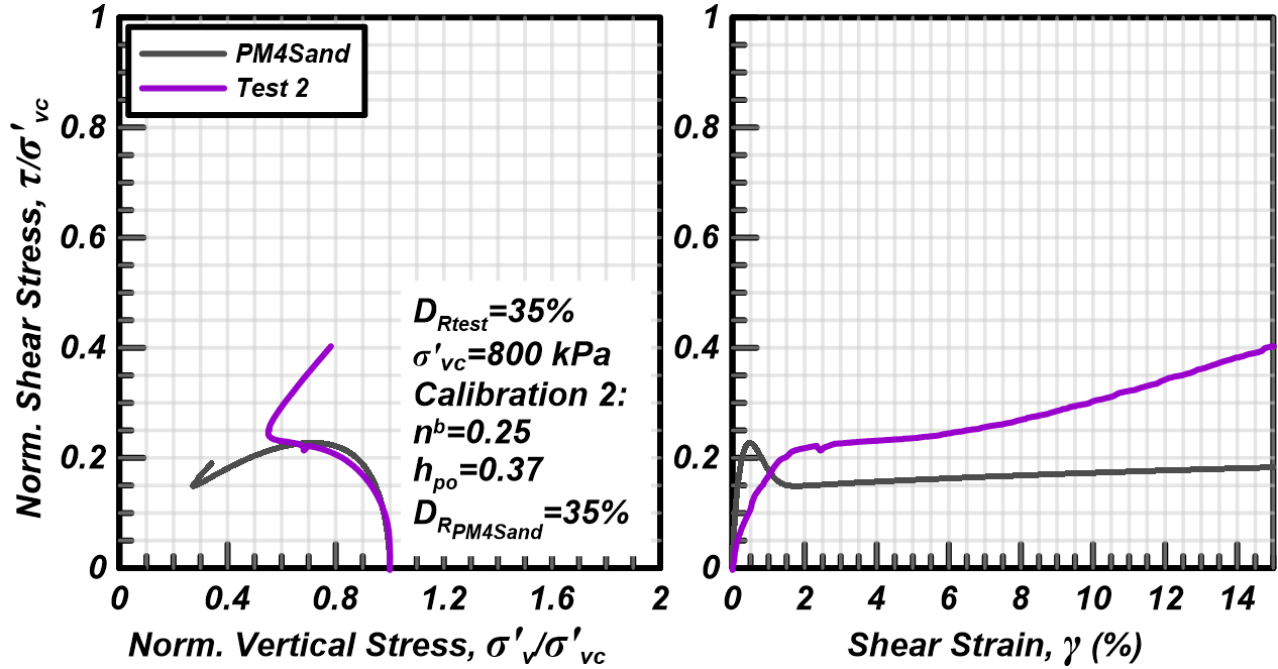


Figure 8.31 Stress-strain responses from monotonic DSS tests and PM4Sand calibration No. 2 simulations on a loose specimen consolidated to 800 kPa

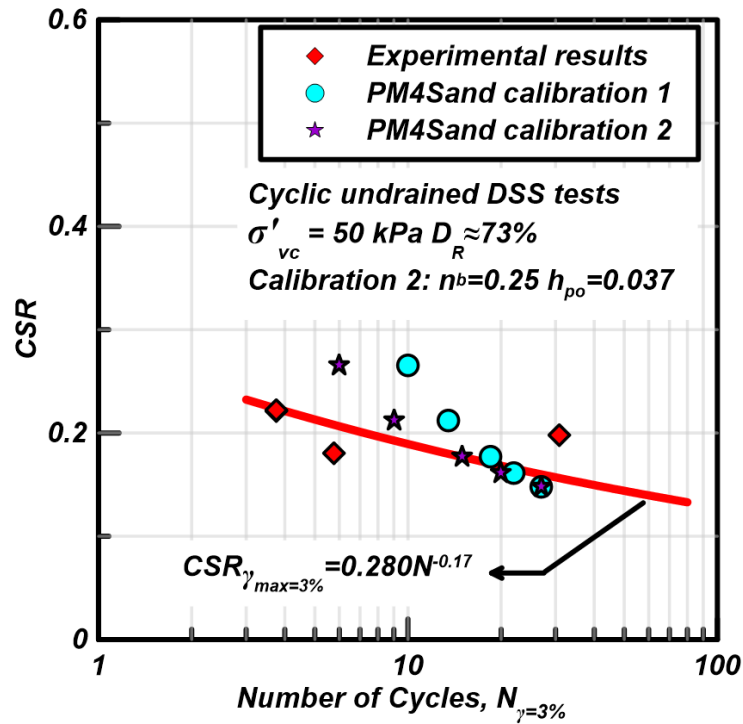


Figure 8.32 CRR curves from DSS tests and PM4Sand calibration No. 2 simulations for dense specimens consolidated to 50 kPa

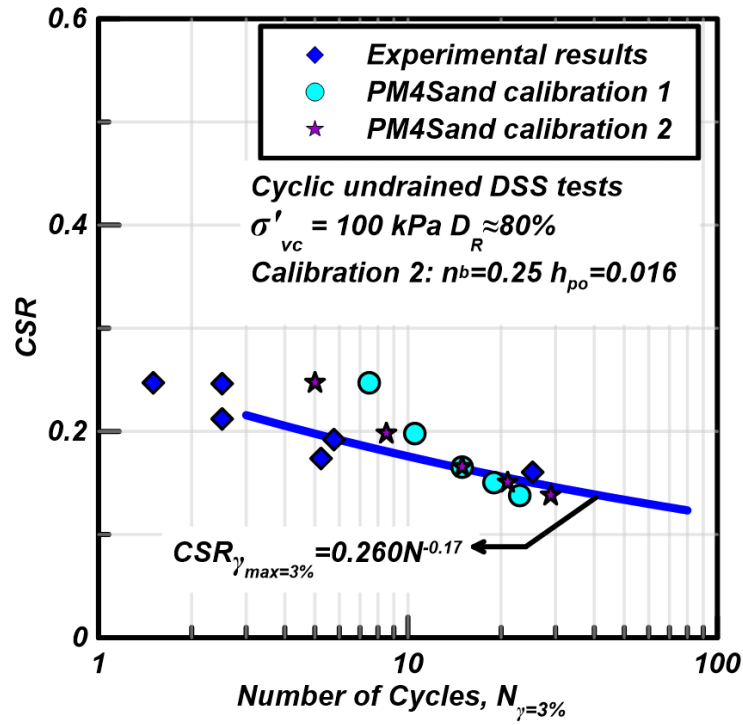


Figure 8.33 CRR curves from DSS tests and PM4Sand calibration No. 2 simulations for dense specimens consolidated to 100 kPa

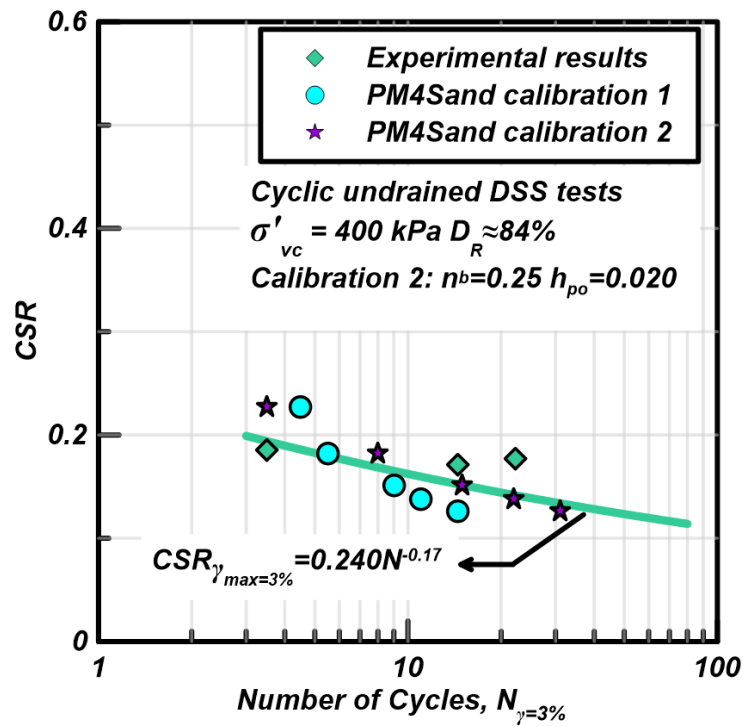


Figure 8.34 CRR curves from DSS tests and PM4Sand calibration No. 2 simulations for dense specimens consolidated to 400 kPa

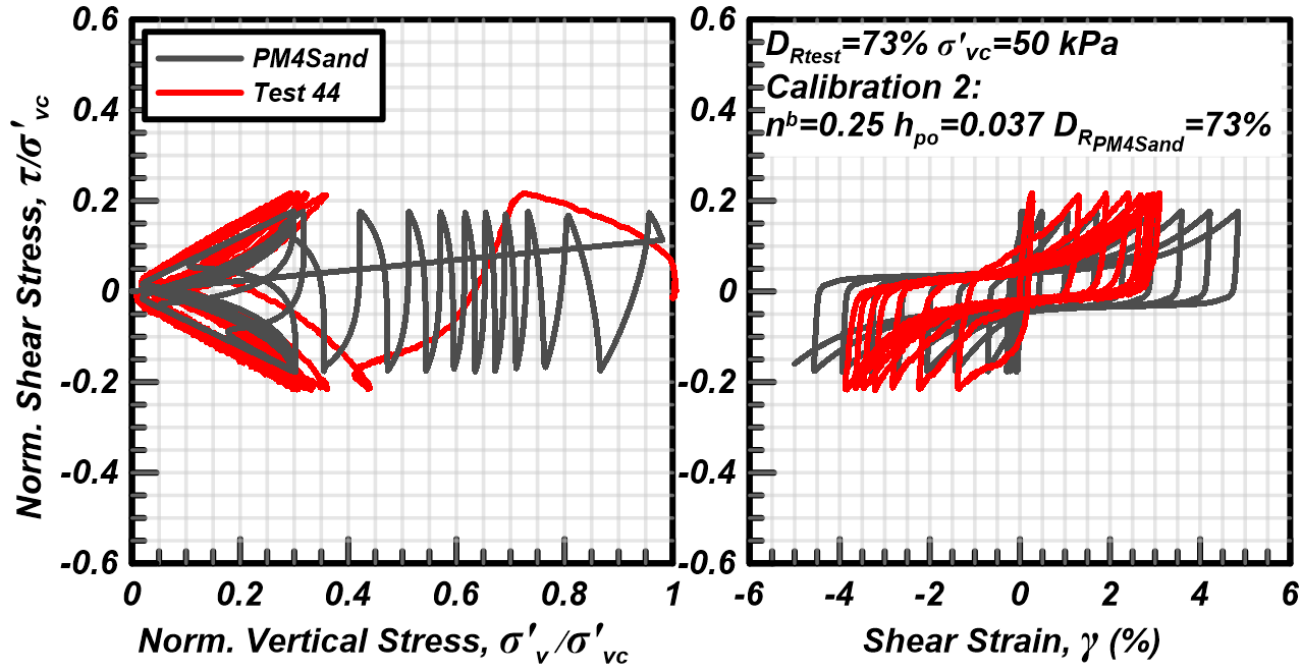


Figure 8.35 Stress-strain responses from cyclic DSS tests and PM4Sand calibration No. 2 simulations on a dense specimen consolidated to 50 kPa

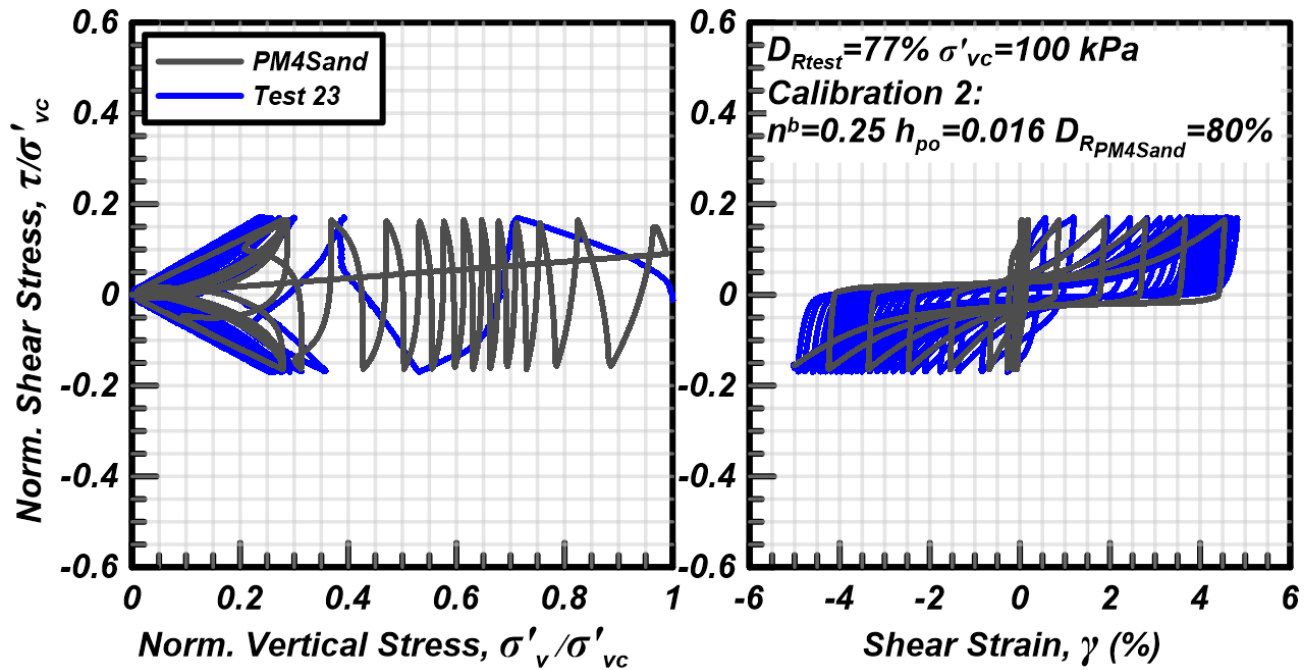


Figure 8.36 Stress-strain responses from cyclic DSS tests and PM4Sand calibration No. 2 simulations on a dense specimen consolidated to 100 kPa

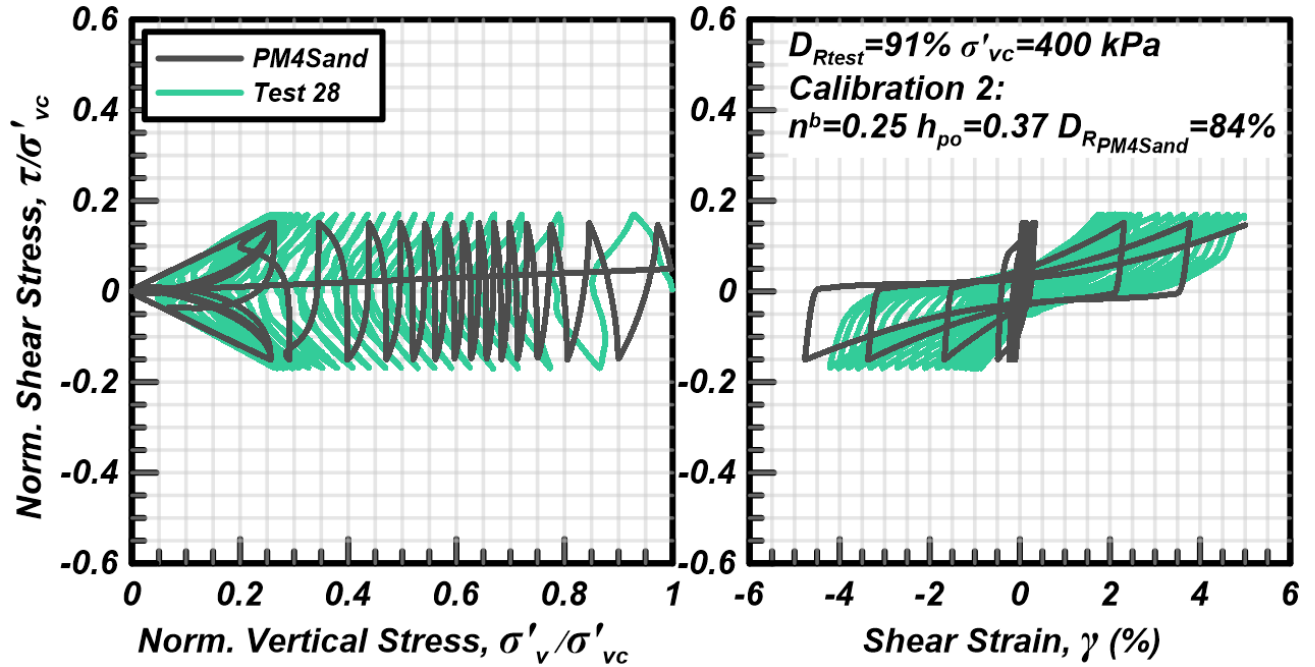


Figure 8.37 Stress-strain responses from cyclic DSS tests and PM4Sand calibration No. 2 simulations on a dense specimen consolidated to 400 kPa

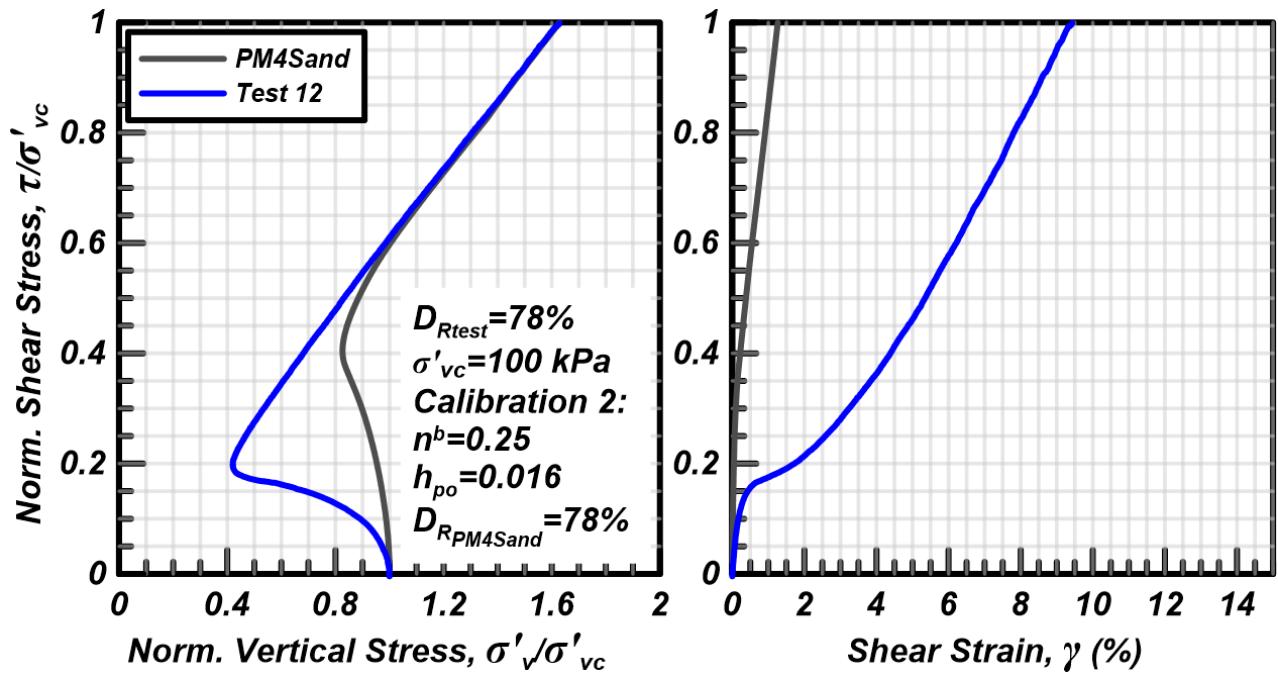


Figure 8.38 Stress-strain responses from monotonic DSS tests and PM4Sand calibration No. 2 simulations on a dense specimen consolidated to 100 kPa

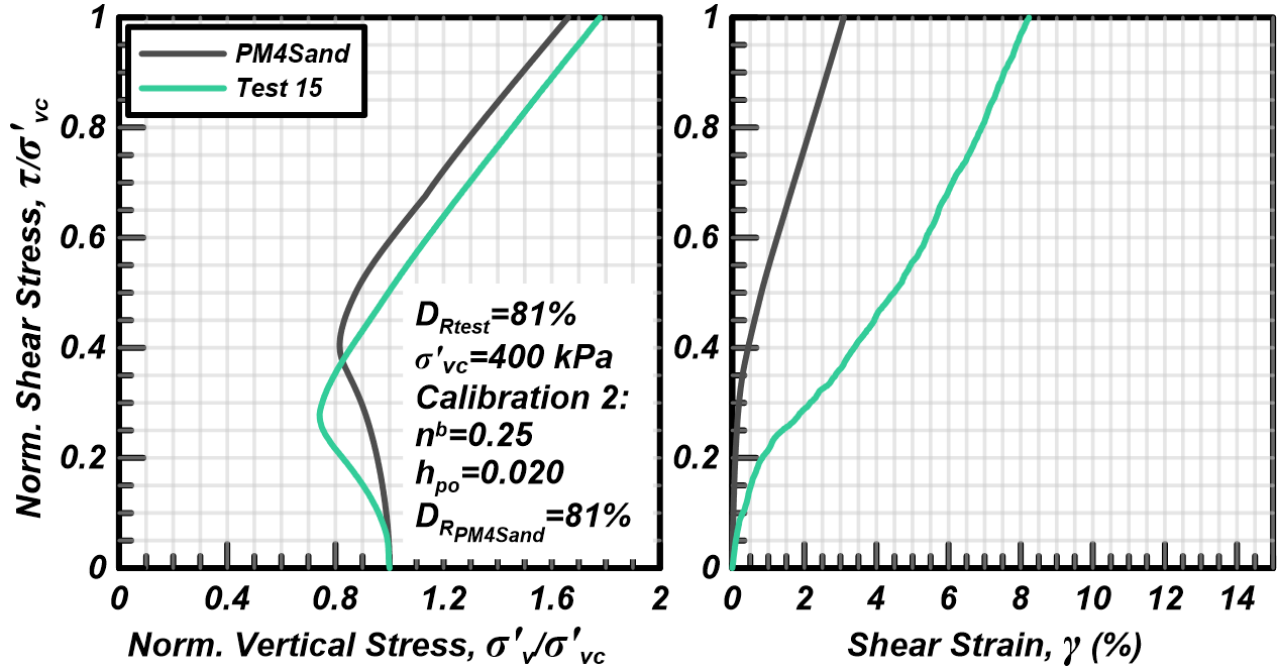


Figure 8.39 Stress-strain responses from monotonic DSS tests and PM4Sand calibration No. 2 simulations on a dense specimen consolidated to 400 kPa

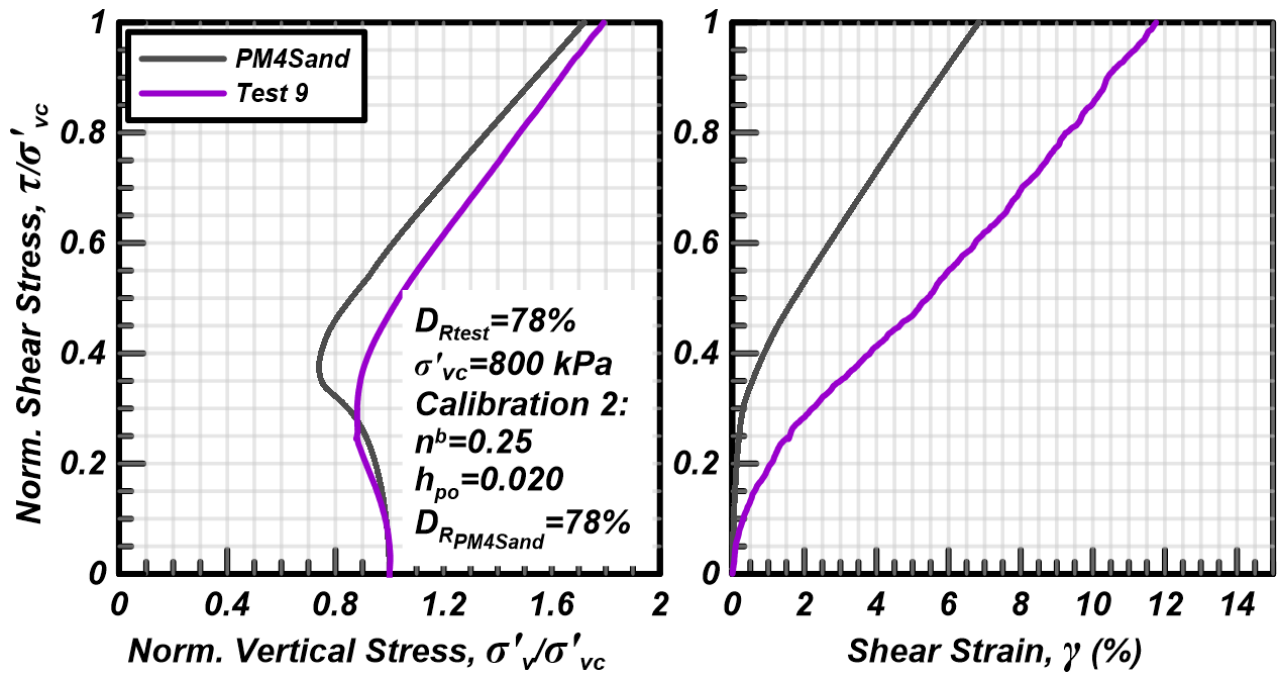


Figure 8.40 Stress-strain responses from monotonic DSS tests and PM4Sand calibration No. 2 simulations on a dense specimen consolidated to 800 kPa

Chapter 9

Conclusions and Future Directions

This dissertation encompasses a thorough characterization of Ottawa F-65 sand. Index tests included obtaining Scanning Electron Microscope (SEM) images of the particles, grain size distributions, specific gravity of solids, minimum dry densities and maximum dry densities. Hydraulic conductivity tests were performed on specimens prepared to different dry densities, and the results were compared with results obtained by others and with results predicted with empirical correlations. One-dimensional compression (1DC) tests were performed on normally consolidated loose and dense prepared specimens loaded to maximum vertical compressive stresses (σ'_v) of 30, 70 and 140 MPa, and post-compression grain size distributions and SEM images were obtained for samples recovered from the compressed specimens. Undrained monotonic direct simple shear (DSS) tests were performed on normally consolidated loose and dense prepared specimens, consolidated to vertical effective stresses (σ'_{vc}) of 100, 400 and 800 kPa, and the results were used to evaluate the critical state friction angle and the inferred position of the critical state line. Undrained cyclic DSS tests were performed on normally consolidated loose and dense prepared specimens consolidated to σ'_{vc} of 50, 100 and 400 kPa, and on over-consolidated loose specimens with an over consolidation ratio (OCR) of 4 at a vertical confining stress of σ'_{vc} of 100 kPa. Undrained pre-straining cyclic DSS tests were performed on normally consolidated loose specimens, consolidated to σ'_{vc} of 100 kPa and subjected to several shearing and reconsolidation stages. Single element loading test simulations using the PM4Sand constitutive model (Boulanger and Ziotopoulou 2015) were performed using two alternative calibration procedures; the simulation results were compared to the monotonic and cyclic loading responses for the loose and dense prepared specimens at the different consolidation stresses.

This chapter contains the main observations and conclusions from each component of the Ottawa F-65 sand's characterization program (Section 9.1 below), followed by discussion of opportunities for future related research (Section 9.2).

9.1 Summary and Conclusions

9.1.1 Index tests (Chapter 2)

The index characteristics of Ottawa F-65 sand were presented. The index characteristics that were evaluated include grain size distributions, specific gravity of solids, minimum dry density and maximum dry density and were compared to those obtained by other researchers. The grain size characteristics include: D_{10} is 0.14 mm, D_{30} is 0.17 mm, D_{50} is 0.20 mm, D_{60} is 0.22 mm, C_u is 1.61 and C_c is 0.96. The grain size distributions from this project and from different researchers are very similar. The fines content is the biggest difference of the grain size distribution obtained in this project compared to those obtained by other researchers. The specific gravity of solids is 2.65. The obtained value of specific gravity is consistent with the expected value for a sand with a high quartz content and is consistent with the values of specific gravity obtained by other researchers. The minimum dry density ($\rho_{d \min}$) and maximum void ratio (e_{\max}) are 1446 kg/m³ and 0.83 respectively and were obtained with the [ASTM D4254-00 \(2000\)](#). Different values of $\rho_{d \min}$ were obtained with different testing methods; however, the range of values of $\rho_{d \min}$ obtained in this project are consistent with the range of values obtained by others. The maximum dry density ($\rho_{d \max}$) and minimum void ratio (e_{\min}) are 1446 kg/m³ and 0.51 respectively and were obtained with the Japanese test method for minimum density of sand [JIS A 1224 \(JIS 2009\)](#). Different values of $\rho_{d \max}$ were obtained with different testing methods; however, the range of values of $\rho_{d \max}$ obtained in this project are consistent with the range of values obtained by others.

9.1.2 Hydraulic Conductivity (Chapter 3)

The hydraulic conductivity characteristics of Ottawa F-65 sand were presented. The effects of initial relative density on the hydraulic conductivity characteristics of clean Ottawa F-65 sand were evaluated using constant head hydraulic conductivity tests. The hydraulic conductivity increased with decreasing relative density. The range of hydraulic conductivities obtained with the tests are comparable with the ranges measured by other researchers for Ottawa F-65 sand. The range of hydraulic conductivities obtained with the tests are comparable with the ranges predicted by empirical equations. The Hazen's equation using the method by [Head \(1988\)](#) provides the closest prediction to the range of hydraulic conductivities obtained with the tests.

9.1.3 One-dimensional Compression Characteristics (Chapter 4)

The IDC characteristics of Ottawa F-65 sand were presented. The effects of initial relative density and maximum vertical effective stress on the one-dimensional compression and particle crushing characteristics of clean Ottawa F-65 sand were evaluated using IDC tests up to vertical effective stresses of 140 MPa, grain size distribution analysis and SEM imaging. Particle crushing increased with increasing maximum vertical effective stress and with decreasing initial relative density. Particle crushing was only observed in the grain size distribution analysis and SEM images on samples from specimens subjected to maximum vertical effective stresses of 70 and 140 MPa; some asperity breakage might have occurred on specimens subjected to a maximum vertical effective stress of 30 MPa, but the change in grain size distribution was small. Particle crushing was the highest in the loose specimens due to the contact stresses between particle contacts being higher due to a smaller quantity of contacts.

9.1.4 Monotonic Direct Simple Shear Characteristics (Chapter 5)

The monotonic DSS characteristics of Ottawa F-65 sand were presented. The effects of initial relative density and consolidation vertical effective stress on the monotonic strength of Ottawa F-65 sand were evaluated using undrained monotonic direct simple shear tests. Dilative tendencies increased with increasing relative density and decreased with increasing consolidation stresses in all the tests, with the exception on the tests with specimens consolidated to 800 kPa; these specimens experienced significant vertical compliance which might have affected the results. The estimated maximum error on the results on the loosest specimen consolidated to 800 kPa is 9%, this error was estimated assuming that the constant height bolts were loose during the shearing phase of the test. The recommended critical state effective friction angle corresponds to the quasi-steady state friction angle and is 24.6 degrees for this sand. Bolton's (1986) dilatancy relationship with $Q=10$ and $R=1$ provides an approximate location of the position of the critical state line (CSL).

9.1.5 Cyclic Direct Simple Shear Characteristics (Chapter 6)

The cyclic DSS characteristics of Ottawa F-65 sand were presented. The effects of initial dry density, consolidation vertical effective stress and over-consolidation ratio (OCR) on the cyclic strength were evaluated using undrained cyclic direct simple shear tests. The shear strain accumulation rate increased with decreasing relative density once the specimens have reached $r_v \approx 1.0$. The general features of the stress-strain accumulation are consistent with the cyclic responses shown in the literature for other silica sands. The cyclic resistance curves are flatter than many curves in the literature for other silica sands. The cyclic resistance ratio against number of cycles to reach a peak shear strain of 3% increased with increasing relative density and OCR, and decreased with consolidation vertical effective stress. The cyclic resistance curves for a peak shear strain of 3% for normally consolidated loose specimens at different consolidation stresses are very close together; the normally consolidated loose specimens consolidated to the higher stresses (e.g., 400 kPa) have a slighter higher initial relative density which offset the expected

trend of decreasing cyclic strength with increasing consolidation stress. The number of loading cycles to reach 1, 3 and 5% peak shear strain is almost the same for the loose specimens, whereas the difference in the number of cycles to reach 1, 3 and 5% was larger for the dense specimens. Consolidation and reconsolidation volumetric strains increased with decreasing relative density and increasing confining stress with the exception of the results of test 4. The consolidation volumetric strains were higher than the reconsolidation volumetric strain in the results from all the tests, with the exception of the results from test 4. Test 4 contained a sudden increase in the vertical strain of this specimen while applying the last loading increment during consolidation, which might indicate that the DCDT sensor stuck during the consolidation process; this might be the reason causing the consolidation and reconsolidation volumetric strains not to follow the trends followed by the specimens from other tests. The reconsolidation volumetric strain values were within the scatter of the results from [Ishihara and Yoshimimi \(1992\)](#). The monotonic stress-strain responses of the pre-strained specimens are initially softer compared to the responses of the virgin specimens

9.1.6 Pre-Straining Cyclic Direct Simple Shear Characteristics (Chapter 7)

The pre-straining cyclic DSS characteristics of Ottawa F-65 sand were presented. The cumulative effects of repeated recurrent liquefaction and cyclic pre-straining on the cyclic strength were evaluated using undrained cyclic direct simple shear tests with multiple stages of uniform cyclic loading followed by reconsolidation. The cyclic resistance ratio against a peak shear strain of 3% in 15 uniform loading cycles increased in all specimens due to the cyclic pre-straining; the effects were more marked in the dense specimens. The rate of shear strain accumulation during uniform loading cycles decreased after $r_v \approx 1.0$ developed (or after shear strains exceeded about 0.5-1.0%) due to cyclic pre-straining. The vertical effective stress did not reach a value of zero in the stress paths from Figures 7.8 and 7.9(b). Friction between the confining rings has been identified as the cause of the vertical effective stress not reaching a value of zero. A couple of other causes were considered including the exiting of water due to small volume

changes during shearing caused by vertical compliance of the equipment and the malfunction of the vertical load cell, but these two causes were discarded due to the lack of evidence indicating those phenomenon were occurring. The recurrent liquefaction and cyclic pre-straining cause densification and the development of a more stable fabric within the test specimens, which increased the cyclic strength of the specimens. These results provide insights to evaluate the behavior of Ottawa F-65 sand when subjected to multiple cyclic shaking events in centrifuge and shake table models. These results also provide insights on the influence of progressive cyclic pre-straining and densification due to multiple seismic events on the cyclic strength of natural sand deposits; however, the cyclic strength of natural deposits over time is also affected by other mechanisms including ageing, cementation, and stress history (e.g., over-consolidation).

9.1.7 PM4Sand Element Tests (Chapter 8)

Two different calibrations of PM4Sand against the experimental data of Ottawa F-65 sand were presented. The effects of the calibrations on the cyclic and monotonic undrained direct simple shear responses were evaluated using single-element numerical simulations in FLAC 2D. In both calibrations, G_o was calibrated to fit published results for the small-strain stiffness of Ottawa sand at different relative densities. Calibration No. 1 consisted of calibrating the parameter h_{po} to match the cyclic resistance ratio required to reach a 3% peak shear strain in 15 loading cycles at a consolidation stress of 100 kPa, while accepting default values for all other parameters. The calibrated model's ability to reproduce the other observed cyclic strength curves, cyclic stress-strain, and monotonic stress-strain responses at other consolidation stresses (50 and 400 kPa) was then evaluated. Calibration No. 2 consisted in reducing the parameter n^b to half its default value (from 0.5 to 0.25) to reduce dilatancy by a factor of 2 for a given relative state parameter, and then recalibrating the parameter h_{po} to match the cyclic resistance ratio required to reach a 3% peak shear strain in 15 loading cycles at each consolidation stress. The calibrated

models ability to reproduce the other observed cyclic strength curves, cyclic stress-strain, and monotonic stress-strain responses at other consolidation stresses (50 and 400 kPa) was then evaluated.

Simulations with calibration No. 1 produced CRR curves that are steeper than the CRR curves from experimental results. This effect increased with increasing relative density and reduced with increasing confinement. The PM4Sand model was able to simulate the general features of cyclic mobility behavior with calibration No. 1, but over predicted the dependence of the CRR on overburden stress and the rate of strain hardening in monotonic and cyclic loading.

Simulations with calibration No. 2 produced CRR curves that are closer to the curves from the experimental results. Simulations with calibration No. 2 produced CRR curves that are flatter than the curves from Calibration No. 1, but are still steeper than the CRR curves from experimental results. This effect increased with increasing relative density and reduced with increasing confinement. The PM4Sand model was able to simulate the general features of cyclic mobility behavior in calibration No. 2, but the stress-strain responses for dense sand were more distant from the experimental responses in certain details compared to the responses from calibration No. 1. The reduction of n^b reduced dilatancy which improved responses for monotonic undrained loading but increased the accumulation of shear strains during cyclic loading for the denser specimens. The results of these comparisons illustrate how the calibration process often requires deciding which feature of monotonic or cyclic loading behavior should be emphasized since a single calibration may not capture all aspects of behavior simultaneously.

9.2 Future Directions

This work provided a thorough characterization of Ottawa sand F-65. The data has been archived at the NEES project warehouse at www.NEESHUB.org for public distribution, and will be used by researchers around the world to validate numerical model responses against experimental results. The results provided in this work include tests results from specimens subjected to a wide range of loading

paths and with a variety of initial dry density conditions. However, other characteristics of this sand under other conditions can be studied to complement this work.

The one-dimensional compression characteristics of Ottawa F-65 sand at elevated pressures could be further studied. These characteristics include:

- The effect of specimen fabric on the one-dimensional compression characteristics of Ottawa F-65 sand compressed to high pressures and on the amount of particle crushing. The specimen's fabric might influence the shape of the one-dimensional compression curves at stresses before the yielding stress. The specimen's fabric might also influence the amount of particle crushing due to a different distribution of the forces within the inter particles contacts. It would be interesting to prepare specimens by different methods and test them up to 140 MPa to compare their compression curves, grain size distributions and SEM images results.
- The effect of one-dimensional cyclic high stresses on the amount of particle crushing. Particle crushing might be affected by the type of loading. It would be interesting to test specimens with different initial relative densities and load them with sinusoidal loads with a maximum amplitude of 140 MPa. Large sinusoidal loads may better mimic the type of loads that the sand grains experience during processes like pile driving.
- The effect of ultra-high pressure on the compression curve characteristics and on particle crushing. It would be interesting to test specimens up to stresses higher than 140 MPa to observe the behavior of the LCC portion of the compression curve and to observe the effect of the ultra-high pressure on the particle crushing. This requires the development of a new testing assembly with smaller diameter if the same compression machine is used, or the use of a compression machine with a greater loading capacity.

The monotonic DSS characteristics of Ottawa F-65 sand could be further studied. These characteristics include:

- The drained monotonic DSS characteristics of Ottawa F-65 sand. The drained peak friction angle was observed to be higher than the undrained peak friction angle for a clean sand tested by [Kutter and Chen \(1997\)](#). It would be interesting to evaluate the stress-strain behavior and the effects of the initial relative density and consolidation stresses on the drained shear strength and drained peak friction angles using both simple shear and triaxial testing devices.
- The inferred position and shape of the critical state line by using different equations available in the literature like the ones proposed by [Sheng et al. \(2008\)](#) and by [Li and Dafalias \(1999\)](#). It would be interesting to evaluate the state parameters using the inferred critical state lines from the different equations and try to correlate those state parameters to the peak friction angles, the monotonic drained and undrained strengths and the cyclic undrained DSS strengths and the observed stress-strain behaviors.

The cyclic DSS characteristics of Ottawa F-65 sand could be further studied. These characteristics include:

- The effect of specimen preparation on the cyclic undrained DSS characteristics of Ottawa F-65 sand. The undrained cyclic resistance of the sand is dependent on fabric as described by several authors. It would be interesting to evaluate the effect of specimen preparation in: the consolidation and re-consolidation characteristics, the position and slope of the cyclic resistance curves for loose and dense specimens, the amount of pore pressure accumulation during the first loading of cycle, the pore pressure accumulation evolution with loading cycles and the rate of shear strain accumulation with loading cycles.

The cyclic pre-straining direct simple shear characteristics of Ottawa F-65 sand could be further studied. These characteristics include:

- The effect of over consolidation on the pre-straining cyclic DSS characteristics of Ottawa F-65 sand. It would be interesting to evaluate the evolution of several characteristics of loose and dense specimens over consolidated during their virgin consolidation stage and normally consolidated during all the other reconsolidation stages. The characteristics that would be evaluated with each shearing stage include: the re-consolidation characteristics, the stress-strain responses, the amount of pore pressure accumulation during the first loading of cycle of each shearing stage, the pore pressure accumulation with loading cycles, the rate of shear strain accumulation with loading cycles, the evolution of the number of cycles to reach 1% and 3% peak shear strain and $r_u \approx 1.0$ and the evolution of the equivalent cyclic stress ratio to cause 1% and 3% peak shear strain in 15 cycles.
- The effect of specimen preparation on the pre-straining cyclic DSS characteristics of Ottawa sand F-65. It would be interesting to test specimens prepared by different preparation methods and track evolution of several characteristics on each shearing stage including: the re-consolidation characteristics, the stress-strain responses, the amount of pore pressure accumulation during the first loading of cycle of each shearing stage, the pore pressure accumulation with loading cycles, the rate of shear strain accumulation with loading cycles, the evolution of the number of cycles to reach 1% and 3% peak shear strain and $r_u \approx 1.0$ and the evolution of the equivalent cyclic stress ratio to cause 1% and 3% peak shear strain in 15 cycles.

The PM4Sand responses using Ottawa F-65 sand elements could be further studied. These responses include:

- The drained monotonic DSS responses of Ottawa F-65 sand using PM4Sand. It would be interesting to run drained simulations on specimens with similar initial relative densities and confinements as specimens from experimental results, calibrated with

the parameters provided in Calibrations No. 1 and No. 2 of this work and compare those responses with the peak stress ratios, the peak friction angles and the stress-strain responses.

- The effect of pre-strain history on the undrained cyclic DSS responses of Ottawa F-65 sand using PM4Sand. It would be interesting to run undrained simulations on specimens with similar initial relative densities and confinements as the specimens from the experimental results, calibrated with the parameters provided in calibration No. 1 and No. 2 of this work and compare the evolution of the following characteristics in the modeled elements: the re-consolidation characteristics, the stress-strain responses, the amount of pore pressure accumulation during the first loading of cycle of each shearing stage, the pore pressure accumulation evolution with loading cycles, the rate of shear strain accumulation with loading cycles, the evolution of the number of cycles to reach 1% and 3% peak shear strain and $r_u \approx 1.0$ and the evolution of the equivalent cyclic stress ratio to cause 1% and 3% peak shear strain in 15 cycles.
 - The normalized shear modulus curves. It would be interesting to run simulations on specimens with similar drainage conditions, initial relative densities and confinements as the specimens from the experimental results by [Alarcon-Guzman et al. \(1989\)](#) and compare the results in terms of shear modulus and equivalent damping ratios.

Bibliography

- Alarcon-Guzman, A., G. A. Leonards, and J. L. Chameau (1988). Undrained monotonic and cyclic strength of sands, *Journal of Geotechnical Engineering, ASCE* **114**(10), 1089-1109.
- Alarcon-Guzman, A., J. L. Chameau, G. A. Leonards, and J. D. Frost (1989). Shear modulus and cyclic strength behavior of sands, *Soils and Foundations*, **29**(4), 105-119.
- Ashmawy, A. K., B. Sukumaran, and V. V. Hoang (2003). Evaluating the influence of particle shape on liquefaction behavior using discrete element modeling, in *13th International Offshore and Polar Engineering Conference*, pp. 542–549, Honolulu, HI, USA.
- ASTM (2007). Standard test method for particle-size analysis of soils, D422 – 63, pp. 1-8.
- ASTM (2000). Standard test methods for minimum index density and unit weight of soils and calculation of relative density D4254 – 00, pp. 1-9.
- ASTM (2000). Standard test method for permeability of granular soils (constant head), D3424 - 68, pp. 1-5.
- ASTM (2006). Standard practice for description and identification of soils (visual-manual procedure), D2488 - 06, pp. 1-11.
- ASTM (2007). Standard test method for consolidated undrained direct simple shear testing of cohesive soils, D6528 – 07, pp. 1-9.
- ASTM (2010). Standard test methods for laboratory determination of water (moisture) content of soil and rock by mass, D2216 - 10, pp. 1-7.
- ASTM (2014). Standard test methods for specific gravity of soil solids by water pycnometer, D854 - 14, pp. 1-8.
- Bardet, J.-P. (1997). Determination of specific gravity, in *Experimental soil mechanics*, Prentice Hall Upper Saddle River, NJ, USA, pp. 142-146.
- Bardet, J.-P. (1997). Constant head permeability test, in *Experimental soil mechanics*, Prentice Hall, Upper Saddle River, NJ, USA, pp. 189-101.
- Bolton, M. D. (1986). The strength and dilatancy of sands, *Geotechnique*, **36**(1), 65-78.
- Boulanger, R. W., and R. B. Seed (1995). Liquefaction of sand under bidirectional monotonic and cyclic loading, *Journal of Geotechnical Engineering, ASCE* **121**(12), 870-878.
- Boulanger, R. W. (2003). Relating K_α to relative state parameter index, *Journal of Geotechnical and Geoenvironmental Engineering, ASCE* **129**(8), 770-773.
- Boulanger, R. W., and J. T. DeJong (2012). CPT-Based characterization of intermediate soils, National Science Foundation.
- Boulanger, R. W., and K. Ziotopoulou (2015). PM4Sand (Version 3) Report No. CGM-15-01_2015, Center for Geotechnical Modeling, University of California, Davis.
- Carey, T. J., B. L. Kutter, M. Manzari, M. Zeghal, A. Vasko (2015). LEAP soil properties and element test data, <https://nees.org/resources/13689>, retrieved on 02/04/2015.
- Carraro, J. A. H., P. Bandini, and R. Salgado (2003). Liquefaction resistance of clean and nonplastic silty sands based on cone penetration resistance, *Journal of Geotechnical and Geoenvironmental Engineering, ASCE* **129**(11), 965-976.

- Carraro, J. A. H., M. Prezzi, and R. Salgado (2009). Shear strength and stiffness of sands containing plastic or nonplastic fines, *Journal of Geotechnical and Geoenvironmental Engineering, ASCE* **135**(9), 1167-1178.
- Cerna, E. (2014). Maximum and minimum dry densities of Ottawa F-65 sand, <https://nees.org/dataviewer/view/1064:ds/1172>, retrieved on 02/04/2015.
- Cerna, E. (2014). Grain size distribution Ottawa F-65 sand, <https://nees.org/dataviewer/view/1064:ds/1203>, retrieved on 02/04/2015.
- Cerna, E. (2014). Specific gravity Ottawa F-65 sand, <https://nees.org/dataviewer/view/1064:ds/1173>, retrieved on 02/04/2015.
- Christoph, G. G. (2005). Influence of particle properties and initial specimen state on one-dimensional compression and hydraulic conductivity, Master's thesis, University of Massachusetts at Amherst, 286 pp.
- Cimini, D. (2015). Hydraulic conductivity data.
- Cooper Lab (2013). Dry densities Ottawa F-65 sand, <https://nees.org/dataviewer/view/1064:ds/1172>, retrieved on 03/12/2015.
- Cooper Lab (2013). Grain size distributions Ottawa F-65 sand, <https://nees.org/dataviewer/view/1064:ds/1203>, retrieved on 02/04/2015.
- Cooper Lab (2013). Specific gravity of Ottawa F-65 sand, <https://nees.org/dataviewer/view/1064:ds/1173>, retrieved on 01/28/2015.
- Dafalias, Y. F., and M. T. Manzari (2004). Simple plasticity sand model accounting for fabric change effects, *Journal of Engineering Mechanics ASCE, ASCE* **130**(6), 622-634.
- Darby, K. M., J. D. Bronner, A. M. Parra Bastidas, R. W. Boulanger, and J. T. DeJong (2016). Effect of shaking history on cone penetration resistance and cyclic strength of saturated sand, in *Geotechnical and Structural Engineering Congress*, Phoenix, AZ, USA.
- Das, B. (1997). Specific gravity, in *Soil mechanics laboratory manual* Engineering press, Austin, TX, USA, pp. 9-4.
- Das, B. (1997). Constant head permeability test in sand, in *Soil mechanics laboratory manual*, Engineering Press, Austin, TX, USA, pp. 69-74.
- De Alba, P., B. Seed, and C. K. Chan (1976). Sand liquefaction in large-scale simple shear tests, *Journal of the Geotechnical Engineering Division, ASCE* **102**(GT9), 909-919.
- Dennis, N. D. (1988). Influence of specimen preparation techniques and testing procedures on undrained steady state shear strength, in *Advanced Triaxial Testing of Soil and Rock, ASTM STP 97*, pp. 642-654, ASTM, Louisville, KY, USA.
- Doygun, O. (2009). Monotonic and cyclic undrained loading behavior of intermediate soils, Master's thesis, University of California, Davis, 336 pp.
- Dyvik, R., T. Berre, S. Lacasse, and B. Raadim (1987). Comparison of truly undrained and constant volume direct simple shear test, *Geotechnique*, **37**(1), 3-10.
- El-Sekelly, W., T. Abdoun, and R. Dobry (2015). Liquefaction resistance of a silty sand deposit subjected to preshaking followed by extensive liquefaction, *Journal of Geotechnical and Geoenvironmental Engineering, ASCE* **142**(4), 04015101-04015101-04015112.
- El-Sekelly, W., T. Abdoun, and R. Dobry (2016). PRESHAKE: a database for centrifuge modeling of the effect of seismic preshaking history on the liquefaction resistance of sands, *Earthquake*

Spectra In-Press., doi:<http://dx.doi.org/10.1193/082515EQS131DP>.

- Erickson, R. P. (2013). The influence of non-plastic fines on intermediate soil compressibility: a laboratory study, Master's thesis, University of California, Davis, 47 pp.
- Fitzpatrick, K. T., and C. H. Summerson (1971). Some observations on electron micrographs of quartz sand grains, *Ohio Journal of Science*, **71**(2), 106-119.
- Frost, J. D., and D. J. Jang (2000). Evolution of sand microstructure during shear, *Journal of Geotechnical and Geoenvironmental Engineering, ASCE* **126**(2), 116-130.
- Geocomp (2014). Dry densities Ottawa F-65 sand, <https://nees.org/dataviewer/view/1064:ds/1172>, retrieved on 03/06/2015.
- Gilbert, P. A. (1984). Investigation of density variation in triaxial test specimens of cohesionless soil subjected to cyclic and monotonic loading Report No. GL-84-10, U.S. Army Corps of Engineers, Waterways Experiment Station, Vicksburg, MS, USA.
- Gomez, M. G., and A. M. Parra Bastidas (2016). SEM images of Ottawa F-65 sand grains, photo album, <https://nees.org/resources/13738>, retrieved on 08/18/2016.
- Goto, S. (1988). Influence of freeze thaw history on undrained cyclic strength of sandy soils, *Soils and Foundations*, **33**(4), 148-158.
- Hagerty, M. M., D. R. Hite, C. R. Ulrich, and D. J. Hagerty (1993). One-dimensional high-pressure compression of granular media, *Journal of Geotechnical Engineering, ASCE* **119**(1), 1-18.
- Hardin, B. O., and F. E. J. Richart (1963). Elastic wave velocities in granular soils, *Journal of Soils Mechanics and Foundations Division, ASCE* **89**(1), 33-65.
- Head, K. H. (1988). Permeability and erodibility tests, in *Manual of soil laboratory testing volume 2 permeability, shear strength and compressibility tests*, Pentech Press, Plymouth, England, pp. 398-468.
- Hicklin, A., and G.-Y. Liu (2012). Spectral imaging facility poster, <http://neat.ucdavis.edu>, retrieved on 08/01/2016.
- Hung, W.-Y. (2014). Centrifuge modeling test by National Central University Ottawa F-65 sand, <https://nees.org/dataviewer/view/1064:ds/1203>, retrieved on 03/06/2015.
- Idriss, I. M., and R. W. Boulanger (2008). *Soil liquefaction during earthquakes*, EERI, Oakland, CA, USA.
- Ishihara, K., M. Sodekawa, and Y. Tanaka (1978). Effects of overconsolidation on liquefaction characteristics of sands containing fines, in *Dynamic geotechnical testing ASTM STP 654*, pp. 246-264, ASTM, Denver, CO, USA.
- Ishihara, K., and S. Okada (1978). Yielding of overconsolidated sand and liquefaction model under cyclic stresses, *Soils and Foundations*, **18**(1), 51-66.
- Ishihara, K., and H. Takatsu (1979). Effects of overconsolidation and K_0 conditions on the liquefaction characteristics of sands, *Soils and Foundations*, **19**(4), 59-69.
- Ishijara, K., and S.-I. Li (1972). Liquefaction of saturated sand in triaxial torsion shear test, *Soils and Foundations*, **12**(2), 19-39.
- Ishijara, K., and M. Yoshimine (1992). Evaluation of settlements in sand deposits in following liquefaction during earthquakes, *Soils and Foundations*, **32**(1), 173-188.
- J. I. S. Committee (2009). Test method for minimum and maximum densities of sands, JIS A 1224

- Kalinski, M. (2006). Measurement of specific gravity of soil solids, in *Soil mechanics lab manual*, John Wiley & Sons, New York, NY, USA, pp. 11-15.
- Kalinski, M. (2006). Measurement of hydraulic conductivity of granular soil using a fixed-wall permeameter, in *Soil mechanics lab manual*, John Wiley & Sons, USA, pp. 86-98.
- Kutter, B. L., and Y.-R. Chen (1997). Constant p' and constant volume friction angles are different, *Geotechnical Testing Journal*, **20**(3), 304-316.
- Lambe, T. W., and R. B. Whitman (1969). Chapter 12 stress-strain relationships in *Soil Mechanics*, John Wiley & Sons, New York, NY, USA, pp 553.
- Lee, K. L., and H. B. Seed (1967). Drained strength characteristics of sands, *Journal of Soils Mechanics and Foundations Division*, ASCE **93**(SM6), 117-141.
- Lee, K. L., and J. A. Focht (1975). Liquefaction potential at Ekofisk Tank in North Sea, *Journal of Geotechnical Engineering Division*, ASCE **101**(GT1), 1-18.
- Lees, J. J., R. H. Ballagh, R. P. Orense, and S. Van Ballegooy (2015). CPT-based analysis of liquefaction and re-liquefaction following the Canterbury earthquake sequence, *Soil Dynamics and Earthquake Engineering*, **79**, 304–314.
- Li, X.-S., Y. F. Dafalias, and Z.-L. Wang (1999). State-dependent dilatancy in critical-state constitutive modelling of sand, *Canadian Geotechnical Journal*, **36**(4), 599-511.
- Liu, C., and J. B. Evett (2013). Determining the specific gravity of soil, in *Soil properties, testing, measurement, and evaluation*, Prentice Hall, Upper Saddle River, NJ, USA, pp. 41-56.
- Liu, C., and J. B. Evett (2013). Permeability test for granular soils (constant-head method), in *Soil properties, testing, measurement, and evaluation*, Prentice Hall, Upper Saddle River, NJ, USA, pp. 241-220.
- Loudon, A. G. (1952). The computation of permeability from simple soil tests, *Geotechnique*, **3**(4), 165-183.
- Manzari, M. T., et al. (2014). LEAP projects: concept and challenges, in *n Proceedings, 4th International Conference on Geotechnical Engineering for Disaster Mitigation and Rehabilitation*, pp. 109-116, CRC Press, Kyoto, Japan, doi:DOI: 10.1201/b17438-14.
- Mesri, G., and B. Vardhanabhuti (2009). Compression of granular materials, *Canadian Geotechnical Journal*, **46**(4), 369-392.
- M. D. o. N. (2016). St. Peter sandstone, <http://dnr.mo.gov/geology/geosrv/imac/stpetersandstone.htm>, retrieved on 08/25/2016.
- Mulilis, J. P., H. B. Seed, C. K. Chan, J. K. Mitchell, and K. Arulanandan (1977). Effect of sample preparation on sand liquefaction, *Journal of the Geotechnical Engineering Division*, ASCE **103**(2), 91-08.
- Nagase, H., S. Yasuda, S. Tsujino, R. Shinji, and T. Yanagihata (1996). Liquefaction strength characteristics of overconsolidated sand samples, in *11th World Conference on Earthquake Engineering*, Acapulco, Mexico.
- Nagase, H., K. Shimizu, A. Hiro-Oka, S. Mochinaga, and M. Ohta (2000). Effects of overconsolidation on liquefaction strength of sandy soil samples, in *12th World Conference on Earthquake Engineering*, pp. 1-8, Auckland, New Zealand.
- Nakata, Y., M. Hyodo, A. F. L. Hyde, Y. Kato, and H. Murata (2001). Microscopic particle crushing of sand subjected to high pressure one-dimensional compression, *Soils and Foundations*, **41**(1), 69-82.

- NEESHub (2016). <https://nees.org/warehouse/welcome>
- Oda, M., K. Kawamoto, K. Suzuki, H. Fujimori, and M. Sato (2001). Microstructural interpretation on reliquefaction of saturated granular soils under cyclic loading, *Journal of Geotechnical and Geoenvironmental Engineering, ASCE* **127**(5), 416-423.
- Okamura, M., M. Ishihara, and T. Oshita (2003). Liquefaction resistance of sand deposit improved with sand compaction piles, *Soils and Foundations*, **43**(5), 175-187.
- Parra Bastidas, A. M., R. W. Boulanger, T. J. Carey, and J. T. DeJong (2016). Ottawa F-65 sand data from Ana Maria Parra Bastidas, <http://dx.doi.org/10.17603/DS2MW2R>, retrieved on 05/30/2016.
- Pestana, J. M., and A. J. Whittle (1995). Compression model for cohesionless soils, *Geotechnique*, **45**(4), 611-631.
- Pestana, J. M., and A. J. Whittle (1999). Formulation of a unified constitutive model for clays and sands, *International Journal for Numerical and Analytical Methods in Geomechanics*, **23**(12), 1215-1243.
- Pillai, V. S., and R. A. Stewart (1994). Evaluation of liquefaction potential of foundation soils of Duncan Dam, *Canadian Geotechnical Journal*, **31**(6), 951-966.
- Price, A. B., J. T. DeJong, R. W. Boulanger, A. M. Parra Bastidas, and D. M. Moug (2016). Effect of prior strain history on cyclic strength and CPT penetration resistance of silica silt, in *Geotechnical and Structural Engineering Congress*, ASCE, Phoenix, AZ, USA.
- Price, A. B., J. T. DeJong, R. W. Boulanger (2016). Cyclic loading response of silt with multiple loading events, *Journal of Geotechnical and Geoenvironmental Engineering* (under review).
- Powrie, W. (2004). *Soil mechanics: Concepts and applications*, Second ed., Taylor & Francis, London, United Kingdom, pp. 704.
- Roberts, J. E., and J. M. DeSouza (1958). The compressibility of sands, *American Society for Testing Materials*, **58**, 1269-1277.
- Roberts, J. E. (1964). Sand compression as a factor in oil field subsidence, PhD thesis, Massachusetts Institute of Technology, 318 pp.
- Ruffatto, M. (2013). Recommendation for a new standard sand for use at the UC Davis Geotechnical Modeling Center Master's thesis, University of California, Davis 50 pp.
- Santamarina, J. C., and G. J. Cho (2001). Determination of critical state parameters in sandy soils—simple procedure, *Geotechnical Testing Journal*, **24**(2), 185-192.
- Sasitharan, S., P. K. Robertson, D. C. Sego, and N. R. Morgenstern (1993). Collapse behavior of sand, *Canadian Geotechnical Journal*, **31**(4), 569-577.
- Sasitharan, S., P. K. Robertson, D. C. Sego, and N. R. Morgenstern (1994). State-boundary surface for very loose sand and its practical implications, *Canadian Geotechnical Journal*, **31**(3), 321-334.
- Seed, H. B., and W. H. Peacock (1971). Test procedures for measuring soil liquefaction characteristics, *Journal of the Soil Mechanics and Foundations Division, ASCE* **97**(SM8), 1099-1119.
- Seed, B., K. Mori, and C. K. Chan (1977). Influence of seismic history on liquefaction of sands, *Journal of Geotechnical Engineering Division, ASCE* **103**(GT4), 257-270.
- Sheng, D., Y. Yao, and J. P. Carter (2008). A volume–stress model for sands under isotropic and critical stress states, *Canadian Geotechnical Journal*, **45**(11), 1639–1645.
- Silica, U. (2016). Product data: F-65 whole grain silica plant: Ottawa, Illinois, US Silica,

- <https://www.ussilica.com>, retrieved on 02/04/2015.
- Singh, S., H. B. Seed, and C. K. Chan (1982). Undisturbed sampling of saturated sands by freezing, *Journal of the Geotechnical Engineering Division, ASCE* **108**(2), 247-264.
- Stringer, M. (2015). Grain size distribution of Ottawa F-65 sand, <https://nees.org/dataviewer/view/1064:ds/1203>, retrieved on 02/04/2015.
- Sukumaran, B., and A. K. Ashmawy (2001). Quantitative characterization of the geometry of discrete particles, *Geotechnique*, **51**(7), 619-627.
- Tatsuoka, F., K. Ochi, S. Fujii, and M. Okamoto (1986). Cyclic undrained triaxial and torsional shear strength of sands for different sample preparation methods, *Soils and Foundations*, **26**(3), 23-41.
- Toki, S., F. Tatsuoka, S. Miura, Y. Yoshimi, S. Yasuda, and Y. Makihara (1986). Cyclic undrained triaxial strength of sand by a cooperative test program, *Soils and Foundations*, **26**(3), 117-128.
- Towhata, I., K. Gunji, Y. A. Hernandez, and S. Yamada (2014). Laboratory tests on cyclic undrained behavior of loose sand with cohesionless silt and its application to assessment of seismic performance of subsoil, in *Soil liquefaction during recent large-scale earthquakes*, CRC Press, London, United Kingdom, pp. 79-94.
- Vasko, A., M. El Ghoraihy, and M. T. Manzari (2014). An investigation into the behavior of Ottawa sand under monotonic and cyclic shear tests, Master's thesis, The George Washington University, 119 pp.
- Wakamatsu, K. (2012). Recurrent liquefaction induced by the 2011 Great East Japan earthquake compared with the 1987 earthquake, in *The International Symposium on Engineering Lessons Learned from the 2011 Great East Japan Earthquake*, pp. 675-686, Tokyo, Japan.
- Wijewickreme, D., A. Dabeet, and P. Byrne (2013). Some observations on the state of stress in the direct simple shear test using 3D discrete element analysis, *Geotechnical Testing Journal*, **36**(2), 1-8.
- Wikipedia (2016). St. Peter sandstone, https://en.wikipedia.org/wiki/St._Peter_Sandstone, retrieved on 08/25/2016.
- Wilson, D. (2012). RESDAQ software.
- Yoshimi, Y., K. Tokimatsu, O. Kaneko, and Y. Makihara (1984). Undrained cyclic shear strength of dense Niigata sand, *Soils and Foundations*, **24**(4), 131-145.
- Yoshimi, Y., K. Tokimatsu, and Y. Hosaka (1989). Evaluation of the liquefaction resistance of clean sands based on high-quality undisturbed samples, *Soils and Foundations*, **29**(1), 93-04.
- Zhou, Y. G. (2014). Ottawa F-65 sand index properties, <https://nees.org/resources/13689>, retrieved on 02/04/2015.
- Ziotopoulou, K., A. B. Price, J. T. DeJong, and R. W. Boulanger (2013). Direct simple shear testing of sands: procedures and specifications Report No. first draft, Soil Interactions Laboratory, University of California, Davis, CA, USA.
- Ziotopoulou, K. (2014). Nevada sand undrained cyclic DSS results.
- Ziotopoulou, K. (2014). A sand plasticity model for earthquake engineering applications, PhD thesis, University of California, Davis, 243 pp.